

EXPERIMENTAL INVESTIGATION AND MODELLING  
OF SURFACE INTEGRITY, ACCURACY AND  
PRODUCTIVITY ASPECTS IN EDM OF AISI D2 STEEL

A DISSERTATION SUBMITTED TO  
THE DEPARTMENT OF MECHANICAL ENGINEERING  
NATIONAL INSTITUTE OF TECHNOLOGY,  
ROURKELA (INDIA)



in partial fulfilment of the requirements  
for the degree of  
**Doctor of Philosophy**

UNDER THE GUIDANCE OF  
Dr. C. K. Biswas

By  
Mohan Kumar Pradhan  
April 2010

EXPERIMENTAL INVESTIGATION AND MODELLING  
OF SURFACE INTEGRITY, ACCURACY AND  
PRODUCTIVITY ASPECTS IN EDM OF AISI D2 STEEL

Thesis submitted in partial fulfilment  
for the Award of the degree of

Doctor of Philosophy

*in*

**Mechanical Engineering**

*by*

**Mohan Kumar Pradhan**

*under the guidance of*

Dr. C. K. Biswas



Department of Mechanical Engineering  
National Institute of Technology,  
Rourkela-769008, Odissa, India



**National Institute of Technology Rourkela**  
**Rourkela-769008, Odissa, India**

**Certificate**

This is to certify that the thesis titled **“Experimental Investigation and Modelling of Surface Integrity, Accuracy and Productivity Aspects of AISI D2 Steel in EDM”** being submitted by Mr. Mohan Kumar Pradhan to the National Institute of Technology, Rourkela for the award of the degree of DOCTOR OF PHILOSOPHY is a record of bonafide research carried out by him under my guidance and supervision. Mr. Pradhan has worked for about three and half years on the above problem and the work has reached the standard fulfilling the requirements and the regulations relating to the degree. To the best of our knowledge the work incorporated in this thesis has not been submitted to any other University or Institute for the award of any other degree or diploma.

Dr. C. K. Biswas,  
Associate Professor,  
Mechanical Engineering Department,  
National Institute of Technology,  
Rourkela (India)

---

## *Acknowledgement*

---

---

I express my deep sense of gratitude and indebtedness to my thesis supervisor, Dr. C. K. Biswas, for providing precious guidance, inspiring discussions and constant supervision throughout the course of this work. His timely help, constructive criticism, and conscientious efforts made it possible to present the work contained in this thesis.

I would like to thank Prof. Sunil Kumar Sarangi, Director, NIT Rourkela, for creating a healthy working environment at NIT campus and for timely help I received from him. I thank Prof. R. K. Sahoo, Head and Prof. B.K. Nanda, former Head of Mechanical Engineering Department for facilitating various equipments for completion of this work. I am grateful to all staff members of the department for their useful suggestions and for the help rendered to me in carrying out this work.

I am grateful to Prof. S. S. Mohapatra, Head, Central Workshop; Prof. B. B. Verma, Head, Metallurgy and Material Engg. Department; Prof. D. Chaira, Head, and Prof. U. K. Mohanty, former Head, SEM centre extended cooperation during experimentation. I would also like to thank Shyamu Hembram, Sameer Pradhan and Rajesh Pattanik for extending their cooperation during the experimental work.

I would also express my gratitude to Prof. Indradev Samajdar, IIT Bombay, and his staff (Late) Miss Sweta for availing facility at National Facility of Texture & OIM for the measurement of residual stress during experimentation.

I am thankful to my wife Smt. Alka Pradhan and my loving son Shri Utkarsh Pradhan (Ayush) for their inspiration, tolerance, sacrifice, moral support, love and encouragement. The thesis would remain incomplete without mentioning the contributions and supports of my parents for making me what I am today.

I am thankful to Mr. R. Das for his advice & support, especially in understanding soft computing techniques. I also thank my fellow research scholar for their support and cooperation during my stay in the campus. I offer my regards and blessings to all of those who supported me in any respect during the completion of my Ph.D work.

Finally, I wish to acknowledge the financial support given by the Ministry of Human Resource Development, Government of India during my tenure of stay at National Institute of Technology, Rourkela.

**Mohan Kumar Pradhan**



## DEDICATION

*This work is dedicated to*

*Almighty Lord Jagannath*

## ABSTRACT

---

---

Electrical Discharge Machining (EDM) is one of the most popular non-traditional machining process for “difficult to machine” conducting materials and is quite extensively and successfully used in industry owing to its favourable features and advantages that it can offer. In EDM, the objective is always to get improved Material Removal Rate (MRR) along with achieving better surface quality of machined component. Furthermore, the essential requirements are as small a thermally affected region of the workpiece surface as possible and a lower radial overcut with minimal tool wear. The quality of a machined surface is becoming increasingly significant to satisfy the increasing demands of superior component performance, longevity, and reliability thus preserving the integrity of the surface is essential. In order to sustain and/or improve reliability of the components, it is always necessary to have knowledge of the effects of the manufacturing parameters on the surface integrity, precision and productivity of the EDMed components.

AISI D2 tool steel has a growing range of application in die and mould industries. They are widely used in the manufacture of blanking and cold-forming dies for the production of a wide range of automotive and electronic components. This steel has greater strength and toughness, and is categorised as “difficult to machine” material, which pose a major challenge during machining.

An experimental investigation is presented to explore the surface integrity, productivity and accuracy of the EDMed surface. Parametric analysis has been carried out by conducting a set of experiments using AISI D2 tool steel workpiece with copper electrode. The investigating factors were discharge current ( $I_p$ ), pulse duration ( $T_{on}$ ), duty factor ( $T_{au}$ ) and discharge voltage ( $V$ ). The effect of the machining parameters on the responses such as surface roughness, residual stress, White Layer Thickness (WLT), Surface Crack Density (SCD), MRR, Tool Wear Rate (TWR), and

overcut are investigated.

An experimental analysis was performed to establish the most important machining parameters that contribute to white layer formation and surface crack density. The experimental plan for these investigations was conducted according to the Response surface methodology and the results were statistically evaluated using analysis of variance. Surface topography and sub-surface structures are investigated by scanning electron microscopy. It is established that average recast layer thickness with an increasing discharge current, pulse duration and duty cycle, but the SCD decreases with increase in discharge current and pulse duration. However, the pulse current is the most dominating parameter followed by pulse duration for both the responses. Results showed that current is the most significant parameter that influenced the machining responses. However, the recast layer thickness increases with increasing discharge current, pulse duration and duty cycle. But the SCD decreases with increase in discharge current and pulse duration.

Besides, similar investigation is conducted for the surface roughness and the input factors that significantly influenced the output response are discharge current, pulse duration and  $Tau$ . Also it reveals that in order to obtain better surface quality the discharge current, pulse on time and the duty factor should be set as low as possible.

Finite Element Method (FEM) was employed to evaluate the residual stress. The results show that the peak temperature sharply increases with pulse current. The workpiece is severely affected by the thermal stresses to a larger depth with increasing pulse energy. The nature of residual stresses is predominantly tensile in nature and the stress levels reaches its maximum values close to the surface but diminishes very rapidly to comparatively low values of compressive residual stresses in the sub-surface area. The residual stresses were obtained by XRD measurement technique and the trend of these stresses with depth has an excellent agreement with the FEM results. The maximum tensile and compressive residual stresses are not effected much by the machining parameters. However, with the pulse energy the depth at which they occur increases.

Full factorial design is employed to evaluate MRR, TWR and Radial overcut (OC). Soft computing predictive modelling (ANN, Neuro-fuzzy Mamdani and Neuro-fuzzy

Sugeno) of these responses has been conducted from experimentally obtained data. The discharge current is the most dominant factor, followed by pulse duration, duty factor and discharge voltage, for MRR and overcut. While, the same for TWR is pulse duration, discharge current, discharge voltage, and duty factor. The performance of soft computing models for predicting these responses are found to be comparable in terms of the prediction accuracy and speed. However, the Mamdani model is converging with a lower Mean Square Error (MSE) than the Sugeno system and the ANN network is in general converging much faster than the other two. The average prediction errors for all these models are quite comparable.

**Keywords:** Electric Discharge Machining, White Layer Thickness, Surface Crack Density, Surface Roughness, Residual Stresses, Finite Element Modelling, Material Removal Rate, Tool Wear Rate, Radial Overcut, Neuro-Fuzzy Model, Artificial Neural Network.

## LIST OF ABBREVIATIONS

ANN	-	Artificial neural network
ANOVA	-	Analysis of variance
CCD	-	Central composite design
DOE	-	Design of experiments
EDM	-	Electro discharge machining/Electrical discharge machining
FEM	-	Finite element method
G	-	Gap
HAZ	-	Heat affective zone
MRR	-	Material/metal removal rate
OC	-	Radial overcut
RSM	-	Response surface methodology
RS	-	Residual stress
SCD	-	surface crack density
SEM	-	Scanning electron microscopy
SR	-	Surface roughness
TWR	-	Tool wear rate
WLT	-	White Layer Thickness
XRD	-	X-ray diffraction

## NOMENCLATURE

$\alpha_t$	coefficient of thermal expansion, ( $K^{-1}$ )
$\beta_i$	unknown linear coefficient in the regression model
$\beta_o$	unknown constant coefficient in the regression model
$\beta_{ij}$	unknown interaction coefficient in the regression model
$\epsilon_{\theta\theta}$	normal strain in circumferential direction
$\epsilon_{rr}$	normal strain in radial direction
$\epsilon_{zz}$	normal strain in axial direction
$\epsilon$	error in the regression model
$\gamma_{rz}$	shear strain
$[D]$	elasticity matrix
$\{\epsilon\}$	strain matrix
$\{\sigma\}$	stress matrix
$\nu$	poisson's ratio
$\rho_t$	density of the electrode, ( $kg/m^3$ )
$\rho_w$	density of the workpiece, ( $kg/m^3$ )
$\sigma_{\theta\theta}$	normal stress in circumferential direction, (Pa)
$\sigma_{rr}$	normal stress in radial direction, (Pa)
$\sigma_{zz}$	normal stress in axial direction, (Pa)

$\sigma_0$	initial stress produced by change in temperature $\Delta T$ , (Pa)
$\sigma_{rz}$	shear stress, (Pa)
$C_p$	specific heat capacity of workpiece material, (J/kgK)
$d_i$	diameter of the impression or cavity produce by the tool on the workpiece, ( $\mu\text{m}$ )
$d_t$	diameter of the tool, ( $\mu\text{m}$ )
$E$	modulus of elasticity, (Pa)
$I_p$	discharge current, (A)
$k$	thermal conductivity of the material, (W/mk)
$l$	discharge length, ( $\mu\text{m}$ )
$P_f$	percentage of heat input distributed to the workpiece
$R^2$	Coefficient of determination
$R_{adj}^2$	Adjusted coefficient of determination
$R_p$	spark radius, plasma radius, ( $\mu\text{m}$ )
$Ra$	centre-line average surface roughness, ( $\mu\text{m}$ )
$T$	temperature (K)
$t$	duration (time) of the machining process, (s)
$T_b$	boiling temperature, (K)
$T_{off}$	cooling period, pulse off time, ( $\mu\text{s}$ )
$T_{on}$	heating period, pulse on time, ( $\mu\text{s}$ )
$T_{on} + T_{off}$	pulse period, ( $\mu\text{s}$ )
$u$	displacement in radial direction, ( $\mu\text{m}$ )
$U_b$	breakdown (discharge) voltage, (V)

$w$	displacement in axial direction, ( $\mu\text{m}$ )
$X_{ii}^2$	square terms in the regression model
$X_i$	input variables in the regression model
$X_i X_j$	interaction terms in the regression model
$Y$	response variable in the regression model
$\Delta T$	change in temperature, (K)
$\Delta V_t$	volume loss from the electrode/tool, ( $\text{mm}^3$ )
$\Delta V_w$	volume loss from the workpiece, ( $\text{mm}^3$ )
$\Delta W_t$	weight loss from the electrode/tool, (g)
$\Delta W_w$	weight loss from the workpiece, (g)



## CONTENTS

<i>DEDICATION</i> . . . . .	v
<i>Abstract</i> . . . . .	vi
<i>1. Introduction</i> . . . . .	2
1.1 Overview . . . . .	2
1.2 Background of Research . . . . .	3
1.2.1 Types of Electric Discharge Machines . . . . .	4
1.2.2 Mechanism of Material Removal in Electrical Discharge Machining . . . . .	6
1.2.3 EDM process parameters . . . . .	9
1.3 Key areas of research in Die Sinking EDM . . . . .	11
1.3.1 EDM performance measures . . . . .	11
1.3.2 Surface integrity of EDMed surface . . . . .	16
1.3.3 EDM Modelling . . . . .	23
1.3.4 EDM on AISI D2 steel . . . . .	26
1.4 Research scope and Problem statement . . . . .	32
1.4.1 Research Design . . . . .	33
1.5 Summary of chapters . . . . .	35
<i>2. Response surface model for prediction of White Layer Thickness and Surface Crack Density</i> . . . . .	38
2.1 Introduction . . . . .	38
2.2 Experimentation . . . . .	41
2.2.1 Equipment and workpiece material . . . . .	41
2.2.2 Experimental Procedure . . . . .	41

2.3	Measurement of Responses . . . . .	42
2.3.1	Measurements of White Layer Thickness . . . . .	42
2.3.2	Measurements of Surface crack density . . . . .	42
2.4	Planning based on RSM . . . . .	43
2.5	Elucidation of response model for WLT . . . . .	44
2.6	Elucidation of response model for SCD . . . . .	55
2.7	Result and discussion . . . . .	62
2.7.1	Effect of machining parameters on WLT . . . . .	62
2.7.2	Scanning Electron Microscopy (SEM) images for WLT . . . . .	68
2.7.3	Effect of the machining parameters on SCD . . . . .	71
2.7.4	Scanning Electron Microscopy (SEM) images for SCD . . . . .	73
2.8	Confirmation Test . . . . .	78
2.9	Conclusion . . . . .	80
3.	<i>Response surface model for prediction of Surface Roughness</i> . . . . .	82
3.1	Introduction . . . . .	82
3.2	Experimentation . . . . .	84
3.3	Surface roughness measurements . . . . .	84
3.4	Planning based on Response Surface Methodology . . . . .	86
3.4.1	RSM model development and Residual Analysis. . . . .	89
3.5	Result and discussion . . . . .	93
3.6	Scanning Electron Microscopy (SEM) results . . . . .	99
3.7	Conclusion . . . . .	102
4.	<i>Finite-Element Modelling of Residual Stress</i> . . . . .	104
4.1	Introduction . . . . .	104
4.2	Model detail . . . . .	105
4.2.1	Assumptions . . . . .	105
4.2.2	Thermal model . . . . .	106
4.2.3	Equilibrium Equations . . . . .	106
4.2.4	Stress-Strain-Temperature Relations . . . . .	108
4.2.5	Spark radius/Plasma radius . . . . .	109

4.2.6	Heat Flux and Energy Portion . . . . .	110
4.2.7	Boundary condition . . . . .	111
4.2.8	Numerical Model . . . . .	112
4.3	Experimentation . . . . .	116
4.3.1	Experimental procedure . . . . .	116
4.3.2	X-ray diffraction measurements and data analysis . . . . .	119
4.4	Discussion of the Results . . . . .	128
4.4.1	Temperature distribution . . . . .	128
4.4.2	Thermal stress distribution . . . . .	133
4.4.3	Residual stress distribution . . . . .	133
4.4.4	Effect of machining parameters on Temperature profile . . . . .	139
4.4.5	Effect of machining parameters on thermal stress . . . . .	141
4.4.6	Effect of machining parameters on residual stress . . . . .	143
4.4.7	Experimental Validation of residual stress . . . . .	145
4.5	Conclusion . . . . .	148
5.	<i>Soft computing models based prediction of MRR, TWR and Overcut . . . . .</i>	153
5.1	Introduction . . . . .	153
5.2	Description of the experiments . . . . .	154
5.2.1	Equipment and workpiece material . . . . .	154
5.2.2	Experimental procedure . . . . .	154
5.2.3	Machining performance evaluations . . . . .	154
5.2.4	Experimental design and parameter selection . . . . .	156
5.3	Proposed models . . . . .	165
5.3.1	Artificial neural network (ANN) . . . . .	165
5.3.2	Neuro-fuzzy (NF) models . . . . .	167
5.4	Result and Discussion . . . . .	173
5.4.1	Analysis on responses . . . . .	174
5.4.2	Model validation . . . . .	180
5.5	Conclusion . . . . .	186

6. <i>Conclusion</i> . . . . .	192
6.1 Major Contribution . . . . .	195
6.2 Recommendations for Future Research . . . . .	196
 <i>Appendix</i>	197
 A. <i>Equipments used</i> . . . . .	198
 B. <i>Design of Experiments</i> . . . . .	209
 C. <i>X-Ray Diffraction Technique</i> . . . . .	221
 D. <i>Artificial Neural Network</i> . . . . .	225
 E. <i>Neuro-Fuzzy</i> . . . . .	233

## LIST OF TABLES

1.1 Comparative analysis on research on AISI D2 steel and copper tool . . . . .	29
1.1 Comparative analysis on research on AISI D2 steel and copper tool.(Contd.) . . . . .	30
1.1 Comparative analysis on research on AISI D2 steel and copper tool.(Contd.) . . . . .	31
2.1 Input variables used in the experiment and their levels. . . . .	42
2.2 Observation for Crack Length and WLT. . . . .	49
2.2 Observation for Crack Length and WLT.(Contd.) . . . . .	50
2.2 Observation for Crack Length and WLT.(Contd.) . . . . .	51
2.3 Comparison of experimental and model prediction results for WLT and SCD. . . . .	52
2.3 Comparison of experimental and model prediction results for WLT and SCD.(Contd.) . . . . .	53
2.3 Comparison of experimental and model prediction results for WLT and SCD.(Contd.) . . . . .	54
2.4 $R^2$ and $R_{adj}^2$ test for WLT regression model. . . . .	54
2.5 Estimated Regression Coefficients for WLT (Before elimination). . . . .	55
2.6 Estimated Regression Coefficients for WLT (After backward elimination). . . . .	55
2.7 The ANOVA for the fitted WLT models. . . . .	56
2.8 $R^2$ and $R_{adj}^2$ test for SCD regression model. . . . .	60
2.9 Estimated Regression Coefficients for SCD (Before elimination). . . . .	60
2.10 Estimated Regression Coefficients for SCD (After backward elimination). . . . .	61
2.11 The ANOVA for the fitted SCD models. . . . .	61
2.12 Sample predicted data from the RSM model. . . . .	80
3.1 Input variables used in the experiment and their levels. . . . .	86
3.2 Observation for Surface Roughness. . . . .	87
3.2 Observation for Surface Roughness.(Contd.) . . . . .	88

3.3	Comparison of experimental and model prediction results for surface roughness. . . . .	88
3.3	Comparison of experimental and model prediction results for surface roughness.(Contd.) . . . . .	89
3.4	$R^2$ and $R_{adj}^2$ test for SR regression model. . . . .	90
3.5	Estimated Regression Coefficients for Surface roughness (Before elimination). . . . .	90
3.6	Estimated Regression Coefficients for Surface roughness(After backward elimination). . . . .	92
3.7	The ANOVA table for the fitted Surface roughness models. . . . .	93
4.1	Spark Radius obtain from Equation 4.12 . . . . .	110
4.2	Input variables used in the experiment and their levels. . . . .	120
4.3	Experimental design matrix for RS . . . . .	120
4.4	X-ray diffraction conditions. . . . .	120
4.5	Experimental result of residual stress for all specimens . . . . .	122
4.6	Peak thermal and residual stress from FEM . . . . .	150
5.1	Experimental conditions . . . . .	156
5.2	Observations for MRR, TWR and G. . . . .	157
5.2	Observation for MRR, TWR and G.(Contd.) . . . . .	158
5.2	Observation for MRR, TWR and G.(Contd.) . . . . .	159
5.2	Observation for MRR, TWR and G.(Contd.) . . . . .	160
5.2	Observation for MRR, TWR and G.(Contd.) . . . . .	161
5.2	Observation for MRR, TWR and G.(Contd.) . . . . .	162
5.2	Observation for MRR, TWR and G.(Contd.) . . . . .	163
5.3	ANOVA for MRR,TWR and G . . . . .	164
5.4	Learning behavior . . . . .	173
5.5	Testing the capability of all the models for prediction of MRR . . . . .	188
5.6	Testing the capability of all the models for prediction of TWR . . . . .	189
5.7	Testing the capability of all the models for prediction of G . . . . .	190
A.1	Technical Specifications of electro discharge machine . . . . .	199
A.2	Chemical composition of AISI D2 (wt %) . . . . .	201

A.3	Thermal properties of workpiece material (Kansal et al., 2007) . . . .	201
A.4	Temperature dependent modulus of elasticity, Poisson's ratio and density of Tool steel (Bhadeshia, 2002) . . . . .	201
A.5	Temperature dependent yield stress of steel (Barsoum, 2008; Jonsson et al., 1985) . . . . .	201

## LIST OF FIGURES

1.1 Schematic of an electric discharge machining machine tool . . . . .	6
1.2 The plasma channel . . . . .	8
1.3 Research Design Flow Chart . . . . .	34
2.1 Surface layers in EDMed workpiece . . . . .	39
2.2 SEM Micrograph (at 1000x) of an EDM surface showing globules and micro-cracks and pores. . . . .	40
2.3 Cut section of workpiece . . . . .	43
2.4 Normal plot of residuals for WLT ( The dotted lines show 95% confi- dence interval). . . . .	46
2.5 Histogram plot of residuals WLT. . . . .	47
2.6 Plot of standardised residuals vs. fitted value for WLT. . . . .	47
2.7 Predicted vs. experimental for WLT. . . . .	48
2.8 Normal plot of residuals for SCD. . . . .	58
2.9 Histogram plot of residuals SCD. . . . .	58
2.10 Plot of standardised residuals vs. fitted value for SCD . . . . .	59
2.11 Predicted vs. experimental SCD. . . . .	59
2.12 Effect of factors on WLT. . . . .	63
2.13 Comparison results for WLT obtained by Guu et al. (2003) and Lee et al. (1988) with different $I_p$ and $Ton$ . . . . .	65
2.14 Interaction effect of factors on WLT. . . . .	66
2.15 (a) Contour plot, (b) Response surface plot representing the effect of $I_p$ and $Ton$ on WLT . . . . .	67
2.16 (a) Contour plot, (b) Response surface plot representing the effect of $I_p$ and $Tau$ on WLT . . . . .	67



2.17 (a) Contour plot, (b) Response surface plot representing the effect of <i>Ton</i> and <i>Tau</i> on WLT. . . . .	67
2.18 SEM snap WLT at 1/75/85/50 . . . . .	70
2.19 SEM snap WLT at 5/75/85/50 . . . . .	70
2.20 SEM snap WLT at 9/75/85/50 . . . . .	70
2.21 SEM snap WLT at 5/50/85/50 . . . . .	70
2.22 SEM snap WLT at 5/100/85/50 . . . . .	70
2.23 SEM snap WLT at 5/75/80/50 . . . . .	70
2.24 SEM snap WLT at 5/75/90/50 . . . . .	70
2.25 Effect of factors on SCD. . . . .	73
2.26 Interaction effect of factors on SCD. . . . .	74
2.27 (a) Contour plot, (b) Response surface plot representing the effect of <i>Ip</i> and <i>Ton</i> on SCD . . . . .	74
2.28 SEM micrograph for 9/100/90/60 (SCD=0.01761 $\mu\text{m}/\mu\text{m}^2$ ) . . . . .	75
2.29 (a) Contour plot, (b) Response surface plot representing the effect of <i>Ip</i> and <i>V</i> on SCD . . . . .	75
2.30 SEM snap SCD at 1/75/85/50 . . . . .	77
2.31 SEM snap SCD at 5/75/85/50 . . . . .	77
2.32 SEM snap SCD at 9/75/85/50 . . . . .	77
2.33 SEM snap SCD at 5/50/85/50 . . . . .	77
2.34 SEM snap SCD at 5/100/85/50 . . . . .	77
2.35 SEM snap SCD at 5/75/85/40 . . . . .	77
2.36 SEM snap SCD at 5/75/85/60 . . . . .	77
2.37 WLT and SCD as a function of power for AISI D2 tool steels. . . . .	78
3.1 SEM micrograph of a EDMed AISI D2 tool steel surface . . . . .	83
3.2 Idealised stylus profile showing the mean line . . . . .	85
3.3 Normal plot of residuals for Ra. . . . .	94
3.4 Histogram plot of residuals for Ra. . . . .	94
3.5 Plot of residuals vs. fitted value for Ra. . . . .	95
3.6 Predicted vs. experimental Ra. . . . .	95
3.7 Effect of factors on Ra. . . . .	96

3.8	Comparison results for Surface roughness obtained by Guu et al. (2003) and Lee et al. (1988) with different $I_p$ and $T_{on}$ . . . . .	97
3.9	Interaction effect of factors on Ra. . . . .	98
3.10	(a) Contour & (b) Response surface plot depicting the effect of $I_p$ & $T_{on}$ on Ra . . . . .	99
3.11	SEM of EDMed surfaces of D2 Steel $I_p=1A$ ; $T_{on}=75 \mu s$ ; $T_{au}=85\%$ & $V=50V$ . . . . .	100
3.12	SEM of EDMed surfaces of D2 Steel $I_p=9A$ ; $T_{on}=75 \mu s$ ; $T_{au}=85\%$ & $V=50V$ . . . . .	101
3.13	SEM of EDMed surfaces of D2 Steel $I_p=5A$ ; $T_{on}=50 \mu s$ , $T_{au}=85\%$ & $V=50V$ . . . . .	101
3.14	SEM of EDMed surfaces of D2 Steel $I_p=5A$ ; $T_{on}=100 \mu s$ , $T_{au}=85\%$ & $V=50V$ . . . . .	102
4.1	Schematic sketch of the physical model. . . . .	107
4.2	An axisymmetric model for the EDM process simulation. . . . .	107
4.3	Mesh generation for FEM full model. . . . .	113
4.4	Temperature dependent bilinear kinematic isotropic hardening. . . . .	115
4.5	Heating and cooling cycle . . . . .	116
4.6	Flow chart for ANSYS solution procedure . . . . .	117
4.7	Convergence graph . . . . .	118
4.8	Isothermal lines at the end of pulse on time for $I_p=9A$ & $T_{on}=100\mu s$ . . . . .	118
4.9	Diffraction patterns obtained by scanning the topmost layer for $2\theta=70^\circ$ to $165^\circ$ . . . . .	123
4.10	X-ray diffraction peak in layer 1 for $2\theta=70^\circ$ to $75^\circ$ . . . . .	124
4.11	d versus $\sin^2\psi$ plot of layer 1 for $2\theta=70^\circ$ to $75^\circ$ . . . . .	124
4.12	X-ray diffraction peak in layer 2 for $2\theta=70^\circ$ to $75^\circ$ . . . . .	125
4.13	d versus $\sin^2\psi$ plot of layer 2 for $2\theta=70^\circ$ to $75^\circ$ . . . . .	125
4.14	X-ray diffraction peak in layer 3 for $2\theta=70^\circ$ to $75^\circ$ . . . . .	126
4.15	d versus $\sin^2\psi$ plot of layer 3 for $2\theta=70^\circ$ to $75^\circ$ . . . . .	126
4.16	X-ray diffraction peak in layer 4 for $2\theta=70^\circ$ to $75^\circ$ . . . . .	127
4.17	d versus $\sin^2\psi$ plot of layer 4 for $2\theta=70^\circ$ to $75^\circ$ . . . . .	127

4.18	Temperature distribution at the end of $T_{on}$ just before material ejection.	129
4.19	Temperature distribution at the end of pulse on time subsequent to material removal. . . . .	130
4.20	Detached/killed elements from the spark vicinity at the end of pulse.	130
4.21	Temperature distribution at the end of pulse off time. ( $I_p=9A, T_{on}=100\mu s$ )	131
4.22	Paths on working domain. . . . .	131
4.23	Variation of temperature with respect to time on diagonal path. . . .	132
4.24	Radial component of thermal stress ( $\sigma_{rr}$ ) at the end of pulse. . . . .	134
4.25	Axial component of thermal stress ( $\sigma_{zz}$ ) at the end of pulse. . . . .	134
4.26	Shear component of thermal stress ( $\sigma_{rz}$ ) at the end of pulse. . . . .	135
4.27	Von Misses thermal stress at the end of pulse. . . . .	135
4.28	Radial component of residual stress ( $\sigma_{rr}$ ) at the end of pulse period. .	137
4.29	Axial component of residual stress ( $\sigma_{zz}$ ) at the end of pulse period. .	137
4.30	Shear component of residual stress ( $\sigma_{rz}$ ) at the end of pulse period. .	138
4.31	Von Misses residual stress at the end of pulse period. . . . .	138
4.32	Residual stresses on surface path. . . . .	139
4.33	Residual stresses on diagonal path. . . . .	140
4.34	Residual stresses on symmetry path. . . . .	140
4.35	The effect of $I_p$ on the temperature variation with depth for $T_{on}=100\mu s$	142
4.36	The effect of $T_{on}$ on the temperature distribution for $I_p=9A$ . . . . .	142
4.37	Effect of $I_p$ and $T_{on}$ on thermal stress in radial direction along the centreline of workpiece. . . . .	144
4.38	Effect of $I_p$ and $T_{on}$ on thermal stress in axial direction along the centreline of workpiece. . . . .	144
4.39	FEA residual stress in radial direction ( $\sigma_{rr}$ ) along symmetric path . .	145
4.40	FEA residual stress in axial direction ( $\sigma_{zz}$ ) along symmetric path. . .	146
4.41	FEA residual shear stress ( $\sigma_{rz}$ ) along symmetric path. . . . .	146
4.42	Experimental residual stress in radial direction ( $\sigma_{rr}$ ) along symmetric path. . . . .	147
4.43	Experimental residual shear stress ( $\sigma_{rz}$ ) along symmetric path. . . . .	147

4.44	Effect of $I_p$ and $T_{on}$ on (a) peak Tensile residual stress (b) Depth at which it occurs ( $\mu\text{m}$ ).	149
5.1	Neural network architecture	166
5.2	Optimal number of neurons in the hidden layer in ANN model	168
5.3	Neuro fuzzy architecture	170
5.4	Optimal number of membership functions in Mamdani model	172
5.5	Main effect plot of the factors on MRR	175
5.6	Effect of pulse on-time ( $T_{on}$ ) on MRR	175
5.7	Interaction effect plot of the factors on MRR	176
5.8	SEM Micrograph at 4A/100 $\mu\text{s}$ /90%/40 V	177
5.9	SEM Micrograph at 10A/100 $\mu\text{s}$ /90%/40 V	177
5.10	Main effect plot of the factors on TWR	178
5.11	Interaction effect plot of the factors on TWR	179
5.12	Main effect plot of the factors on G	180
5.13	Interaction effect plot of the factors on G	180
5.14	Residuals of the validation data on MRR for the models.	182
5.15	Residuals of the validation data on TWR for the models.	182
5.16	Residuals of the validation data on G for the models.	183
5.17	Comparison of model predictions with experimental MRR	184
5.18	Comparison of model predictions with experimental TWR	184
5.19	Comparison of model predictions with experimental G	185
A.1	Die Sinker EDM, Brand : Electronica Elektra Plus; Model : PS 50ZNC	198
A.2	Copper Electrode and AISI D2 workpiece for MRR, TWR and OC	200
A.3	AISI D2 workpiece for WLT, SCD, SR and RS	200
A.4	Induction furnace	202
A.5	Electronic Balance	203
A.6	Talysurf Surface Roughness Analyser	203
A.7	Electro Polishing	204
A.8	Tool maker microscope	205
A.9	Scanning electron microscopy	206

A.10 Panalytical MRD System for Bulk Texture and Residual Stress Measurement . . . . .	207
A.11 X-ray texture and/or residual stress measurements . . . . .	208
B.1 Two-Variable Face Centered CCD . . . . .	216
C.1 Schematic diagram of x-ray diffraction stress measurement of the orientation of the measured lattice planes related specimen structure. D:x-ray detector; S: X-ray source; N: normal to the surface. . . . .	222
C.2 Plane stress elastic model of a flat specimen . . . . .	223
D.1 A Biological Neuron . . . . .	226
D.2 Mathematical model of a neuron . . . . .	227
D.3 A representation of a simple 3-layer feed-forward ANN . . . . .	228
D.4 Hyperbolic tangent sigmoid transfer function . . . . .	230
D.5 Supervised learning model . . . . .	231
E.1 Crisp and Fuzzy sets for SHORT, MEDIUM and TALL . . . . .	234
E.2 Fuzzy inference system . . . . .	235
E.3 Commonly used fuzzy if-then rules and fuzzy reasoning mechanisms .	236
E.4 Defuzzification using the centre of mass . . . . .	239
E.5 Block-diagram of the back-propagation learning algorithm . . . . .	240

# Chapter I

## *Introduction*

## 1. INTRODUCTION

The history of Electrical Discharge Machining (EDM) techniques goes as far back as the 1768 when it was discovered by Sir Joseph Priestley an English Scientist. It took more than a century to make use of this some practical use. However, EDM was not fully taken advantage of until 1943 when Russian scientists learned how the erosive effects of the technique could be controlled and used for machining purposes. The popularity of this machining was grown by leaps and bounds in last sixty years. The advantages of EDM over other machining processes are in terms of accuracy, surface quality (SQ), and as the hardness and stiffness of the workpiece material are not important for the material removal. The researches and improvements of the process are still going on because, still there does not exist a machining process that could successfully substitute the EDM process.

### *1.1 Overview*

There is a growing trend to use light, slim and compact mechanical component in recent years, thus there has been an increased interest in development of new generation of advance materials having high hardness, temperature resistance, and high strength to weight ratio; used in mould and die making industries, aerospace component, medical appliance, and automotive industries. In response to this, there is a heavy demand for new technologies to meet the unique challenges posed while manufacturing components with such materials. The development of appropriate machining systems to support this growth is essential because the traditional processes are unable to cope up with those challenges. EDM has been a mainstay of manufacturing for more than six decades, providing unique capabilities to machine “difficult to machine” materials with desire shape, size, and required dimensional accuracy. It is the most widely and successfully applied machining process for various workpiece materials in the said

---

advance industries [Snoeys et al. (1986)]. Today's advance die sinking EDM systems are much more capable than their manual predecessors were, and effectively implemented to manufacture die casting moulds, plastics moulding and forging dies. EDM is a thermal process of eroding electrically conductive materials with a series of successive electric sparks and the complex phenomenon involving several disciplines of science and branches of engineering. The theories revolving around the formation of plasma channel between the tool and the workpiece, thermodynamics of the repetitive spark causing melting and evaporating the electrodes, micro-structural changes, and metallurgical transformations of material, are still not clearly understood. However, it is widely accepted that the mechanism of material erosion is due to intense local heating of the workpiece causing melting and evaporation of workpiece.

EDM is one of the most important manufacturing processes extensively useful in the die and mould making industry to generate intricate shape, mould cavity, complex shapes. Its distinctive attribute of using thermal energy to machine electrically conductive materials, regardless of hardness, has been an advantage in the manufacturing of mould, die, surgical, automotive and aeronautic components.

## 1.2 Background of Research

EDM is the most vital manufacturing processes extensively useful in the die and mold making industry to generate intricate shape, mould cavity, complex shapes. There are no physical cutting forces between the tool and the workpiece. This process is finding an increasing demand owing to its ability to produce geometrical complex shapes as well as its ability to machine hard materials that are extremely difficult to machine when using conventional process. It is essential especially in the machining of super tough, hard and electrically conductive materials such as the new space age alloys [Lee and Li (2001)]. It is better than other machining processes in terms of precision, SQ and the fact that hardness and stiffness of a workpiece material is not important for the material removal. Though EDM has become an established technology, and commonly used in manufacturing of mechanical works, yet its low efficiency and poor SQ have been the vital matter of concern. Hence, the investigations and improvements of the process are still going on, since no such process exists, which could successfully



replace the EDM.

EDM was originally observed by Joseph Priestly by an English Scientist in 1770, but it was not fully taken advantage of until 1943 when Russian scientists learned how the erosive effects of the technique could be controlled and used for machining purposes. During the 1930s, attempts were made for the first time to machine metals and diamonds with electrical discharges. Erosion was caused by intermittent arc discharges occurring in air between the tool electrode and workpiece connected to a DC power supply. These processes were not very precise due to overheating of the machining area and may be defined as ‘arc machining’ rather than ‘spark machining’ [Ho and Newman (2003)].

During 1980s, with the arrival of Computer Numerical Control (CNC) in EDM that brought about an extraordinary progresses in improving the efficiency of the machining operation. CNC has made possible total EDM, which indirect an automatic and unattended machining from inserting the electrodes in the tool changer to a finished polished cavity or cavities. These emergent virtues of EDM have since then been intensely sought after by the manufacturing industries yielding enormous economic benefits and generating keen research interests.

### 1.2.1 Types of Electric Discharge Machines

EDM facilitates the machining in a number of ways, a lot of these operations are similar to conventional machining operation, for instance milling and die sinking. A variety of classifications are possible and recent developments in its technology append new operations owing to increase in various requirements. A simple and general classification can be given in view of standard applications such as,

1. Wire EDM
2. Micro-EDM
3. Electric Discharge Grinding (EDG)
4. Die Sinking EDM

Wire-EDM: In this process, a very thin wire serves as an electrode which is continuously fed by a series of motors and pulleys through the material. The travelling wire, size ranging from 0.02 to 0.40 mm in diameter, usually made of brass or stratified copper and the sparking takes place between the wire and the workpiece that actually cut the later. The wire is continuously moving and new wire is constantly being fed during the machining process. Extrusion dies and blanking punches and several other forms of jigs and fixtures are frequently machined by this process. It is a very accurate process and machining can accomplish with an accuracy of  $\pm 0.0025$  mm.

Micro-EDM: The recent trend of miniaturization of mechanical parts has given  $\mu$ -EDM a considerable research attention. Using this process, it is possible to produce not only micro holes and shafts as small as  $5 \mu\text{m}$  in diameter, but also complex three-dimensional shapes [Rajurkar and Yu (2000)]. It is extensively used for manufacture of micro structures, tooling inserts for micro-injection moulding and hot embossing. In the beginning,  $\mu$ EDM was applied mostly for fabricating small holes in metal foils. Owing to the versatility of the EDM process, currently it is used in a lot of applications. For instance, it is employed for manufacturing micro parts for accelerometer, micro mould and dies, keyhole surgery, housings for micro-engines and also tooling inserts for fabrication of micro-filters, housings and packaging solutions for micro-optical, and micro fluidics devices, fiber optics light detector fixtureing. Micro EDM is used to produce parts like, super fine nozzles (such as the fuel injection nozzles for diesel engines), and to make high-precision masks used in microelectronic manufacturing processes.

Wire Electric Discharge Grinding: A major improvement of micro-EDM process was the advent of wire-electro discharge grinding (WEDG) [Masuzawa et al. (1985)]. When a small hole is desired, an electrode with comparatively larger diameter may be in situ eroded against a sacrificial workpiece. The polarity is reversed in this case and so the material removal takes place mostly on the electrode. The EDMed electrode (with smaller diameter) serves as an electrode in  $\mu$ EDM process.

Die Sinking/Ram EDM: The Sinker EDM, consists of an electrode and workpiece submerged in an insulating dielectric fluid. A schematic diagram of such a machine

tool is shown in Fig. 1.1. The tool and the workpiece form the two conductive electrodes in the electric circuit. Pulsed power is supplied to the electrodes from a separate power supply unit. The RC circuit was widely used in the 1950s and later MOSFET technology has replaced it. The proper feed motion of the tool towards the workpiece is usually given for maintaining a constant gap distance between the tool and the workpiece during machining. This is executed by a servo motor control of the tool holder. When material gets eroded from the workpiece, the tool is fed downward towards the workpiece to maintain a constant inter-electrode gap. The flushing arrangements are made for the proper flow of dielectric into the inter-electrode gap. The tool electrode has the complementary shape of finished component and accurately sinks into the workpiece, by which intricate shapes are achievable.

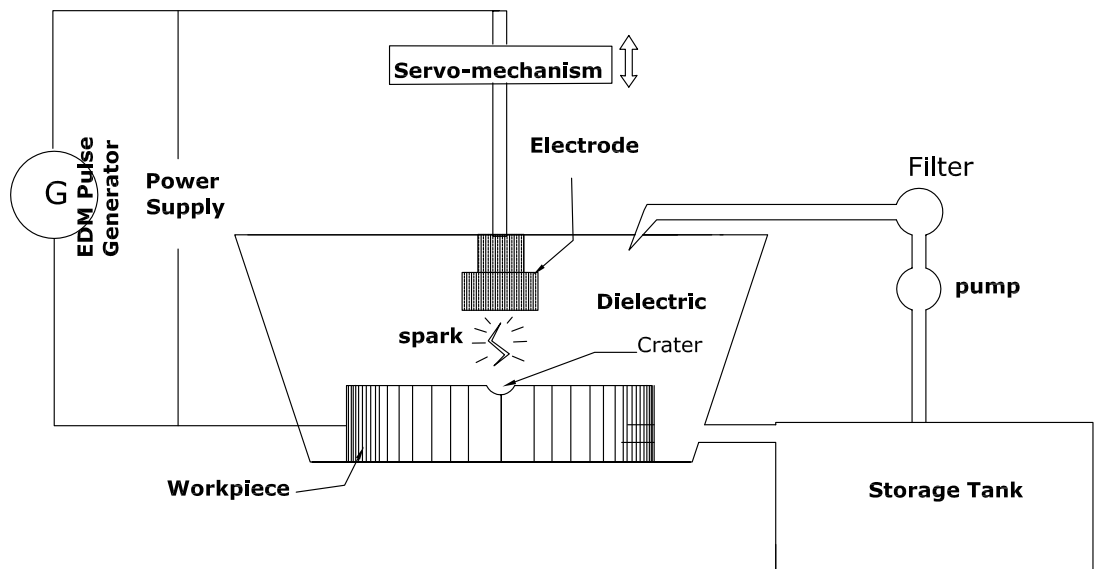


Fig. 1.1: Schematic of an electric discharge machining machine tool

### 1.2.2 Mechanism of Material Removal in Electrical Discharge Machining

Electric discharge machining is the most widely-used non-conventional machining process. Despite the fact that the mechanism of material removal of EDM process is not yet completely understood and is still debatable, the most widely established principle is the conversion of electrical energy into thermal energy through a series of discrete electrical discharges occurring between the electrode and workpiece immersed inside a dielectric medium and separated by a small gap. Material is removed from

the workpiece by localized melting and even vaporization of material. The sparks are created in between two electrodes in presence of dielectric liquid. A simple explanation of the erosion process due to the discharge is presented in Fig. 1.2. There is no mechanical contact between the electrodes (held at a small distance) and a high potential difference is applied across them (Fig. 1.2(b)). The breakdown of the dielectric is originated by moving the electrode towards the workpiece, which will enhance the electric field in the gap, until it arrives at the required value for breakdown. The spot of breakdown is normally between the closest points of the electrode and of the workpiece, but it is also depend on particles or debris present in the gap. When the breakdown takes place, the voltage falls and the current rises abruptly. The flow of a current is possible at this point, because the dielectric has been ionized and a plasma channel has been created between the electrodes (Fig. 1.2(c)).

The flow of discharge current is then continuing and there will be a constant attack of ions and electrons on the electrodes leads to strong heating of the workpiece material, leading to temperature rise between 8,000°C and 12,000°C [Boothroyd and Winston (1989)]. This results in quick formation of a small molten metal pool at both the electrode surfaces, out of which some fraction of metals are directly vaporized due to the heating. During this discharge, the plasma channel expands and therefore, the radius of the molten metal pool increases with time (Fig 1.2(d)).

Towards the end of the discharge, current and voltage are cut off and thus the plasma implodes under the pressure imposed by the surrounding dielectric, as a result, the molten metal pool is strongly sucked up into the dielectric, producing a tiny crater at the workpiece surface (Fig 1.2(e)). The machining process successively removes small volumes of workpiece material, molten or vaporized during a discharge and is carried away from the inter-electrode gap by the dielectric flow in the form of debris. Sparking occurs where the gap between the tool and the workpiece surface is smallest. The gap increases after material removal at the point of spark, and the position of the next spark shifts to a different place, where gap is smallest on the workpiece surface. In this manner thousands of sparks occur at different locality over the whole surface of the workpiece corresponding to the workpiece-tool gap. As a consequence, a replica of the tool surface shape is produced in the workpiece.

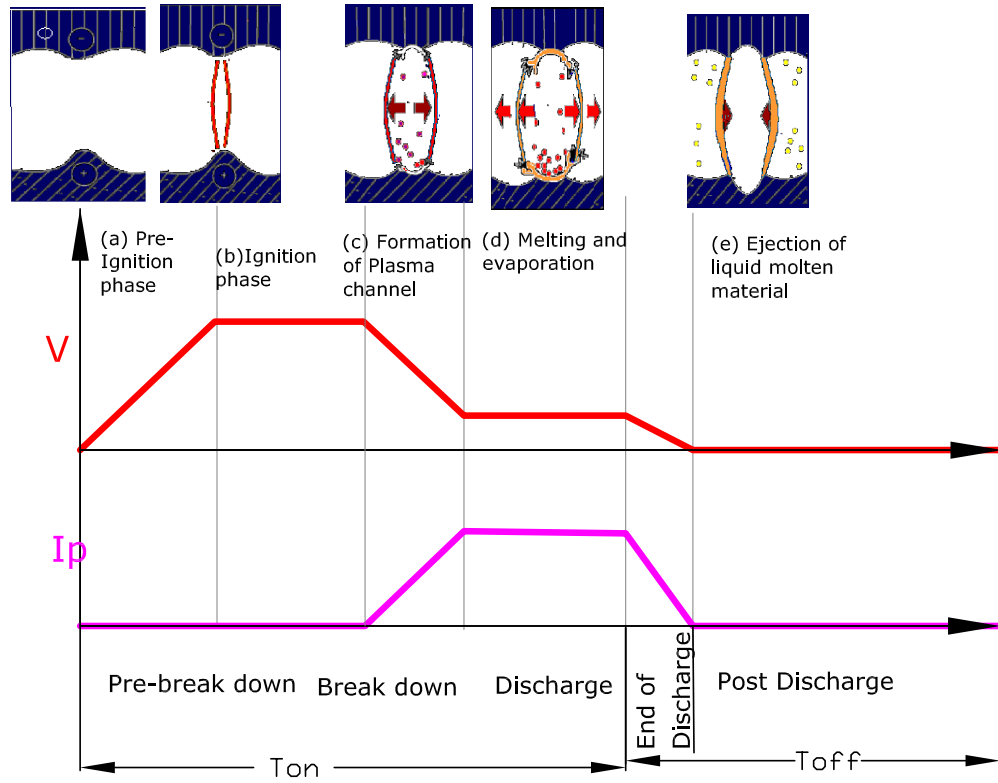


Fig. 1.2: The plasma channel

It is well-known and elucidated by many EDM researchers that Material Removal Mechanism (MRM) is the process of migration of material from the work-piece and electrode to dielectric medium in solid, liquid or gaseous state. The appreciable amount of material is transformed between workpiece and electrode undergo alloying with the contacting surface by means of a solid, liquid or gaseous phase reaction [Roethel et al., 1976; Soni and Chakraverti, 1996]. Phases of sparking of MRM (breakdown, discharge and erosion) is highly influenced by the types of eroded electrode and work-piece elements together with disintegrated products of dielectric fluid [Erden (1983)]. Additionally, reversing the polarity of sparking alters the material removal phenomenon with an significant amount of electrode material set down on the workpiece surface [Gangadhar et al. (1992)]. The MRM are also been reported differently by many authors. Singh and Ghosh (1999) showed that the electrostatic forces and stress distribution acting on the cathode electrode were the major causes of metal removal for short pulses. Gadalla and Tsai (1989) elucidated the material

removal of WC-Co composite to the melting and evaporation of disintegrated Co followed by the dislodging of WC gains, which have a lower electrical conductivity on the other hand, Lee and Lau (1991) argued that thermal spalling as well contributes to the mechanism of material removal during the sparking of composite ceramics due to the physical and mechanical properties promotes abrupt temperature gradients from normal melting and evaporation.

### 1.2.3 EDM process parameters

As per the discharge phenomena explained earlier, some of the important process parameters which influence the responses are.

Discharge voltage( $V$ ): It is the open circuit voltage which is applied between the electrodes. The discharge voltage de-ionizes the dielectric medium, which depends upon the electrode gap and the strength of the dielectric, prior to the flow of current. Once the current flow starts, the open circuit voltage drops and stabilizes the electrode gap. It is a vital factor that influences the spark energy, which is responsible for the higher MRR, higher Tool wear rate and rough surfaces.

Discharge current or Pulse current ( $I_p$ ): It is the most important machining parameter in EDM because it relates to power consumption of power while machining. The current increases until it reaches a preset level which is expressed as discharge current. The maximum amount of amperage that can be used is governed by the surface area of the cut for a workpiece tool combination. Higher currents will improve MRR, but at the cost of surface finish and tool wear. This is all more important consideration in EDM because the accuracy of machined cavity, which is a replica of tool electrode, will be effected due to excessive wear.

Pulse-on time ( $T_{on}$ ): It is the time during which actual machining takes place and it is measured in  $\mu s$ . In each discharge cycle, there is a pulse on time and pause time, and the voltage between the electrode is applied during  $T_{on}$  duration. The longer the pulse duration higher will be the spark energy that creates wider and deeper crated. it is because the material removal is directly proportional to the amount of energy applied during this on-time. Though with higher  $T_{on}$ , the MRR will be more, but rough surfaces are produced by the higher spark energy.

Pulse-off time or pause time ( $T_{off}$ ): In a cycle, there is a pulse off time or pause time during which the supply voltage is cut off as a consequence the  $I_p$  diminishes to zero. It is also the duration of time after which the next spark is generated and is expressed in  $\mu s$  analogous to  $T_{on}$ . Since, the dielectric must de-ionized after sparking and regain its strength, it required some time and moreover the flushing of debris also takes place during the  $T_{off}$  time. The cycle is completed when sufficient  $T_{off}$  is allowed before the start of the next cycle. Since, Pulse-off time is a non productive time, but it should not be too small because too small  $T_{off}$  makes the next spark to be unstable. The sum of pulse on time and pulse off time in a cycle is called pulse period or Total cycle time. Duty cycle ( $Tau$ ): It is the ratio of pulse on-time and the pulse period. Duty cycle is defined in the equation below.

$$Tau = \frac{T_{on}}{T_{on} + T_{off}} \times 100 \quad (1.1)$$

At higher  $Tau$ , the spark energy is supplied for longer duration of the pulse period resulting in higher machining efficiency.

Polarity: Polarity refers to the potential of the workpiece with respect to tool i.e. in straight or positive polarity the workpiece is positive, whereas in reverse polarity workpiece is negative. Varying the polarity can have dramatic effect, normally electrode with positive polarity wear less, whereas with negative polarity cut faster. On the other hand, some of the metals do not respond this way. Carbide, Titanium and copper are generally cut with negative polarity.

Dielectric Fluid: The dielectric fluid carry out three most important purposes in the EDM. The first function of the dielectric fluid is to insulate the inter electrode gap and after breaking down at the appropriate applied voltages conducting the flow of current. The second function is to flush away the debris from the machined area, and lastly, the dielectric act as coolant to assists in heat transfer from the electrodes. Most commonly used dielectric fluids are hydrocarbon compounds, like light transformer oil and kerosene.

Inter electrode gap: The inter electrode gap is a vital factor for spark stability and proper flushing. The most important requirements for good performance are gap

---

stability and the reaction speed of the system; the presence of backlash is particularly undesirable. The reaction speed must be high in order to respond to short circuits or open gap conditions. Gap width is not measurable directly, but can be inferred from the average gap voltage. The tool servo mechanism is responsible for maintaining working gap at a set value. Mostly electro mechanical (DC or stepper motors) and electro hydraulic systems are used, and are normally designed to respond to average gap voltage.

Flushing Pressure and Type of flushing: Flushing is an important factor in EDM because debris must be removed for efficient cutting, moreover it brings fresh dielectric in the inter electrode gap. Flushing is difficult if the cavity is deeper, inefficient flushing may initiate arcing and may create unwanted cavities which can destroys the workpiece. There are several methods generally used to flush the EDM gap: jet or side flushing, pressure flushing, vacuum flushing and pulse flushing. In jet flushing, hoses or fixtures are used and directed at the inter electrode gap to wash away the debris, in pressure and vacuum flushing dielectric flow through the drilled holes in the electrode, workpiece or fixtures. In pulse flushing the movement of electrode in up and down, orbital or rotary motion creates a pumping action to draw the fresh dielectric. The usual range of pressure used is between 0.1 to 0.4  $kgf/cm^2$ .

### 1.3 Key areas of research in Die Sinking EDM

The common assessment about the direction of study is relates to machining performance evaluation for instance material removal, tool wear and surface integrity achieved after machining. However, the majority of the investigations are inclined towards monitoring and control of the process parameters. A vivid literature review of the development of EDM technology between 1993 to 2003 has been reported by Ho and Newman (2003) and the research trends in EDM on ultrasonic vibration, dry EDM machining, EDM with powder additives, EDM in water and modelling technique in predicting EDM performances by Mohd Abbas et al. (2007). In this section, the contribution by various researchers in the area of die sinking and related EDM and their development is discussed.



### 1.3.1 EDM performance measures

A considerable number of papers have been paying attention on approach of yielding optimal EDM performance measures of high MRR, low TWR and acceptable OC. This section provides a study into each of the performance measures and the scheme for their enhancement. In past, significant improvement has been carried out to enhance productivity, accuracy, and the versatility of EDM process. The key issue is to pick the process parameters such as  $I_p$ ,  $Ton$ ,  $Tau$  and  $V$ , flushing pressure, dielectric fluid, polarity in such a way that MRR and accuracy increases; and concurrently overcut or gap, tool wear and surface roughness should diminish.

Wang and Tsai (2001) presented semi-empirical models of MRR for various workpiece (EK2, D2 and H13) and tool electrode combinations (Copper, graphite and silver-tungsten alloy). To achieve higher MRR in EDM, a stable machining process is required, which is partly influenced by the contamination of the gap between the workpiece and the electrode, and it also depends on the size of the eroding surface at the given machining regime [Valenticic and Junkar (2004)]. Jaharah et al. (2008) investigated MRR, TWR on AISI H13 tool steel.  $I_p$  was found to be the major factor which influence MRR. Higher MRR was obtained with high  $I_p$ , medium  $Ton$ , and low  $Toff$ . However, smaller TWR was obtained at high  $I_p$ , high  $Ton$ , and lower value of  $Toff$ . Kanagarajan et al. (2008) used electrode rotation,  $Ton$ ,  $I_p$ , and FP to study MRR on Tungsten carbide/cobalt cemented carbide and shown experimentally that  $I_p$  and  $Ton$  are the most significant factors. Kuppan et al. (2007) derived mathematical model for MRR of deep hole drilling of Inconel 718. The experiments were planned using Central Composite Design (CCD) and Response Surface Methodology (RSM) was used to model the same. It revealed that MRR is more influenced by peak current and duty factor, and the parameters were optimised for maximum MRR with the desired Ra value using desirability function approach. Puertas et al. (2004) analysed the impact of EDM parameters on MRR and electrode wear in cobalt-bonded tungsten carbide workpiece. A quadratic model was developed for each of the responses, and it was reported that for MRR, the current intensity factor was the most influential, followed by  $Tau$ ,  $Ton$  and the interaction effect of the first two. The value

of MRR increased, when current intensity and  $Tau$  were increased, and decreased with  $Ton$ .

Khan et al. (2009) discuss the performance (MRR and TWR) of EDMed mild steel due to the shape configuration of the electrode. The maximum MRR was found for round electrodes followed by square, triangular and diamond shaped electrodes. However, the highest EWR were found for the diamond shaped electrodes. It is also considered as an off-line process planning technique as the simulation algorithm is largely based on MRR, TWR and spark gap. However, the simulation of discharge location and spark gap, which are dependent on the distribution of debris concentration, was reported to yield a more realistic representation of the sparking phenomenon. Subsequently, Khan (2008) reported overall performance comparison of copper and brass electrodes and observed that the highest MRR was observed during machining of aluminium using brass electrodes. Comparatively low thermal conductivity of brass as an electrode material does not allow the absorption of much heat energy, and most of the heat is utilized in the removal of material from aluminium workpiece at a low melting point.

Dhar et al. (2007) estimated the effect of  $I_p$ ,  $Ton$ , and  $V$  on MRR, TWR and G on EDM of Al-4Cu-6Si alloy-10 wt.% SiCP composites. Using three factors, three level full factorial designs, a second order non-linear mathematical model has been developed for establishing the relationship among machining parameters. It was revealed that the MRR, TWR and G increase with increase in  $I_p$  and  $Ton$ . Salonitis et al. (2009) developed a simple thermal based model to determine the MRR and asserts that the increase of  $I_p$ ,  $V$  or  $Ton$  results in higher MRR. Besides, reducing  $Toff$  MRR increases. They reported that model predictions and experimental results are in good agreement. El-Taweel (2008) investigated the correlation of process parameters in EDM of CK45 steel with Al-Cu-Si-TiC composite produced using powder metallurgy technique and evaluated MRR and TWR. It is found that such electrodes are more sensitive to  $I_p$  and  $Ton$  than conventional electrodes. To achieve maximum MRR and minimum TWR, the process parameters are optimised and on experimental verification the results are found to be in good agreement. Chiang (2008) had explained the influences of  $I_p$ ,  $Ton$ ,  $Tau$  and voltage on the responses; MRR and electrodes wear ra-

tio. The experiments were planned according to a CCD on  $Al_2O_3+TiC$  workpiece and the influence of parameters and their interactions were investigated using ANOVA. A mathematical model was developed and claimed to fit and predict MRR accurately with a 95% confidence. The main two significant factors affecting the response were  $I_p$  and  $Tau$ . Dvivedi et al. (2008) identified the machining performance in terms of MRR and TWR by obtaining an optimal setting of process parameters ( $Ton$ ,  $Toff$ ,  $I_p$ , and  $FP$ ) during EDM of Al 6063 SiCp metal matrix composite. It was revealed that  $I_p$  is predominant on MRR than other significant parameters. MRR increases with increasing  $I_p$  and  $Ton$  up to an optimal point and then dropped. Karthikeyan et al. (1999) develop mathematical models for optimizing EDM characteristics such as the MRR, TWR and the surface roughness on aluminium silicon carbide particulate composites, using full factorial design. The process parameters taken in to consideration were  $I_p$ ,  $Ton$  and the percent volume fraction of SiC ( $V$ ) present in LM25 aluminium matrix. Wang (2009) investigated the feasibility and optimization of EDM for inspecting the machinability of W/Cu composites using the Taguchi method utilizing  $L_{18}$  orthogonal table to obtain the polarity,  $I_p$ ,  $Ton$ ,  $Tau$ , rotary electrode rotational speed, and  $V$  in order to explore the MRR and TWR.

The tool wear is moderately analogous to the MRM in EDM. Mohri et al. (1995) ascertained that tool wear is affected by the precipitation of turbostratic carbon from the hydrocarbon dielectric on the electrode surface during sparking. Also the rapid wear on the electrode edge was because of the failure of carbon to precipitate at difficult-to-reach regions of the electrode. From this easy understanding of tool wear, some useful applications exploiting both the advantages and disadvantages of electrode wear have been developed. Marafona and Wykes (2000) used energy dispersive X-ray analysis of tool surfaces measuring their compositions and established a wear inhibitor carbon layer on the electrode surface by adjusting the settings of the machining parameters prior to normal EDM conditions. Although the thickness of the carbon inhibitor layer made a significant improvement on the TWR, it has little effect on the MRR. Conversely, for applications requiring higher MRR, a large pulse current is encouraged to increase electrode wear implanting electrode material onto the workpiece [Mohri et al. (2000)]. Bleys et al. (2002) devised an online tool

---

wear compensation method based on the pulse analysis and controlled the tool feed movement in real time. Kunieda and Kobayashi (2004) clarifies the mechanism of determining tool electrode wear ratio in EDM by spectroscopic measurement of the vapour density of the tool electrode material. Longer *Ton* is known to result in lower TWR and deposition of a thicker carbon layer on the tool electrode surface. Conversely, the density of copper vapour evaporated from the tool electrode surface was found to be lower when the carbon layer was thicker, indicating that tool electrode wear is prevented by the protective effects of the carbon layer. The well-known machining strategy of recompense the tool wear is the orbiting of the electrode relative to the workpiece, where a planetary motion creating an effective flushing action, get better part accuracy and process efficiency [Snoeys et al. (1986)]. This technique also trims down the number of different electrodes necessary for initial roughing and final finishing operations [Staelens and Kruth (1989)]. Yu et al. (1998) established a uniform tool wear machining method to compensate the longitudinal tool wear by applying an overlapping backward and forward machining motion. Dauw and Snoeys (1986) derived the measurement of tool wear from the study of pulse characteristics based on discharge voltage fall time.

The analogous tool wear compensation approach have also been applied to  $\mu$ EDM, which is usually implemented in thin layers using simple cylindrical or tubular electrodes. On the other hand, Kunieda and Yoshida (1997) reduced the tool wear ratio by performing  $\mu$ EDM using high velocity gas as the dielectric medium. The different methods of simulating the EDM process also offer a tremendous prospect of considerate and compensate the tool wear. Dauw (1988) developed a geometrical simulation of EDM demonstrating the development of tool wear and part geometry. Caydas and Hascalik (2007) made an attempt to analyse the electrode wear in EDM of Ti alloy using statistical analysis technique. ANOVA and regression analysis were done, the proposed mathematical models obtained can adequately describe the performances within the limits of factors being studied. The experimental and predicted values were in a good agreement.

The EDMed cavity produced are always larger than the electrode this difference (size of the electrode and the size of the cavity) is referred as Overcut (OC). It

becomes important when close tolerance components are required to be produced for space application and also in tools, dies and moulds for press work. The dimensional accuracy of EDM is greatly influenced by the OC resulting from the discharge gap and electrode wear. The parameters such as  $I_p$ ,  $T_{on}$ , voltage applied and the workpiece material are significantly influence OC. It increases with the increase of  $I_p$  but up to a certain limit besides it depends upon the gap voltage and chip size, which vary with the amperage used [Singh et al. (2004)]. When low diametral OC is the requirement En-31 may be preferred over copper and aluminium electrodes.

CNC EDM commonly makes use of 3D profile electrodes that are expensive and time consuming to manufacture for EDM process. Further for producing complex 3D shaped parts, the capacity of CNC in providing multi-axis movements for simple electrodes in EDM. Wong and Noble (1986) experiment and investigated the machining with cylindrical electrodes with microcomputer controllers. In recent times MRR improvement technique has been developed by modifying the basic principle of EDM, which delivers single discharge for each electrical pulse. Kunieda and Masuzawa (1988) investigated a multi-electrode discharging system delivering additional discharge simultaneously from a corresponding electrode connected serially. An oxygen assisted EDM system, which greatly improves the MRR was tested by supplying oxygen into the discharge gap [Kunieda et al. (1999)], besides MRR can be substantially improved with reduced TWR using a multi-electrode discharging system using without any improvement in surface roughness.

### 1.3.2 Surface integrity of EDMed surface

The term surface integrity is used to describe the quality and condition of the surface region of a machine component. It includes the topological, mechanical, metallurgical and chemical conditions of the surface region as well as surface and sub-surface structure. It is well established that EDMed surfaces usually experiences a transformed or altered layer having different characteristics from those of the parent metal. A comprehensive description of surface integrity of EDMed components necessitates the measures of Surface Roughness (SR), White Layer Thickness (WLT), Heat-Affected Zones (HAZ), micro-cracks, and Residual Stresses (RS), diffusion of tool material and

carbon, and endurance limit [Rajurkar and Pandit (1988)]. It has been ascertained that the surface integrity is significantly distorted by EDM and thus efforts are being made to negate the transformations in surface integrity of machined components. EDM surfaces are quite intricate and investigation on the effects of EDM machining on surface integrity have been reported by many researchers. The thermal changes may cause cracks in the top layer and residual stresses in the underlying base layers [Cogun and Savsar (1990)]. Although EDM has many advantages but, the recast layer with cracks, caused by rapid cooling results in poor surface accuracy [Kruth et al., 1995; Schumacher, 2004].

Surface texture, surface topography or surface finish are the terms, which are used to express the machined surface relate to the geometric irregularities and to quality the surface. An ideal surface roughness are commonly specified by the peak to valley height or the center line average,  $R_a$  ( $\mu\text{m}$ ). The EDMed surfaces consist of plenty of craters formed by the discharge energy. If the energy content is high, deeper craters will be accomplished, leading to poor surface. The surface roughness has also been found to be inversely proportional to the frequency of discharge [Pandey and Shan (1980)]. A spark-eroded surface is a surface with a matt appearance and random distribution of overlapping craters and is often covered with a network of micro-cracks [Pandey and Jilani (1986)]. The molten metal were expelled randomly during the discharge and later solidified on the electrode surfaces. The crack formation is associated with the development of high thermal stresses of the material, as well as with plastic deformation.

Many attempts had been made for modelling of EDM process and investigation of the process performance to improve the surface quality. For the prediction of surface roughness empirical models as well as multi-regression analysis are usually applied. It has been observed that there are many process variables that affect the surface finish such as  $I_p$ ,  $T_{on}$ , open circuit voltage, electrode polarity, thermal properties of the tool, work, and dielectric liquid and debris concentration. Kiyak and Cakir (2007) investigated the influences of EDM parameters on  $R_a$  for machining of AISI P20 tool steel and emphasized that the choice of the machining parameters to achieve good surface quality of EDMed component should be smaller pulsed current and

shorter pulse time. This is because, small particle size and crater depths created by discharge and consequently, the smooth surface will be produced. Jaharah et al. (2008) investigated SR with copper electrode and AISI H3 tool steel workpiece and the input parameters taken are  $I_p$ ,  $Ton$ , and  $Toff$ . The optimum condition for Ra was obtained at low  $I_p$ , low  $Ton$ , and  $Toff$  and concluded that the  $I_p$  was the major factor effecting Ra. Keskin et al. (2006) in their experimental study obtained a regression equation and asserted that the results will help to manufacture steel parts with definite surface roughness requirements instead of trial and error. In addition, it is revealed that Ra has an increasing trend with an increase in the  $Ton$ , which is probably due to more discharge energy released during this time and expanding the discharge channel. Khan et al. (2009) discuss the SR performance of EDMed mild steel for different shape configuration of the electrode. The minimum surface roughness was found for the round electrodes followed by square, triangular and diamond shaped electrodes. Jaharah et al. (2008) investigated SR on AISI H13 tool steel. However, the optimum condition for Ra was obtained at low  $I_p$ , low  $Ton$ , and  $Toff$ .  $I_p$  was the major factor affecting the response. Tsai and Wang (2001c) reported several surface finish models by taking the effects of electrode polarity into account. They subsequently reported a semi-empirical model dependent on the thermal, physical and electrical properties of the workpiece and electrode together with relevant process parameters such as  $Ton$ ,  $I_p$ , polarity, input power, material density, conductivity, specific heat capacity, heat conductivity, melting point, and boiling point. The later model was found to be a more trustworthy surface finish prediction for various workpiece material (EK2 and H13) under various process conditions [Tsai and Wang (2001a)]. Salonitis et al. (2009) in their study developed a model for SR and started that with the increasing in process parameters,  $I_p$ ,  $Ton$  and  $V$ , coarser workpiece surfaces are achieved. Latter, it is verified experimentally and found to be in good agreement with predicted results.

The surface characteristics of the machined surface were explored extensively by Kanagarajan et al. (2008). They had chosen  $I_p$ ,  $Ton$ , electrode rotation, and flushing pressure as design factor to study the EDM process performance such as SR on Tungsten carbide/cobalt cemented carbide. The most influential parameters for minimising the SR have been identified using the RSM and experimentally verified by

conducting confirmation experiments.

Chiang (2008) proposed a mathematical model and investigated the influence of  $I_p$ ,  $Ton$ ,  $Tau$ , voltage and their interactions on SR. The experiments are conducted on  $Al_2O_3+TiC$  workpiece and found that  $I_p$  and  $Ton$  have statistical significance on SR. It is claimed to fit and predict SR narrowly with a 95% confidence interval.

In the EDMed component, a unique structure on the surfaces of the machined parts has been observed. The microscopic observations showed that unusual phase changes occur due to high local temperature attained during the machining. The top layer is a recast layer formed by resolidification of the molten metal and this layer is found to be heavily alloyed with the pyrolysis products of the cracked dielectric. The material surface is found to be fairly resistant to etching by conventional metallographic reagents. Therefore, the recast layer on ferrous alloys is often referred to as an unetchable 'white' layer. Micro-hardness measurements have shown that for ferrous alloys, the recast layer generally has a hardness value much higher than that of the underlying matrix and may exceed that attainable by normal quenching techniques [Ekmekci, 2007; Mamalis et al., 1988].

Heat Affected Zone (HAZ) lies beneath the white layer structure, which generally has a tempered microstructure and has a hardness value fairly less than that of the underlying hardened metal. An intermediate layer between the recast and the tempered layers was also observed and reported. This layer was found to exhibit a carbon gradient and contamination of materials from the tool electrode. It is possible that this layer includes part of the melted layer plus a region beyond which diffusion has occurred in solid state. The hardness of this layer is found to be comparable to or, sometimes, a little higher than that of the recast layer [Lim et al. (1991)]. Under optical microscope, it generally has a darker appearance than the parent material. The bulk of the material beyond the tempered zone remains unaffected by machining. In the past a number of attempts have been made to study the relationship of white layer thickness with the machining parameters. The structural change of EDMed surface have been studied extensively by

Lee et al. (2004) revealed experimentally that the influence of the EDM parameters on the surface integrity of AISI 1045 carbon steel and furnished that average



WLT and induced residual stress tend to increase at higher values of  $I_p$  and  $Ton$ . However, for an extended  $Ton$ , it is noted that the surface crack density decrease. Besides, obvious cracks are always apparent in thicker white layers. A smaller  $I_p$  (i.e. 1 A) tends to increase the surface crack density, while a prolonged  $Ton$  amplifies the opening degree of the surface crack, thereby reducing the surface crack density. Correlation between EDM parameters and surface crack formation for D2 and H13 tool steels was studied by Lee and Tai (2003). It was shown that crack formation and white layer thickness is correlated to the machining parameters. High  $Ton$  will increase both the WLT and the induced stress and both of them tend to support the formation crack. Bhattacharyya et al. (2007) developed mathematical models based on RSM for correlating  $I_p$  and  $Ton$  different aspects of surface integrity of M2 Die Steel machined through EDM at the transverse section of the EDMed M2 Die Steel and experimentally validated using the SEM micrographs and the graphs plotted and reveal the correctness of the developed models. Optimal combination of parameters has been estimated, which can be used to minimize surface integrity. Rebelo et al. (1998) have reported quantitatively and qualitatively that the formation of plasma channel between tool (steel) and workpiece, resulting in metallurgical transformations, residual tensile stresses and surface cracking. The dimension of random overlapping surface craters increases with machining pulse energy. The cracks radiate from, and circumvent, the craters. The density and penetration depth of the cracks in the re-cast layer increases with the machining pulse energy. Ramasawmy et al. (2005) experimentally investigated the effect of the EDM process parameters  $I_p$  and  $Ton$  on the thickness of the white layer. Stainless martensitic chromium tool steel was used for the EDM test. Relation of WLT with 3D surface texture amplitude, spatial and volume parameters are discussed and shown that the  $I_p$  has comparatively more significant effect on the dimension of the crater as compared to  $Ton$ . It is said that the dimension characteristics of the molten metal pool define the magnitude of the surface tension, and eventually the thickness of the white layer. Mamalis et al. (1987) in their experimental study revealed that the physico-chemical changes occur during EDM of steel and a correlation among surface morphology and overall process parameters have been noticed. "White layer" and crack formation are related with the

development of high thermal stresses exceeding the fracture strength of the material in addition to plastic deformation and are determined quantitatively by the use of regression equations; it is clearly shown that their dimensional dependence on pulse energy. Lim et al. (1991) provided a review on the metallurgy of EDMed surface, which is dependent on the solidification behaviour of the molten metal after the discharge cessation and subsequent phase transformation. Solidification of the molten metal takes place simultaneously from the top interface with the dielectric and the bottom interface with the underlying metal into the melt, as well as from within the melt towards both interfaces. This leads to the formation of three distinctive sub layers within each recast layer resolidified from a given pool of molten metal. Wang et al. (2009) studied the feasibility of removing the recast layer from molds and dies using etching and mechanical grinding for Ni-based super alloy materials by means of EDM. The analysis has been carried out in three stages. The first stage is to obtain a thick recast layer by using EDM with a larger discharging energy applying the Taguchi  $L_{18}$  analytical method. Furthermore in the second stage optimizes the recast layer removal technique using Taguchi's  $L_9$  orthogonal for the etching and mechanical grinding parameters and observe the recast layer removal quantity analysis.

Crack development can be attributed to the existence of thermal and tensile stresses within the EDMed component. Tensile stresses are generated since the melted material contracts more than the unaffected parent material. Diffusion of carbon from dielectric liquid and possibly alloying materials from tool electrode can also affect the material contraction rate. When the stress in the surface exceeds the material's ultimate tensile strength, cracks are formed [Thomson, 1989]. Results from previous studies [Lee et al., 1990, 1992] have indicated that cracking increases as the pulse energy increases. But, it was stated that maximum crack density actually occurs under the minimum  $I_p$  and maximum  $T_{on}$  [Lee and Tai (2003)].

Cracks are initiating from the surface and travelling down perpendicularly toward the parent material. In most cases the cracks terminate within the white layer or just on the interface zone between the white layer and heat affected zone. However, under some critical machining settings, cracks can penetrate to the parent material. Grain boundary cracking is evident under such circumstances. Surface cracks that are

initiated at the surface, travel down perpendicularly toward the interferential zone, and terminate at this interference, are primarily produced due to an increase in non-homogeneities of metallurgical phases within the white layer [Ekmekci (2009)]. Lee et al. (2004) presented EDM of H13 and D2 tool steels and analysed the concept of a Crack Critical Line (CCL) is introduced to explore the influence of electrode size, EDM parameters and material thermal conductivity on surface cracking. It is noted that cracks tend not to appear when the machining is performed with a decreased  $I_p$  and an increased  $T_{on}$ . The fatigue strength of mechanical components is dependent on the properties of the surface and near surface regions [Abu Zeid, 1996; Zeid, 1997]. Among the surface defects, cracking was found the most significant since it leads to a reduction in the material resistance to fatigue and corrosion [Lim et al. (1991)], especially under tensile loading conditions.

Due to the non-homogeneity of heat flow and metallurgical alteration or to localised inhomogeneous plastic deformation in EDMed surfaces, residual stresses are produced. Sharp temperature rise causes stresses even more than the yielding point of the material and severe slip, twinning and cleavage depending upon the crystal structure. The degree and nature of residual stresses considerably influence, as they concern with the main material properties. In the past many attempts have been made to measure residual stresses due to EDM, the stresses were deemed to arise mainly as a result of the thermal contraction of the resolidified metal, which was not expelled from the craters, onto the relatively unaffected parent metal, inducing plastic deformation and biaxial tensile stress. Mamalis et al. (1988) used X-ray diffraction (XRD) method in parallel beam modification to determine the residual stress profile of EDMed micro alloyed steel. They detected considerable amount of residual stresses at the sub-surface layer and found that the peak stresses were almost independent of the discharge energy and approaches the ultimate tensile strength of the material. Rebelo et al. (1998) also measured residual stress with XRD technique and found similar stress pattern for martensitic steels. The residual stress increases from the bulk material to a maximum and then decreases again near to the surface. Ghanem et al. (2003) have analysed on martensitic hardenable and non-hardenable steels and reported a high tensile stress level and a wide profile associated with sur-

---

face stress relaxation for hardenable steels. Simulation of the mechanical effect due to the heat gradient induced by the electric discharge (thermal and residual stresses) is the objective of even fewer numerical recent studies [Youshen and Yoshitsugu (1992)], where generally commercial codes are used. Salah et al. (2008) presents numerical results concerning the temperature distribution, the thermal and residual stresses also compared with experimental data and found to be in good agreement.

Although a number of experimental effort have been made to make better understanding of the EDM process, but modelling efforts of the process are really few in comparison. There are may be number of explanation for this, the complex and stochastic nature of the EDM process, the understanding of the complex phenomena inside a plasma channel is deficient and the duration of single discharges are tiny. Every single discharge in EDM process is accompanying with extreme thermal effect and pressure pulse effects. Besides the pulse pressure created by discharge causes a violent erosion effect, and thus a part of the molten material is get rid of to from a crater. Ekmekci et al. (2006) suggested a semi-empirical equation for scaling residual stresses in EDMed surfaces and reported that the stress increases from the surface and attains to a maximum value, which is approximately equals the ultimate tensile strength of the material, and then it falls gradually to zero or even to a small compressive residual stress at greater depths. Residual tensile stress increases with the increase in pulse current and pulse-on duration. Investigation of the residual stresses of EDMed components revealed their tensile nature, the extremely narrow superficial zone where they appear, their high magnitude at the surface layers, and their increase with increasing pulse energy. The formation of surface cracks has attributed to the differentials of high contraction stresses exceeding the material's ultimate tensile stress within the white layer [Lee et al. (2004)]. A qualitative relationship with the operating parameters was presented by Ekmekci et al. (2005) using AISI P20 workpiece material. Mamalis et al. (1988) experimentally investigated on low-carbon steel St37, medium carbon steel C45 and alloyed steel 100Cr6 workpiece and found that the peak stresses are almost independent of the discharge energy and approach the ultimate tensile strength of the material. Rebelo et al. (1998) in his investigation using XRD methodology found that the residual stress of steel workpiece increases

from the bulk material to a maximum and decreases again approaching the surface. Also the peak stresses are almost independent of the discharge energy and the greater the discharge energy, the greater the depth at which the maximum value of residual stress occurs.

### 1.3.3 EDM Modelling

Several modelling attempts have been made to characterize the EDM process based on electro-thermal theory since 1971. Many researchers has analysed in terms of the temperature distribution, crater geometry, and material removal at the cathode. Yeo et al. (2008) showed that the disk heat source models can be enhanced by improving the approximation of the heat flux and energy fraction, however, a simple cathode erosion model using a point heat-source model was presented by Dibitono et al. (1989). The original energy balance for gas discharges was modified and the model uses the photo electric effect as the principal source of energy supplied to the cathode surface. Later, Patel et al. (1989) developed the anode erosion model which accepts power as boundary condition at anode interface and the power supplied is assumed to produce the Gaussian-distributed heat flux on the surface of the anode material. A variable mass, cylindrical plasma model was developed for sparks by Eubank et al. (1989) which consists of three differential equations, one each from fluid dynamics, an energy balance, and the radiation equation, combined with a plasma equation of state.

### *Soft computing modelling*

The use of the artificial neural network (ANN), Fuzzy logic and hybrid intelligent method in modelling using responses obtained from experiments connecting different materials and machining conditions is gaining popularity. There are numerous ANN applications in EDM, as it is an effective method to solve non-linear problem. Mandal et al. (2007) attempted to model the EDM process using ANN with back propagation as the learning algorithm. They modelled surface roughness, MRR and tool wear, with various input parameters and found suitable for predicting the responses. Panda and Bhoi (2005) developed an artificial feed forward neural network based on the Levenberg-Marquardt back propagation technique of logistic sigmoid

activation function to predict MRR of AISI D2 steel. This model performs well under the stochastic environment of actual machining conditions without understanding the complex physical phenomena exhibited in EDM, and provides faster and more accurate results. They found that the 3-4-3-1 neural architecture has the highest correlation coefficient and used it for the analysis. Wang et al. (2003) combined the capabilities of ANN and genetic algorithm to find an integrated solution to the existing problem of modelling and optimisation of EDM processes. Gao et al. (2008) established machining process models based on different training algorithms of ANN, namely Levenberg-Marquardt algorithm, Resilient algorithm, Scaled Conjugate Gradient algorithm and Quasi-Newton algorithm. All models have been trained by same experimental data, checked by another group data, their generalization performance are compared. Levenberg-Marquardt algorithm found to be the better generalization performance and convergence speed is faster. Pradhan (2009) offered a RSM and ANN predictive modelling using  $I_p$ ,  $Ton$ , and dielectric flushing pressure (FP) to predict OC, MRR and TWR. A close agreement was observed among the actual experimental, RSM, and ANN predictive results.

In recent times, a new trend has been introduced to hybridize the features of two or more than two techniques to take advantage of the potential of each technique and shrink their disadvantages. Such technique with combined features is called as hybrid modelling technique. Neuro-fuzzy (NF) systems are synergistic fusion of fuzzy logic and neural networks, hence it can learn from data and retain the inherent interpretability of fuzzy logic. Adaptive Network Based Fuzzy Interface System (ANFIS) was first established by Jyh-Shing and Jang (1993). ANFIS is a network structure consisting of a number of nodes connected through directional links. Each node has a node function with adjustable or fixed parameters. Learning or training phase of network is a process to determine parameter values to sufficiently fit the training data. Tsai and Wang (2001a) in their study, compared six different ANN models and an ANFIS model on MRR in EDM. ANFIS shown to be more accurate and in their further investigations, [Tsai and Wang (2001b)] have applied the same method to predict the Ra. Results show that tangent sigmoid multi layered perceptron (TAN-MLP), radial basis function network (RBFN), Adaptive RBFN and ANFIS models

have shown consistent results. The NF approach is becoming one of the major areas of interest because it gets the benefits of neural networks as well as of fuzzy logic systems, and it removes the individual disadvantages by combining them on the common features. Tsai and Wang (2001a) in their study, compared six different ANN models and an ANFIS model on MRR in EDM. Results show that ANFIS is more accurate and the prediction error is 16.33%.

### *Numerical modelling*

Several approach for solving the thermal problem are enumerated and comprehensive review of mathematical models for EDM has been given in Erden et al. (1995), but at the present time the majority of research work is passionate to numerical models based either on the finite element method or in the finite differences method.

A FEM model has been developed by Yadav et al. (2002) to approximate the temperature field and thermal stresses due to Gaussian heat flux distribution of a spark during EDM of HSS material. The effects of process variables such as ( $I_p$  and  $Tau$ ) on these responses have been reported. A single spark produces significant compressive and tensile stresses beneath of the spark location and mostly the thermal stresses exceed the yield strength of the workpiece in an extremely thin zone near the spark.

Salah and Ghanem (2006) presented numerical results relating to the temperature distribution in EDM process and from these thermal results, MRR and roughness are inferred and compared with experimental explanation. It is revealed that temperature variation of conductivity is of vital significance and provides the better correlations with experimental data. Subsequently, analysed numerical results concerning the temperature distribution, the thermal and residual stresses of EDMed stainless steel AISI 316L workpiece with experimental data, which was in good agreement [Salah et al. (2008)]. Marafona and Chousal (2006) developed a thermal-electrical model using copper and iron as anode and cathode, sparks generated by electrical discharge in a liquid media and the obtained FEM results were compared with the experimental values of the table of AGIE SIT used by other researchers. The TWR and MRR as well as surface roughness results agree reasonably well with them. Allen and Chen

(2007) reported a thermo-numerical model for material removal on molybdenum by a single spark, the effects of EDM parameters on the crater dimension and the tool wear percentage are studied. FEM results are also presented to show how the thermal action of the micro-EDM process affected the surface integrity of machined workpiece. A FEM base model was reported by Das et al. (2003) using process parameters such as power input, pulse duration, etc., to predict the transient temperature distribution, liquid and solid state material transformation, and residual stresses induced in L6 steel. An attractive feature of the model is its ability to predict. The shape of the crater formed during the material removal is also predicted and validated experimentally.

#### 1.3.4 EDM on AISI D2 steel

The latest research represented here is related to EDMachining of AISI D2 steel, which has a very widely growing range of application in dies and mould making industries. Lee et al. (1988) investigated the surface transformation and damage in EDMed AISI D2 tool and other tool steels and reported that the recast layer is composed of two layers and the depth of surface cracks is found to correlate well with the WLT. They attempted were made to quantify the depth of white (or damaged) layer with respect to the process parameters and surface roughness after EDM. It was found that with a fixed dielectric and flushing condition, for a range of  $I_p$  levels varying from 5 to 25 A, the damaged layer correlates well with the pulse energy irrespective of the tool steel material, however the magnitude of the white layer depends only on the area or size of the current pulse-form but not its shape. Guu and Hocheng (2001a) studied the effects of machining parameters of a rotary EDM such as  $I_p$ ,  $T_{on}$ , and workpiece rotation on MRR and surface roughness, and found to be increase with the increase of rotation speed. Also, the results were compared with the conventional EDM and found to more MRR, improved SR and reduced recast layer. Guu et al. (2003) studied experimentally the surface characteristics and machining damage caused by EDM on AISI D2 steel. The recast layer were measured using SEM, residual stresses using XRD machine and surface roughness were measured using surface profilometer and the empirical relations were proposed. It reported that a HAZ is formed just



beneath the recast layer and introduces tensile residual stress on the surface due to the non-homogeneity of heat flow (heated and cooled at a high rate) and metallurgical transformations or to localized inhomogeneous plastic deformation. This tensile stress is the main cause of surface degradation. Subsequently, with experimental analysis. Guu (2005), investigated the surface morphology, surface roughness and micro crack of EDMed AISI D2 tool steel using Atomic Force Microscope (AFM) and assets that the discharge energy is the factor which determines the surface texture. The range of  $I_p$  were taken in the range of 0.5 A to 1.5 A and  $T_{on}$  of 3.2 and 6.4  $\mu s$ . To avoid excessive machined damage and to get good machined surface with low crack depth can be attained by setting low pulse energy. Marafona and Araujo (2009) have reported their research on effect of the workpiece hardness but, they did not provide conclusive result that hardness significantly effect MRR. They suggested that the interaction of workpiece hardness with various factors may be responsible for variation in MRR. Whereas, the surface roughness obtained is marginally influenced by workpiece hardness. The workpiece hardness does effects MMR and Ra of AISI D2 material, but the effect is negligible in comparison to other factors.

Pradhan et al. (2009a) have presented a radial basis function and a back propagation neural network model for the prediction of surface roughness. The input parameters used for this investigation were  $I_p$ ,  $T_{on}$  and duty fraction and both the models could predict surface roughness with reasonable accuracy. However, radial basis function was faster and the back propagation is reasonably more accurate model. Further, Pradhan et al. (2009b) presented a second order regression model and ANOVA is used to check the sufficiency of the model and compared with the radial basis function and a back propagation models. The model predictions were compared with experimental data and prediction errors have been calculated for a different set of testing data and were found to be successful, for reliable prediction of Ra and it is found that the ANN models are comparatively more accurate. Pradhan and Biswas (2009) A neuro-fuzzy model and a regression model was developed to predict MRR, experiments were conducted with various levels of  $I_p$ ,  $T_{on}$  and duty fraction. The models predictions were compared and found that the neuro fuzzy model has better predictive capability than the regression model.

Available literature on die sinking and related electro discharge machining of D2 steel is summarised in Table 1.1. The table shows that machining of D2 steel has been reported by Lee et al. (1988), whereas, Guu and Hocheng, 2001b; Guu et al., 2003 has reported their works on EDM Turning of the same tool steel. They also reported an AFM study of D2 with die sinking EDM.

Table 1.1: Comparative analysis on research on AISI D2 steel and copper tool

Author	Dielectric	$I_p$	$T_{on}$	$T_{au}$	$V$	Other	Responses studied	Major finding
Lee 1988	Paraffin (Sommentor31)	5, 7.5, 15, 25	50, 100, 220, 400, 600, 800	33, 50, 68,80 85,88	30		WLT  SR	WLT $\propto$ Pulse energy WLT no effect material type WLT $\propto$ Ra but scatted Empirical modelling of WLT & Ra
Guu 2001	Kerosene	1,5 10	20, 100, 180, 260	50,83, 90,93		RMP=0, 1200, 2200 5000	MRR  SR	MRR $\propto I_p, T_{on}$ & speed SR $\propto 1/I_p, \propto 1/T_{on}$ $\propto$ & 1/ Rotational speed EDM Turning
Guu 2003	Kerosene	1, 5 10	20, 100 180	50, 83 90,93			WLT  SR	WLT $\propto I_p$ and $T_{on}$ Good SR $\propto 1/$ Pulse energy. RS $\propto 1/$ Pulse energy. EDM Turning
Guu 2005	Kerosene	0.5, 1 1.5	3.2, 6.4				SR and $\mu$ cracks	SR $\propto$ Pulse energy AFM for $\mu$ cracks

(continued on next page)

Table 1.1: Comparative analysis on research on AISI D2 steel and copper tool.(Contd.)

Author	Dielectric	$I_p$	$Ton$	$Tau$	$V$	Other	Responses studied	Major finding
								EDM die sinking EDM Turning
Marafona 2009**		10, 11, and 12	16 18 19	50 65 80	2 4 6	Ram Speed 350 525 700	MRR and SR	$MRR \propto I_p, Tau,$ Ram speed, $Ra \propto I_p, Ton,$ Tau, Comp, ram speed, hardness
Pradhan 2009*	EDM Oil	1,5 10,20 30,50	5, 10, 20 30, 50 100, 200	50 93	50		SR	BPN is Accurate RBFN is faster
Pradhan 2009a	EDM Oil	1,5 10,20 30,50	5, 10, 20 30, 50 100, 150 200, 500 750	50 93	50		SR	$SR \propto I_p$ and $Ton$ ANN models are comparatively more accurate than Regression model

(continued on next page)

Table 1.1: Comparative analysis on research on AISI D2 steel and copper tool.(Contd.)

Author	Dielectric	$I_p$	$T_{on}$	$T_{au}$	$V$	Other	Responses studied	Major finding
Pradhan 2009b*	EDM	10	50	50	50		MRR	$MRR \propto I_p$ and $T_{on}$
	Oil	20	100	85				Neuro fuzzy predicts
		30	150	93				more accurately than regression model
** 1 quenched and tempered specimen and 1 Normalised specimen.* These papers are Outside the scope of present work.								

### 1.4 Research scope and Problem statement

Surface integrity and surface finish are two facets affecting quality of an EDMed component. Further, productivity is constantly a matter of concern with a high level of accuracy for any process, rather it is the driver of economic growth of industry. Therefore, it is always desirable to have machining with maximum MRR, minimal TWR and minimum radial OC, along with better surface integrity. Various research works carried out with workpiece materials like tool steels, ceramics, composites and titanium alloys. Among the tool steels, AISI D2 is treated as a material that is difficult to machine, which has a wide range of application in die and mould making and often machined by EDM. From the available literature, it can be seen that a comprehensive knowledge of electro discharge machining with a wide parametric range is lacking, especially the modelling of MRR, TWR and OC with Neuro-fuzzy technique. Also, FEM modelling of residual stresses on EDMed D2 steel is not been attempted. Experimental work and RSM modelling of WLT, SCD and SR has not been reported yet. Modelling of the process is required for its better understanding of the influence of the machining parameters on the responses. An exact model will help the experimenter to trim down the experimental cost associated with it and optimise the process by setting the required objective.

Thus, the objectives of proposed investigation are as follows,

1. Experimental study of the machining parameters influencing WLT, SCD using RSM model and determining the optimum setting to minimise WLT.
2. To determine the optimal setting of parameters for minimal Surface Roughness applying RSM.
3. Finite element simulations of residual stresses in EDMed components and its parametric study with partial experimental validation.
4. Experimental study of the parameters influencing MRR, TWR and OC and development of soft computing based predictive models and analysis of influence of machining parameters.

---

Title of the thesis is “Experimental investigation and modelling of surface integrity, accuracy and productivity of AISI D2 steel in EDM”.

#### 1.4.1 Research Design

Appropriate experimental plan is considered necessary to realize the high-quality results in carrying out research. In this thesis, the equipments used in this research are explained in Appendix A.

**Research Design Variables:** The design variables are expressed into two most important category, namely response parameters and machining parameters.

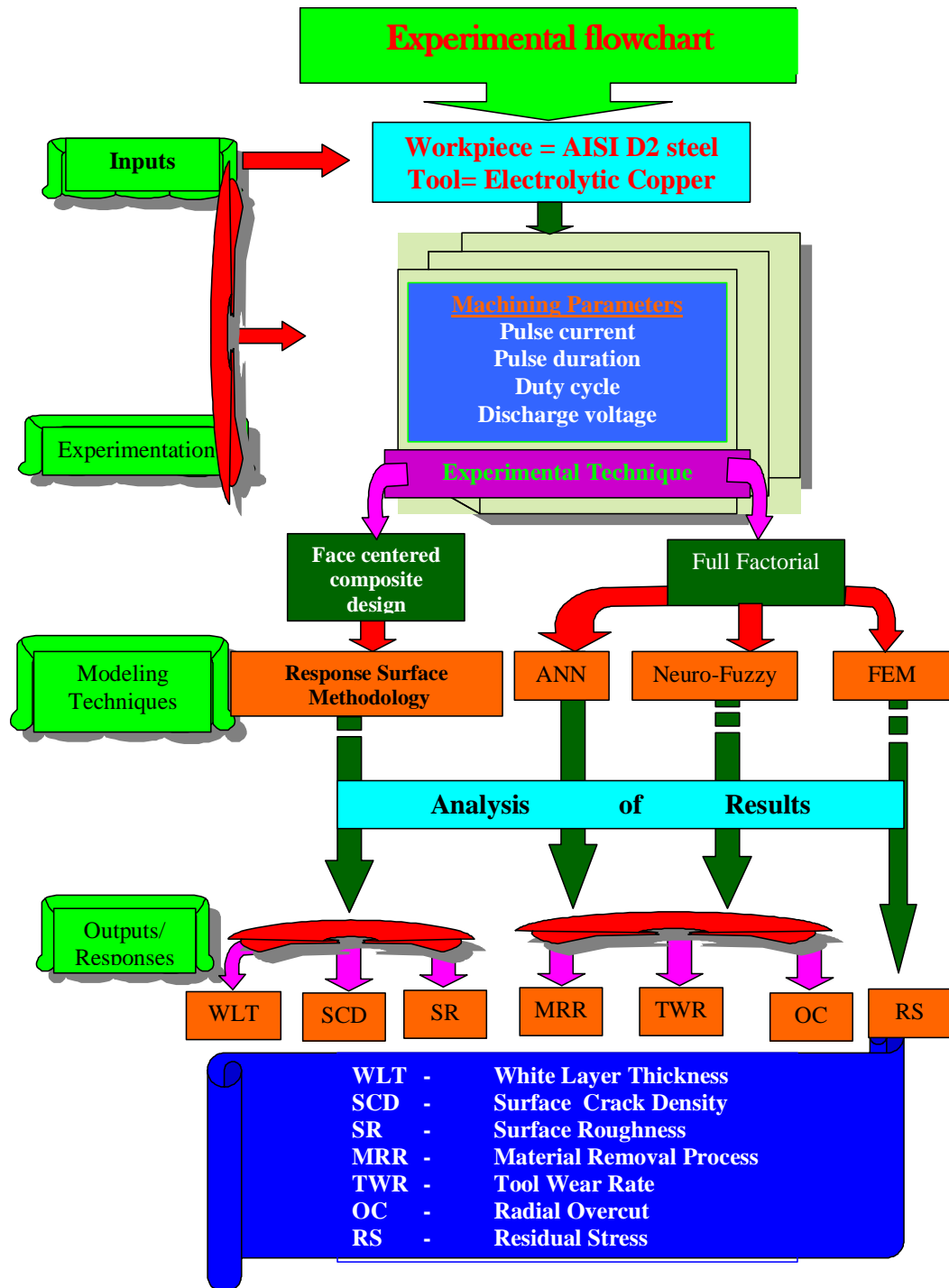
**The response parameters include:**

1. Material removal rate (MRR)
2. Tool wear rate (EWR)
3. Overcut (OC)
4. Surface Roughness (SR)
5. White layer thickness (WLT)
6. Surface Crack Density (SCD)
7. Residual Stress (RS)

**Machining Parameters:**

1. Pulse Current ( $I_p$ )
2. Pulse duration ( $T_{on}$ )
3. Duty Cycle ( $Tau$ )
4. Discharge Voltage ( $V$ )

A summary of the research flowchart is shown in Fig. 1.3.



Note:-Process parameters considered for RS are  $I_p$  and  $T_{on}$ .

Fig. 1.3: Research Design Flow Chart



## 1.5 Summary of chapters

The present work is an effort to develop various prediction models from the experiment trials. Analysis and discussion are made on the quality, productivity and accuracy of EDM process. The quality is analysed in terms of surface integrity of the EDMed product. Surface integrity includes analysis of WLT, SCD, SR and Residual stresses in the surfaces and sub-surface layers. Productivity relates to maximise MRR and accuracy related to minimise TWR and OC. The thesis is divided into six chapters. In the first chapter, an introduction and reviews of the literatures related to die sinking EDM are discussed.

Chapter 2: In this chapter, RSM models are used to investigate the effects of process parameters on the WLT and SCD. Important machining parameters like  $I_p$ ,  $T_{on}$ ,  $T_{au}$  and  $V$  are considered for investigation. The measurements of WLT and SCD are performed on SEM micrograph. Optimal parameter setting for minimum WLT was obtained and the confirmatory tests were conducted and compared using the prediction errors.

Chapter 3: In this chapter, a RSM model to predict the surface roughness is described, and the influences of the process parameters on Ra values are studied. Qualitative assessment of the surface characteristic is attempted with the help of SEM micrographs.

Chapter 4: The finite element modelling of residual stress using the commercial package ANSYS is presented in this chapter. Hence, a simplified 2D axisymmetric FEM model is developed to assess the temperature distribution, thermal stresses and residual stress created by a single spark during EDM.

Chapter 5: Soft computing approaches have recently emerged as a highly promising alternative to physically based models. The current trend in soft computing research is concerned with the integration of artificial intelligent tools (neural networks, fuzzy technology, and evolutionary algorithms.) in a complementary hybrid framework for solving complex problems. The present work is concerned with the modelling of EDM process by the pioneering Neuro-Fuzzy models (Mamdani and Sugeno types) and ANN (back propagation) for the prediction of MRR. TWR and

Radial OC. The influence of the process parameters is analysed and the predictive capability of these models is compared for all the responses.

Conclusively, the intention of this thesis is to develop predictive process models of EDM of AISI D2 tool steel that is capable of predicting the responses such as WLT, SCD, SR, RS, MRR, TWR and Radial OC. In addition, this thesis makes an attempt to explain the effect of various machining factors on these responses using three different approaches. The major achievements and contributions of the present thesis have been summarised in Chapter 6 and scope for further research has been enumerated.

# Chapter II

## Response surface model for prediction of White Layer Thickness & Surface Crack Density

## 2. RESPONSE SURFACE MODEL FOR PREDICTION OF WHITE LAYER THICKNESS AND SURFACE CRACK DENSITY

### 2.1 *Introduction*

With the development of workpiece material of better hardness, strength and higher temperature resistance, it has become difficult to process them by conventional machining methods. Extensive research and development in the field has finally shown the way to a number of modern machining methods to machine such “difficult to machine” materials. Electro-Discharge Machining (EDM) is one of such modern machining process, which has been used extensively primarily in automobile, aircraft, tool, die, and mould making industries. The EDMed surface is created by a sequence of distinct precisely controlled spark produced between electrodes, which create craters in the exposed surface. This process is suitable for machining any conducting materials regardless of its hardness, brittleness, strength, or toughness of the workpiece and the tool doesn't have to be harder than the workpiece as there is no mechanical contact during machining. The electrical discharges generate impulsive pressure by dielectric explosion to remove the melted material. Due to rapid local heating and quenching and random attack of the spark, a multi layered surface is created on the workpiece. This consists of three layers namely: recast or white layer on the top of the work surface, the Heat Affected Zone (HAZ), and the transformed layer, where a change in grain structure from the base structure is apparent [Kruth et al., 1995] as shown (Fig. 2.1). The formation of these layers depends on the process conditions and workpiece properties like chemical composition and thermal conductivity [Ramasawmy et al., 2005]. The molten material produced during the spark is partly flushed away by the dielectric, and the rest re-solidifies that forms the white layer at the top. It has altered metallurgical structure after going through the extremely high energy thermal process accompanied by dielectric cooling process. This layer

usually differs significantly from the base material and it is typically very fine grained and hard. It may be alloyed with carbon released from the cracked dielectric or with material transferred from the tool. It is observed that the white layer contains pock marks, pores, micro-cracks (Fig: 2.2) and also the residual stress are developed (see Chapter 4), which are unfavourable for the functional behaviour of the components.



Fig. 2.1: Surface layers in EDMed workpiece

The next layer, the HAZ is the base material that has been structurally altered by the heat produced during EDM, due to elevation to the austenitising temperature range. This zone may contain rehardened or hard, brittle, untempered martensite that formed during the rapid cooling from this temperature. This can be expected to increase crack susceptibility, because this microstructure stores considerable strain energy that decomposes with heat. Below this layer usually a transformed layer exists where the temperature attained is not as high, and the hardness is therefore, less than the original material. The relative depth of these layers, and even their presence, depends on what type of EDM method used.

The quick heating and cooling effect in EDM persuade a high-temperature gradient within the heat affected area and therefore cause a significant stress within the machined surface. The formation of crack is due to the differential of high contraction stresses induced during the EDM process. When the induced stress exceeds the material's ultimate tensile strength there is formation of crack in the EDMed surface [Lee et al., 1992].

To enhance the life of the EDMed product, the recast layer is normally removed as this layer plays a critical role particularly for applications in which the part is

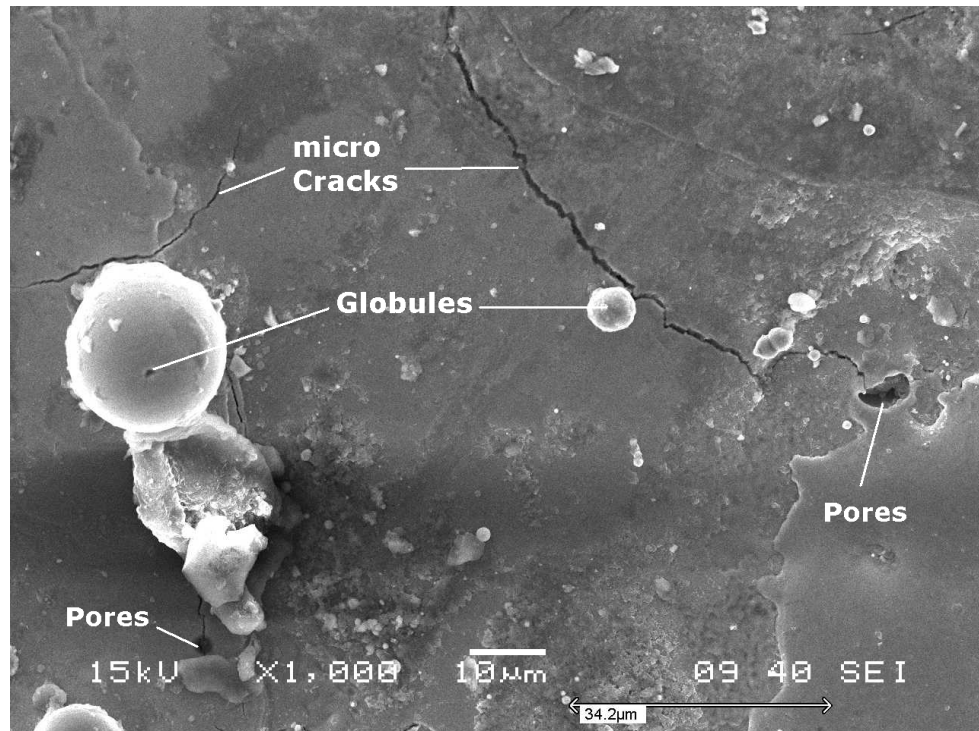


Fig. 2.2: SEM Micrograph (at 1000x) of an EDM surface showing globules and micro-cracks and pores.

subjected to cyclical stress or fluctuating loads. It is usually observed that the cracks are initiated from the top surface and propagate in the white layer and terminate at the white layer and HAZ interface, and rarely do they cross the HAZ. It is well known fact that for characterisation of quality of EDMed component surface plays a vital role. The component having a good surface improves the fatigue strength, wear resistance and corrosion resistance of the surface [Tai and Lu (2009)]. Consequently, the white layer must be removed either by hand polishing, etching or heat treatment, to improve the properties and make the component functional. Instead, burnishing or shot peening is also employed in order to impose a compressive residual stress regime. Usually with abrasive grains such as silicon carbide, alumina, or diamond, are used to polish the surface in the presence of a lubricant, to achieve the mirror-like finish. The polishing must be done appropriately just to remove the white layer, which causes damage to the component, but excessive polishing may lead to removal of excess material and loose precision. However, such processes are supplementary and may increase cost and time. Therefore, it is necessary to determine/predict the

WLT appropriately, which is produced by a given set of machining condition and ultimately, by removing that exact thickness the required tolerance and dimension can be achieved, else the component may be rejected as defective item.

Even though several illustration of surface cracking, surface damage in EDM of AISI D2 steel were presented and the formation of cracks are elucidated in terms of white layer composition, and the process parameters, such as  $I_p$  and  $Ton$ , the studies are limited in the higher range of these parameters, also parameters such as Duty Cycle ( $Tau$ ) and discharge Voltage ( $V$ ) are rarely included. Thus, in this study attempt have been made to visualise the effect of lower range of  $I_p$ ,  $Ton$  along with the process parameter  $Tau$  and  $V$ . In addition, the modelling of WLT and Surface Crack Density (SCD) of D2 steel in EDM using Response Surface Methodology (RSM) with the above machining parameters is carried out.

## 2.2 Experimentation

### 2.2.1 Equipment and workpiece material

Experiments were conducted to study the effects of four machining parameters;  $I_p$ ,  $Ton$ ,  $Tau$  and  $V$  on WLT and intensity of cracking of AISI D2 tool steel on die sinking EDM (Appendix A). An electrolytic pure copper with a diameter of 30 mm was used as a tool electrode (reverse polarity). Appendix A shows the detail of workpiece materials. The workpiece was of size  $35 \times 35$  mm square and 4 mm thick. Commercial grade EDM oil was used as dielectric fluid. Lateral flushing with a pressure of  $0.4 \text{ kgf/cm}^2$  was used.

### 2.2.2 Experimental Procedure

CCD was used to conduct the experiments with four variables, having sixteen cube, eight axial and six central points, in total of 30 runs in three blocks [Minitab14 (2003)]. The different levels of factors considered for this study are illustrated in Table 2.1. Machining was carried out to remove approximately 1 mm from the top surface. Table 2.2 presents run order, point type (Pt Type), block, the various combination of input parameters and the responses (Crack length and WLT) obtained from these experimentations.

Table 2.1: Input variables used in the experiment and their levels.

Variable	Unit	levels		
		1	2	3
Discharge current( $I_p$ )	A	1	5	9
Pulse on time( $T_{on}$ )	$\mu s$	50	75	100
Duty Cycle( $Tau$ )	%	80	85	90
Voltage( $V$ )	volt	40	50	60

## 2.3 Measurement of Responses

### 2.3.1 Measurements of White Layer Thickness

In order to compute the thickness of the white layer, after EDM operations, the cross-section (Fig. 2.3) of each specimen was cut off and polished successively with silicon carbide papers of grit sizes 120, 220, 320, 400, and 800. Finally, the surface was subsequently electro polished with a slurry of Trinity diamond compound and HIFIN Fluid “OS” Type. This was necessary in order to expose the white layer structure and the boundary line. The micrograph of white layer was then seen at magnification of  $500\times$  under Scanning Electron Microscopy (SEM) (Model; Jeol JSM-6480LV, Japan) for the analysis. The area of white layer was measured on each SEM micrograph and the mean deposition of white layer was obtain on division of the measured area by the length of the micrograph (i.e.  $258\mu m$ ). The observations are tabulated in Table 2.2 as column ‘WLT’.

### 2.3.2 Measurements of Surface crack density

The EDMed surfaces were viewed from top under the SEM at  $1000\times$  magnification. The measurement of surface cracks was carried out by measuring the length of cracks on randomly selected six sample areas on each specimen, which are tabulated in Table 2.2. The average crack length on each specimen is divided by the micrograph area ( $12400 \mu m^2$ ) to obtain the SCD and these are tabulated in Table 2.3 as column ‘Average SCD expt’.



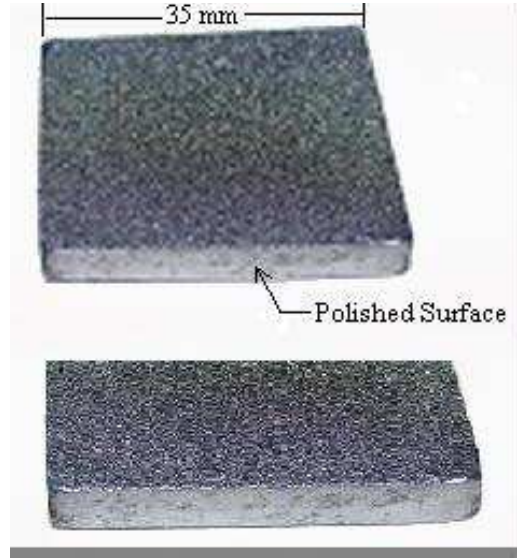


Fig. 2.3: Cut section of workpiece

## 2.4 Planning based on RSM

RSM is a collection of mathematical and statistical techniques that are useful for modelling and analysis of problems in which output or response is influenced by several input variables and the objective is to find the correlation between the response and the variables investigated (Appendix B). The second-order model is normally used when the response function is not known or non-linear and the same is adopted. The experimental values are analysed and the mathematical model is then developed that illustrate the relationship between the process variable and response. The following second-order model explains the behaviour of the system.

$$Y = \beta_0 + \sum_{i=1}^k \beta_i X_i + \sum_{i=1}^k \beta_{ii} X_i^2 + \sum_{i,j=1, i \neq j}^k \beta_{ij} X_i X_j + \epsilon \quad (2.1)$$

where  $Y$  is the corresponding response,  $X_i$  is the input variables,  $X_i^2$  and  $X_i X_j$  are the squares and interaction terms, respectively, of these input variables. The unknown regression coefficients are  $\beta_0$ ,  $\beta_i$ ,  $\beta_{ii}$  and  $\beta_{ij}$  and the error in the model is depicted as  $\epsilon$ .

Minitab14 (2003)(a statistical software package) was used to estimate the coefficient of regression Equation 2.1 from the data obtained from the experiments. The response surface models are developed, which are used to predict the results by iso-

response contour plot and 3D response surface plots to study the main effect of the variables and the mutual interactions between the variables of the responses.

## 2.5 Elucidation of response model for WLT

The effect of the machining parameters ( $Ip$ ,  $Ton$ ,  $Tau$  and  $V$ ) on the response variable WLT was evaluated by conducting experiments as described in Section 2.2. Minitab software was used to find out the relationship between the input factors and the response WLT. To decide the degree of the regression model, the values of the coefficient of determination ( $R^2$ ) and adjusted  $R^2$ -statistic ( $R_{adj}^2$ ) are compared and summarised in Table 2.4 for various models. The full quadratic model is the best among all the models, listed in the table, where  $R^2 = 95.8\%$  indicates that 95.8% of total variation in the response is explained by predictors or factors in the model. However,  $R_{adj}^2$  is 90.7%, which accounts for the number of predictors in the model describe the significance of the relationship. Therefore, the full quadratic model is considered for further analysis in this study.

Table 2.5 represents the regression coefficients in coded units and its significance in the model. The columns in the table correspond to the terms, the value of the coefficients (Coef.), and the standard error of the coefficient (SE Coef), t-statistic and p-value to decide whether to reject or fail to reject the null hypothesis. To test the adequacy of the model, with a confidence level of 95%, the p-value of the statistically significant term should be less than 0.05. The terms marked “\*” in the last column of the table are exceeding 0.05 value. Thus, these terms are insignificant and therefore eliminated for the further analysis. The blocking does not have any significant effect on the response, which reveals that the uncontrollable factors of the experiment conducted were held constant. The backward elimination process discards the insignificant terms to adjust the fitted quadratic model. The model, with rest of the terms after elimination, is presented in Table 2.6. After elimination, the values of  $R^2$  and  $R_{adj}^2$  are 91.6% and 90.3%, respectively. The truncated model has lower  $R^2$  than that of full quadratic model (95.8%), and  $R_{adj}^2$  value is 90.3%, exhibiting significance of relationship between the response and the variables and the terms of the adequate model after the elimination are  $Ip$ ,  $Ton$ ,  $Tau$ , and  $Ton^2$ .

ANOVA is used to check the sufficiency of the second-order model, which includes test for significance of the regression model, model coefficients and test for lack-of-fit. Table 2.7 summaries the ANOVA of the model that comprises of two sources of variation, namely, regression and residual error. The variation due to the terms in the model is the sum of linear and square terms whereas the lack of fit and pure error contribute to residual error. The table depicts the sources of variation, degree of freedom (DF), sequential sum square error (Seq SS), adjusted sum square error (Adj SS), adjusted mean square error (Adj MS), F statistic and the p-values in columns. The p-value of lack of fit is 0.74, which is  $\geq 0.05$ , and certainly indicate that there is statistically insignificant “lack of fit” at 95% confidence level. However, the p-value of regression model and its all linear and square terms have p-value 0.000, hence they are statistically significant at 95% confidence and thus the model adequately represent the experimental data (see Appendix B).

Multi-regression analysis was performed to the data to obtain a quadratic response surface model and the equation thus obtained in uncoded unit is,

$$WLT = -105.0236 + 2.006 Ip + 1.156 Ton + 0.869 Tau - 0.0065 Ton^2 \quad (2.2)$$

To investigate the influence of the machining parameters on the response WLT on EDMed AISI D2 steel components, this mathematical model can be used. Estimated responses are calculated from the fitted model and the residuals from the differences between the fitted and observed responses. Table 2.3 presents the machining parameters for each run order, along with the experimental results (expt.), the predicted response (Pred.) and the residues (Resi.). Where the residues are the difference between the experimentally observed data and the model predictions. The predicted values of WLT achieved using Equation 2.2 are close to the experimental values confirming the sufficiency of the model (Table 2.3) and the residues are further analysed in the following section.

The normal probability plot is a graphical technique for evaluating whether a data set is approximately normally distributed. The standardised residuals are plotted on a normal probability plot (Fig. 2.4) to check the departure of the data from normality. It

can be seen that the residuals are almost falling on a straight line, which indicates that the residues are normally distributed and the normality assumption is valid. Fig. 2.5 depicts the histogram plot of standardised residue for all the observations. The figure shows the symmetry of the residues. It is in the form of Gaussian distribution (bell shape), and the residues are distributed with mean zero. In addition, the plot of the residues verse run order illustrates that there is no noticeable pattern or unusual structure present in the data as depicted in Fig. 2.6. The residues, which lies in the range of -4.72 to 4.58 are scattered randomly about zero, i.e., the errors have a constant variance (Table 2.3). Residual plots are an important accompaniment to the model calculations and may be plotted against the fitted values to offer a visual check on the model assumptions. Experimental observations are compared with the predicted values in Fig. 2.7. It can be examined that the regression model is fairly well fitted with the experimental values.

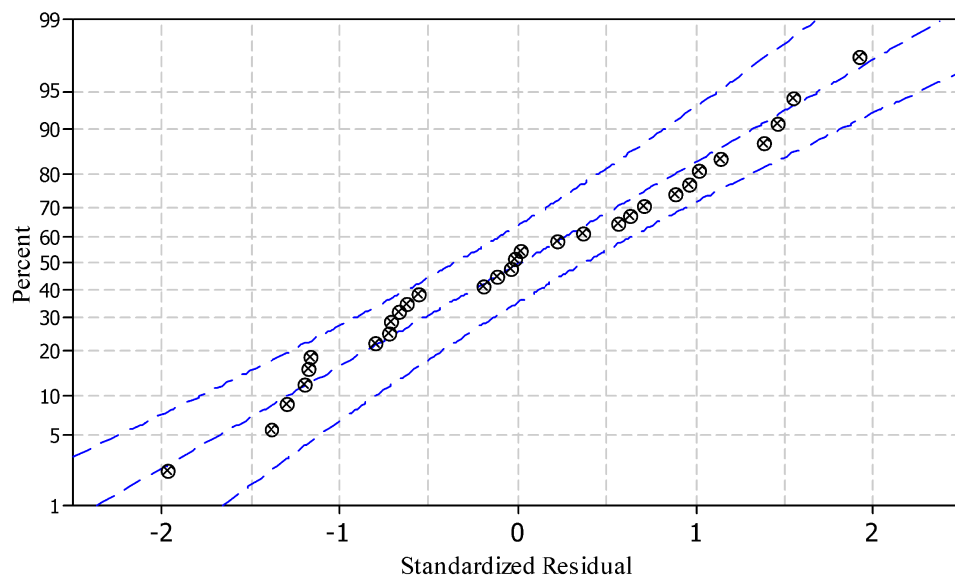


Fig. 2.4: Normal plot of residuals for WLT ( The dotted lines show 95% confidence interval).

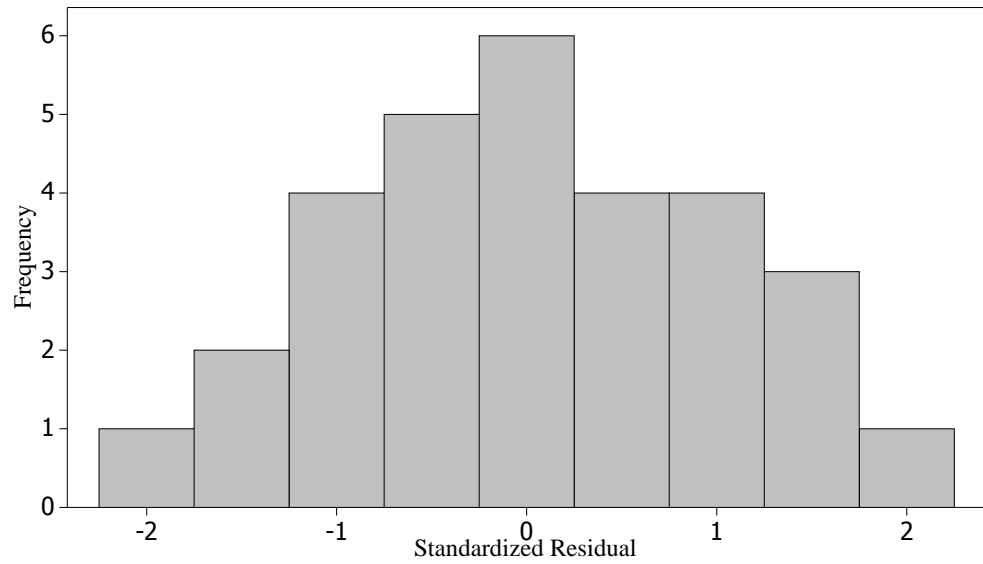


Fig. 2.5: Histogram plot of residuals WLT.

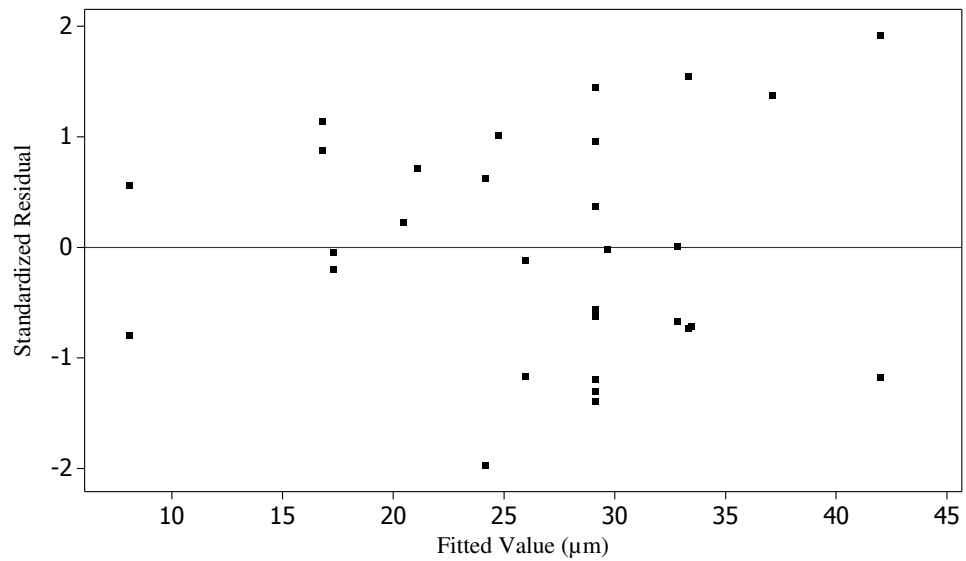


Fig. 2.6: Plot of standardised residuals vs. fitted value for WLT.

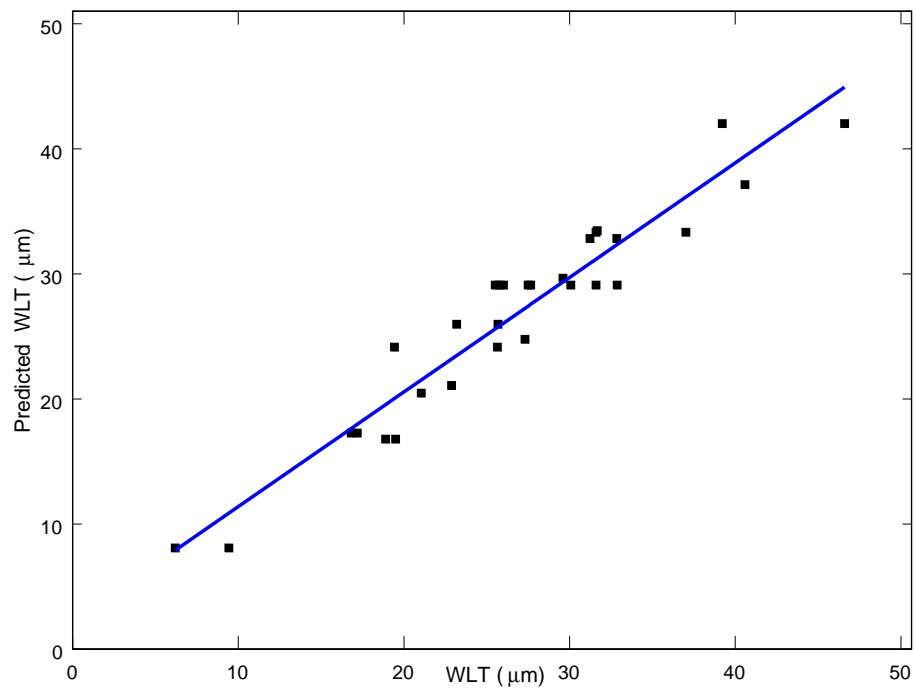


Fig. 2.7: Predicted vs. experimental for WLT.

Table 2.2: Observation for Crack Length and WLT.

Run Order	Pt Type	Blocks	$I_p$	$T_{on}$	$T_{au}$	$V$	Crack Length in $\mu\text{m}$						WLT
			A	$\mu\text{s}$	%	volt	sample no.						$\mu\text{m}$
							1	2	3	4	5	6	
1	1	1	9	100	90	40	224.36	192.02	222.02	201.53	219.19	251.09	39.21
2	1	1	9	50	90	60	235.56	265.49	169.27	128.21	253.94	151.91	31.23
3	1	1	1	100	90	60	776.05	678.56	813.95	698.64	807.38	781.48	25.68
4	1	1	1	100	80	40	664.28	702.68	596.09	766.68	664.62	677.34	16.81
5	0	1	5	75	85	50	308.14	245.64	170.43	308.27	239.75	288.28	26.00
6	1	1	9	100	80	60	188.62	217.01	210.97	240.38	254.60	201.86	37.02
7	1	1	9	50	80	40	210.83	215.56	159.64	157.94	224.92	120.25	19.43
8	0	1	5	75	85	50	361.90	237.03	281.96	190.45	248.21	301.67	25.51
9	1	1	1	50	80	60	688.63	709.18	644.43	551.58	683.11	563.03	9.43
10	1	1	1	50	90	40	579.10	518.88	677.52	550.65	606.27	551.97	19.50
11	1	2	9	50	90	40	140.25	273.25	107.08	209.89	205.70	198.32	32.85
12	1	2	9	100	80	40	195.62	261.58	302.80	175.86	130.97	223.21	31.59
13	1	2	1	50	90	60	679.45	684.27	643.42	732.56	724.74	628.61	18.89

(continued on next page)

Table 2.2: Observation for Crack Length and WLT.(Contd.)

Run	Pt		$I_p$	$T_{on}$	$T_{au}$	$V$	Crack Length in $\mu\text{m}$						WLT
Order	Type	Blocks	A	$\mu\text{s}$	%	volt	sample no.						$\mu\text{m}$
							1	2	3	4	5	6	
14	1	2	1	100	90	40	724.80	773.73	611.01	638.29	833.49	720.48	23.18
15	1	2	9	100	90	60	265.25	227.61	210.29	227.98	205.62	215.18	46.60
16	0	2	5	75	85	50	255.88	197.5	349.18	233.41	258.62	282.76	31.59
17	1	2	9	50	80	60	273.12	132.64	181.17	144.00	246.36	155.52	25.64
18	1	2	1	100	80	60	832.15	715.05	721.46	809.69	772.66	802.15	17.18
19	0	2	5	75	85	50	315.56	249.99	169.59	217.03	302.64	305.56	27.65
20	1	2	1	50	80	40	618.45	541.23	636.28	644.47	552.55	590.55	6.19
21	-1	3	5	75	85	40	393.01	206.37	323.57	208.64	239.76	256.23	30.07
22	-1	3	5	50	85	50	242.83	166.38	253.26	274.38	203.77	259.95	21.04
23	-1	3	5	100	85	50	362.85	253.49	339.30	257.07	247.35	283.52	29.60
24	-1	3	9	75	85	50	149.34	220.33	192.36	282.47	139.52	242.02	40.59
25	-1	3	5	75	80	50	281.27	240.58	259.63	219.16	222.84	276.49	27.30
26	0	3	5	75	85	50	148.18	235.56	249.8	194.97	490.15	304.88	32.87
27	-1	3	1	75	85	50	711.73	668.24	677.76	578.40	767.48	669.28	22.87

(continued on next page)



Table 2.2: Observation for Crack Length and WLT.(Contd.)

Run	Pt		$I_p$	$T_{on}$	$T_{au}$	$V$	Crack Length in $\mu\text{m}$						WLT
Order	Type	Blocks	A	$\mu\text{s}$	%	volt	sample no.						$\mu\text{m}$
							1	2	3	4	5	6	
28	-1	3	5	75	90	50	331.61	332.90	335.58	189.08	160.96	148.87	31.66
29	-1	3	5	75	85	60	269.98	279.94	226.56	198.42	318.58	296.52	27.49
30	0	3	5	75	85	50	321.24	262.84	320.31	179.98	218.06	257.55	25.74
<p>PtType 1 indicates a cube point of the design;                      PtType 0 indicates a center point;                      PtType -1 indicates an axial point;</p>													

Table 2.3: Comparison of experimental and model prediction results for WLT and SCD.

Run Order	$I_p$ A	$T_{on}$ $\mu s$	$T_{au}$ %	$V$ Volt	Average SCD $\mu m/\mu m^2$			Average WLT $\mu m$		
					expt	Pred.	Resi	expt	Pred.	Resi
1	9	100	90	40	0.0176	0.0175	0.0001	39.21	42.02	-2.81
2	9	50	90	60	0.0162	0.0155	0.0007	31.23	32.84	-1.61
3	1	100	90	60	0.0612	0.0616	-0.0004	25.68	25.97	-0.29
4	1	100	80	40	0.0547	0.0564	-0.0016	16.81	17.28	-0.47
5	5	75	85	50	0.0210	0.0211	-0.0001	26.00	29.11	-3.11
6	9	100	80	60	0.0177	0.0178	-0.0001	37.02	33.33	3.69
7	9	50	80	40	0.0146	0.0152	-0.0006	19.43	24.15	-4.72
8	5	75	85	50	0.0218	0.0211	0.0007	25.51	29.11	-3.60
9	1	50	80	60	0.0516	0.0531	-0.0015	9.43	8.10	1.33
10	1	50	90	40	0.0468	0.0478	-0.0010	19.50	16.79	2.71
11	9	50	90	40	0.0152	0.0152	0.0000	32.85	32.84	0.01
12	9	100	80	40	0.0173	0.0175	-0.0002	31.59	33.33	-1.74
13	1	50	90	60	0.0550	0.0531	0.0019	18.89	16.79	2.10
14	1	100	90	40	0.0578	0.0564	0.0015	23.18	25.97	-2.79

(continued on next page)

Table 2.3: Comparison of experimental and model prediction results for WLT and SCD.(Contd.)

Run Order	$I_p$ A	$T_{on}$ $\mu s$	$T_{au}$ %	$V$ Volt	Average SCD $\mu m/\mu m^2$			Average WLT $\mu m$		
					expt	Pred.	Resi	expt	Pred.	Resi
15	9	100	90	60	0.0182	0.0178	0.0004	46.60	42.02	4.58
16	5	75	85	50	0.0212	0.0211	0.0001	31.59	29.11	2.48
17	9	50	80	60	0.0152	0.0155	-0.0003	25.64	24.15	1.49
18	1	100	80	60	0.0625	0.0616	0.0009	17.18	17.28	-0.10
19	5	75	85	50	0.0210	0.0211	-0.0001	27.65	29.11	-1.46
20	1	50	80	40	0.0482	0.0478	0.0004	6.19	8.10	-1.91
21	5	75	85	40	0.0219	0.0198	0.0022	30.07	29.11	0.95
22	5	50	85	50	0.0188	0.0184	0.0004	21.04	20.47	0.57
23	5	100	85	50	0.0234	0.0238	-0.0004	29.60	29.65	-0.05
24	9	75	85	50	0.0165	0.0165	0.0000	40.59	37.13	3.46
25	5	75	80	50	0.0202	0.0211	-0.0009	27.30	24.77	2.53
26	5	75	85	50	0.0218	0.0211	0.0007	32.87	29.11	3.76
27	1	75	85	50	0.0547	0.0547	0.0000	22.87	21.09	1.78

*(continued on next page)*

Table 2.3: Comparison of experimental and model prediction results for WLT and SCD.(Contd.)

Run Order	$I_p$ A	$T_{on}$ $\mu s$	$Tau$ %	$V$ Volt	Average SCD $\mu m/\mu m^2$			Average WLT $\mu m$		
					expt	Pred.	Resi	expt	Pred.	Resi
28	5	75	90	50	0.0201	0.0211	-0.0010	31.66	33.46	-1.80
29	5	75	85	60	0.0214	0.0225	-0.0011	27.49	29.11	-1.62
30	5	75	85	50	0.0210	0.0211	-0.0001	25.74	29.11	-3.37

Table 2.4:  $R^2$  and  $R_{adj}^2$  test for WLT regression model.

Degree of model	$R^2(\%)$	$R_{adj}^2(\%)$
Linear	91.0	88.7
Linear + square	94.0	90.8
Linear + interaction	92.8	87.8
Full quadratic	95.8	90.7

Table 2.5: Estimated Regression Coefficients for WLT (Before elimination).

Term	Coef	SE Coef	t	p
Constant	28.2619	0.9984	28.307	0.000
Block1	-1.1709	0.7426	-1.577	0.139*
Block2	-0.0168	0.7426	-0.023	0.982*
$I_p$	8.0239	0.6236	12.868	0.000
$Ton$	4.5928	0.6236	7.365	0.000
$Tau$	4.3450	0.6236	6.968	0.000
$V$	1.1297	0.6236	1.812	0.093*
$I_p \times I_p$	2.2439	1.6605	1.351	0.200*
$Ton \times Ton$	-4.1661	1.6605	-2.509	0.026
$Tau \times Tau$	-0.0061	1.6605	-0.004	0.997*
$V \times V$	-0.7083	1.6605	-0.427	0.677*
$I_p \times Ton$	1.0269	0.6614	1.553	0.145*
$I_p \times Tau$	-0.0894	0.6614	-0.135	0.895*
$I_p \times V$	0.7444	0.6614	1.125	0.281*
$Ton \times Tau$	-0.6069	0.6614	-0.918	0.376*
$Ton \times V$	0.5294	0.6614	0.800	0.438*
$Tau \times V$	-0.4744	0.6614	-0.717	0.486*
$S = 2.646$	$R^2 = 95.8\%$ $R^2_{(adj)} = 90.7\%$			

Table 2.6: Estimated Regression Coefficients for WLT (After backward elimination).

Term	Coef	SE Coef	T	P
Constant	29.111	0.7809	37.276	0.000
$I_p$	8.024	0.6376	12.584	0.000
$Ton$	4.593	0.6376	7.203	0.000
$Tau$	4.345	0.6376	6.814	0.000
$Ton \times Ton$	-4.051	1.0082	-4.018	0.000
$S = 2.705$	$R^2 = 91.6\%$ $R^2_{(adj)} = 90.3\%$			

## 2.6 Elucidation of response model for SCD

The experiments are conducted as per the experimental plan described in Section 2.2 and estimated the influence of process parameters ( $I_p$ ,  $Ton$ ,  $Tau$  and  $V$ ) on the response SCD. To find out the relationship between the input factors and the response SCD, Minitab software was used as described in Section 2.5. In Table 2.8,  $R^2$ -statistic ( $R^2$ ) and adjusted  $R^2$ -statistic ( $R^2_{adj}$ ) are reviewed to choose the degree of regression

Table 2.7: The ANOVA for the fitted WLT models.

Source	DF	Seq SS	Adj SS	Adj MS	F	P
Regression	4	1996.57	1996.57	499.142	68.20	<b>0.000</b>
Linear	3	1878.40	1878.40	626.133	85.55	0.000
Square	1	118.17	118.17	118.170	16.15	0.000
Residual Error	25	182.96	182.96	7.319		
Lack-of-Fit	10	56.16	56.16	5.616	0.66	<b>0.740</b>
Pure Error	15	126.80	126.80	8.453		
Total	29	2179.53				

for SCD model. It can be clearly seen that the full quadratic model has highest value of  $R^2$  and  $R_{adj}^2$ , where  $R^2 = 99.8\%$  indicates that 99.8% of total variation in the response is explained by predictors or factors in the model. On the other hand,  $R_{adj}^2$  is 99.6%, which accounts for the number of predictors in the model describes the significance of the relationship. Thus, the full quadratic model is considered for further analysis in this study similar to WLT.

Table 2.9 represents the regression coefficients in coded units and its significance in the model. The columns in the table correspond to the terms, the value of the coefficients (Coef.), and the standard error of the coefficient (SE Coef), t-statistic and p-value to decide whether to reject or fail to reject the null hypothesis as described earlier in Section 2.5. Thus the terms marked “\*” are insignificant terms and are discarded for further analysis. Insignificance of blocking reveals that the uncontrollable factors of the experiment conducted were held constant. The model, with rest of the terms after elimination, is presented in Table 2.10. After elimination of non-significant terms, the values of  $R^2$  and  $R_{adj}^2$  are 99.7% and 99.7%, respectively. The truncated model has lower  $R^2$  value than that of full quadratic model (99.8%), and  $R_{adj}^2$  value is 99.6%, exhibiting significance of relationship between the response and the variables and the terms of the adequate model after the elimination are  $I_p$ ,  $Ton$ ,  $V$ ,  $I_p \times I_p$ ,  $I_p \times Ton$  and  $I_p \times V$ .

To check the sufficiency of the SCD model, AVOVA was used and shown in Table 2.11. It can be observed that the p-value of lack of fit is 0.59 ( $\geq 0.05$ ), and indeed specify that there is statistically insignificant “lack of fit” at 95% confidence

level. Nevertheless, the p-value of regression model and its all linear and square terms have p-value 0.000, therefore they are statistically significant at 95% confidence and consequently the model adequately represents the experimental data.

Multi-regression analysis was performed to the data to obtain a quadratic response surface model and the equation thus obtained in un-coded unit was,

$$\begin{aligned} SCD = & 0.0388 - 0.0111 I_p + 0.000187 Ton + 0.000296 V \\ & + 0.000905 I_p^2 - 0.0000156 I_p \times Ton - 0.0000316 I_p \times V \end{aligned} \quad (2.3)$$

To investigate the influence of the machining parameters on the response SCD in EDMed AISI D2 steel components manufactured, this mathematical model can be used. The predicted values of SCD achieved using Equation 2.3 were close to the experimental values confirming the sufficiency of the model. The experimental results of SCD along with the predicted values and residuals in the run order of design matrix are tabulated in Table 2.3. To show the sufficiency of the model the residues are analysed in the following section.

This mathematical model has been obtained to reflect the independent, quadratic, and interactive effects of the various machining parameters on the EDM process. The normal probability plot of residuals for SCD is illustrated in Fig. 2.8; this graph plots the residuals versus their expected values when the distribution is normal. The residuals from the analysis should be normally distributed. It can be seen that the residuals are almost falling on a straight line, which indicates that the residues are normally distributed and the normality of errors assumption is valid. It could be noted that the residue is the difference of experimentally observed data and the model predictions. The figure shows the symmetry of the residues. Few point exhibit significantly large variation and are plotted as outliers as encircled in Fig. 2.8. The standardised residues are within  $\pm 2$  and few points are marginally outliers due to measurement error in estimating the crack length from SEM micrograph. Fig. 2.9 depicts the histogram plot of standardised residue for all the observations. It is in the form of Gaussian distribution (bell shape), and the residues are distributed with mean zero. In addition, the plot of the residues verse run order illustrates that there is no noticeable pattern or unusual structure present in the data as depicted in Fig. 2.10.

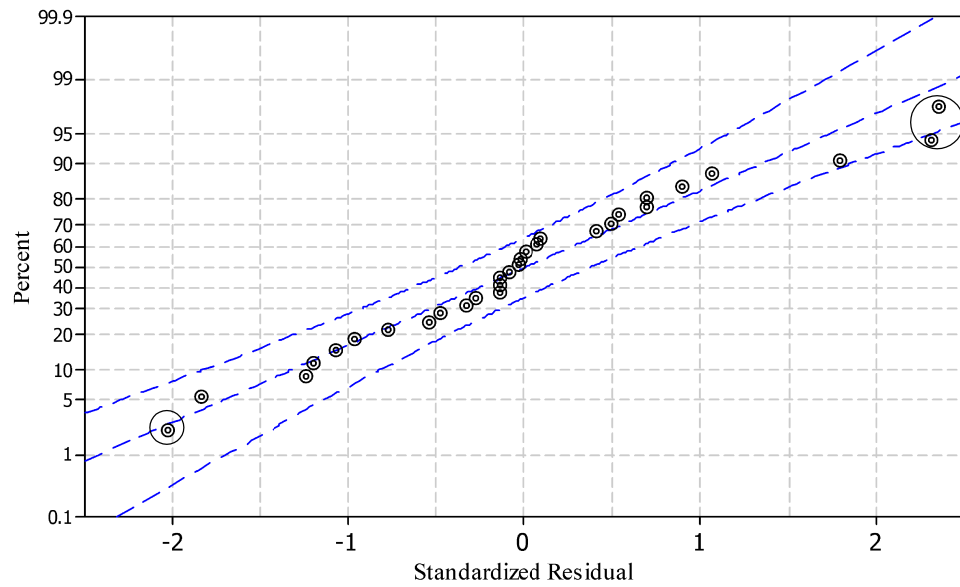


Fig. 2.8: Normal plot of residuals for SCD.

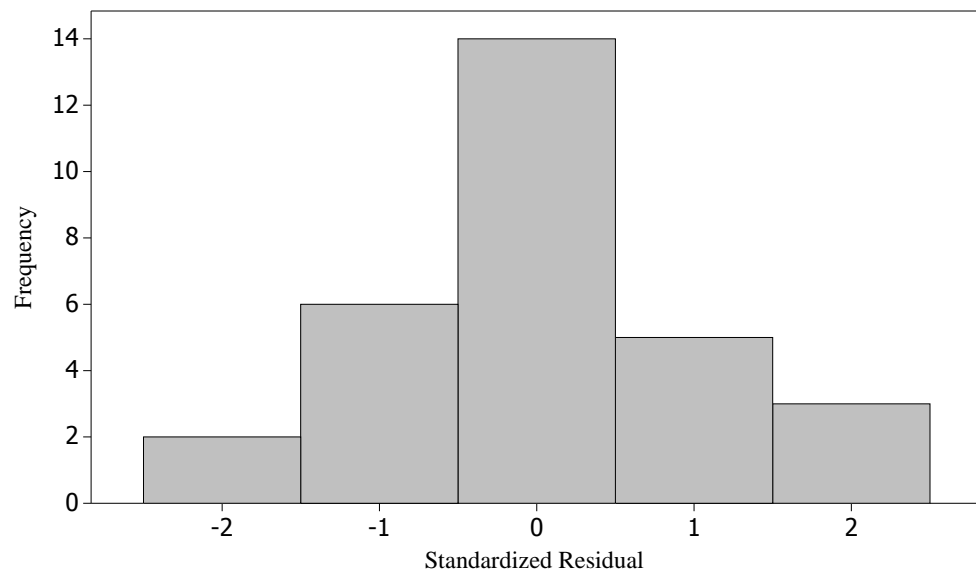


Fig. 2.9: Histogram plot of residuals SCD.



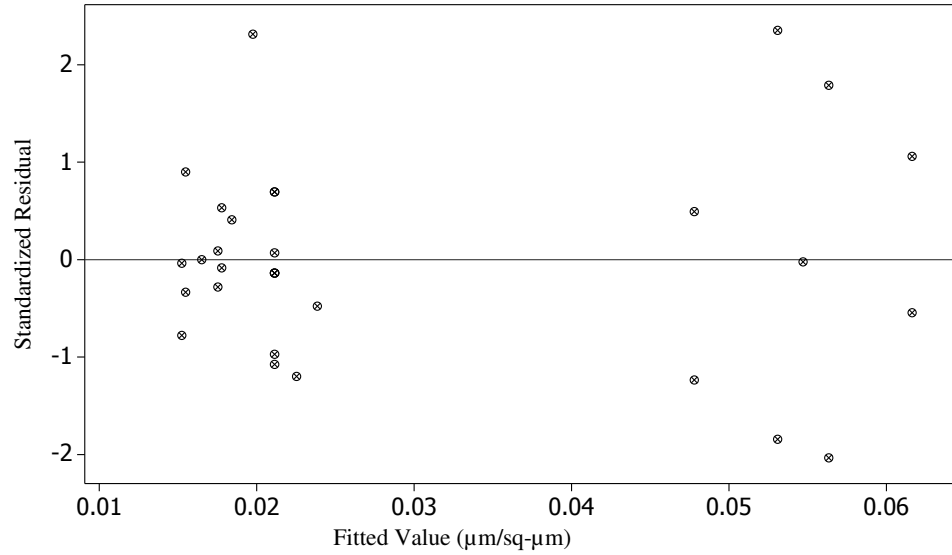


Fig. 2.10: Plot of standardised residuals vs. fitted value for SCD

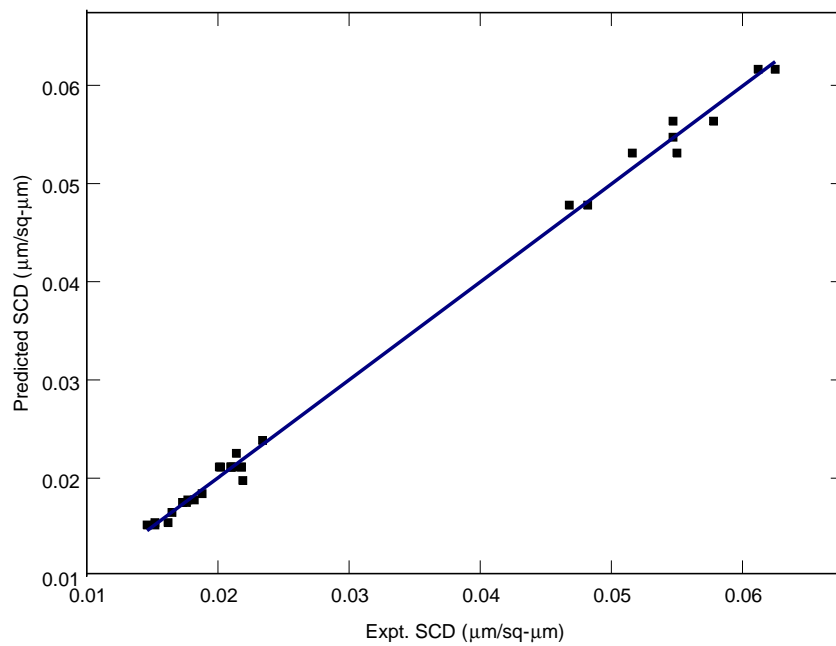


Fig. 2.11: Predicted vs. experimental SCD.

Further, the plot of the residue versus fitted value of SCD is illustrates that there is no noticeable pattern or unusual structure present in the data as depicted in Fig. 2.10. The residues, which lies in the range of -0.0016 to 0.0022 are scattered randomly about zero, i.e., the errors have a constant variance. Further, each experimental observation is compared with the predicted value in Fig. 2.11. It can be examined that the regression model is fairly well fitted with the experimental values.

Table 2.8:  $R^2$  and  $R_{adj}^2$  test for SCD regression model.

Degree of model	$R^2(\%)$	$R_{adj}^2(\%)$
Linear	87.1	83.7
Linear + square	99.0	98.5
Linear + interaction	87.8	79.2
Full quadratic	99.8	99.6

Table 2.9: Estimated Regression Coefficients for SCD (Before elimination).

Term	Coef	SE Coef	T	p
Constant	0.021229	0.000402	52.783	0.000
Block 1	-0.000364	0.000299	-1.216	0.246*
Block 2	0.000476	0.000299	1.592	0.135*
$I_p$	-0.019111	0.000251	-76.081	0.000
$Ton$	0.002711	0.000251	10.793	0.000
$Tau$	0.000339	0.000251	1.349	0.200*
$V$	0.001383	0.000251	5.507	0.000
$I_p \times I_p$	0.014555	0.000669	21.759	0.000
$Ton \times Ton$	0.000055	0.000669	0.082	0.936*
$Tau \times Tau$	-0.000895	0.000669	-1.339	0.204*
$V \times V$	0.000605	0.000669	0.904	0.383*
$I_p \times Ton$	-0.001562	0.000266	-5.865	0.000
$I_p \times Tau$	-0.000087	0.000266	-0.328	0.748*
$I_p \times V$	-0.001263	0.000266	-4.739	0.000
$Ton \times Tau$	-0.000063	0.000266	-0.235	0.818*
$Ton \times V$	-0.000062	0.000266	-0.235	0.818*
$Tau \times V$	0.000062	0.000266	0.235	0.818*
S = 0.001066	$R^2 = 99.8\%$ $R_{(adj)}^2 = 99.6\%$			

Table 2.10: Estimated Regression Coefficients for SCD (After backward elimination).

Term	Coef	SE Coef	T	P
Constant	0.021133	0.000289	73.002	0.000
$I_p$	-0.019111	0.000236	-80.853	0.000
$T_{on}$	0.002711	0.000236	11.470	0.000
$V$	0.001383	0.000236	5.852	0.000
$I_p \times I_p$	0.014478	0.000374	38.739	0.000
$I_p \times T_{on}$	-0.001562	0.000251	-6.232	0.000
$I_p \times V$	-0.001263	0.000251	-5.036	0.000
S = 0.001003 $R^2 = 99.7\%$ $R^2(adj) = 99.7\%$				

Table 2.11: The ANOVA for the fitted SCD models.

Source	DF	Seq SS	Adj SS	Adj MS	F	p
Regression	6	0.008315	0.008315	0.001386	1377.99	<b>0.000</b>
Linear	3	0.006741	0.006741	0.002247	2234.36	0.000
Square	1	0.001509	0.001509	0.001509	1500.68	0.000
Interaction	2	0.000065	0.000065	0.000032	32.10	0.000
Residual Error	23	0.000023	0.000023	0.000001		
Lack-of-Fit	8	0.000007	0.000007	0.000001	0.83	<b>0.590</b>
Pure Error	15	0.000016	0.000016	0.000001		
Total	29	0.008338				

## 2.7 Result and discussion

### 2.7.1 Effect of machining parameters on WLT

The recast layer and HAZ thickness are dependent on heat transfer and the micro structural change undergone by the workpiece during the EDM process. The existence of white layer on EDMed surface is anticipated and it is governed by the efficiency of heat transfer through the rapidly solidifying metal. The heat transfer is a function of the amount of heat supplied by pulse energy. The pulse energy emphasised by Marmalis et al. (1987), usually quoted in the literature as being an important machining parameter, is given by

$$\text{Pulse energy} = \int_t V(t)Ip(t)dt = V Ip Ton \quad (2.4)$$

where  $V(t)$  and  $Ip(t)$  are discharge voltage and current as functions of time  $t$ . The heat transfer during the process is dependent of the spark energy supplied, thus  $Ip$  and the length of  $Ton$  as well as  $Toff$  are important factors. Pulse current and pulse duration are important, which in turn establishes the size and depth of the craters caused by the spark. In other words, if  $Ip$  and  $Ton$  are reduced then small spark energy will be supplied, therefore, there will be formation of smaller craters, and less heat will reduce thickness of the recast layer and HAZ. However, if  $Toff$  is more, which is the time between the end of a spark to the beginning of successive spark, will allow the workpiece to dissipate the heat and thus lower WLT. The effect of the machining parameters on the white layer thickness are enlightened distinguishably and demonstrated by main effect and interaction plots, three dimensional plots and contour plots.

Fig. 2.12 depicts the plots of the main effects on WLT, those can be used to graphically assess the effects of the factors on the response. It indicates that  $Ip$ ,  $Ton$  and  $Tau$  have significant effect on WLT, which is supported by the results in Table 2.6. However,  $Ip$  is the most influencing parameter showing a sharp increase of 7.29  $\mu\text{m}$  and 5.75  $\mu\text{m}$  in the mean of WLT when  $Ip$  increases from 1A to 5 A and 5A to 9A, respectively. In addition, the mean of WLT is directly proportional to  $Ton$ , but its main effect is sharply increasing by 8.65  $\mu\text{m}$  when  $Ton$  increases from 50 to

75  $\mu\text{s}$  and then by 0.531  $\mu\text{m}$  when  $Ton$  increases for a 75 to 100 $\mu\text{s}$ . While,  $Tau$  is also directly proportional to the mean WLT and its effect increases by 7.24  $\mu\text{m}$  in the range of  $Tau$  80% to 85% whereas it is 1.45  $\mu\text{m}$  in the range of 85% to 90 %.

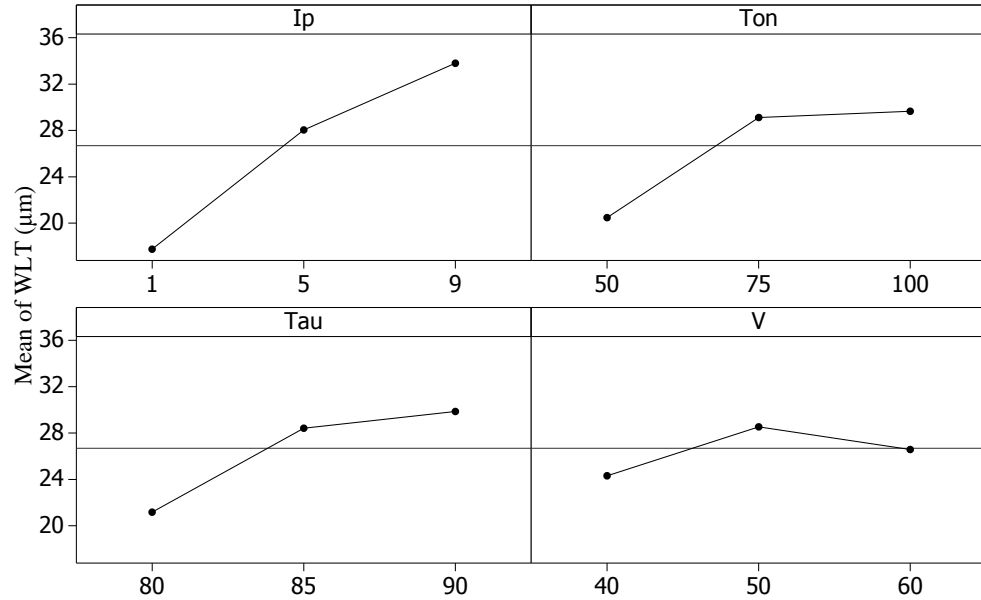


Fig. 2.12: Effect of factors on WLT.

The empirical model reported by previous investigators Guu et al. (2003) and Lee et al. (1988) are compared with the present RSM model for the average thickness of white layer. It is found that the WLT increases with an increase in  $I_p$  and  $Ton$  in all the three cases. The values of WLT reported by Lee et al. (1988) were minimum as the experiments were conducted with discharge voltage of 30 volt and  $Toff$  was taken as 100  $\mu\text{s}$  therefore, ( $Tau = 33, 43$  and  $50$  %) and the dielectric used was Paraffin (Sommentor 31). In the present study, though  $Tau$  is found to be insignificant parameter, but its influence cannot be ignored here for comparison, and the graphs are plotted for the same values (80 % to 90 %) of  $Tau$  in Fig. 2.13. The discharge voltage set in the present study was 50 v, which was higher than that used by Lee et al. (1988). They have reported that the WLT increases with the pulse energy, however, referring to Equation 2.4, it can be seen that  $V$  is an important factor which is responsible for pulse energy, thus with lower pulse energy the WLT will be lower. Moreover, the dielectric (EDM oil) used in the current investigation was different from that used by Lee et al. (1988) might have caused more deposition of

white layer. Similarly, in the study by Guu et al. (2003), they also found similar trend in their study while conducting experiments on EDM turning with kerosene as dielectric. They have not reported the voltage considered in their study, and probably this parameter was set beyond the range of the present study, which may be the reason for variations in the results. Moreover, Guu et al. (2003) has reported that in EDM turning WLT will be less due to better flushing than die sinking EDM hence, a subtle comparison may not be possible with the experimental conditions considered in this study.

Fig. 2.14 contain six interaction plots for various two-factor interactions between  $I_p$ ,  $Ton$  and  $Tau$ . Each pair of the factor is plotted keeping the other factors constant at the mean level. In each plot, the factors of interest are varied from its low level to its medium and medium to high level. If the lines in the interaction plot are parallel, there is no interaction between the process parameters. This implies that the change in the mean response from low to medium and medium to high level of a factor does not depend on the level of the other factor. On the other hand, if the lines are non-parallel, an interaction exists between the factors. The greater the degree of departure from parallelism, the stronger is the interaction effect. It can be seen in the figure that none of them are intersecting each other significantly and hence showing no significant interaction at a confidence level of 95%, which is also evident from Table 2.6.

Fig. 2.15 (a) and (b) represents contour plot and response surface, respectively, for WLT in relation to the machining parameters of  $I_p$  and  $Ton$ . It is seen from the figure that, the WLT tends to increase significantly with the increase in  $I_p$  for any value of  $Ton$ . This can be attributed to the increase in  $I_p$  generates stronger sparks causing a higher temperature and there is a formation of more molten material. The dielectric used for flushing is unable to flush away progressively the molten metal, and hence it gets deposited in the parent material. Subsequently, the unflushed molten metal is quenched, and re-solidifies and thus thicker WLT is formed. However, it can also be seen with the increase in  $Ton$ , the WLT also increases sharply to an extent and then the increase is comparatively slow, which appears to be vital controlling variable. With the longer  $Ton$ , the produced heat, which is generally very high, conducted deep

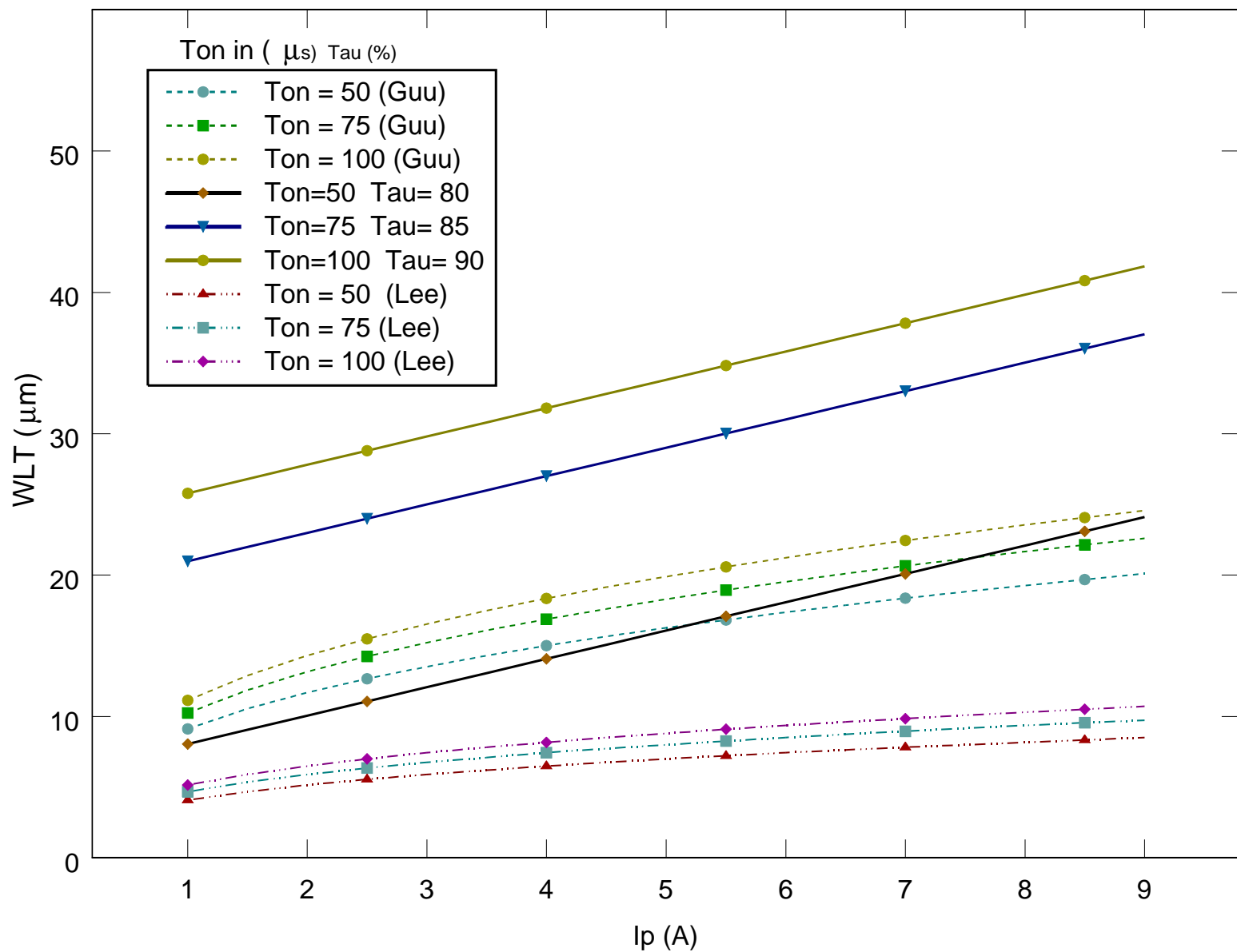


Fig. 2.13: Comparison results for WLT obtained by Guu et al. (2003) and Lee et al. (1988) with different  $I_p$  and  $T_{on}$

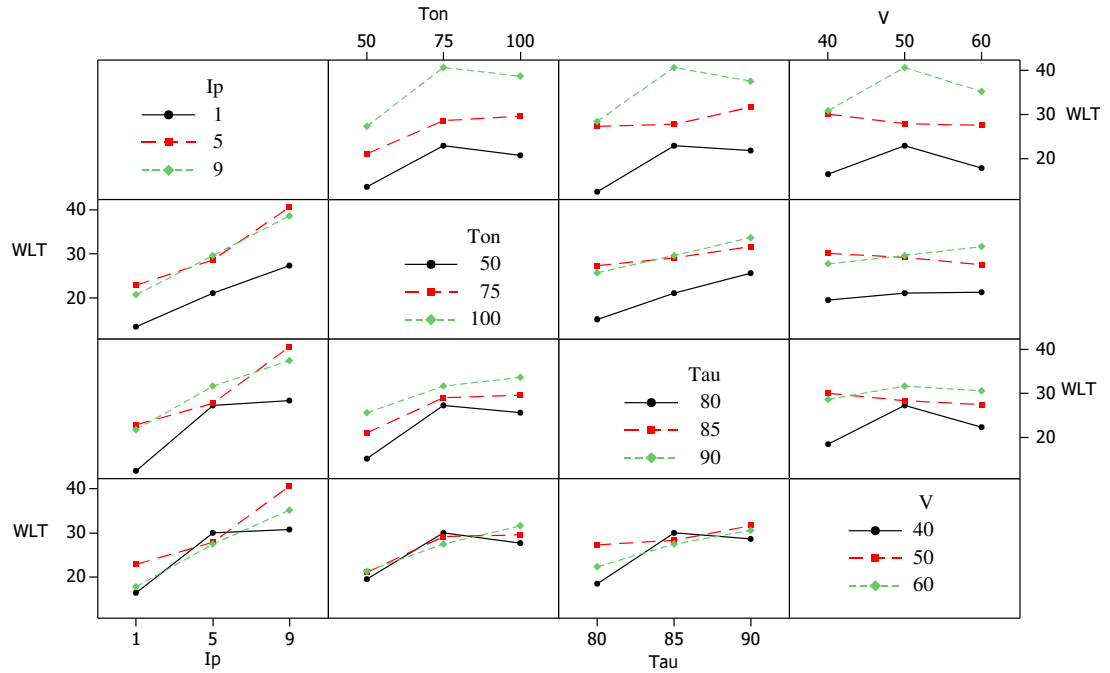


Fig. 2.14: Interaction effect of factors on WLT.

into the material, melts more material, and thus after subsequent quenching, deeper white layer is formed. However, beyond a certain value of  $Ton$  the heat supplied is distributed to the surrounding and the temperature rise is comparatively less, this leads to produce comparatively slight increase in the amount of molten material. Therefore, the initial gradient is sharper than that of later. Hence, the maximum WLT is obtained at the high peak current (9 A) and the high pulse on time (80 to  $100\mu s$ ) and to minimise WLT,  $Ip$  and  $Ton$  should be shorten and lengthen the pulse off time ( $Toff$ ), which will allow the heat to dissipate.

The effect of  $Ip$  and  $Tau$  on the estimated contour and response surface of WLT is depicted in Fig. 2.16 (a) and (b), respectively, where  $Ton$  remains constant at its mean level of  $75\mu s$ . It can be noted that, when  $Ip$  increases WLT also increases, the explanation is same, as stated earlier, nevertheless, with the increase in  $Tau$ , WLT also increases. Since, duty cycle ( $Tau$ ) is the ratio of  $Ton$  to pulse period (sum of  $Ton$  and  $Toff$ ), for a constant  $Ton$ , higher the duty cycle, lower will be  $Toff$  and vice versa. So to achieve lower WLT, the  $Toff$  should be high i.e.  $Tau$  should be as low as possible as depicted in the figure.

Finally, Fig. 2.17 (a) and (b) represents WLT as a function of  $Ton$  and  $Tau$ ,



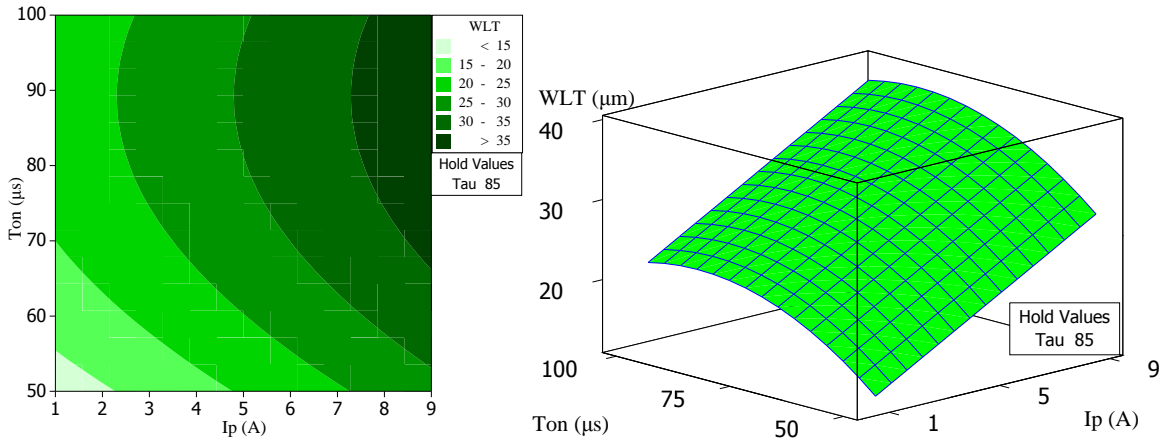


Fig. 2.15: (a) Contour plot, (b) Response surface plot representing the effect of  $I_p$  and  $T_{on}$  on WLT

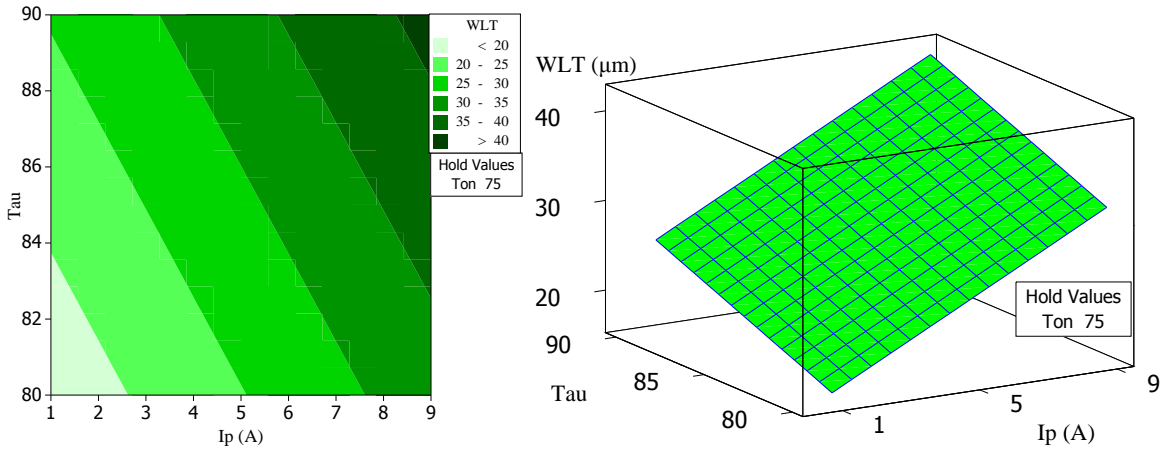


Fig. 2.16: (a) Contour plot, (b) Response surface plot representing the effect of  $I_p$  and  $\tau$  on WLT

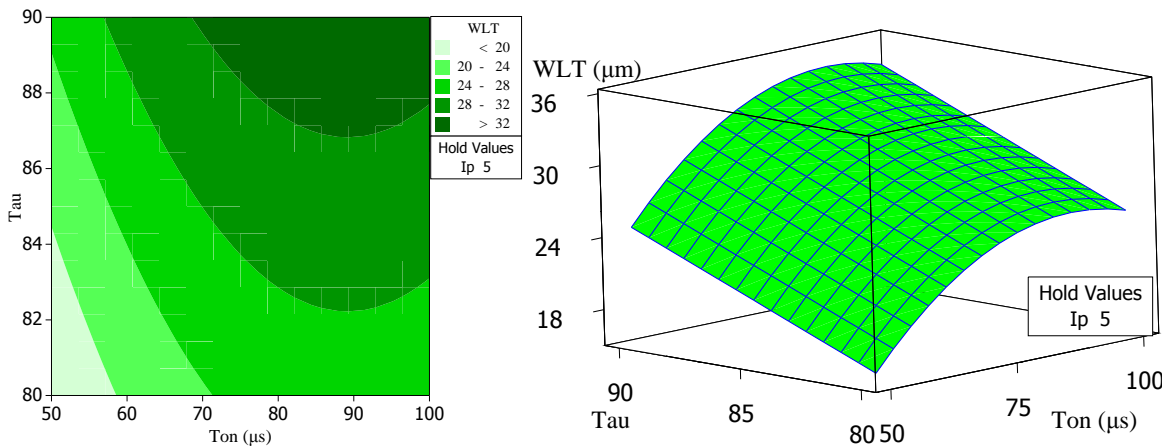


Fig. 2.17: (a) Contour plot, (b) Response surface plot representing the effect of  $T_{on}$  and  $\tau$  on WLT.

whereas the  $I_p$  remains constant at 5 A. The lowest possible WLT value occurred at smaller  $T_{on}$  and at smaller  $\tau$  as evident from the figure. From these observations, it can be concluded that  $I_p$ ,  $T_{on}$  and  $\tau$  are directly proportional to the WLT for the given range of experiments conducted for this test.

### 2.7.2 Scanning Electron Microscopy (SEM) images for WLT

The typical morphology of an EDMed surface is produced due to the discharge energy which generates very high temperatures (more than 10,000°C) at the point of spark on the surface of the workpiece, removing the material by melting and vaporisation of the material, subsequently the molten metal resolidifies and quenched. This material was heated up to the molten state but neither ejected nor removed by the flushing action of the dielectric. This resolidified/ recast layer has been called the white layer, and it contains numerous pock marks, globules, cracks and micro-cracks, whose thickness and density depends on the process conditions. Under the white layer, other layers may be noticed, and the number of layers differs from sample to sample as reported by Kruth et al. (1995).

The micrographs of EDMed surfaces, with the high magnification (500×), for the machining parameter combination  $I_p/T_{on}/\tau/V$  of 1/75/85/50 is shown in Fig. 2.18. Keeping other parameters at their mean levels, Fig. 2.18, Fig. 2.19 and Fig. 2.20 revealed the trend of WLT with increasing  $I_p=1A, 5A, 9A$ , respectively. Average WLT of these micrographs are 22.87  $\mu\text{m}$ , 27.65  $\mu\text{m}$  and 40.59  $\mu\text{m}$  for  $I_p=1A, 5A, 9A$ , respectively, showing the increase in WLT with the pulse current. The increase in average WLT can also be qualitatively scrutinised by the micrographs with increasing  $I_p$  from 1A. Higher discharge current certainly facilitate the rise in temperature of the machined surface producing more molten metal readily. The flushing pressure of the dielectric is increasingly inadequate to carry away the additional molten material produced by higher pulse current. In such circumstances, the vaporisation pressure is incapable to send out the molten metal away from the surface of the workpiece, and during subsequent quenching causes the metal to re-solidify on the machined surface to form the added thickness of white layer.

In the same way, the SEM micrographs for  $T_{on}$  at 50  $\mu\text{s}$ , 75  $\mu\text{s}$  and 100  $\mu\text{s}$  are

shown in Fig. 2.21, Fig. 2.19 and Fig. 2.22, respectively, maintaining  $I_p$ ,  $Tau$  and  $V$  at 5A, 85% and 50 volt (at their mean level). The respective average WLT are 21.04  $\mu\text{m}$ , 27.65  $\mu\text{m}$  and 29.60  $\mu\text{m}$ , where the increase of WLT can be qualitatively visualised from the SEM micrographs presented. This increase is probably due to the reason that with the increase of  $Ton$ , the fraction of the supplied spark energy required for vaporisation decreases and the fraction of melting increases. This will lead to penetrate heat deep in to the material causing increase of formation of molten material rather than vaporisation with smaller  $Ton$ . The increased molten material is not able to increasingly flush away by the constant flushing pressure provided. Hence, partly resolidify during subsequent quenching and forms white or recast layer, the thickness of which is higher for higher  $Ton$  as depicted in the figures.

With increasing duty factor,  $Tau = 80\%$ , 85% and 90%, the SEM micrographs are presented in Fig. 2.23, Fig. 2.19 and Fig. 2.24, respectively, and the corresponding WLT are 27.3 $\mu\text{m}$ , 27.65 $\mu\text{m}$  and 31.66 $\mu\text{m}$ . WLT increases slightly with increase in  $Tau$ , as compared to  $I_p$  and  $Ton$ . As revealed in Section 2.7.1,  $Tau$  increases with the decrease in pulse off time ( $Toff$ ) and vice-versa, which is the time between the end of a spark and the next spark. This is the time during which the molten material is flushed away by the dielectric. With larger  $Tau$ ,  $Toff$  is small, therefore there is less time to flush the molten material, which resolidifies on the machined surface resulting in thicker whitelayer.

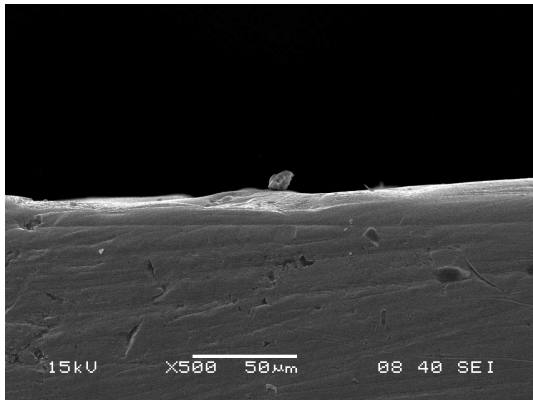


Fig. 2.18: SEM snap WLT at 1/75/85/50

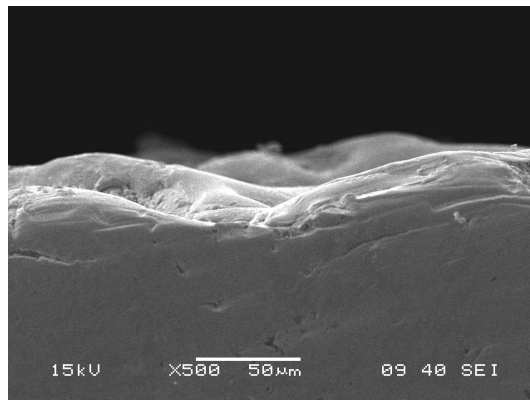


Fig. 2.19: SEM snap WLT at 5/75/85/50

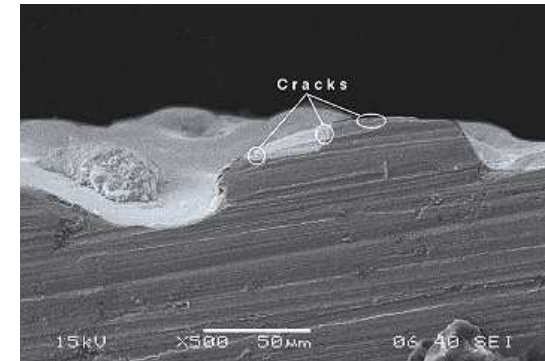


Fig. 2.20: SEM snap WLT at 9/75/85/50

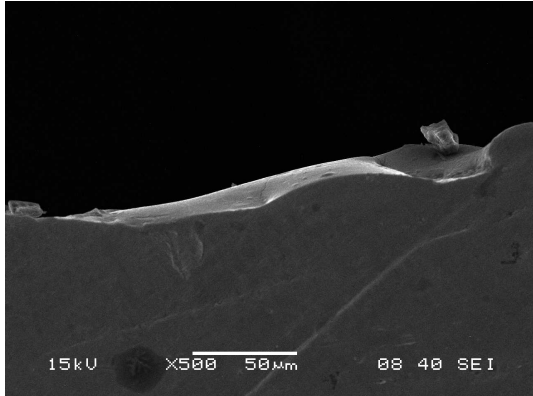


Fig. 2.21: SEM snap WLT at 5/50/85/50

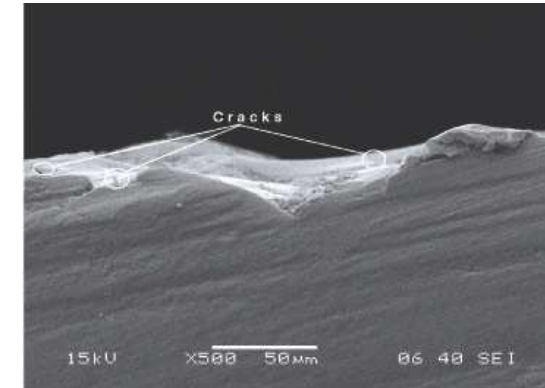


Fig. 2.22: SEM snap WLT at 5/100/85/50

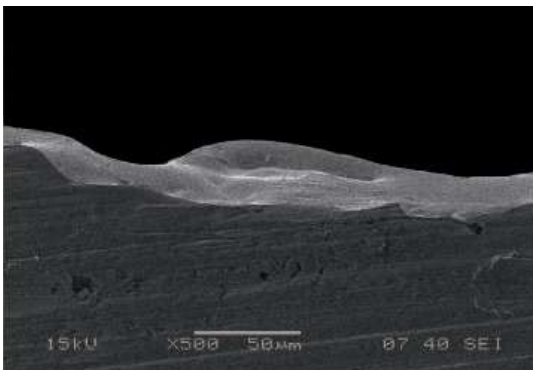


Fig. 2.23: SEM snap WLT at 5/75/80/50

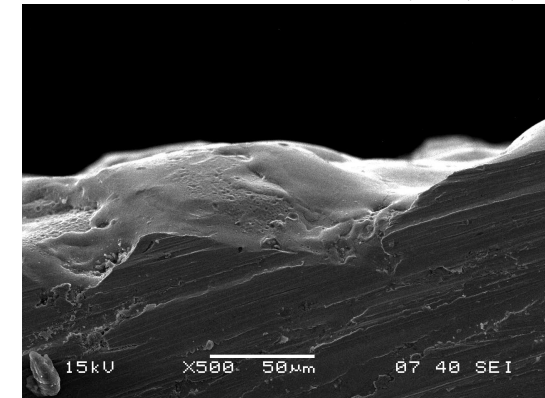


Fig. 2.24: SEM snap WLT at 5/75/90/50

### 2.7.3 Effect of the machining parameters on SCD

EDM process is very complex due to rapid local heating, quenching and random attack of the spark. At each discharge, the local temperature increase more than the boiling points of the material. The thermal nature of the EDM process, which involve melting/ vapourisation followed by rapid cooling/ quenching, results in surface damage in the form of crack formation, coupled with the development of high thermal stresses exceeding the fracture strength of the material, as well as with plastic deformation. Cracks, typically refer to as micro-cracks, caused by incompatible internal permanent strains due to quick local heating cycle. These are initiated at the machined surface and propagate through the recast layer. The white layer is so compactly penetrated with carbon that it has a separate and distinct structure, absolutely diverse from that of parent material. Carbon enhancement of the white layer takes place when the hydrocarbon dielectric breaks down and enters into the workpiece surface while it is molten and hot. Due to increased carbon content and alloying effects from the tool electrode, the brittleness of the 'white layer' increases, which is favourable for crack generation. However, the length and density of cracks depend on the pulse energy and also on the thermal properties of the workpiece material [Mamalis et al., 1987]. The pulse energy is the function of pulse current, pulse duration and discharge voltage and the effect of these machining parameters are illustrated by main effect and interaction plots, contour plot and three dimensional response surface plots as well as SEM micrograph.

In Fig. 2.25, the mean response curves are showing the influence on the SCD by various process parameters  $I_p$ ,  $Ton$ ,  $Tau$  and voltage are presented. It is an estimate of the effect of an input parameter that independently expresses the alteration in response due to an alteration in that parameter, regardless of other parameters that may be present in the system. In this case,  $I_p$ ,  $Ton$  and voltage have significant effect on SCD and it is also supported by Table 2.9. Also it can be observed that the  $I_p$  is the most influencing factor followed by  $Ton$  and  $V$ , however,  $Tau$  does not have any impact on SCD. The results of which show that SCD decreases with the increasing of  $I_p$ , although SCD decreases by  $0.033588 \mu\text{m}/\mu\text{m}^2$  with the increase in  $I_p$  from 1A to

5 A and then by  $0.004633 \mu\text{m}/\mu\text{m}^2$  for the increase of  $I_p$  from 5A to 9A. SCD increase by  $0.0054 \mu\text{m}/\mu\text{m}^2$  when  $Ton$  increase from  $50 \mu\text{s}$  to  $100\mu\text{s}$  with min SCD of  $0.02355 \mu\text{m}/\mu\text{m}^2$  occurring at  $75 \mu\text{s}$ . It increases by  $0.0028 \mu\text{m}/\mu\text{m}^2$  with the increase of  $V$  from 40 to 60 volt and the optimal value ( $0.02345 \mu\text{m}/\mu\text{m}^2$ ) occurring at  $V=50$ .

Fig. 2.26 contain six interaction plots for various two-factor interactions between  $I_p$ ,  $Ton$ ,  $Tau$  and  $V$ . Interaction plots are created by plotting both variables jointly on the same graph, and the distinguishing feature of strong interactions is the degree of non-parallelism between the lines. On this basis, it is obvious that there is a interaction exists between  $I_p \times Ton$  and  $I_p \times V$  for the SCD for a confidence level of 95%, which is also evident in Table 2.10. These interacting factors contribute to higher pulse energy and also increase the white layer thickness.

Fig. 2.27 (a) and (b) represents contour plot and response surface, respectively, for SCD in relation to the machining parameters of  $I_p$  and  $Ton$ . It is seen from the figure that, the SCD tends to decrease significantly with the increase in  $I_p$  for any value of  $Ton$ . When  $I_p$  increases, due to the production of higher spark energy, there is increase in white layer thickness, because the constant rate of flushing is unable to increasingly flush away the additional molten material produced, which gets deposited and overlays on the crack surface and try to fill it. It is also evident from Fig. 2.28 that the visible cracks are partially hidden under the overlaid layers. However, it can also be seen with the increase  $Ton$  the SCD also increases sharply to certain extend and then the increase is comparatively slow, which appears to be vital controlling variable. The most effective erosion of the material takes place during the EDM is the initial moment during which the when pulse energy released vaporises the workpiece. If the heat, which is generally very high, is supplied for a shorter duration, the high heat vaporises the material and is eroded away by flushing. With better flushing efficiency, the WLT is less as well as reducing cracking phenomena is observed. However, when the heat is supplied for a longer  $Ton$ , the produced heat is deeply conducted to the material, melts the workpiece, and thus after subsequent quenching there will be development of more induced thermal stress and thicker white layer formation. Both of them tends to support the formation of crack. Therefore, the initial gradient is competitively sharper than that of the ending (Fig. 2.27 (b)).

Hence, minimum crack density is obtained at a high peak current (9 A) and low pulse on time (50  $\mu\text{s}$ ) and the results confirm that SCD can be reduced by increasing the pulse current and reducing the pulse-on duration.

The effect of  $I_p$  and  $V$  on the estimated contour and response surface of SCD are depicted in Fig. 2.29 (a) and (b), respectively, where  $T_{on}$  remains constant at its mean level of 75  $\mu\text{s}$ . It can be noted that with the increase in  $V$ , SCD also increases. Since, the pulse energy is directly proportional to voltage and with the increase of pulse energy cracks increase and so is for the voltage. The crater sizes increase with pulse energy, as does the length of surface cracks. Furthermore, the cracks can penetrate into the heat-affected zone depending on pulse energy. The outcome of the study is similar to the observation of Hascalyk and Caydas (2004). Overall, the results suggest that surface cracking can be suppressed by increasing the pulse current reducing the pulse-on duration and keeping the discharge voltage at their lowest level.

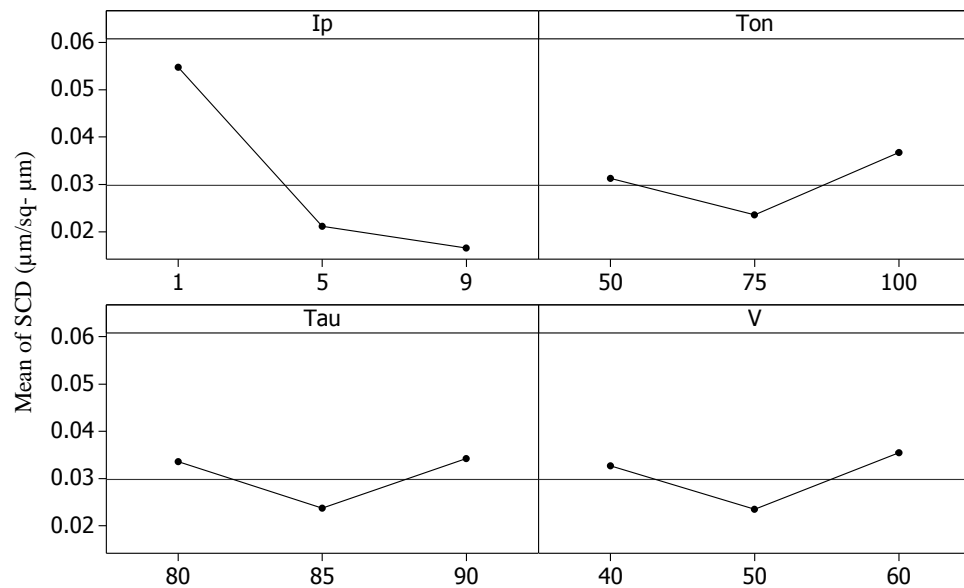


Fig. 2.25: Effect of factors on SCD.

#### 2.7.4 Scanning Electron Microscopy (SEM) images for SCD

Minutely inspecting of the machined surfaces surface under SEM revealed that the surface cracks are frequently micro-cracks. With the high magnification (500 $\times$ ) graphs, it can be seen clearly that the existence of cracks are limited to the white layer thick-

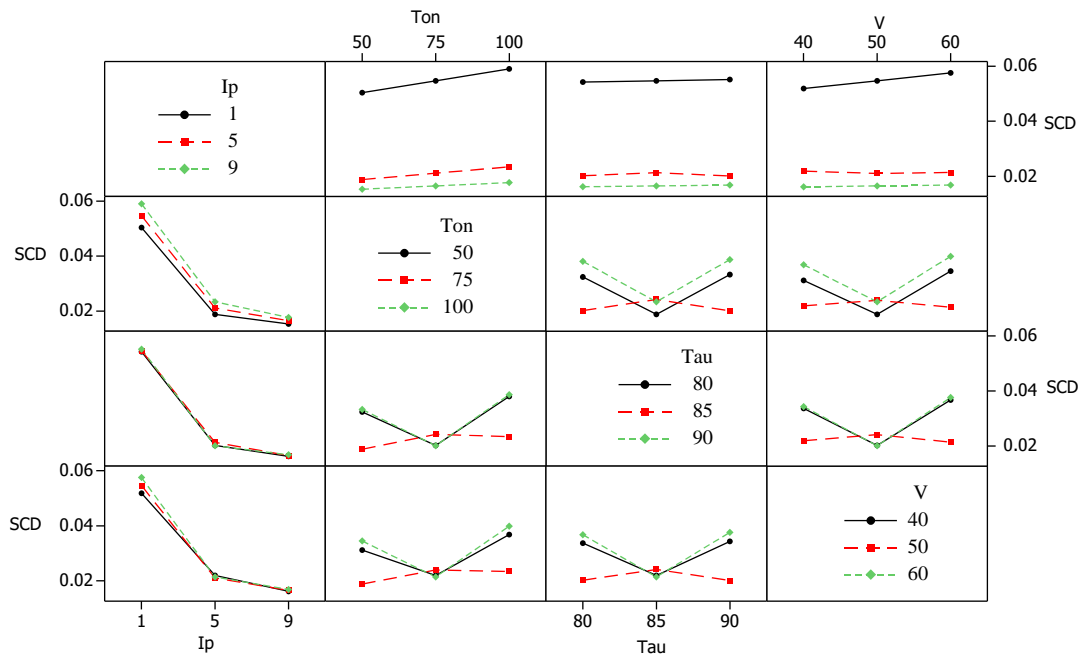


Fig. 2.26: Interaction effect of factors on SCD.

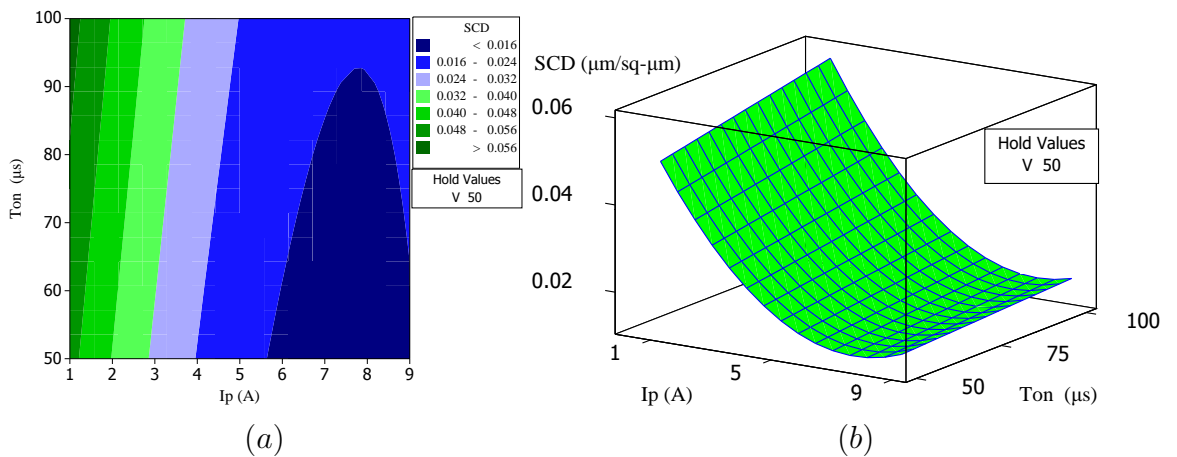


Fig. 2.27: (a) Contour plot, (b) Response surface plot representing the effect of  $I_p$  and  $Ton$  on SCD



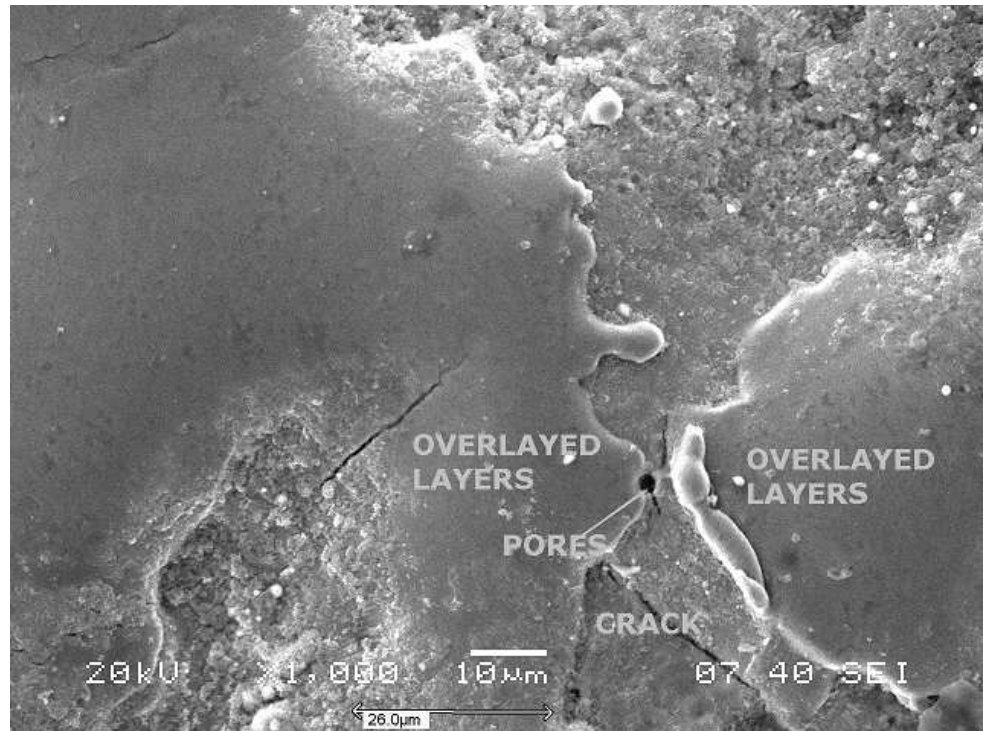


Fig. 2.28: SEM micrograph for 9/100/90/60 ( $SCD=0.01761\mu\text{m}/\mu\text{m}^2$ )

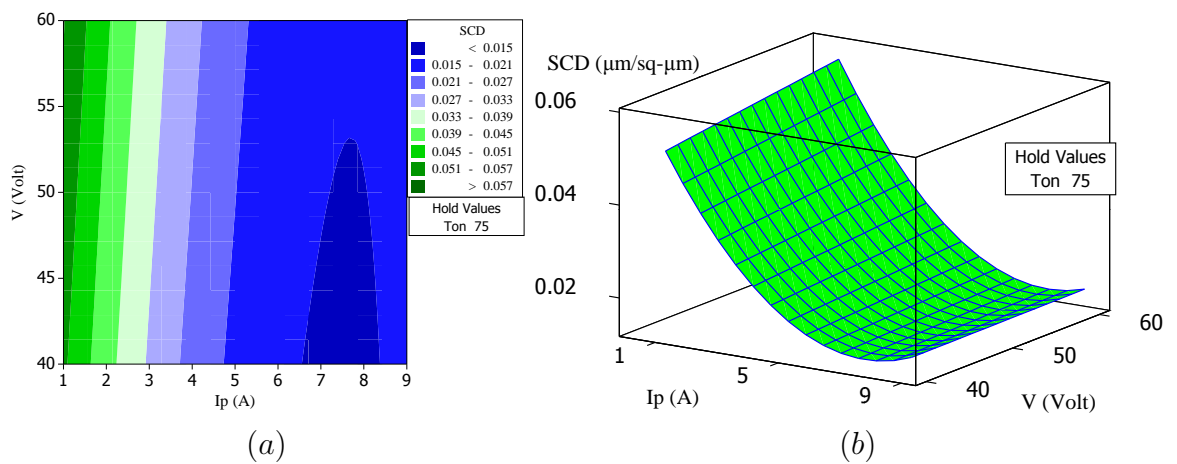


Fig. 2.29: (a) Contour plot, (b) Response surface plot representing the effect of  $I_p$  and  $V$  on SCD

ness only. Though a lot of cracks exist in the top surface, the transverse sections portrays a few cracks, which initiated at the top surface, propagates towards the parent material and diminishes on the interface. Hardly ever the cracks go through the whole thickness of the white layer to extend into the parent material. This advocates that the mechanism of crack formation is due to solidification shrinkage during the rapid quenching at the end of discharge and not from the mechanical action of spark. Machining damage limits the strength to a large extent and establishes the strength distribution of component since it influences crack growth under stress. Surface cracks upshot from machining are a common source of failure in EDMed components. The morphological characteristics of the EDMed surfaces are directly associated to the input variables. The surface topography observed from the SEM photographs at various levels of  $I_p$ ,  $T_{on}$ ,  $T_{au}$  and  $V$ , as mentioned along with the figures, reveals the effect of pulse current, pulse duration and voltage on the surface quality of D2 alloy steel.

The SEM micrographs of the EDM machined surfaces for various  $I_p$  keeping other parameters at their mean level are shown in Fig. 2.30, Fig. 2.31 and Fig. 2.32. On assessment of the micrographs shown, the associated crack length measured on these figures are  $0.05389 \mu\text{m}/\mu\text{m}^2$ ,  $0.02086 \mu\text{m}/\mu\text{m}^2$  and  $0.01777 \mu\text{m}/\mu\text{m}^2$ , signifies the diminishing trend of SCD with the increase in pulse current.

Correspondingly, the SEM micrographs for  $T_{on}$  at  $50 \mu\text{s}$ ,  $75 \mu\text{s}$  and  $100 \mu\text{s}$ , keeping other parameters at their mean level are shown in Fig. 2.33, Fig. 2.31 and Fig. 2.34, respectively. The SCD of the corresponding  $T_{on}$  are  $0.02042 \mu\text{m}/\mu\text{m}^2$ ,  $0.02086 \mu\text{m}/\mu\text{m}^2$  and  $0.02494 \mu\text{m}/\mu\text{m}^2$ . Qualitatively, it is clear from the micrograph that SCD is directly proportional to  $T_{on}$ . Similar observation has been reported by Lee and Tai (2003).

The SEM micrograph for discharge voltage at 40, 50 and 60 volt are also depicted in Fig. 2.35, Fig. 2.31 and Fig. 2.36, respectively, keeping the other parameters at their mean level. The SCD for these micrographs are  $0.02066 \mu\text{m}/\mu\text{m}^2$ ,  $0.02086 \mu\text{m}/\mu\text{m}^2$ , and  $0.02177 \mu\text{m}/\mu\text{m}^2$ . It can be clearly seen that the increase of SCD with the increase in voltage, though it is very small when compared to the change with  $I_p$ , it is still a significant term in the model. It can be attributed to the fact that as

the pulse energy increases with voltage (Equation 2.4), it leads to form comparatively more WLT and induced stress, consequently increasing the tendency of cracking.

The graphs of WLT and SCD against average pulse power ( $I_p \times V \times \text{Tau}$ ) are shown in Fig. 2.37. The data points represent the average WLT and SCD obtained from the parameter combination as per the design matrix (Table 2.3). The figure illustrates that WLT and SCD are function of power. It can be clearly seen that the WLT increase along a parabolic curve with an increase in the magnitude of power. Similar conclusions were drawn by Lee et al. (1988) that increasing pulse energy in machining will result in an increase in the dimension of the WLT though they have reported for higher pulse energy. The magnitude of SCD decreases drastically with power and such findings are substantiated by Lee and Tai (2003). The SCD values observed in the present work are trivially less than that by Lee and Tai (2003), however, they have experimented with higher  $I_p$  and lower  $T_{on}$  at 120 volts for which the results cannot be directly comparable.

## 2.8 Confirmation Test

In majority of the industrial applications of EDMed components, the formation of a white/recast layers are believed to be undesirable, rather can be extremely detrimental especially where fluctuating or cyclic stress are applied in these components. Thus efforts are made to trim down its formation. In this research, it is tried out to find the factors and its level to perform the operation such that the formation of WLT will be minimal. If the pulse current and voltage are short, small discharge energy will be released and narrow spark duration will lead to complete the spark cycle during the build-up period of the discharge channel, in that case the temperature in the channel may remain so high that material removal takes place only by vaporisation and thus very negligible white layer will form. Although with these setting, there exists a few micro cracks due to low pulse current, but these cracks are limited to the white layer only and can be got rid off during polishing. Therefore, the minimisation of WLT is the prime concern and it can be concluded from Fig. 2.37, that this can be achieved with minimal power in the experimental domain. The SCD is measured and reported for checking the consistency of prediction.

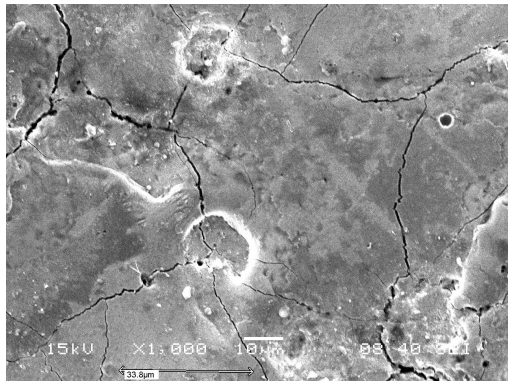


Fig. 2.30: SEM snap SCD at 1/75/85/50

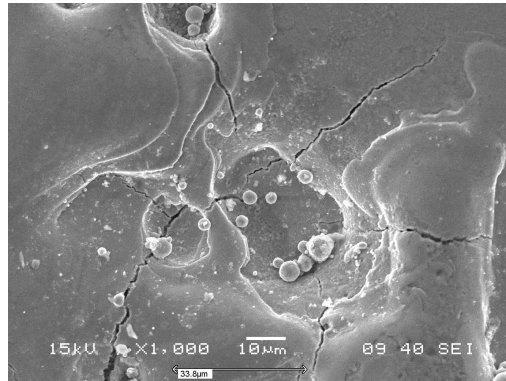


Fig. 2.31: SEM snap SCD at 5/75/85/50

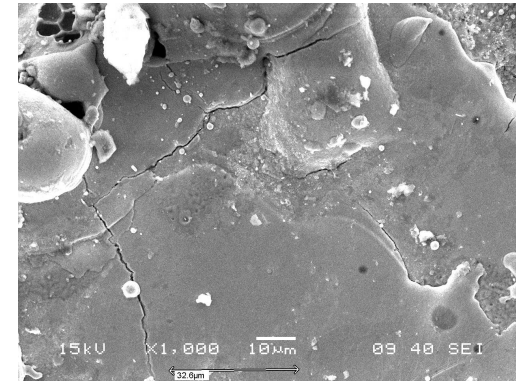


Fig. 2.32: SEM snap SCD at 9/75/85/50

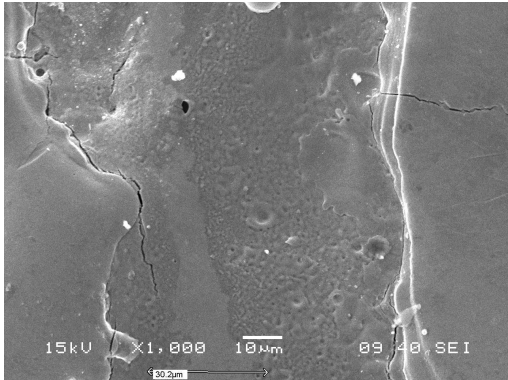


Fig. 2.33: SEM snap SCD at 5/50/85/50

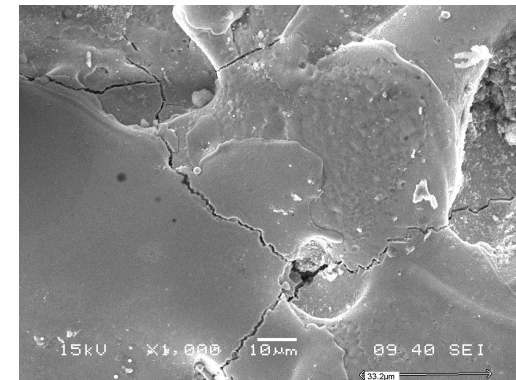


Fig. 2.34: SEM snap SCD at 5/100/85/50

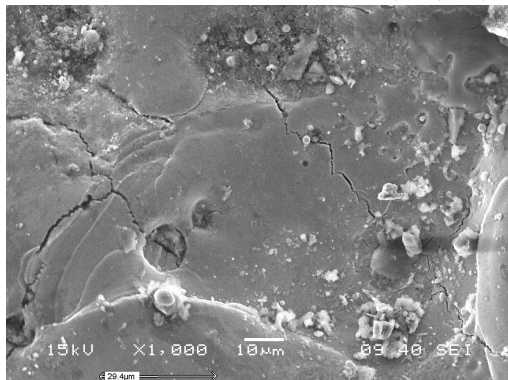


Fig. 2.35: SEM snap SCD at 5/75/85/40

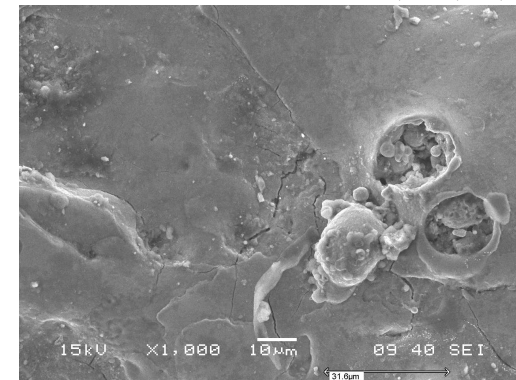


Fig. 2.36: SEM snap SCD at 5/75/85/60

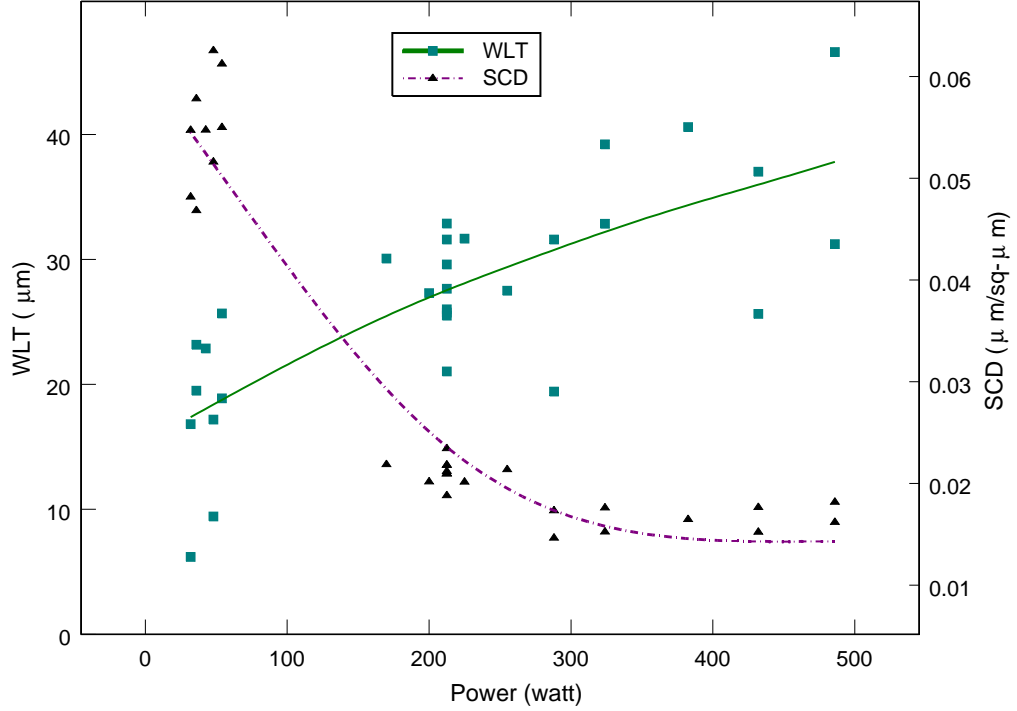


Fig. 2.37: WLT and SCD as a function of power for AISI D2 tool steels.

To validate the findings and conclusions drawn during the analysis phase, it is customary to conduct the confirmation experiments. These experiments serve the purpose of testing the specific combination of factors and their level to demonstrate the validity of the model derived from the designed experiments. In order to substantiate the precision of the model developed, a new confirmation experiment was design and conducted. The test condition for the confirmation test was so selected that the desired response (WLT here) should be at its lowest level and the level of the factors should be in the range of the levels defined earlier. So the response equations (Equation 2.2 and 2.3) for the WLT and SCD developed through RSM can be used to successfully predict the responses for any combination of the  $I_p$ ,  $Ton$ ,  $Tau$  and  $V$  within the range of the experiment conducted. In order to assess the accuracy of the models, Prediction error is used and defined as follows

$$Prediction\ Error(PE) = \frac{|Experimental\ value - Predicted\ value|}{Experimental\ Value} \times 100 \quad (2.5)$$

From the predicted value and the associated experimental value the percentage prediction error was calculated and are found to be within permissible limits as depicted in Table 2.12. The average prediction errors are 5.76% and 5.79% for WLT and SCD, respectively.

Table 2.12: Sample predicted data from the RSM model.

Run Order	$I_p$ A	$Ton$ $\mu s$	$Tau$ %	$V$ Volt	Optimal WLT $\mu m$			Average SCD $\mu m/\mu m^2$		
					expt	Pred.	PE %	expt	Pred.	PE %
1	1	50	80	40	7.74	8.10	4.43	0.0499	0.0478	4.34
2	1	50	80	40	7.72	8.10	7.36	0.0507	0.0478	5.76
3	1	50	80	40	7.51	8.10	7.23	0.0515	0.0478	7.26
Average prediction error							5.76 %			5.79%

## 2.9 Conclusion

In this chapter, the study is connected with describing the average white layer thickness and surface crack density of EDMed AISI D2 steel surfaces, machined with different machining conditions using SEM micrograph. It is found that the pulse current is the most dominating parameter followed by pulse duration for both the responses. However, the recast layer thickness increase with increasing discharge current, pulse duration and duty cycle. But the surface crack density decreases with increase in discharge current, pulse duration. As a consequence the surface crack density is related to white layer thickness and the thicker the white layer the lower the surface crack density was obtained. The average SCD is inversely proportional to the average pulse power and the WLT increases monotonically with power. The result reveals that in order to minimise the white layer the factors should be kept at their low levels, however this parameter setting tends to increase the surface crack density. A RSM model can effectively relate the machining parameters with the responses, WLT and SCD. The optimal parameter setting for WLT was found to be  $I_p = 1$ ,  $Ton = 50$ ,  $Tau = 80$ ,  $V = 40$ . The verifying experiment has shown that the predicted value agrees with the experimental evidence. These findings will be ready to lend a hand to the EDM users and manufacturing engineers in selecting the appropriate parametric combinations for EDM processes to accomplish desired levels of WLT.

# Chapter III

## Response surface model for prediction of Surface Roughness

### 3. RESPONSE SURFACE MODEL FOR PREDICTION OF SURFACE ROUGHNESS

#### *3.1 Introduction*

Electrical discharge machining is a non-conventional manufacturing process, based on removing material from a component by a series of repetitive electrical spark between electrode, and the workpiece being machined in the existence of a dielectric fluid [Pandey and Shan (1980)]. Due to the rapid thermal cycle of the process, some undesirable transformation of the material is ought to be. It produces a layer of recast material and weakens the region below the surface which is known as the heat affected zone (HAZ). EDMed surface exhibits overlapping spherical craters with resolidified protrusions and cracks produced during quenching. The recast layer degrades surface integrity and affects the geometry of the component at the micro scale. Craters and cracks are observable on the surface of the tool shown in Fig. 3.1. The surface topography is complex and consists of an uneven cusp surface form caused by the crater left by each spark discharge. The cusps are randomly distributed, overlap and contain cracks which can be clearly seen in Fig. 3.1. Globules are scattered over the surface and blow-holes also exist within the surface caused by blistering. The surface chemistry and metallurgy are also too complex. Each spark discharge causes a small area of the workpiece to be heated to an extremely high temperature to vaporise or melt and is erode away by the dielectric. However, not all is eroding away; some portion of it is recast onto the surface in the form of carbon rich layers and globules.

Majority of the mechanical component failure in practice are surface instigated, through mechanisms such as fatigue cracking, stress corrosion cracking, fretting wear, excessive abrasive or adhesive wear, corrosion, erosion etc. Therefore it is important to understand the properties of the surface and sub-surface zones of a component. The ideal surface of the components should be perfectly smooth, straight, clean and free



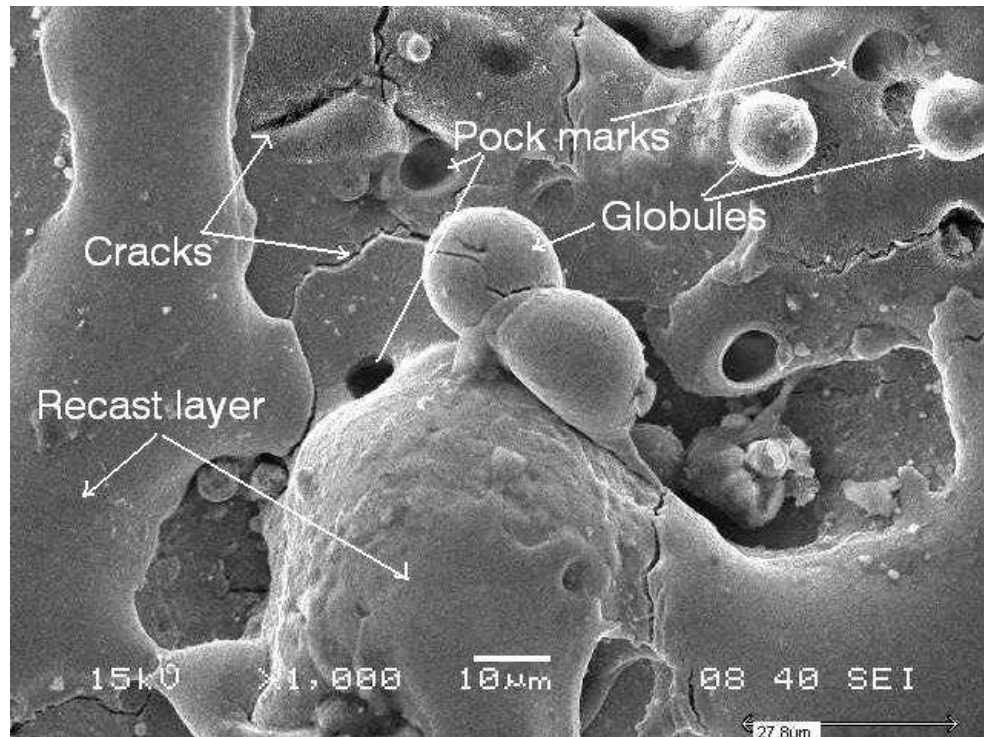


Fig. 3.1: SEM micrograph of a EDMed AISI D2 tool steel surface

from defects which is expected to be manufacture, but the processing method leave a micro-scale “fingerprint” on the surface which vary from process to process. The nature of the surface is referred as the surface texture or surface topography of the component and this consists of a series of peaks and valleys that have characteristic shape size and spacing.

Importance of Surface:- Surface technology is at present receiving attention in the engineering industry, since it is well established that there exists some correlation between the surface properties and reasons of failure modes of the components and service performance. The fatigue strength of the components is seriously affected by the surface roughness, i.e., as the roughness increases the fatigue life decreases. In addition, it is now understood that damage caused to the surface and sub-surface leads to catastrophic failures of the components. Moreover, to face the global competition it desired in the industry to reduce the cost and improve the quality. Better surface morphology helps to improve the precision and quality of conformance of the product. Therefore, it is important to concentrate on measuring the surface roughness as both a means of quality assurance and as a means of inferring functional performance.

EDM process is very demanding but the mechanism of process is complex and far from completely understood. Therefore, it is hard to establish a model that can accurately predict the performance by correlating the process parameter. The optimal processing parameters are very essential to be established to enhance the production rate largely and shrink the machining time, since the materials, which are processed by EDM, are generally costly and even the processing cost is very high [Mandal et al. (2007)].

The aim of this study is to investigate the surface roughness of EDMed parts and explores possible ways to adjust its parameters to achieve better SR by statistical methods. A RSM is used for development of a second-order polynomial model and analysis of Ra with  $I_p$ ,  $Ton$ ,  $Tau$  and  $V$  as input parameters. In this chapter, the experiments were conducted on AISI D2 tool steel with copper electrode using a face-centered CCD (for details see Section 2.2.2). Surface integrity was also studied by SEM micrography and the shape and the size of the crater of the machined parts under specific process parameters are presented.

### 3.2 Experimentation

Experiments were conducted to study the effects of various machining parameters;  $I_p$ ,  $Ton$ ,  $Tau$  and  $V$  on SR of workpiece material AISI D2 tool steel on die sinking electro discharge machine. The detail of the experimental conditions are mentioned in Section 2.2. The different factors and their levels considered for this study are illustrated in Table 3.1.

### 3.3 Surface roughness measurements

Surface roughness is a measure of the technological quality of a product, which mostly influence the manufacturing cost of the product. The term surface texture refers to the fine irregularities (peaks and valleys) produced on a surface by the machining process. The texture comprises two components namely roughness (characteristics of the process) and waviness (characteristics of the machine). Usually, however the texture and roughness are used interchangeably, because roughness is measured more often

than waviness. There are many types of statistical descriptors to characterise such surfaces, among these centreline average (Ra) is most commonly used. The centreline average Ra, is the universally recognised and most used international parameter for roughness. Roughness average is used in the automotive and other metalworking industries to specify the surface finish of many types of components, ranging from cylinder bores to brake drums. It is the arithmetic mean of the departures of the profile from the mean line (Fig. 3.2) and expressed as

$$Ra = \frac{1}{L} \int_0^L |y(x)| dx = \frac{\text{Total shaded area}}{L} \quad (3.1)$$

where  $y(x)$  is the profile curve sampled by the set of N points and  $x$  is the profile direction. The average 'Ra' is measured within the sampling length L as shown in Fig. 3.2. Centre-line average 'Ra' surface roughness measurements of electro-discharge machined surfaces were taken to provide quantitative evaluation of EDMed component.

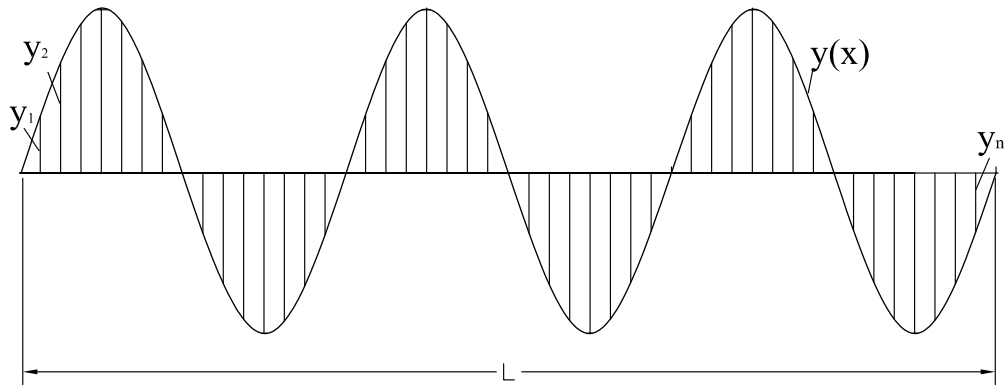


Fig. 3.2: Idealised stylus profile showing the mean line

Roughness measurement was carried out using a portable stylus type profilometer, Talysurf as shown in Fig. A.6. The profilometer was set to a cut-off or sample length of 0.8 mm and evaluation length of 4 mm with traverse speed 1 mm/s and filter 2CR (ISO). The measured profile was digitised and processed through the dedicated advanced surface finish analysis software, Talyprofile for evaluation of the roughness parameters. Roughness measurements, in the transverse direction, on the workpieces

were repeated four times and shown in the observation table (Table 3.2). Table presents run order, point type (Pt Type), block, the different combination of input parameters and the measurements of response Ra. Table 3.3 shows the machining parameters for each run order, along with the experimental Ra values (average of four measurements), the predicted value and the residues. Where the residues are the difference between the experimentally observed data and the model predictions.

### 3.4 Planning based on Response Surface Methodology

RSM is a collection of mathematical and statistical techniques that are useful for modelling and analysis of problems in which output or response is influenced by several input variables and the objective is to find the correlation between the response and the variables investigated [Montgomery, 2001]. The second-order model is normally used when the response function is not known or non-linear and the same is adopted. The experimental values are analysed and the mathematical model is then developed that illustrate the relationship between the process variable and response as shown in Equation 2.1.

Table 3.1: Input variables used in the experiment and their levels.

variable	Unit	levels		
		1	2	3
Discharge current ( $I_p$ )	A	1	5	9
Pulse on time ( $T_{on}$ )	$\mu s$	50	75	100
Duty Cycle ( $Tau$ )	%	80	85	90
Voltage ( $V$ )	volt	40	50	60

Table 3.2: Observation for Surface Roughness.

Run Order	Pt Type	Blocks	$I_p$ A	$T_{on}$ $\mu s$	$T_{au}$ %	$V$ volt	Surface roughness $\mu m$ sample no.			
							1	2	3	4
1	1	1	9	100	90	40	7.68	8.02	7.34	9.08
2	1	1	9	50	90	60	7.56	5.12	6.04	6.24
3	1	1	1	100	90	60	2.08	1.90	2.52	2.08
4	1	1	1	100	80	40	1.25	1.45	2.20	1.71
5	0	1	5	75	85	50	5.48	5.42	5.40	5.34
6	1	1	9	100	80	60	7.74	8.52	7.60	6.70
7	1	1	9	50	80	40	6.22	7.16	5.04	6.04
8	0	1	5	75	85	50	5.46	4.90	5.64	4.88
9	1	1	1	50	80	60	1.98	2.06	2.34	2.06
10	1	1	1	50	90	40	2.34	2.32	2.56	2.36
11	1	2	9	50	90	40	5.86	5.34	6.04	6.80
12	1	2	9	100	80	40	8.08	6.82	6.62	8.18
13	1	2	1	50	90	60	2.68	2.44	2.46	2.20
14	1	2	1	100	90	40	2.00	2.08	2.18	2.08
15	1	2	9	100	90	60	7.22	7.38	8.16	7.58
16	0	2	5	75	85	50	4.94	5.76	5.02	5.44
17	1	2	9	50	80	60	5.44	5.88	6.26	5.76
18	1	2	1	100	80	60	1.94	1.66	1.74	1.62
19	0	2	5	75	85	50	5.66	4.69	5.88	5.22
20	1	2	1	50	80	40	2.12	2.38	1.92	2.18
21	-1	3	5	75	85	40	5.14	5.38	5.44	6.34
22	-1	3	5	50	85	50	4.92	4.58	4.88	4.70
23	-1	3	5	100	85	50	5.58	6.42	5.46	5.76
24	-1	3	9	75	85	50	6.58	7.20	5.98	6.16

(continued on next page)

Table 3.2: Observation for Surface Roughness.(Contd.)

Run	Pt		$I_p$	$T_{on}$	$T_{au}$	$V$	Surface roughness $\mu\text{m}$			
Order	Type	Blocks	A	$\mu\text{s}$	%	volt	1	2	3	4
25	-1	3	5	75	80	50	6.14	5.98	4.96	5.06
26	0	3	5	75	85	50	6.54	5.16	5.54	5.14
27	-1	3	1	75	85	50	1.80	1.96	2.44	1.72
28	-1	3	5	75	90	50	6.30	5.48	5.74	5.56
29	-1	3	5	75	85	60	5.48	5.12	6.14	5.32
30	0	3	5	75	85	50	5.32	5.44	5.50	5.86

PtType 1 indicates a cube point of the design;  
PtType 0 indicates a center points;  
PtType -1 indicates an axial points;

Table 3.3: Comparison of experimental and model prediction results for surface roughness.

Run	$I_p$	$T_{on}$	$T_{au}$	$V$	Expt.	Predicted	Residuals
	A	$\mu\text{s}$	%	volt	Ra $\mu\text{m}$	Ra $\mu\text{m}$	$\mu\text{m}$
1	9	100	90	40	8.03	7.818	0.212
2	9	50	90	60	6.24	6.149	0.091
3	1	100	90	60	2.15	2.085	0.065
4	1	100	80	40	1.65	1.806	-0.156
5	5	75	85	50	5.41	5.408	0.002
6	9	100	80	60	7.64	7.539	0.101
7	9	50	80	40	6.11	5.870	0.240
8	5	75	85	50	5.22	5.408	-0.188
9	1	50	80	60	2.11	2.128	-0.018

(continued on next page)

Table 3.3: Comparison of experimental and model prediction results for surface roughness.(Contd.)

Run	$I_p$ A	$Ton$ $\mu s$	$Tau$ %	$V$ volt	Expt. Ra $\mu m$	Predicted Ra $\mu m$	Residuals $\mu m$
10	1	50	90	40	2.39	2.406	-0.016
11	9	50	90	40	6.01	6.149	-0.139
12	9	100	80	40	7.43	7.539	-0.109
13	1	50	90	60	2.45	2.406	0.044
14	1	100	90	40	2.09	2.085	0.005
15	9	100	90	60	7.58	7.818	-0.238
16	5	75	85	50	5.29	5.408	-0.118
17	9	50	80	60	5.83	5.870	-0.040
18	1	100	80	60	1.74	1.806	-0.066
19	5	75	85	50	5.36	5.408	-0.048
20	1	50	80	40	2.15	2.128	0.022
21	5	75	85	40	5.57	5.408	0.162
22	5	50	85	50	4.77	5.072	-0.302
23	5	100	85	50	5.81	5.745	0.065
24	9	75	85	50	6.48	6.598	-0.118
25	5	75	80	50	5.54	5.515	0.025
26	5	75	85	50	5.60	5.408	0.192
27	1	75	85	50	1.98	1.860	0.120
28	5	75	90	50	5.77	5.794	-0.024
29	5	75	85	60	5.52	5.408	0.112
30	5	75	85	50	5.53	5.408	0.122

#### 3.4.1 RSM model development and Residual Analysis.

The effect of the machining parameters ( $I_p$ ,  $Ton$ ,  $Tau$  and  $V$ ) on the response variable Ra was evaluated by conducting experiments as described in Section 3.2. Minitab14

Table 3.4:  $R^2$  and  $R_{adj}^2$  test for SR regression model.

Degree	$R^2$ (%)	$R_{adj}^2$ (%)
Linear	91.9	89.8
Linear + square	96.3	94.3
Linear + interaction	95.4	92.1
Full quadratic	99.7	99.4

Table 3.5: Estimated Regression Coefficients for Surface roughness (Before elimination).

Term	Coef	SE Coef	t	p
Constant	5.36797	0.05827	92.120	0.000
Block1	0.01988	0.04334	0.459	0.654*
Block2	-0.08212	0.04334	-1.895	0.081*
$I_p$	2.36889	0.03639	65.090	0.000
$Ton$	0.33667	0.03639	9.251	0.000
$Tau$	0.13944	0.03639	3.832	0.002
$V$	-0.00944	0.03639	-0.260	0.799*
$I_p \times I_p$	-1.16652	0.09691	-12.037	0.000
$Ton \times Ton$	-0.10652	0.09691	-1.099	0.292*
$Tau \times Tau$	0.25848	0.09691	2.667	0.019
$V \times V$	0.14848	0.09691	1.532	0.149*
$I_p \times Ton$	0.49750	0.03860	12.888	0.000
$I_p \times Tau$	-0.03625	0.03860	-0.939	0.365*
$I_p \times V$	-0.02875	0.03860	-0.745	0.470*
$Ton \times Tau$	0.03125	0.03860	0.810	0.433*
$Ton \times V$	-0.00375	0.03860	-0.097	0.924*
$Tau \times V$	-0.00500	0.03860	-0.130	0.899*
S = 0.1544	$R^2 = 99.7\%$ $R_{(adj)}^2 = 99.4\%$			



(2003) software was used to find out the relationship between the input factors and the response Ra. The value of the coefficient of determination ( $R^2$ ) and adjusted  $R^2$ -statistic ( $R_{adj}^2$ ) are compared and summarised in Table 3.4 for various models. The full quadratic model is the best among all the models, listed in Table 3.4, where  $R^2 = 99.7\%$  indicates that nearly 99.7% of the total variability in the response variable is accounted for by the predictor variable or factors in the model. However,  $R_{adj}^2$  is 99.4%, which accounts for the number of predictors in the model describes the significance of the relationship. Therefore, the full quadratic model is considered for further analysis in this study.

Table 3.5 shown presents the estimated regression coefficients (coef) in coded units and other valuable informations for each term in the model in coded units. The column “SE Coef” lists the standard error for each term, and t-statistic is obtained by dividing the Coef with “SE Coef” listed in the t column. t-statistic and p-value to decide whether to reject or fail to reject the null hypothesis. If the t-statistic value is high then it indicates that the effect is statistically significant. When p-value  $\leq 0.05$ , it is concluded that  $H_0$  is true and the treatments have a statistically significant effect. The terms marked “\*” in the last column of the table are exceeding 0.05, thus, these terms are insignificant and therefore eliminated for the further analysis. The blocking does not have any significant effect on the response, which reveals that the uncontrollable factors of the experiment conducted were held constant. The backward elimination process discards the insignificant terms to adjust the fitted quadratic model. The model, with rest of the terms after elimination, is presented in Table 3.6 in coded units. After elimination, the values of  $R^2$  and  $R_{adj}^2$  are 99.6% and 99.4%, respectively. A higher value of  $R^2$  indicates a better model. When comparing different models, compare the adjusted  $R^2$  value, labeled  $R_{adj}^2$ . Using the labeled  $R_{adj}^2$  to compare models leads to selecting the simplest model that adequately explains the data. In this experiment, the labeled  $R_{adj}^2$  of the reduced model is 99.4%. The adequate model after the elimination are  $Ip$ ,  $Ton$ ,  $Tau$ ,  $Ip^2$ ,  $Tau^2$  and  $Ip \times Ton$ .

ANOVA is used to check the sufficiency of the second-order model, which includes test for significance of the regression model, model coefficients and test for lack-of-fit. Table 3.7 summaries the ANOVA of the model that comprises of two sources of

variation, namely, regression and residual error. The variation due to the terms in the model is the sum of linear and square terms where as the lack of fit and pure error contribute to residual error. The table depicts the sources of variation, degree of freedom (DF), sequential sum square error (Seq SS), adjusted sum square error (Adj SS), adjusted mean square error (Adj MS), F statistic and the p-values in columns. The p-value of lack of fit is 0.464, which is  $\geq 0.05$ , and certainly indicate that there is statistically insignificant lack of fit at 95% confidence level. However, the p-value of regression model and its all linear and square terms have p-value 0.000, hence they are statistically significant at 95% confidence and thus the model adequately represent the experimental data.

Multi-regression analysis was performed to the data to obtain a quadratic response surface model and the equation thus obtained in uncoded units is,

$$Ra = 70.1746 + 0.956 Ip - 0.0114 Ton - 1.6447 Tau - 0.0737Ip^2 + 0.0098Tau^2 - 0.005IpTon \quad (3.2)$$

Table 3.6: Estimated Regression Coefficients for Surface roughness(After backward elimination).

Term	Coef	SE Coef	t	p
Constant	5.4082	0.04515	119.794	0.000
$Ip$	2.3689	0.03520	67.303	0.000
$Ton$	0.3367	0.03520	9.565	0.000
$Tau$	0.1394	0.03520	3.962	0.001
$Ip \times Ip$	-1.1790	0.08046	-14.653	0.000
$Tau \times Tau$	0.2460	0.08046	3.057	0.006
$Ip \times Ton$	0.4975	0.03733	13.326	0.000
S = 0.1493 $R^2 = 99.6\%$ $R^2_{(adj)} = 99.4\%$				

To explore the effect of the machining parameters on the surface roughness, this mathematical model can be used. Estimated responses are calculated from the fitted model and the residuals from the differences between the fitted and observed responses. Table 3.3 presents the machining parameters for each run order, along with the experimental results, the predicted response and the residues. Where the

Table 3.7: The ANOVA table for the fitted Surface roughness models.

Source	DF	Seq SS	Adj SS	Adj MS	F	p
<b>Regression</b>	6	114.788	114.788	19.1314	857.93	<b>0.000</b>
<i>Linear</i>	3	103.400	103.400	34.4665	1545.63	0.000
<i>Square</i>	2	7.428	7.428	3.7142	166.56	0.000
<i>Interaction</i>	1	3.960	3.960	3.9601	177.59	0.000
<b>Residual Error</b>	23	0.513	0.513	0.0223		
<i>Lack-of-Fit</i>	8	0.180	0.180	0.0225	1.02	<b>0.464</b>
<i>Pure Error</i>	15	0.333	0.333	0.0222		
<b>Total</b>	29	115.301				

residues are the difference between the experimentally observed data and the model predictions. The predicted values of Ra achieved using Equation 3.2 are close to the experimental values confirming the sufficiency of the model (Table 3.3) and the residues are further analysed in the following section.

Fig. 3.3 exhibit the normal probability plot of the residuals, which is used to test the normal distribution of the errors. It can be seen that the residuals are almost falling on a straight line, which indicates that the errors are normally distributed and the normality assumption is valid. One outlier (encircled in Fig. 3.3) point is observed from the graph for run number 22 with standard residual of -2.186, which may be due to the measurement error.

Fig. 3.4 depicts the histogram plot of standardised residue for all the observations. It is in the form of Gaussian distribution (bell shape), and the residues are distributed symmetrically with mean zero. In addition, the plot of the residues verse run order illustrates that there is no noticeable pattern or unusual structure present in the data as depicted in Fig. 3.5. The residues calculated as the difference between the predicted and observed value lies in the range of  $-0.302$  to  $0.240$ . Further, each experimental observation is compared with the predicted value in Fig. 3.6. It can be inspect that the regression model is fairly well fitted with the experimental values.

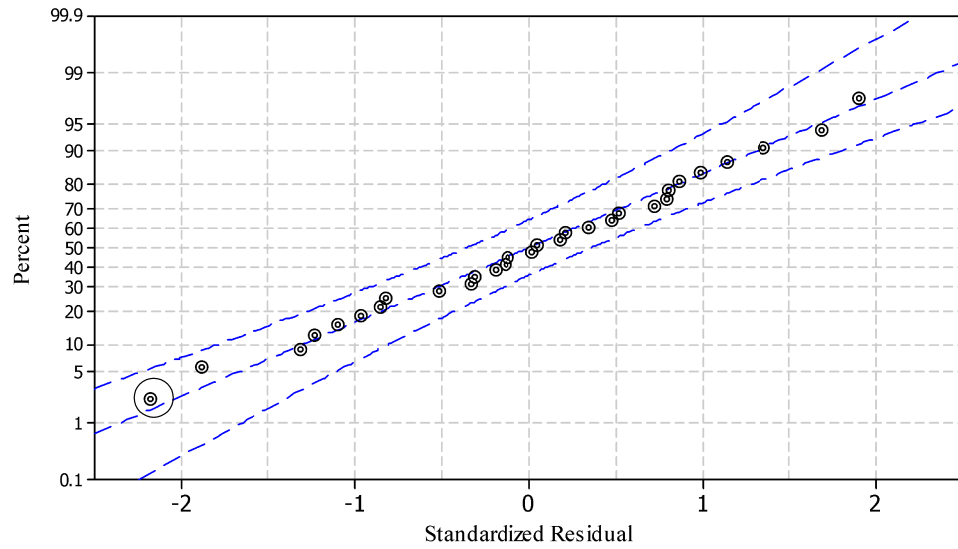


Fig. 3.3: Normal plot of residuals for Ra.

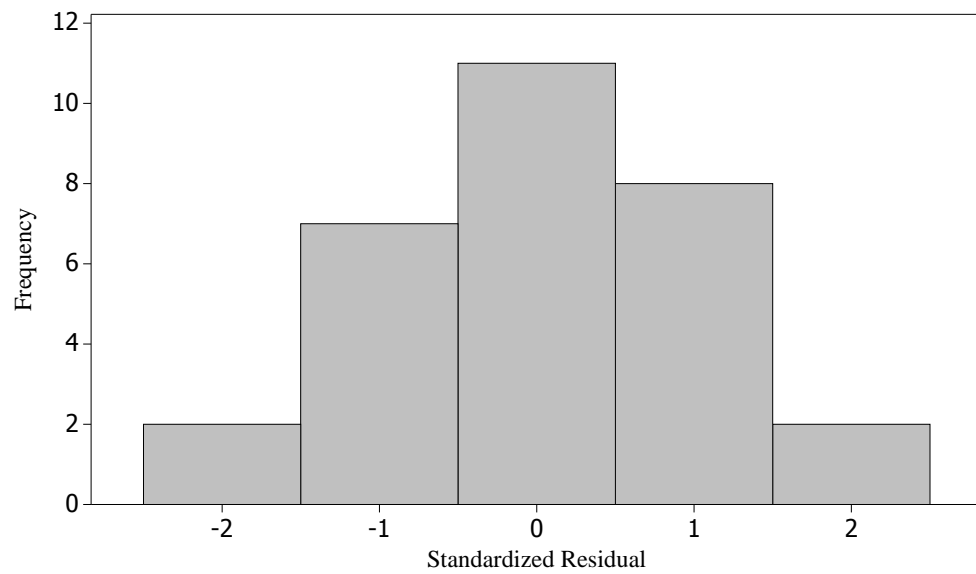


Fig. 3.4: Histogram plot of residuals for Ra.

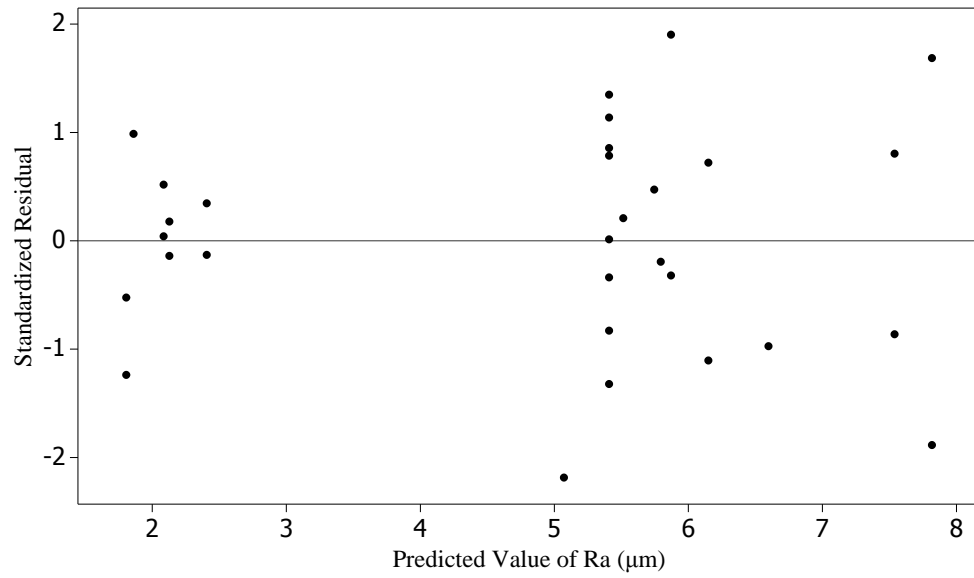


Fig. 3.5: Plot of residuals vs. fitted value for Ra.

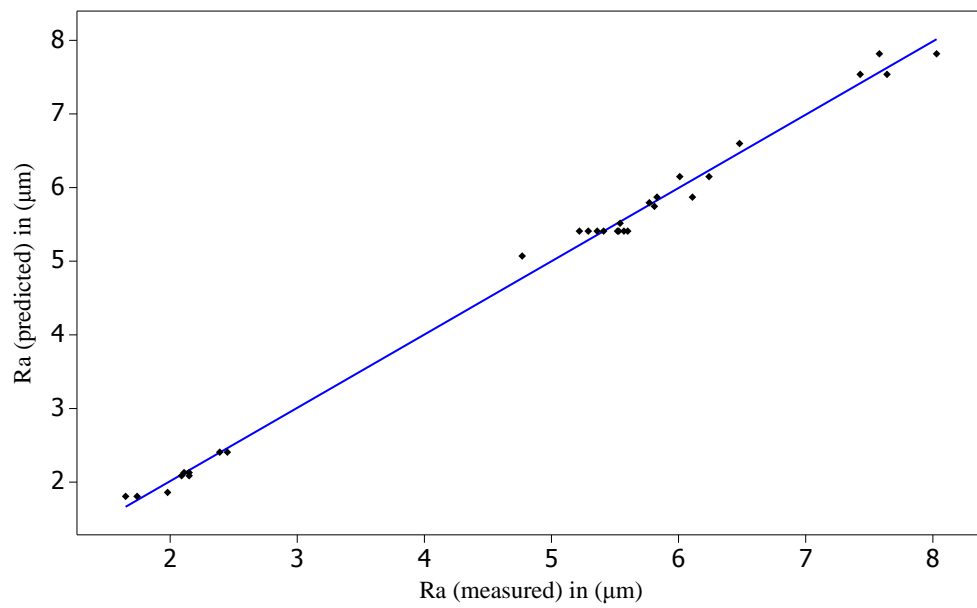


Fig. 3.6: Predicted vs. experimental Ra.

### 3.5 Result and discussion

Fig. 3.7 depicts the plots of main effects on Ra, those can be used to graphically assess the effects of the factors on the response. It indicates that  $I_p$ ,  $Ton$  and  $Tau$  have significant effect on Ra, which is supported by results in Table 3.6. However,  $I_p$  is the most influencing parameter showing a sharp increase in Ra of  $3.403 \mu\text{m}$  when  $I_p$  increases from 1 to 5 A and then the increases in Ra by  $1.362 \mu\text{m}$ , when  $I_p$  increases from 5 to 9A. This implies that  $I_p$  has a more dominant effect on the surface roughness. In addition, Ra increases by  $1.063 \mu\text{m}$ , and then slightly decreases by  $0.389 \mu\text{m}$  with  $Ton$  increases from  $50 \mu\text{s}$  to  $75 \mu\text{s}$ , and  $75 \mu\text{s}$  to  $100 \mu\text{s}$  respectively. Furthermore, for  $Tau$  the trend is analogous, Ra increases by  $0.765$  and then decrease by  $0.485$  with increases of  $Tau$  from  $80 \%$  to  $85 \%$  and  $85\%$  to  $90\%$ , respectively. Nevertheless,  $Ton$  is also an important factor which influences the Ra after  $I_p$ . This can be evident from Table 3.6 and from Lee et al., 1988, where they also found  $I_p$  has a more dominant effect on Ra than that of  $Ton$ .

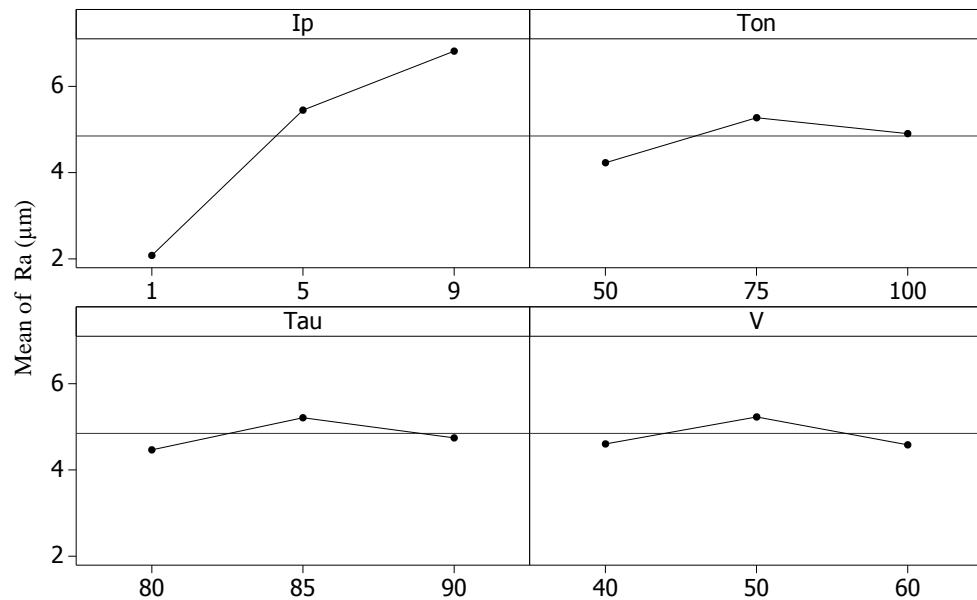


Fig. 3.7: Effect of factors on Ra.

Similar model for surface roughness has been suggested by Guu et al. (2003) and Lee et al. (1988) relating the  $I_p$  and  $Ton$  and their results, supported by experimental findings, are shown in Fig. 3.8 along with the present model. It can be seen that the Ra values obtained by Lee et al. (1988) using paraffin (Sommentor 31) dielectric is slightly

higher than the present study. This is because Ra values are inversely proportional to pulse energy and for the same range of  $I_p$  and  $T_{on}$  if  $V$  decreases pulse energy decreases and Lee et al. (1988) uses voltage of 30 volt which is lower than the present study. Guu et al. (2003) reported his work on EDM turning and though, D2 tool steel was machined by them in the presence of kerosene, the Ra values are comparable to those obtained in the present study (EDM Oil) within the range of experimental domain.

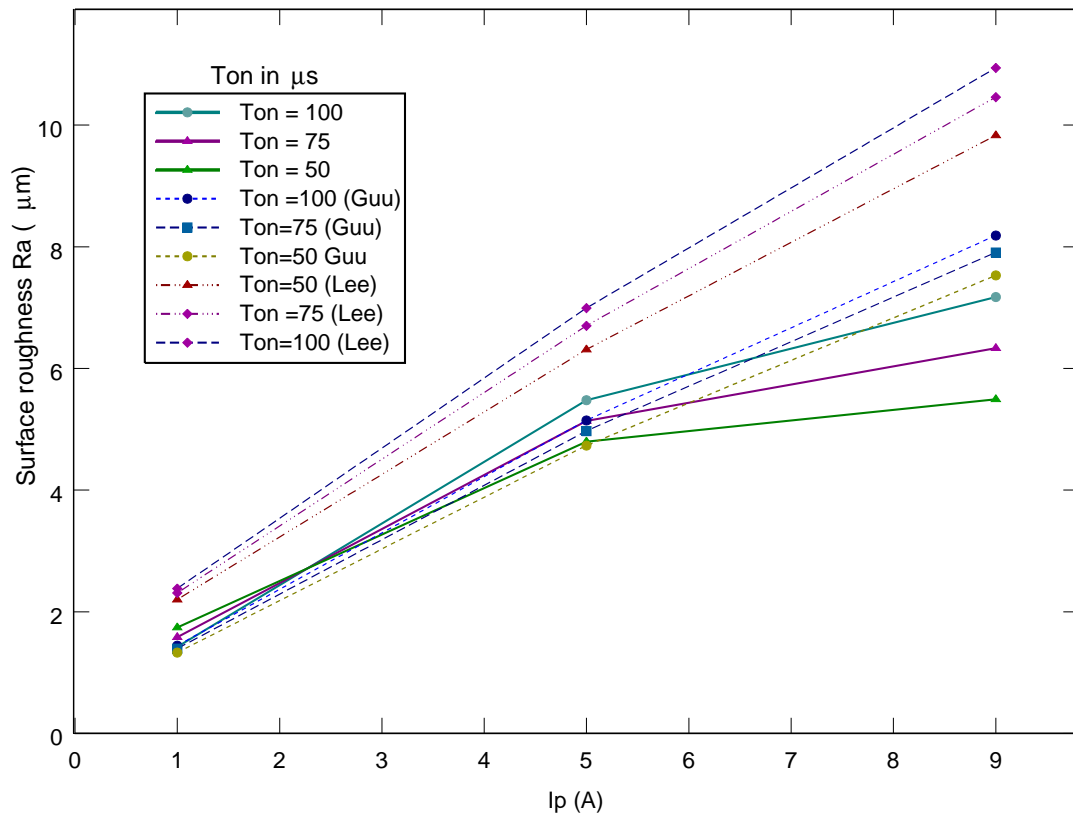


Fig. 3.8: Comparison results for Surface roughness obtained by Guu et al. (2003) and Lee et al. (1988) with different  $I_p$  and  $T_{on}$

Fig. 3.9 contains twelve interaction plots for various two-factor interactions between  $I_p$ ,  $T_{on}$ ,  $T_{au}$  and  $V$ . Each pair of the factor is plotted keeping the other factors constant at the mean level. In each plot, the factors of interest are varied in three levels, low, medium and high levels. If the lines in the interaction plot are parallel, there is no interaction between the process parameters. This implies that the change in the mean response from low to medium and medium to high level of a factor does

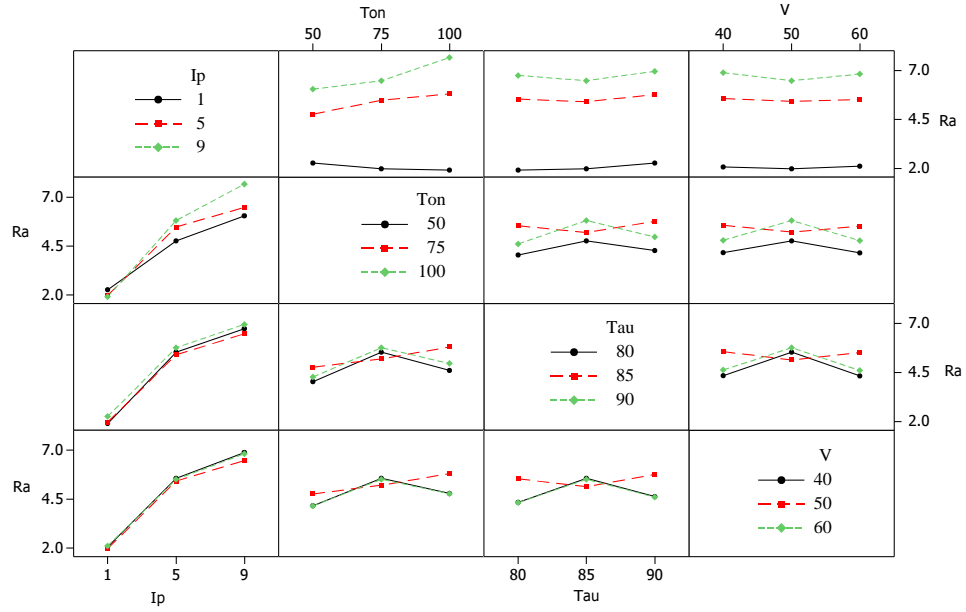


Fig. 3.9: Interaction effect of factors on Ra.

not depend on the level of the other factor. On the other hand, if the lines are non-parallel, an interaction exists between the factors. The greater the degree of departure from parallelism, the stronger is the interaction effect. It can be seen in the figure that the most important interaction effect is produced between  $I_p$  and  $Ton$ , because in the matrix second row, first column and first row, second column are the places where the lines are intersecting each other. Although in the third row and second column, fourth row second and third column, at the middle level, some interaction exist, but at the lower and higher level, the lines are parallel to each other, hence there is no much interaction exists between the parameters. They are not significant for a confidence level of 95%, which is also evident in Table 3.6. Thus, these terms are not the part of the model.

Fig. 3.10 (a) represents contour plot and Fig. 3.10 (b) response surface for Ra in relation to the machining parameters of  $I_p$  and  $Ton$ . From the figure, it is unambiguous that Ra value is more with higher  $I_p$  and longer  $Ton$ , the value Ra tends to increase significantly with the increase in  $I_p$  for any value of  $Ton$ . This can be attributed to their dominant control over the input energy. A higher  $I_p$  and longer  $Ton$  may cause more frequent breakdown of the dielectric medium, and hence repeated melt expulsion with stronger spark. Thus, due to a higher temperature larger craters are formed on the machined surface. Hence, minimum Ra is obtained at low peak



current (1A) and pulse on time ( $50 \mu\text{s}$ ). The same trend was reported by the previous researchers [Lee et al., 1988; Guu, 2005; Guu et al., 2003]. From these observations, it can be concluded that  $I_p$  and  $T_{on}$  are directly proportional to the Ra and for  $T_{au}$  the effect is very less as compared to the other parameters, for the given range of experiments conducted for this test.

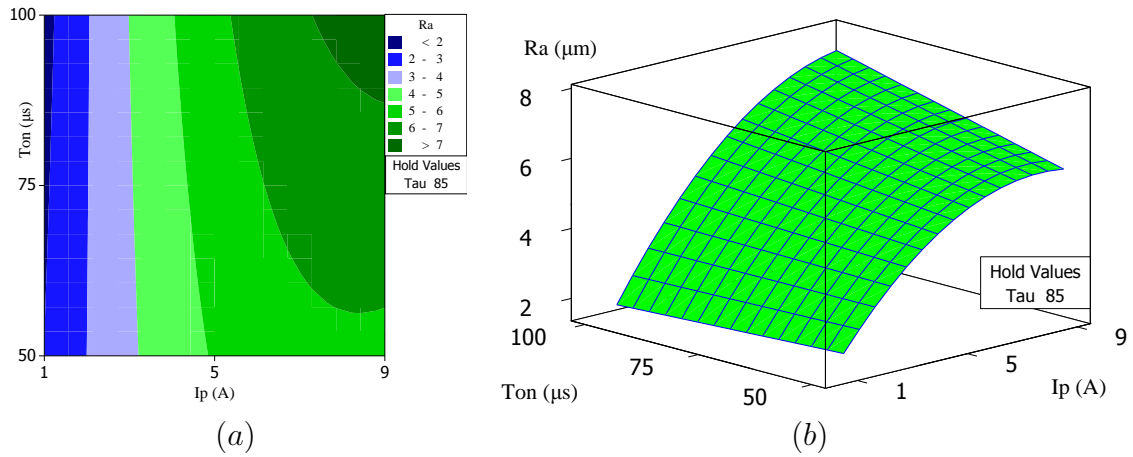


Fig. 3.10: (a) Contour & (b) Response surface plot depicting the effect of  $I_p$  &  $T_{on}$  on Ra

### 3.6 Scanning Electron Microscopy (SEM) results

A thermally affected layer will form due to melting and resolidification on the surface of an EDMed workpiece without being ejected nor removed by flushing. The structure of this layer is quite different from the parent material and it is typically very fine grained and hard. The top surface contains globules, cracks, and micro cracks, whose density depends on the process conditions. This structure of the surface gives rise to higher roughness and highly dependent of  $I_p$ . The effect of EDM parameters on crater and rough surface formed during EDM can clearly be observed from the SEM micrographs under different parametric combinations. To study the surfaces and sub surfaces, the samples are electro polished, and examined using a Scanning Electron Microscope.

Investigation of SEM revealed that the surfaces have complex appearance with shallow craters, spherical particles, melted drops, globules of debris, pockmarks and voids due to the high heat energy released by discharges and subsequently quenching. The spherical particles are molten metals that are expelled randomly during the

discharge and then solidified and attached to the surface. SEM photograph of D2 steel at various levels of  $I_p$ ,  $Ton$ ,  $Tau$  and  $V$ , as mentioned along with the figures are presented to qualitatively access the surface topography.

The variation of the shape of crater rims and globular attachments can be observed in the figures for various machining parameters. There is a noticeable increase in the size of the crater in the specimens for 1A and 9A as shown in Fig. 3.11 and Fig. 3.11 respectively. This is because spark energy increases with pulse currents cause deeper and wider craters on surface. However, the crater diameter is also influenced by  $Ton$  and increases with it. Accordingly and based on the presented figures in Fig. 3.13 and Fig. 3.14, the heat is supplied for more duration when  $Ton$  increases, so more molten material is produced with larger globules and craters.

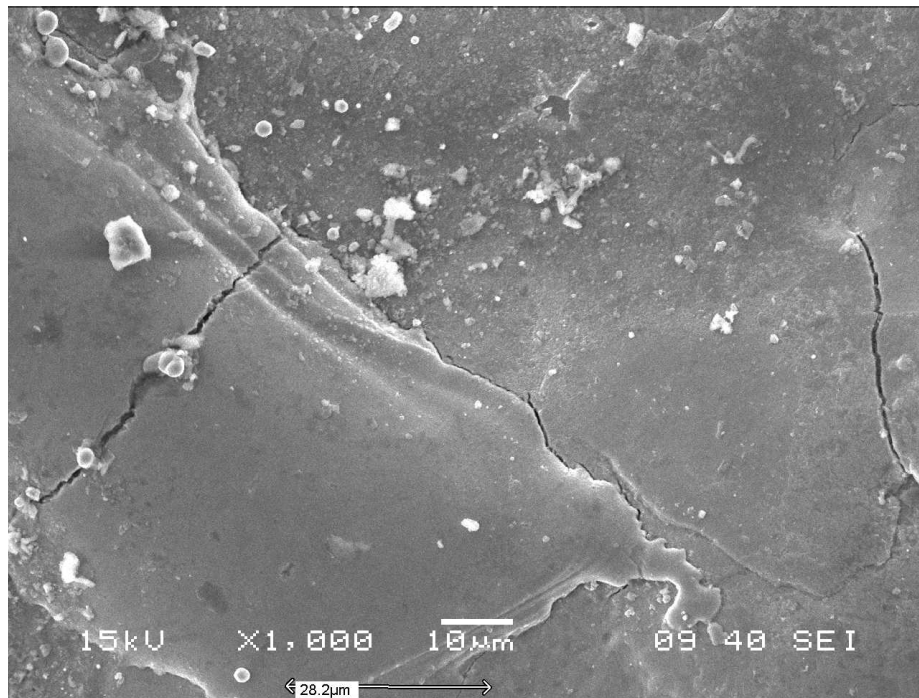


Fig. 3.11: SEM of EDMed surfaces of D2 Steel  $I_p=1A$ ;  $Ton=75 \mu s$ ;  $Tau=85\%$  &  $V=50V$

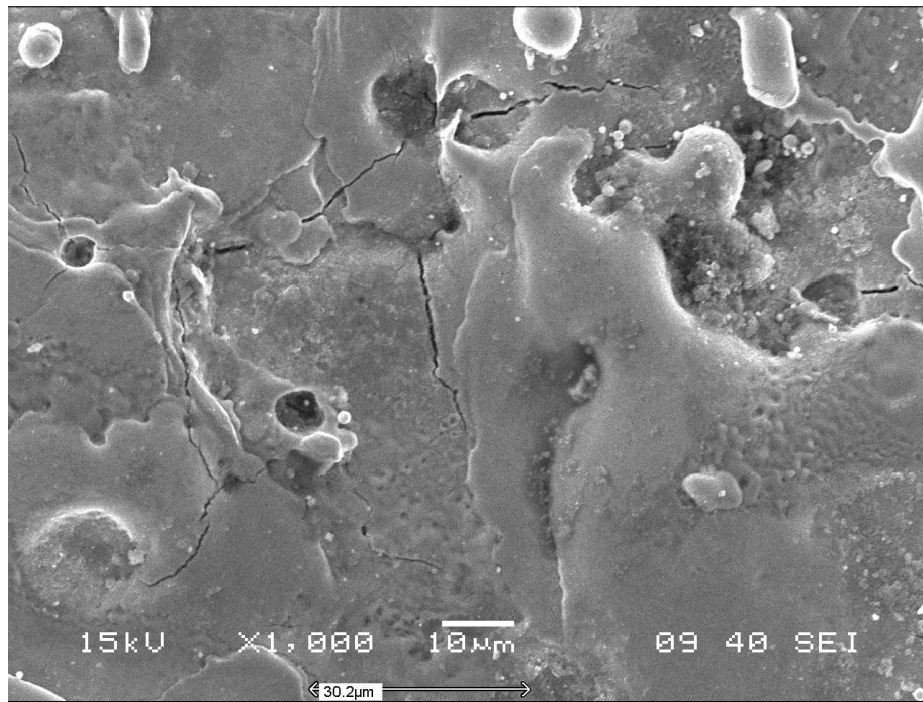


Fig. 3.12: SEM of EDMed surfaces of D2 Steel  $I_p=9A$ ;  $T_{on}=75 \mu s$ ;  $T_{au}=85\%$  &  $V=50V$

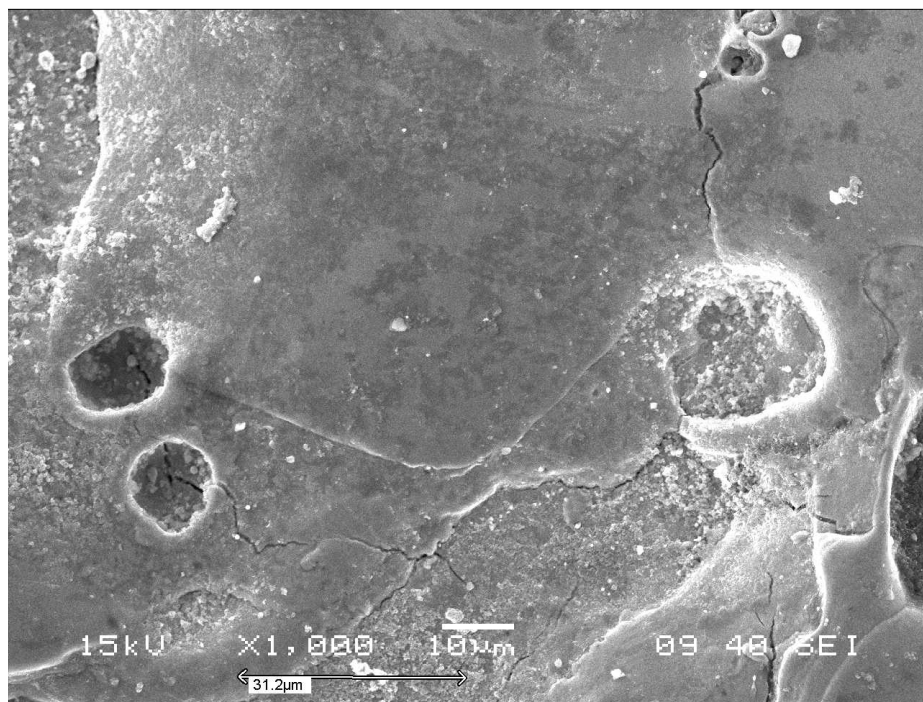


Fig. 3.13: SEM of EDMed surfaces of D2 Steel  $I_p=5A$ ;  $T_{on}=50 \mu s$ ,  $T_{au}=85\%$  &  $V=50V$

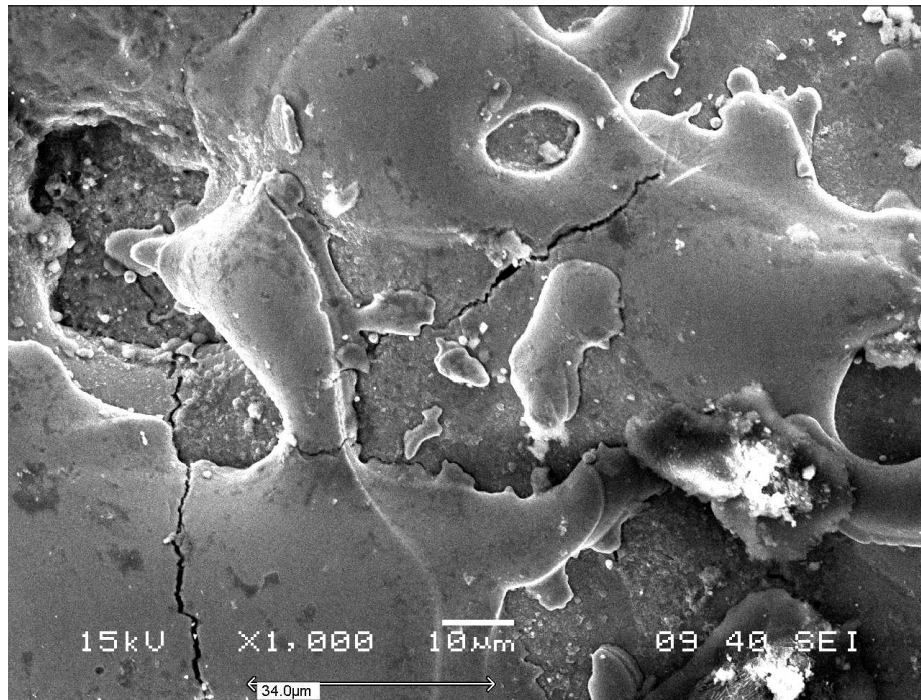


Fig. 3.14: SEM of EDMed surfaces of D2 Steel  $I_p=5A$ ;  $T_{on}=100 \mu s$ ,  $Tau=85\%$  &  $V=50V$ .

### 3.7 Conclusion

In this study, the influence of the most significant factors on surface roughness has been studied for AISI D2 tool steel. A face centred central composite design was used to conduct the experiment with discharge current, pulse on time, duty factor, time and gap voltage as input parameters. The ranges of these parameters were chosen which are widely used by machinists to control EDM machine. The input factors that significantly influenced the output responses were discharge current, pulse duration, square of pulse current and interaction between discharge current and pulse duration with a confidence level of 95%. The result reveals that in order to obtain a low value of Ra within the work interval of this study, discharge current, pulse on time and duty cycle should be fixed as low as possible. However, the developed mathematical model for the Ra can be effectively employed for the optimal selection of the EDM process parameters to achieve good surface of D2 workpieces. The surface craters, recast layers, and heat affected zones were observed. The size of the crater increases with the increase in current intensity and pulse on time, since these factors are responsible for producing stronger spark energy, bigger crater and thus rough surface.

# Chapter IV

## Finite-Element Modelling of Residual Stress

## 4. FINITE-ELEMENT MODELLING OF RESIDUAL STRESS

### 4.1 *Introduction*

In this chapter, a finite element modelling of the EDM process using ANSYS software is presented. The high-density thermal energy discharge produces during machining causes the local temperature in the workpiece gets close to the vaporization temperature of the workpiece, leading to the thermal erosion and also produces recast layer with micro-cracks on machined surface. A non-uniform heating of the workpiece material favours formation a multi-layered Heat Affected Zone (HAZ) in the sub surface inducing thermal stresses. If these stresses overpass the yield stress of the material, they will remain as residual stress in the workpiece during subsequent cooling, which plays a key role in fatigue crack growth, crack closure, and fracture. The residual stresses are self equilibrating internal stresses existing within a component when no external tractions are applied to it. The state of the residual stress typically comes up as a cumulative effect of the processes it has undergone, and the material properties. The residual stresses are particularly detrimental when they are tensile in nature, as it instigates the crack and become critical if subjected to fatigue load. Prediction and measurement of residual stress in engineering components have been a pursuit of researchers as residual stresses not only have an effect on the initiation and onset of the propagation of surface crack but also change the path/growth of the crack as it grows below the surface.

In this research, an attempt is made to investigate the effects of the machining parameters (pulse current and pulse duration) on the residual stresses developed beneath the spark by a single spark FEA model. The major aim of developing this model is to predict the nature of residual and thermal stresses occurring during EDM. The FEA model is also used to study the relation between these parameters and temperature variation with depth at the end of heating cycle. The temperature

distribution in the workpiece at the end of pulse duration was modelled.

## 4.2 Model detail

An EDM model involves electrical field, temperature field, and stress and strain field equations. In this process, two electrodes, namely workpiece and tool, are submerged in dielectric and they are physically separated by a gap, called inter-electrode gap. The discharge phenomenon in EDM can be modelled as the heating of the work-electrode by the incident plasma channel. Fig. 4.1 shows the idealised case where workpiece is being heated by a heat source with Gaussian distribution [Madhu et al. (1991), Bhattacharya et al. (1996), Yadav et al. (2002)]. Due to axisymmetric nature of the heat transfer in the electrode and the workpiece, a two-dimensional physical model is assumed and shown in Fig. 4.1.

### 4.2.1 Assumptions

Due to random and complex nature of EDM, the following assumptions are made for the finite element model:

1. The analysis is done for one spark only.
2. The domain is considered as axisymmetric about r-z plane.
3. The workpiece material is homogeneous and isotropic.
4. The thermal properties of workpiece material are considered as a function of temperature. It is assumed that due to thermal expansion, density and element shape are not affected.
5. The heat transfer to the workpiece is by convection.
6. Gaussian heat flux distribution is considered on spark incident surface of the workpiece material during pulse on time period.
7. Inertia and body force effects are negligible during stress development.
8. The workpiece material is elastic-perfectly plastic and yield stress in tension is same as that in compression.

9. The workpiece is assumed as stress-free before EDM.
10. Thermal stresses are evaluated only up to the time for which the transient temperature distribution is known above dielectric temperature.
11. The latent heat of the material during phase change is not considered.

#### 4.2.2 Thermal model

The domain is treated as a semi-infinite object in considering the microcosmic characteristics of the single discharge. The upper surface of the cylinder is the machining surface and its centre is the focus of the ionized channel. When a single spark is incident in to the workpiece, the heat propagates symmetrically in all direction, so taking advantage of its symmetry a small cylindrical portion of the workpiece around the spark is used as the domain as shown in Fig. 4.1. A convective heat transfer boundary conditions are applied on the surface that is exposed to the dielectric. All of the equations in this study are based on the cylindrical coordinate system, as shown in Fig. 4.2.

Heating of workpiece due to a single spark is assumed to be axisymmetric and governed by the following thermal diffusion differential equation below

$$\rho C_p \frac{\partial T}{\partial t} = \frac{1}{r} \frac{\partial}{\partial r} \left( k \frac{\partial T}{\partial r} \right) + \frac{\partial}{\partial z} \left( k \frac{\partial T}{\partial z} \right) \quad (4.1)$$

where T is temperature, t is time,  $\rho$  is density, k is thermal conductivity,  $C_p$  is specific heat capacity of workpiece material in solid state and r and z are coordinate axes as shown in Fig. 4.2.

#### 4.2.3 Equilibrium Equations

In elasticity theory, neglecting the initial and body forces, the stresses in the structure must satisfy the following equilibrium equations,

$$\frac{\partial \sigma_{rr}}{\partial r} + \frac{\partial \sigma_{rz}}{\partial z} + \frac{\sigma_{rr} - \sigma_{\theta\theta}}{r} = 0 \quad (4.2)$$

$$\frac{\partial \sigma_{rz}}{\partial r} + \frac{\partial \sigma_{zz}}{\partial z} + \frac{\sigma_{rz}}{r} = 0 \quad (4.3)$$



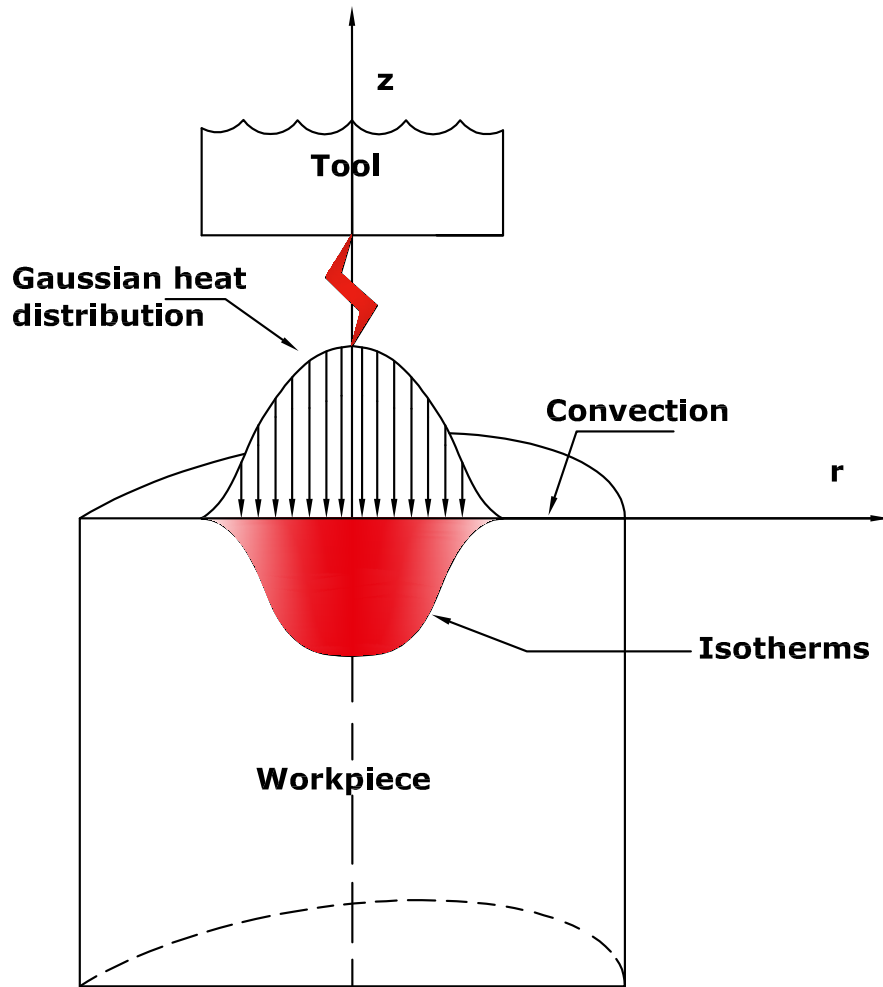


Fig. 4.1: Schematic sketch of the physical model.

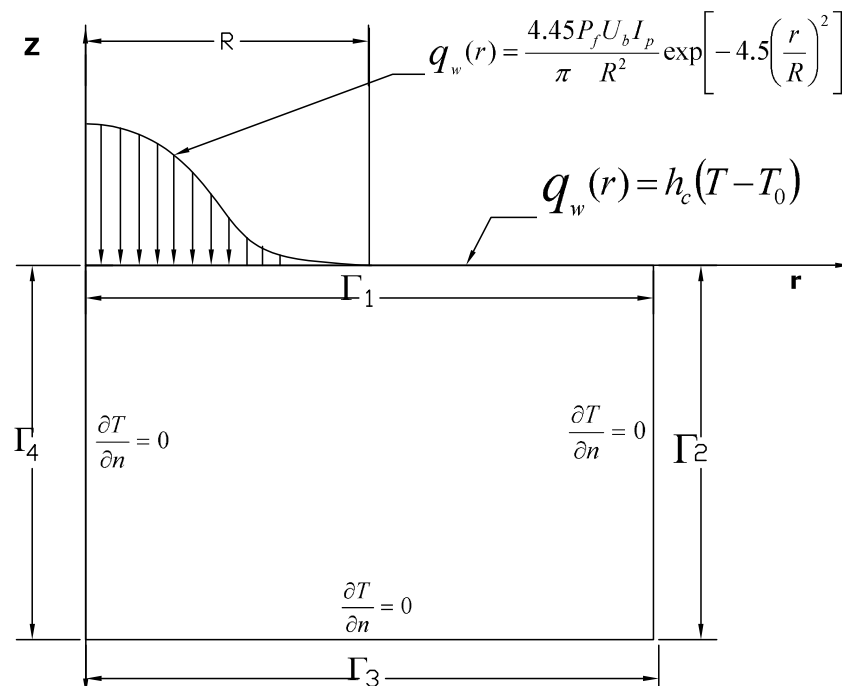


Fig. 4.2: An axisymmetric model for the EDM process simulation.

where  $\sigma_{rr}, \sigma_{\theta\theta}, \sigma_{zz}$  are normal stresses and  $\sigma_{rz}$  is shear stress.

#### 4.2.4 Stress-Strain-Temperature Relations

The constitutive relation of linearly elastic material is

$$\sigma = E \epsilon + \sigma_0 \quad (4.4)$$

where  $\sigma$  is normal stress,  $\epsilon$  is normal strains,  $E$  is elastic modulus, and  $\sigma_0$  is initial stress.

For a isotropic material, with initial stress  $\sigma_0 = 0$ , the stresses produced by temperature change  $\Delta T$ , symbolise the relation by the equation below:

$$\begin{pmatrix} \sigma_{rr} \\ \sigma_{\theta\theta} \\ \sigma_{zz} \\ \sigma_{rz} \end{pmatrix} = \frac{E}{(1+\nu)(1-2\nu)} \begin{bmatrix} (1-\nu) & \nu & \nu & 0 \\ \nu & (1-\nu) & \nu & 0 \\ \nu & \nu & (1-\nu) & 0 \\ 0 & 0 & 0 & \frac{(1-2\nu)}{2} \end{bmatrix} \begin{pmatrix} \epsilon_{rr} \\ \epsilon_{\theta\theta} \\ \epsilon_{zz} \\ \gamma_{rz} \end{pmatrix} - \frac{E\alpha_t\Delta T}{1-2\nu} \begin{pmatrix} 1 \\ 1 \\ 1 \\ 0 \end{pmatrix} \quad (4.5)$$

where  $\nu$  is Poisson's ratio and  $\alpha_t$  is the coefficient of thermal expansion of work-piece material.  $\epsilon_{rr}$ ,  $\epsilon_{\theta\theta}$  and  $\epsilon_{zz}$  are normal strain,  $\gamma_{rz}$  shear strain.

Equation 4.5 can be written as

$$\{\sigma\} = [D] \{\epsilon\} - \{m\} \quad (4.6)$$

where  $[D]$  is the elasticity matrix,  $\{\sigma\}$  is the stress matrix and  $\{\epsilon\}$  is the strain matrix.

The strain-displacement relations for axisymmetric model, for small strains and small rotations, are

$$\epsilon_{rr} = \frac{\partial u}{\partial r}, \quad \epsilon_{\theta\theta} = \frac{u}{r}, \quad \epsilon_{zz} = \frac{\partial w}{\partial z} \quad \text{and} \quad \gamma_{rz} = \frac{\partial u}{\partial z} + \frac{\partial w}{\partial r} \quad (4.7)$$

where  $u$  and  $w$  are the displacement in  $r$  and  $z$  direction, respectively.

#### 4.2.5 Spark radius/Plasma radius

It is well recognized that the size of plasma channel is an expanding quantity and its radius changes with time [Dibitono et al. (1989)]. Its expansion depends on many factors such as electrode material, electrode arrangement and polarity. Many attempts have been made to determine the spark radius theoretically and experimentally. Dibitono et al. (1989) experimentally showed that the radius of the channel changes proportional to the 3/4 power of time. Further, Erden (1983) integrated this equation  $R_p(t)$ , which is dependant on the discharge power and time as follows:

$$R_p(t) = ZP^m t^n \quad (4.8)$$

where, P is the discharge power, t is time and Z, m and n are empirical constants, with Z being a function of the discharge length. Further, these constants have been defined in terms of experimental coefficients L, M and N as:

$$Z = \frac{L}{lm + 0.5N}; \quad m = M + 0.5N \quad \text{and} \quad n = N \quad (4.9)$$

where, l is the discharge length.

Shankar et al. (1997) have found that the spark shape is non-cylindrical when they used the integrated approach model to analyse the electrodes and dielectric together. Pandey and Jilani (1986) have proposed the following model for calculation of spark radius:

$$T_b = \frac{E_0 R_p}{K \pi^{0.5}} \tan^{-1} \left[ \frac{4\alpha t}{R_p^2} \right]^{0.5} \quad (4.10)$$

where  $T_b$  is boiling temperature,  $E_0$  is energy density and  $\alpha$  is thermal diffusivity.

The above expression has limited application as they are applicable merely for few cases of particular electrode pairs and dielectric. There are many research attempts made to evaluate the spark radius, and though the significance of spark radius is well accepted, but to evaluate the shape and size of the radius, extensive work is still lacking. Hence, in most of the cases, particularly in a theoretical analysis, a typical value of spark radius is generally assumed. For the present workpiece material and dielectric combination under consideration, it is suggested that, since power is function of  $I_p$ , by modifying Equation 4.8, the radius of spark is

$$R_p(t) = ZIp^mTon^n \quad (4.11)$$

where,  $I_p$  is the discharge current,  $Ton$  is pulse on time, the value of  $Z = 325$ ,  $m = 0.55$  and  $n = 0.247$  are used as empirical constants, and the spark radius can be expressed as:

$$R_p(t) = 325 I_p^{0.55} Ton^{0.247} \quad (4.12)$$

And the calculated value of  $R_p$  for various  $I_p$ - $Ton$  combination used in this study are presented in Table 4.1.

Table 4.1: Spark Radius obtain from Equation 4.12

Pulse current (A)	Pulse duration ( $\mu$ s)	Spark radius, R ( $\mu$ m)
9	100	112
9	20	75
1	100	33
1	20	22

#### 4.2.6 Heat Flux and Energy Portion

Many researchers [Jilani and Pandey (1982), Pandey and Jilani (1986), Dibitono et al. (1989)] have considered a uniformly distributed heat source of a spark impinges into the workpiece, which is far from reality. However, some researchers Patel et al. (1989), Madhu et al. (1991) and Yadav et al. (2002) have considered a Gaussian heat flux distribution and the same is assumed in the present work. If the maximum intensity at the axis of the spark  $q_o$  and its radius ( $R_p$ ) are known, then the heat flux  $q_w(r)$  at radius  $r$  is given by

$$q_w(r) = q_o \exp \left\{ -4.5 \left( \frac{r}{R_p} \right)^2 \right\} \quad (4.13)$$

Yadav et al. (2002) presented this model to analyse the thermal stress due to EDM. They assumed that for each pulse,

$$q_o = \frac{4.45P_fU_bI_p}{\pi R_p^2} \quad (4.14)$$

If the total power which is used only by one single spark then Equation 4.13 becomes

$$q_w(r) = \frac{4.45P_f U_b I_p}{\pi R_p^2} \exp \left\{ -4.5 \left( \frac{r}{R_p} \right)^2 \right\} \quad (4.15)$$

where  $P_f$  is the percentage of heat input distributed to the workpiece,  $U_b$  the breakdown discharge voltage (different from the applied voltage),  $R_p$  the spark radius and  $I_p$  is the current.

One more vital factor requisite for analysis of EDM is the percentage of heat input distributed among cathode, anode, and dielectric. But, it seems that there is no comprehensive method available to calculate the value of energy sharing. It is a common agreement that the amount of energy shared is dependent largely on electrode material and dielectric. Previously, in the modelling of EDM, it was assumed that the total heat supplied on the surface is transferred to the workpiece and there is no heat sharing with the dielectric and tool electrode. Later on, Dibitono et al. (1989) and Patel et al. (1989) have assumed that a constant fraction  $P_f$  as 8% of total power is transferred to the electrodes, about 18% is absorbed by cathode and the rest is rejected to the dielectric. Yadav et al. (2002) also adopted the same, however, Kansal et al. (2007) considered  $P_f$  as 9%. Shankar et al. (1997) has calculated that 40%-45% of the heat input is absorbed by the workpiece. Panda and Bhoi (2005), for machining of D2 steel by copper as tool-electrode with kerosene as dielectric, assumed that the energy received by work-electrode varies from 17% to 20%. In the present model, it has been assumed that 8% of the total heat is used by the workpiece which is the lower bound of the  $P_f$  values considered by other reserchers.

#### 4.2.7 Boundary condition

Fig. 4.2 demonstrates a schematic diagram of the thermal model with the applied boundary conditions during heating cycle. During the spark on-time (heating cycle) on the top surface  $\Gamma_1$ , the energy transfer to the workpiece is represented by a Gaussian heat flux distribution upto spark radius  $R_p$ . Beyond  $R_p$ , the heat loss to the coolant is modelled using convective boundary conditions. However, during cooling cycle, on the entire top surface  $\Gamma_1$ , the convection heat transfer takes place due to the

cooling effect caused by the dielectric fluid. No heat transfer occurs across surfaces on  $\Gamma_2$  and  $\Gamma_3$ , because they are assumed to be sufficiently far away for any heat transfer to take place as the duration of spark is very small. The boundary  $\Gamma_4$  is the axis of symmetry, hence the heat flux has been taken as zero as there is no net heat gain or loss across this boundary.

The initial and boundary conditions are listed below.

- At boundary  $\Gamma_1$ ,

when  $0 > t \geq Ton$

$$q_w(r) = \begin{cases} \frac{4.45P_f U_b I}{\pi R_p^2} \exp \left\{ -4.5 \left( \frac{r}{R_p} \right)^2 \right\} & \text{for } r \leq R_p \\ h_f(T - T_0) & \text{for } r > R_p. \end{cases} \quad (4.16)$$

when  $t > Ton$ ,

$$q_w(r) = h_f(T - T_0) \quad \text{for } 0 < r < \infty. \quad (4.17)$$

- At boundaries  $\Gamma_2$ ,  $\Gamma_3$  and  $\Gamma_4$ ,  $\frac{\partial T}{\partial n} = 0$

where,  $n$  is normal direction on surface,  $h_f$  is coefficient of convective heat transfer at the work-dielectric fluid interface and  $T_0$  is ambient temperature.

#### 4.2.8 Numerical Model

##### *Model of thermo-analysis for single discharge*

The EDM process involves a complex coupling among thermal, electrical, physical, and chemical processes, which makes it difficult to be modelled. A thermo-structural finite element model based on heat transfer principles has been developed for the simulation of single-spark machining of AISI D2 tool steel. For simplicity, a 2-D plane stress analysis with ANSYS software is performed [Kohnke (2004)]. ‘PLANE 13’ coupled field quadrilateral element with capabilities of handling the thermo-structural properties are used to model the specimen. The domain is treated as a semi-infinite object in which the model dimensions are eight times the dimension (radius and

thickness) of plasma radius,  $R_p$ . There is no significant change found in the FEM results with larger semi infinite boundary conditions of the domain.

Mapped meshing is carried out using the quadrilateral-shaped elements with a non-uniformly spread mesh, with more elements intended in the heat-affected regions where the high temperature gradient and stress concentration exists (Fig. 4.3). In addition, the area away from the sparking point is meshed with coarse mesh as there is less variation of temperature and stress. The FEA mesh had a total of 2640 elements and 2734 nodes. The size of the smallest element is of the order of  $1.28 \times 1.28 \mu\text{m}$ . The dimensions shown in Fig. 4.3 are in  $\mu\text{m}$  so it is clear that a very small area is considered around the vicinity of the point where the spark strikes. In ANSYS, the radial coordinate ( $r$ ) is depicted as x axis and axial coordinate ( $z$ ) is y-axis as shown in the figure.

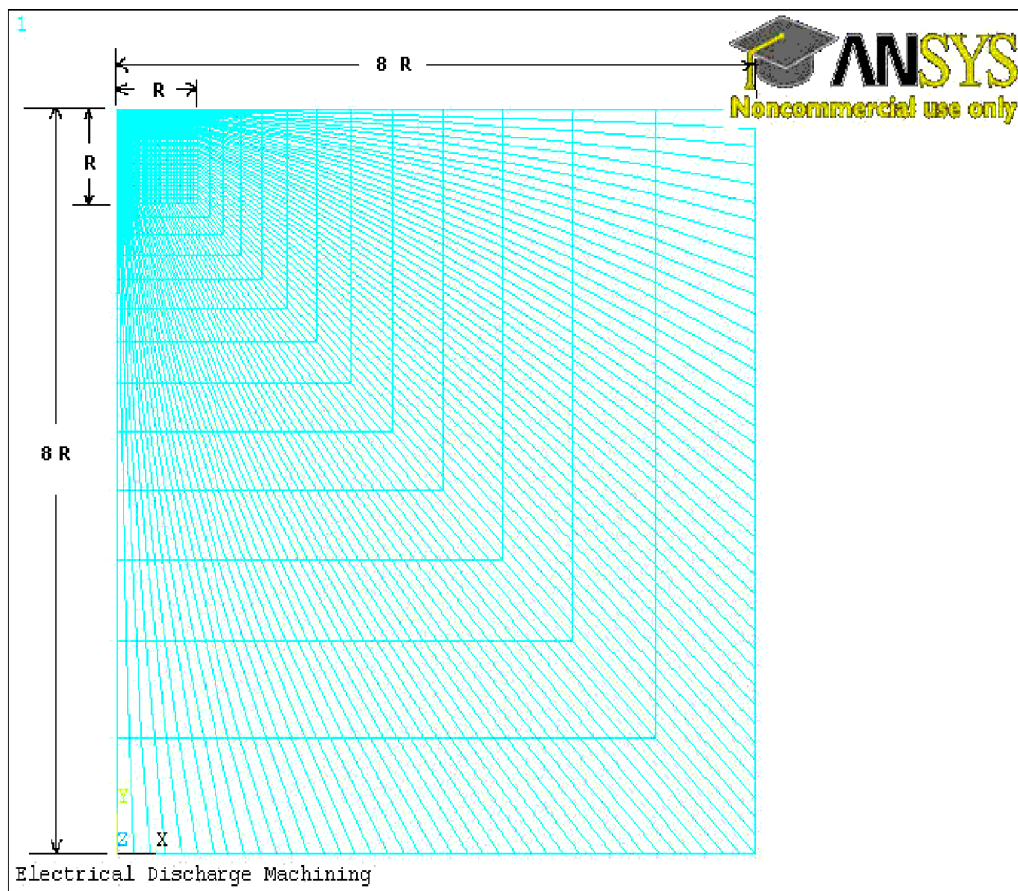


Fig. 4.3: Mesh generation for FEM full model.

When the arc strikes the workpiece the temperature rises tremendously from the

ambient temperature to the boiling point (even more) of the material and comes back to the ambient temperature before the subsequent arc strikes within a few microseconds. Due to this rapid temperature gradient the workpiece material melts and even vaporises. The whole vaporised metal and a fraction of molten metal is ejected, however, residual fraction of the molten metal gets re-solidified and deposited in the workpiece as white layer. Thus it is very important to use temperature-dependent thermo-physical properties for the simulation of the EDM process. The Young's modulus for D2 material used are as reported in the literature [Kansal et al. (2007)]. Since residual stress is caused by heterogeneous plastic deformation of the material, temperature dependent material properties are used. Plastic deformation of material is modelled using bilinear kinematic hardening (BKIN) option in ANSYS program as presented in Fig.4.4, where 'SIG' and 'EPS' mean  $\sigma$  and  $\epsilon$ , respectively [Ansys-12.0 (2010)].

The approximate temperature-dependent material properties (Thermal conductivity, Coefficient of thermal expansion and Specific heat) of AISI D2 tool steel, which are given to ANSYS modeller, are summarised in Table A.3. The melting temperature,  $T_m$  and boiling temperature,  $T_b$  of the workpiece material are 1984 K and 2590 K, respectively. Since the temperature dependent modulus of elasticity and Poisson's ratio of workpiece material is not available in the referenced papers, the data that has been used here are very close to the material properties of common tool steel [Table A.4]. Analyses are performed to study the effect of  $I_p$  and  $T_{on}$  on the temperature, thermal stress and residual stress distributions with various levels as shown in Table 4.1. The spark radius upto which the heat flux imposed is tabulated in the same table. The heating period considered for this analysis is  $T_{on}$  and the cooling period is  $39 \times T_{on}$ . The heat energy supplied is modelled using function utility in ANSYS in accordance to Equation 4.16 and Equation 4.17. The coefficient of convection  $h_f$  is 10 kW/mK. The reference temperature,  $T_o$  is 298 K for the solutions procedure. In the model, the left edge is the centreline of the 2D axisymmetric section is made adiabatic along with the bottom and right hand edges [Fig. 4.2]. The bottom surface is free to move horizontally, but its vertical movement is restricted.

The solution procedure adopted was implemented in three load steps as shown in



Fig. 4.5. The first load step consists of heating cycle for  $T_{on}$  duration and solution was obtained with a time step of  $\frac{1}{40}^{th} T_{on}$ . The cooling process was carried out in the second and the third solution steps with durations of  $4 \times T_{on}$  and  $35 \times T_{on}$ , respectively. The time steps adopted were  $\frac{1}{40}^{th} T_{on}$  and  $T_{on}$  for the last two steps, respectively, to ensure faster convergence. The flow chart of the finite element analysis procedure is shown in Fig. 4.6.

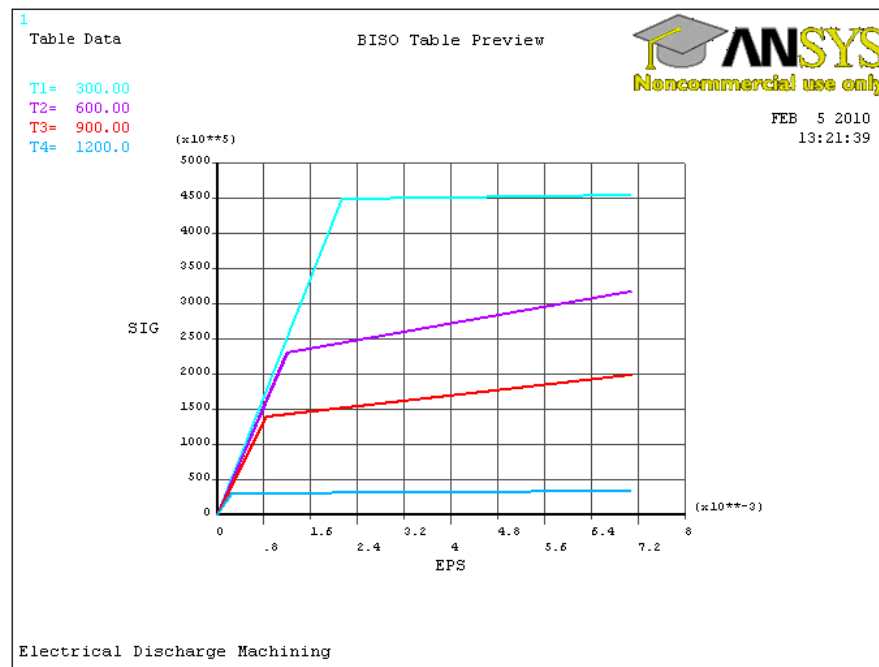


Fig. 4.4: Temperature dependent bilinear kinematic isotropic hardening.

Owing to the workpiece material's temperature dependent thermo-physical properties, this type of problem is of non-linear characteristic. To solve the non-linear equations, the Newton-Raphson method was used, which is an iterative method to solve above equations with line search option. Typical number of cumulative iterations required for convergence were found to be 1137 for  $I_p=9$  A and  $T_{on}=100 \mu s$ , and the error convergence plot is shown in Fig. 4.7.

First, the whole domain is considered to obtain the temperature profile during the heating cycle. The temperature profile just after the heating period is shown in Fig. 4.8, which depicts four distinct regions signifying the state of the workpiece material. Those elements attain the boiling temperature (2590 K) are shown as 'D'

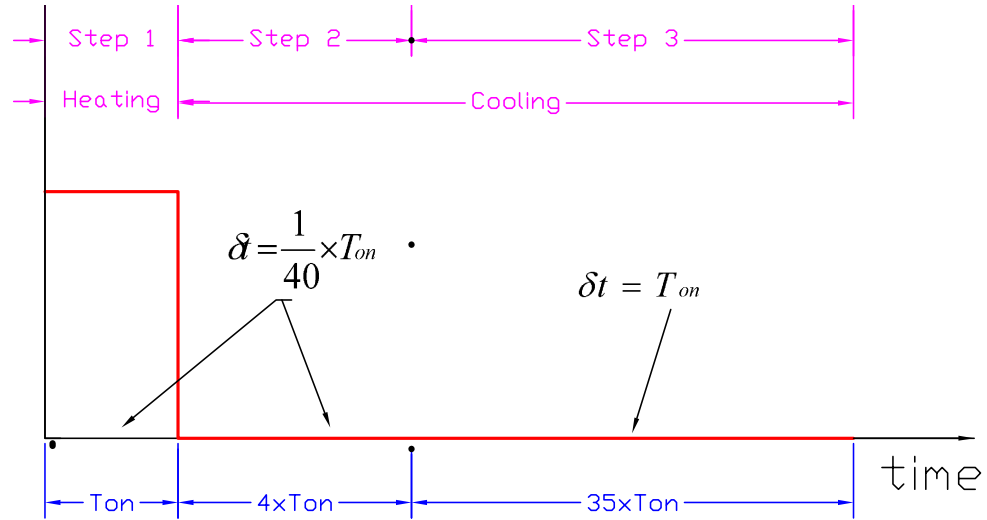


Fig. 4.5: Heating and cooling cycle

region, which are completely removed by vaporisation, are killed. Only, Lim et al. (1991) stated that 15% of the molten material is flushed away from the workpiece. Since, there are few references quantifying the amount of molten metal ejected during heating cycle, it is assumed that 50% of the total molten metal is ejected out. ‘C’ and ‘B’ regions are molten zones, of which the molten metal in ‘C’ region is ejected and flushed away as debris. Thus, these elements were eradicated/killed from the domain at the end of pulse duration. However, the molten metal in ‘B’ region is quenched and resolidifies as recast layer. The zone depicted by ‘A’ is HAZ which is susceptible to residual stresses. In the second and third load steps, the model without the killed elements was solved. The stress obtain at the end of the cooling cycle is entrapped in the workpiece and it is known as residual stress.

### 4.3 Experimentation

This research is focused on measuring the residual stresses in EDMed component using X-ray diffraction (XRD) technique for the experimental validation of the FEM results. The workpiece preparation and its machining procedure is explained in this section along with the XRD measurement and its data analysis.

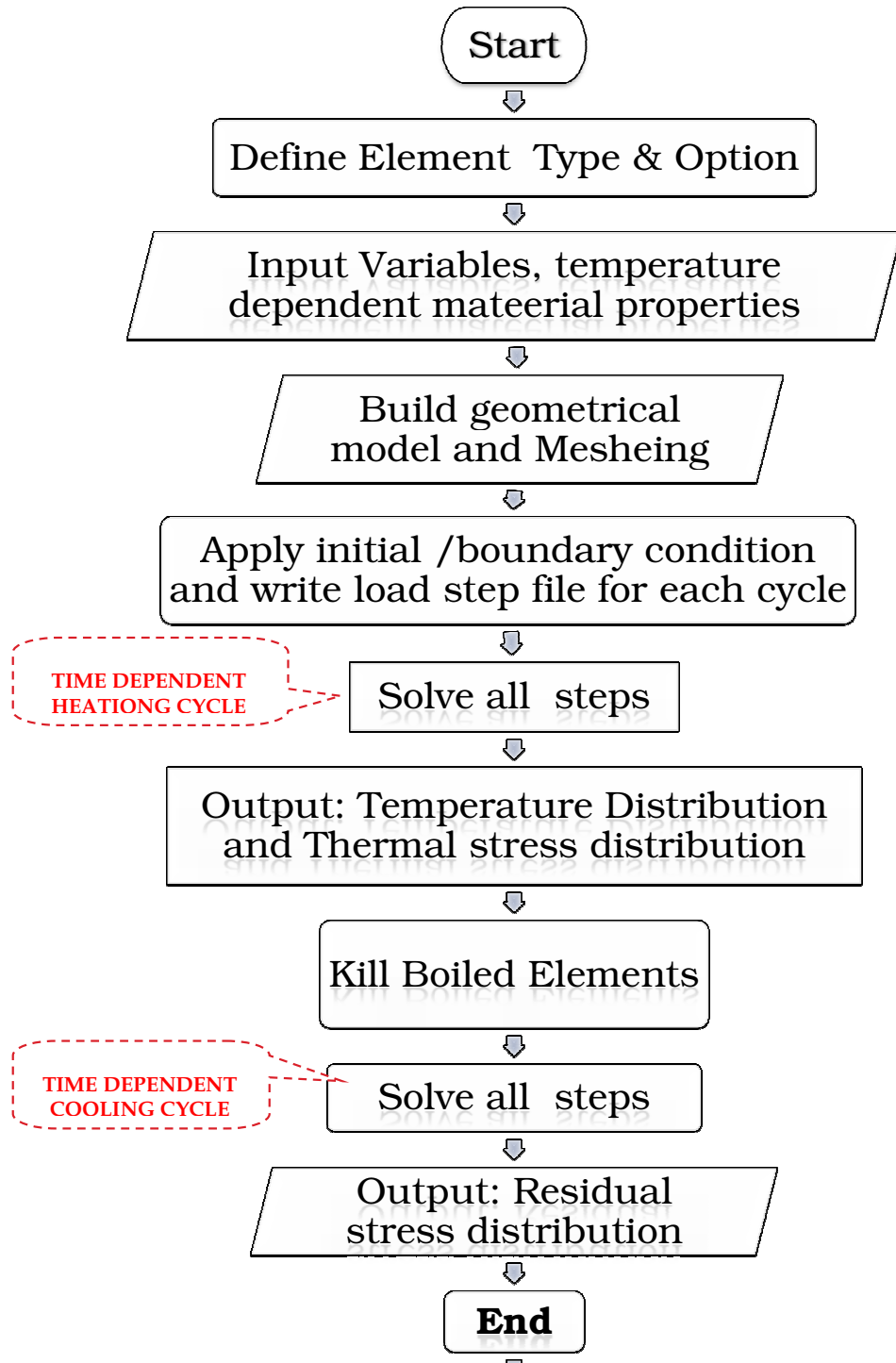


Fig. 4.6: Flow chart for ANSYS solution procedure

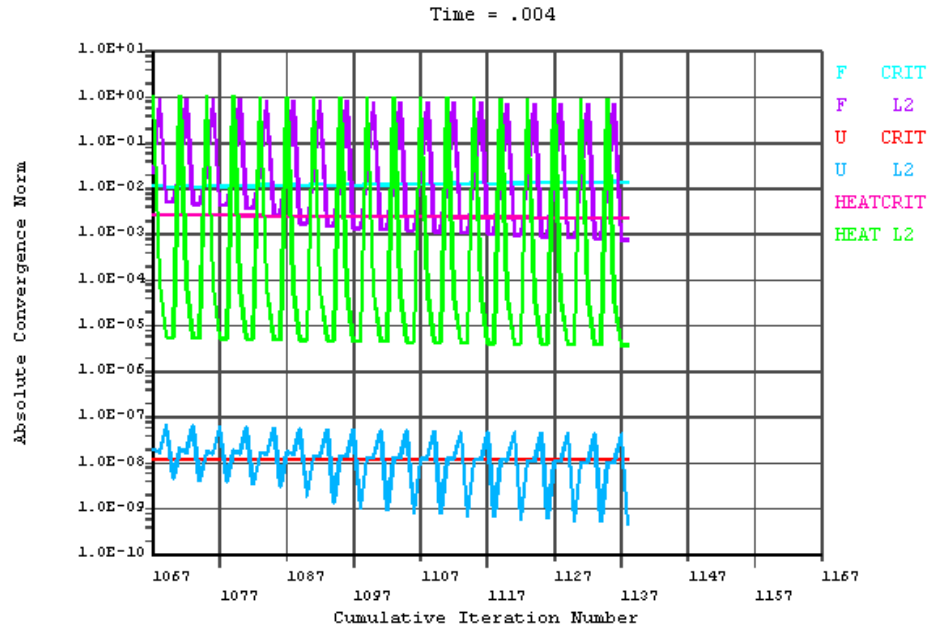


Fig. 4.7: Convergence graph

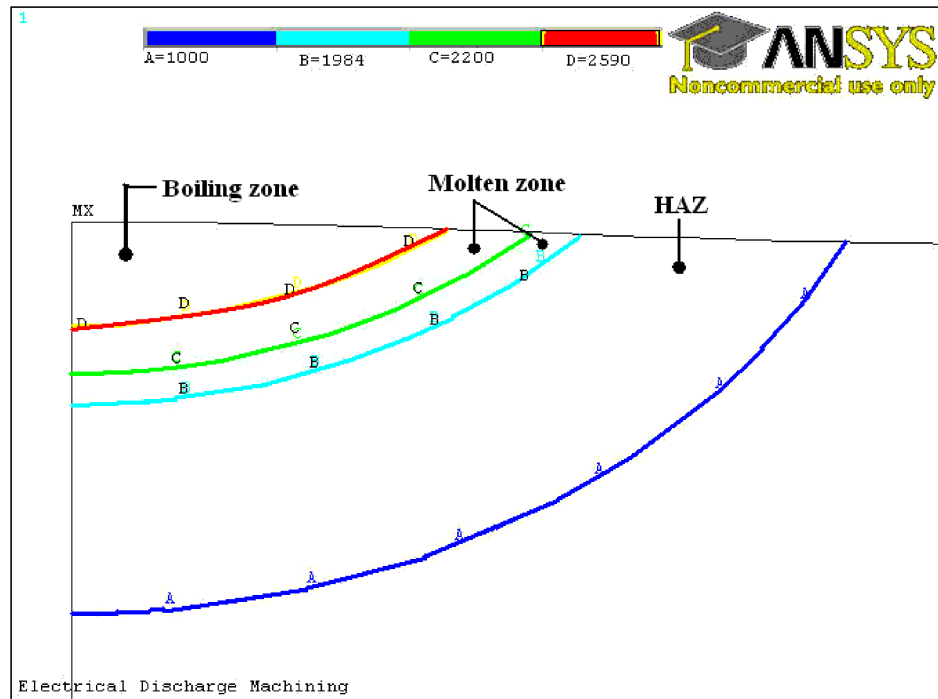


Fig. 4.8: Isothermal lines at the end of pulse on time for  $I_p=9A$  &  $T_{on}=100\mu s$ .

### 4.3.1 Experimental procedure

Workpiece was initially circular bar of diameter 100 mm and was cut into specimens of size  $15 \times 15$  mm square and thickness of 10 mm by a power hacksaw. The top and bottom faces of the workpiece were ground to make it flat and good quality surface finish prior to the heat treatment. The specimens were stress relieved prior to electric discharge machining to ensure stress free condition. After grinding, the specimens were heated up to  $700^\circ\text{C}$ , holding them for 2 hours at that temperature and then was cooled slowly to room temperature in a furnace (see Appendix A.4). The top surface was machined by a CNC electrical discharge die sinking machine (see Appendix A.1). In this work, a cylindrical pure copper (99.9% Cu) was used as a tool electrode with a diameter of 30 mm (Fig. A.3). Commercial grade EDM oil was used as dielectric fluid, the power supply was linked with the tool electrode (tool: positive polarity, workpiece: negative polarity). A lateral flushing system was employed for effective flushing of machining debris from the working gap region with a pressure of  $0.4\text{ kgf/cm}^2$ . The experimental conditions are summarised in Table 4.2. The bottom of the cylindrical electrode was polished by a very fine grade emery sheet prior to every experimental run. Experiments were conducted to study the effects of  $I_p$  and  $T_{on}$  on the temperature profile, thermal stress and residual stress induced in the EDMed components. The arrangement to conduct the experiments using a full factorial design in four experimental runs is illustrated in Table 4.3. Machining was carried out to remove approximately 1 mm of material from the top surface.

In this work, the variation of residual stress with depth is studied. Therefore, after measuring the residual stress on the top surface, a layer was removed to measure the residual stress in subsequent surface. Thus, it is necessary to remove layers of material in succession without further changing the residual stress state of the material by electro polishing. The specimens were successively polished with 1000 grit silicon carbide emery paper and then with fine diamond paste (size  $1\mu\text{m}$ ). For subsequent characterizations by X-ray diffraction, the samples were electro polished by using an electrolyte of 80:20 methyl alcohol and perchloric acid under 21 V.

Table 4.2: Input variables used in the experiment and their levels.

Variable	Unit	levels	
		1	2
Discharge current ( $I_p$ )	A	1	9
Pulse on time ( $T_{on}$ )	$\mu s$	20	100
Voltage of discharge ( $V$ )	volt	50	
Dielectric used		Commercial grade EDM oil	
Dielectric flushing		Side flushing with pressure 0.4 $kgf/cm^2$	
Work material		AISI D2 steel	
Electrode material		Electrolytic Copper (99.9% pure)	
Electrode polarity		Positive	
Work material polarity		Negative	

Table 4.3: Experimental design matrix for RS

Expt No	$I_p$ (A)	$T_{on}$ ( $\mu s$ )
1	9	100
2	9	20
3	1	100
4	1	20

Table 4.4: X-ray diffraction conditions.

Target	Cu
Wavelength ( $\text{\AA}$ )	1.54188
Current (mA)	40
Voltage (kV)	40
Method	Unidirectional stress analysis
Material	AISI D2 (Fe-Cr)
s1	-1.31 1/TPa
1/2s2	5.96 1/TPa
Wavelength for calc.	$K_{\alpha 1+2}$
Strain-free $\sin^2\Psi$	0.500
Shear stress	Yes

### 4.3.2 X-ray diffraction measurements and data analysis

X-ray diffraction measurements were carried out in a Philips X'Pert MRD horizontal goniometer (see Appendix A), operating at 40 kV and 40 mA, equipped with a Cu radiation source,  $\lambda_{CuK\alpha} = 1.54188 \text{ \AA}$ . The goniometer was used with Bragg-Brentano configuration and  $\psi$ -geometry. The plane chosen for strain analysis was (0 2 2) and side angle  $\psi$  range was from  $\pm 40^\circ$ . The diffraction conditions are reported in Table 4.4. Macroscopic residual stresses were measured only in the martensite phase, which is the majority phase. The stresses in carbides, bainite and retained austenite were not measured because the volume fraction of these phases were very small and because there were no suitable diffraction peaks for the measurement of residual stresses in these phases.

The measurement of residual stresses is based in the determination of the variations in peak positions due to distortions of the crystalline lattice. If the specimen is stressed, lattice spacing varies according to the orientation of planes relatively to stress direction (see Appendix C). The refractometer was equipped with a wide range goniometer and a scintillation counter. All the specimen were first scan through  $2\theta$  value ranging from  $70^\circ$  to  $165^\circ$  and the result obtained on the topmost layer is presented in Fig. 4.9 for  $I_p = 9\text{A}$  and  $T_{on} = 100\mu\text{s}$ . All figures presented in this section are meant for said specimen only, unless otherwise stated. The figure reveals that although there are many peaks present, but the first peak was observed at an angle  $2\theta \approx 73.81^\circ$ . Hence, for further scanning the range of  $2\theta$  was set from  $72^\circ$  to  $75^\circ$  and the obtained peaks on the topmost layer (layer 1) with eleven  $\psi$  tilts. The Lorentz-polarization, back-ground and  $K_{\alpha 1+2}$  splitting corrections were applied to the measured intensities. The diffraction spectrum are shown in Fig. 4.10.

Residual stress depth profiles are conventionally analysed using  $\sin^2\psi$  method. The lattice spacing was measured with eleven  $\psi$  tilts and the graph between d-spacing and  $\sin^2\psi$  was plotted (Fig. 4.11). Peak positions were calculated using the conventional Gaussian curve fitting and the slope of the line represents the mean d-spacing for a given  $\sin^2\psi$ . In the plot the normal stress,  $\sigma_\phi$  is 812 MPa with SD of 11.6 MPa and shear stress is 61.7 MPa (SD 1.9 MPa). Assuming a biaxial stress state

exists in the layer and the elastic properties of the films are isotropic, the residual stress obtained are tabulated in Table 4.5. This calculation was performed using the commercial software PC-Stress 2.61 by Philips. The XRD patterns and  $d$  versus  $\sin^2\psi$  plots for layer 2, layer 3 and layer 4 are shown in Fig. 4.12, Fig. 4.13, Fig. 4.14, Fig. 4.15, Fig. 4.16 and Fig. 4.17, respectively. Similar procedure was adopted to measure the residual stresses for other specimens at various depths.

It is understandable that compressive residual stresses can be correlated to sample thickness, since residual stresses within plastically deformed layers are equilibrated with elastic stresses in the core of the material. Though, by removing the top layer produces a slit stress relaxation, but there will be a negligible alteration in the stress state [Garcia Navas et al. (2008)]. To obtain a noticeable correction, it is required to remove layers in millimetres, however in this case the maximum depth reached after removal of several layers was around  $200\mu\text{m}$  so the stress relaxation is practically zero.

Table 4.5: Experimental result of residual stress for all specimens

Expt. No.	$I_p$ (A)	$T_{on}$ ( $\mu\text{s}$ )	depth ( $\mu\text{m}$ )	$\sigma_\phi$ (MPa)	$SD\sigma_\phi$ (MPa)	$\tau_\phi$ (MPa)	$SD\tau_\phi$ (MPa)	$\sigma_{11} + \sigma_{22}$ (MPa)	$SD\sigma_{11} + \sigma_{22}$ (MPa)
1	9	100	0	812.0	11.6	61.7	1.9	1840.7	13.7
			24.6	792	12.8	62.3	2.1	1259.6	15.2
			54.7	-113.0	10.8	38.3	1.8	-389.0	12.8
			128	105.0	13.1	-10.7	2.2	196.0	15.6
2	9	20	0	797.9	12.6	43	2.1	1782.9	14.9
			20	732.0	14.1	23	2.4	1681.0	16.7
			44	-95.0	7.4	-4	1.2	-249.0	8.8
			117	136.0	10.4	7.1	1.7	193.0	12.4
3	1	100	0	167.0	5.3	34	0.9	610.0	6.3
			11	588.0	2.7	20.5	0.5	1268.0	3.3
			35	-47.9	2.8	-3.5	0.5	-174.9	3.3
			125	7.0	6.6	3.4	1.1	64.0	7.8
4	1	20	0	106.0	20.2	41.3	3.4	589.0	23.9
			8	470.0	6.1	31	1	1007.0	7.3
			34	-37.0	32.9	13.6	5.5	-146.0	39
			121	8.9	5	-15.3	0.8	155.9	6



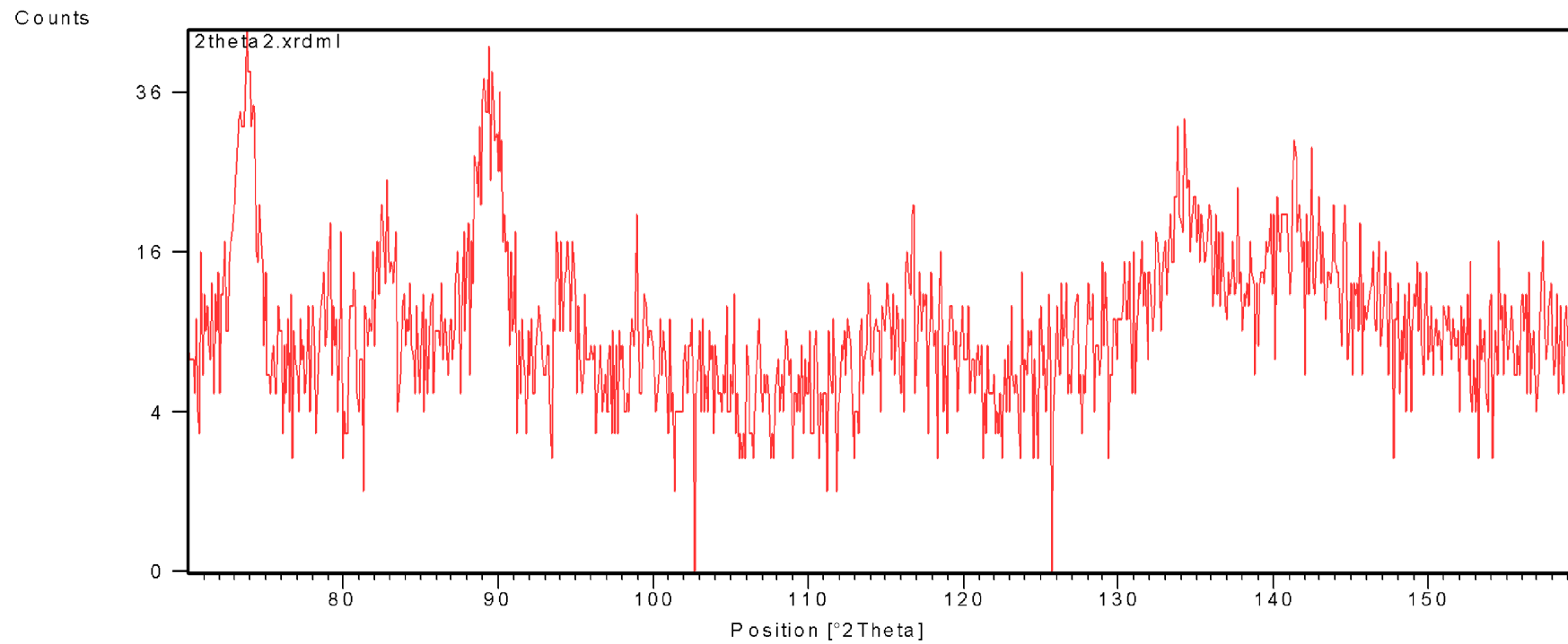


Fig. 4.9: Diffraction patterns obtained by scanning the topmost layer for  $2\theta=70^\circ$  to  $165^\circ$

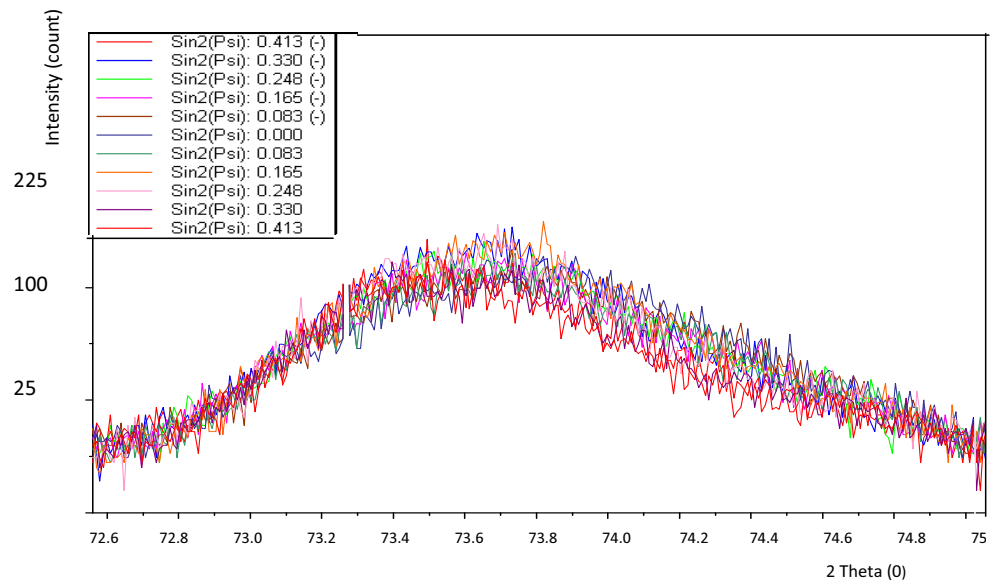


Fig. 4.10: X-ray diffraction peak in layer 1 for  $2\theta=70^\circ$  to  $75^\circ$

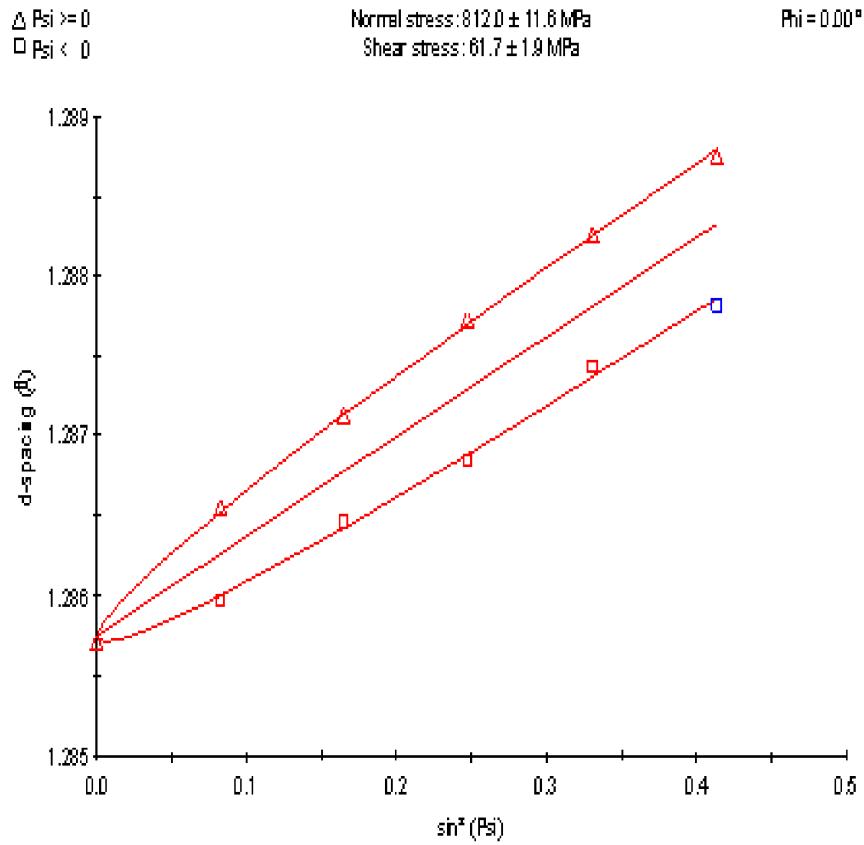


Fig. 4.11:  $d$  versus  $\sin^2\psi$  plot of layer 1 for  $2\theta=70^\circ$  to  $75^\circ$

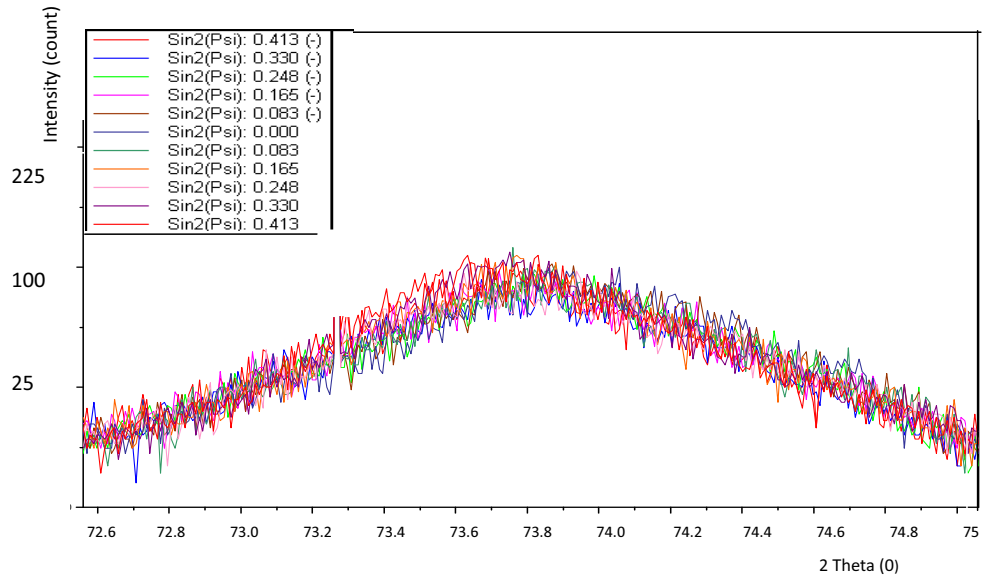


Fig. 4.12: X-ray diffraction peak in layer 2 for  $2\theta=70^\circ$  to  $75^\circ$

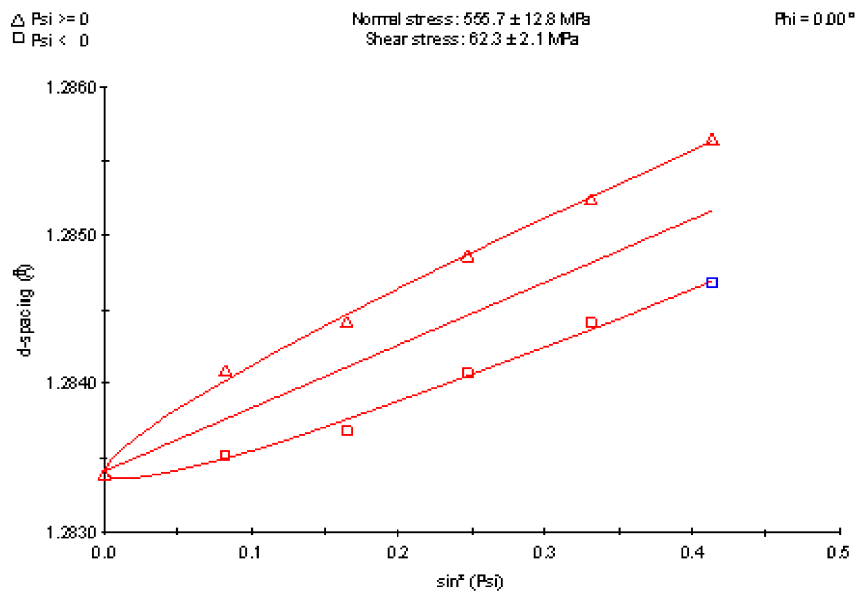


Fig. 4.13:  $d$  versus  $\sin^2\psi$  plot of layer 2 for  $2\theta=70^\circ$  to  $75^\circ$

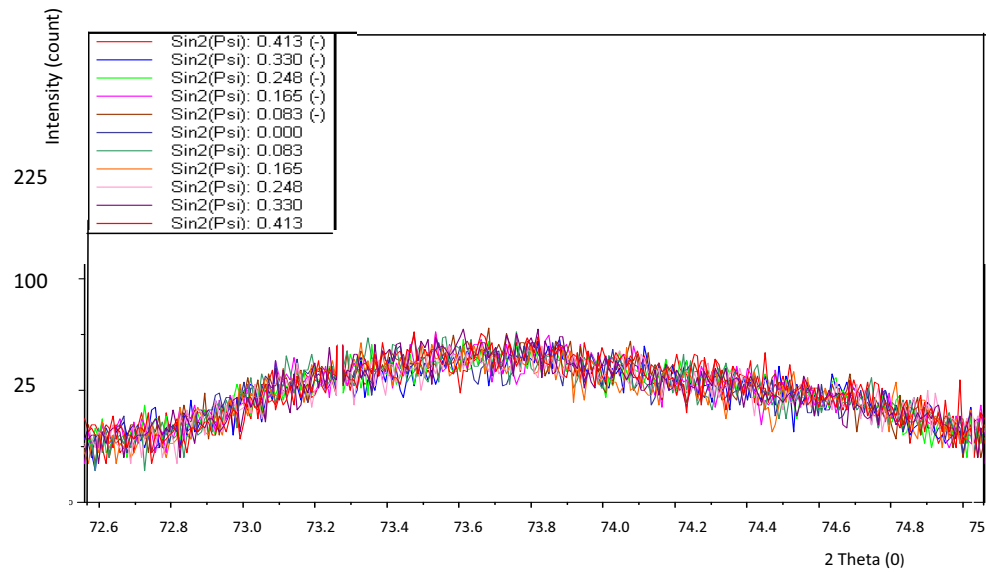


Fig. 4.14: X-ray diffraction peak in layer 3 for  $2\theta=70^\circ$  to  $75^\circ$

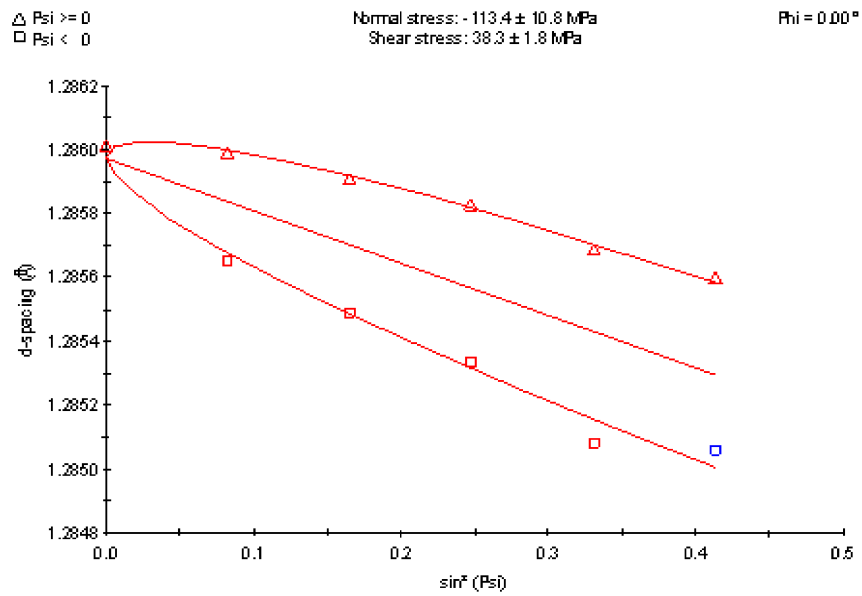


Fig. 4.15:  $d$  versus  $\sin^2\psi$  plot of layer 3 for  $2\theta=70^\circ$  to  $75^\circ$

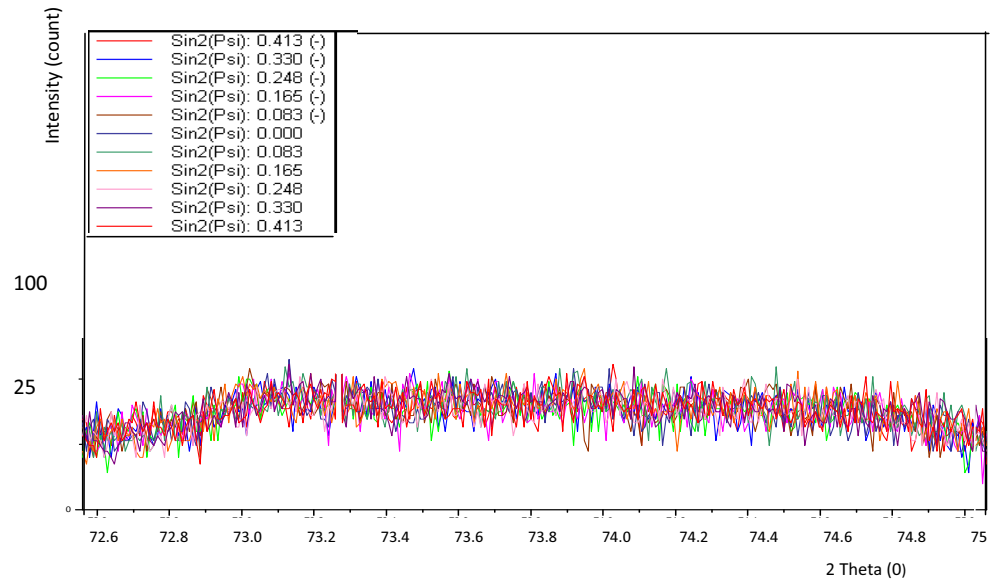


Fig. 4.16: X-ray diffraction peak in layer 4 for  $2\theta=70^\circ$  to  $75^\circ$

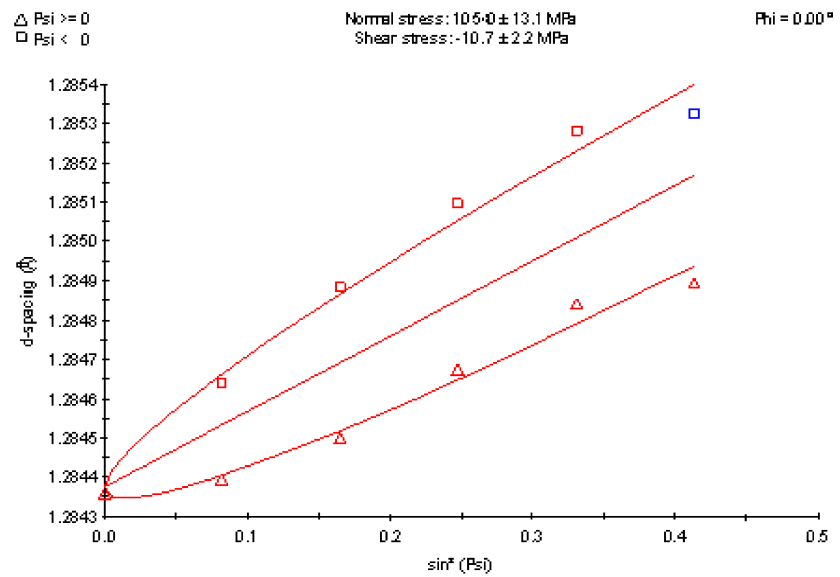


Fig. 4.17:  $d$  versus  $\sin^2\psi$  plot of layer 4 for  $2\theta=70^\circ$  to  $75^\circ$

## 4.4 Discussion of the Results

Ansys-12.0 (2010) software was used to model the electrical discharge process with various  $I_p$ - $T_{on}$  combinations. It is known that temperature pattern at the end of pulse duration is a key point to estimate phase transformation of the material. The phase changes from solid to liquid and to gas at regions that have temperatures higher than the melting point. While the fusion zone experiences solid-liquid transformation, the heat-affected zone experiences solid-solid phase transformation. This transformation is initiated at approximately 1000K. Once this temperature is exceeded the parent material transforms to austenite. Subsequently, as the austenite cools several daughter phases, such as ferrite, pearlite or bainite could be created. The cooling rate is an important factor to estimate such changes. In EDM process cooling rate is extremely high and thus expected that most of the HAZ will have transformed to martensite. In this section, the results obtained using the FEM analysis and experimentations described in Section 4.3, the temperature profiles, and the thermal and the residual stresses are discussed. The effect of process parameters such as  $I_p$  and  $T_{on}$  on these responses are also evaluated. In addition, the developed FEM model is partially validated by comparing the predicted residual stress results with the experimental data.

### 4.4.1 Temperature distribution

To know the thermal effects on the electro-discharged machined surface, there is the need to analyse temperature profiles at the end of the pulse. The temperature distribution during single discharge is calculated with the energy input for  $I_p=9$  A and  $T_{on} = 100\mu s$ . The temperature isotherms of single discharge at the end of pulse (before ejection) is shown in Fig. 4.18. Nine isotherms representing the nodal average temperature with the corresponding values are depicted in colour code in the figure. The maximum temperature attained in the workpiece under this heat flux is found to be 3679 K at the centre of the discharge and it gradually decreases away from upper-left corner of the model. It is expected because the intensity of the heat flux is highest at this point and as the distribution is Gaussian, the temperature is

gradually diminishing away from the centre. Out of these nine isotherms the top three isotherms are in the boiling region, next three isotherms are in molten region, and last two isotherms are in HAZ.

The jagged periphery in the close-up image demonstrates how those elements, which are in elevated temperature, are eroded/killed from the workpiece. In actual practice, the face after erosion of material is expected to be much smoother, however, it is jagged here in the modelling because partial removal of element is not possible in modelling, only whole element could be removed which attains the requisite temperature. The molten material portion recast on the parent material is called recast layer. The portion above the melting point (top two isotherms in Fig. 4.19) is recast layer and subsequent four layer (above 1000k and melting temperature) are HAZ.

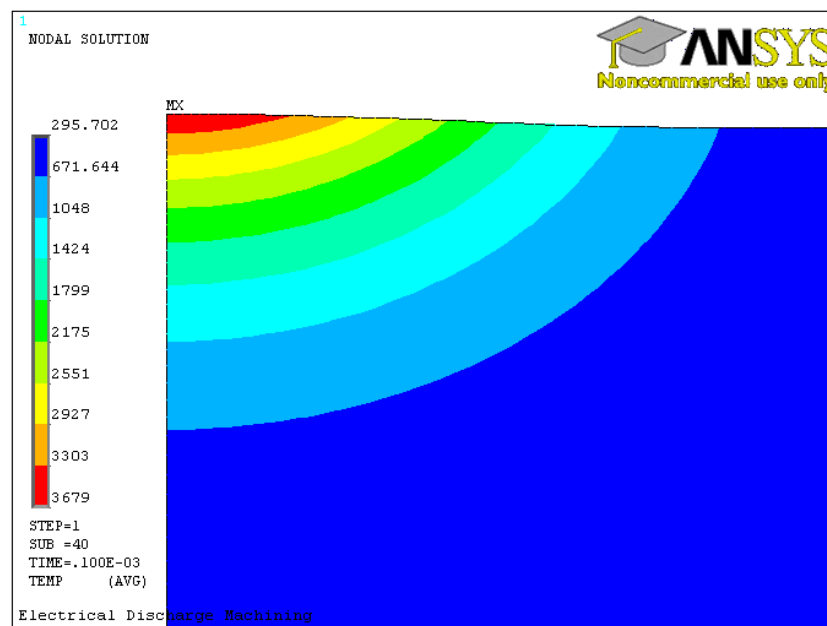


Fig. 4.18: Temperature distribution at the end of  $T_{on}$  just before material ejection.

A shallow shape crater has been formed due to single spark, which is a cavity with a concave shape on the workpiece surface. The volume of the crater equals that of the removed material by the spark depicted in Fig. 4.20. The craters determine the surface topography of the machined workpiece. The height and radius of a crater created by a single spark are  $13.4 \mu\text{m}$  and  $45 \mu\text{m}$ , respectively. It could be observed that the radius of the crater hemisphere formed in the radial direction is more than that of depth resulting in elliptical shape shallow craters.

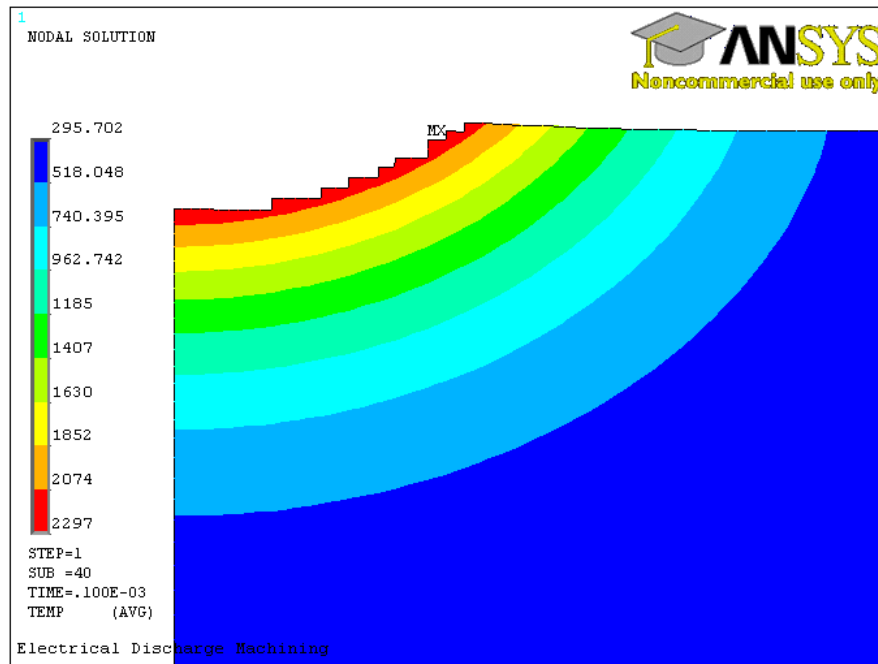


Fig. 4.19: Temperature distribution at the end of pulse on time subsequent to material removal.

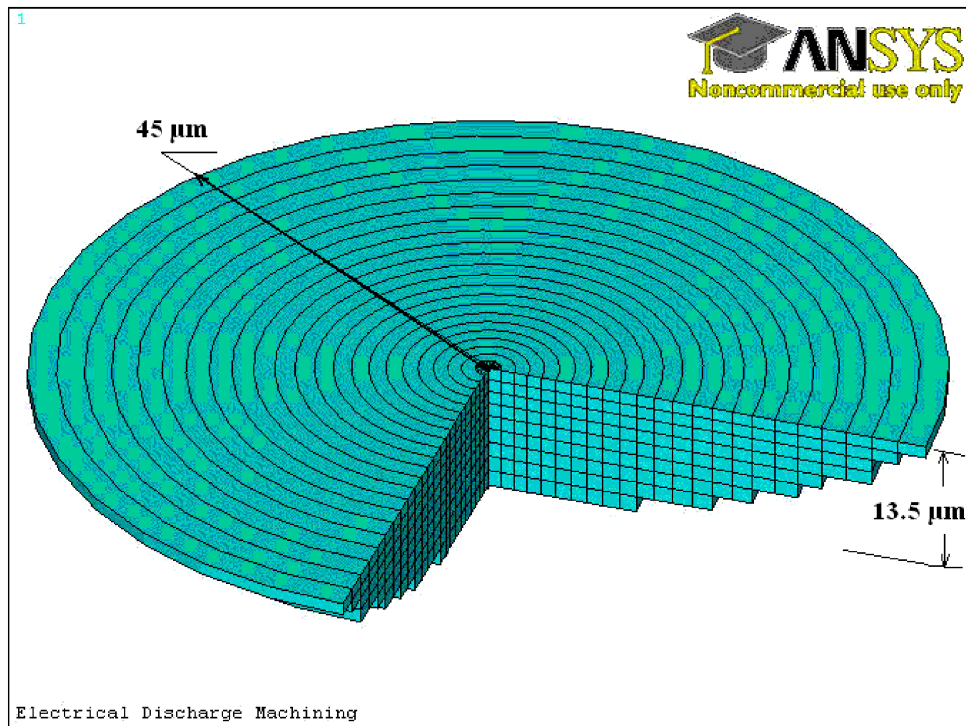


Fig. 4.20: Detached/killed elements from the spark vicinity at the end of pulse.



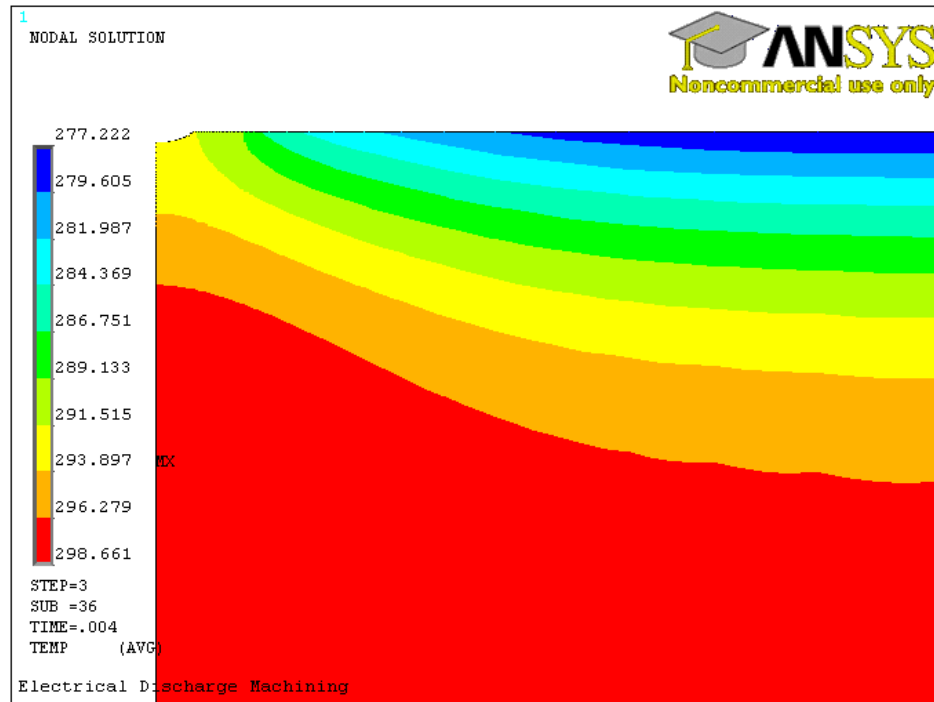


Fig. 4.21: Temperature distribution at the end of pulse off time. ( $I_p=9A$ ,  $T_{on}=100\mu s$ )

Fig. 4.21 shows the temperature profile of the domain at end of cooling cycle when the workpiece cools down. The shapes of the isotherms in Fig. 4.21 are different from that of Fig. 4.19 as during cooling convective heat transfer takes place in top surface.

The surface, diagonal and symmetry paths (depicted in Fig. 4.22) are defined to emphasis the variation of responses along those path. The time history of temperature of a few specific points depicted in Fig. 4.22, over entire the heating and cooling cycle is presented in Fig. 4.23. It can be observe that, there is a sharp temperature rise during the heating cycle and then rapid quenching. The temperature variation with respect to time of various points on diagonal path reveals solid-solid phase transformation just after removal of pulse within heat-affected zone. Besides this, in this figure, it is observed that the peak of the time history temperature profile shift rightwards as the depth increases. This is possibly due to the fact that as the distance of the point from the interface increases, the effectiveness of the cooling process is delayed. Since, after the heating cycle, the molten metal starts solidifying, the top surface is quenched and solidifies rapidly due to rapid heat transfer from the surface to the dielectric. Thus forming a sub-layer and the solidification is delayed for the inner points.

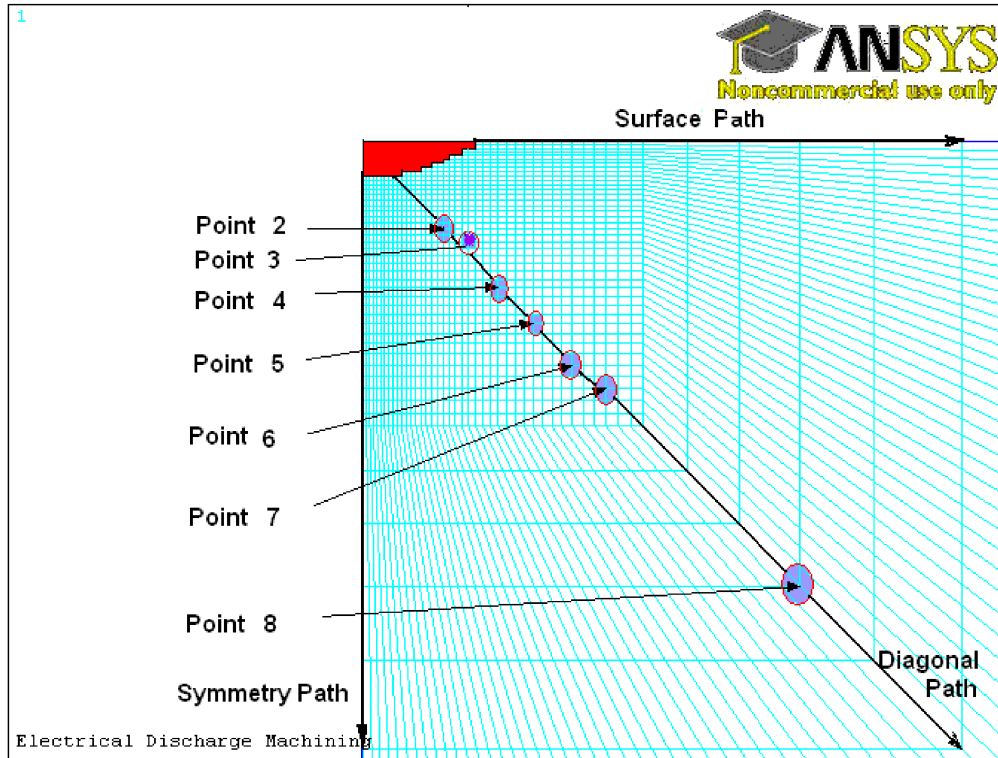


Fig. 4.22: Paths on working domain.

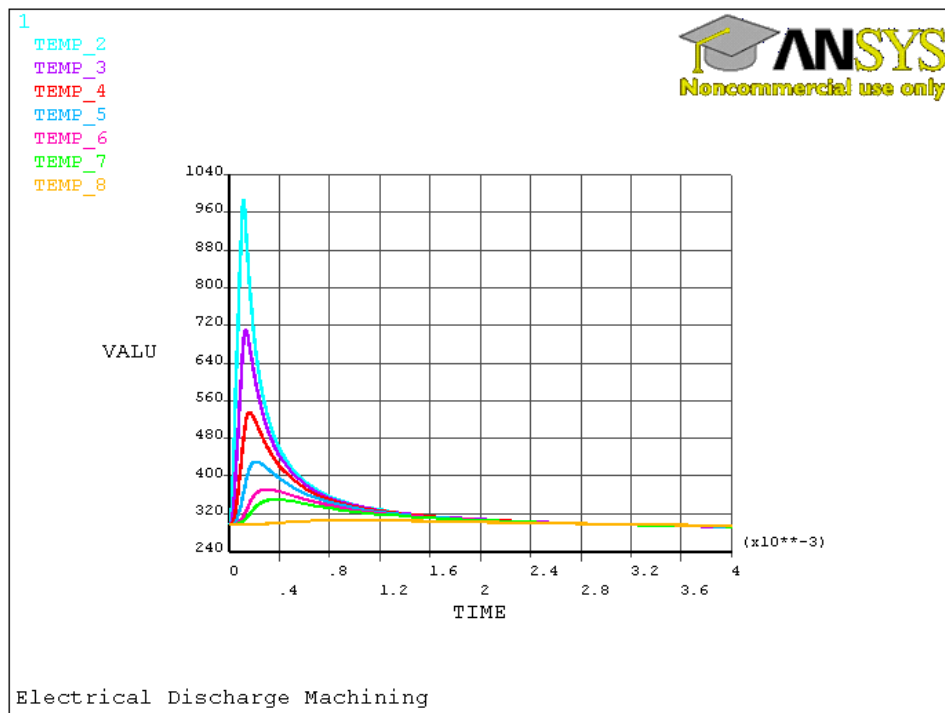


Fig. 4.23: Variation of temperature with respect to time on diagonal path.

#### 4.4.2 Thermal stress distribution

The distinctive stress developed at the end of the heating cycle is known as thermal stress and its distribution in the workpiece for various parametric combinations are discussed. Later on, by varying the two parameters i.e. pulse duration and current, a parametric study of thermal stress is presented in the subsequent section.

Fig. 4.24, Fig. 4.25 and Fig. 4.26 gives a qualitative assessment of the radial component ( $\sigma_{rr}$ ), axial component ( $\sigma_{zz}$ ) and shear component ( $\sigma_{rz}$ ) of the thermal iso-stresses attained, respectively, for  $I_p = 9\text{A}$  and  $T_{on} = 100\mu\text{s}$ . The maximum compressive stresses are located on the surface of the newly created crater and decreases away from the crater radially as well as axially.

The nature of the maximum stress is compressive and it is due to the fact that during the pulse duration, the heat flux supplied to the workpiece for a very short duration (in  $\mu\text{s}$ ). Thus, the area nearer to the spark expands significantly, however the surrounding materials which are not able to expand instantaneously, will restraint them, causing compressive thermal stresses. The radial component is found to be highest amongst them closely followed by axial component and shear component. The radial component of maximum compressive thermal stress obtained is approximately 355 MPa (Fig. 4.24), while the axial component and shear component of the same are approximately 98.3 MPa (Fig. 4.25) and 85.9 MPa (Fig. 4.26), respectively. Yadava et al. (2002) and Salah et al. (2008) had published similar results. In addition, the radial component of maximum tensile thermal stress attain is 46 MPa, axial component is 63.1 MPa and shear component is 52.6 MPa. The maximum tensile stresses attained in the workpiece material are much below the yield strength of the material, thus inhibiting development of cracks in the sub-layers.

The Von Mises thermal stress distribution at the end of heating cycle is shown in Fig.4.27, it can be seen that the stress varies from 0.7 MPa to 316 MPa.

#### 4.4.3 Residual stress distribution

Sharp temperature gradient caused by the rapid thermal cycle at the surface and thermal contraction of re-solidified material on the base material, in conjunction with plastic deformation, results of the formation of tensile residual stress. Residual stress

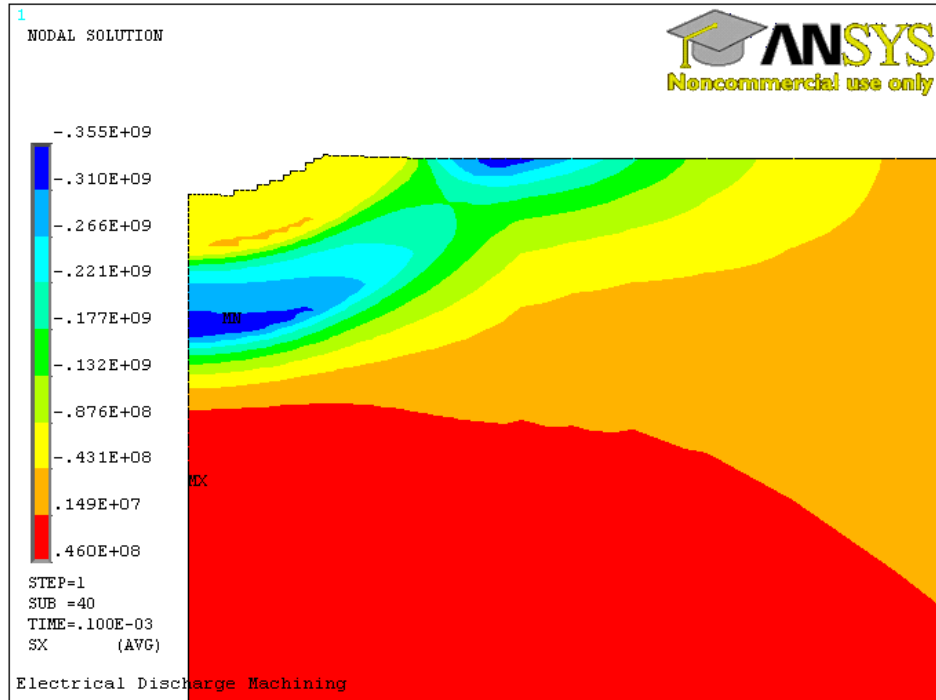


Fig. 4.24: Radial component of thermal stress ( $\sigma_{rr}$ ) at the end of pulse.

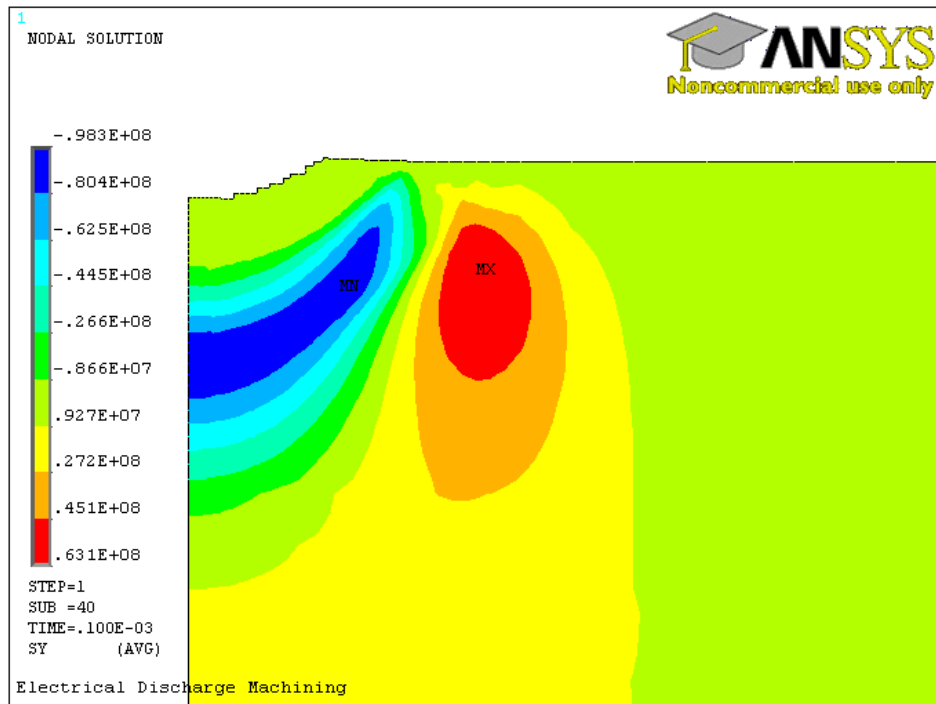


Fig. 4.25: Axial component of thermal stress ( $\sigma_{zz}$ ) at the end of pulse.

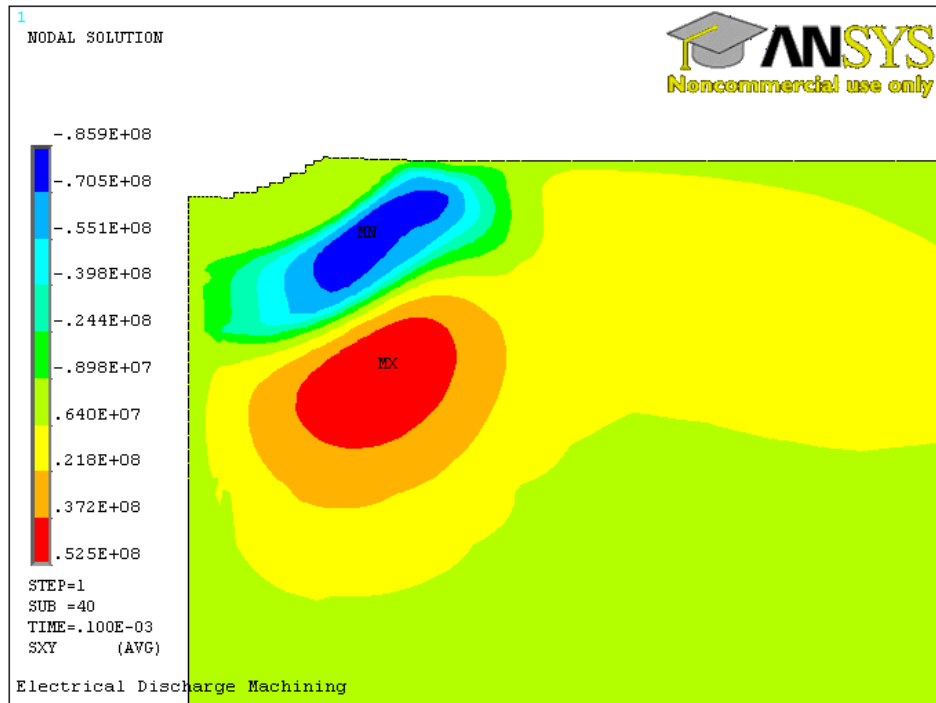


Fig. 4.26: Shear component of thermal stress ( $\sigma_{rz}$ ) at the end of pulse.

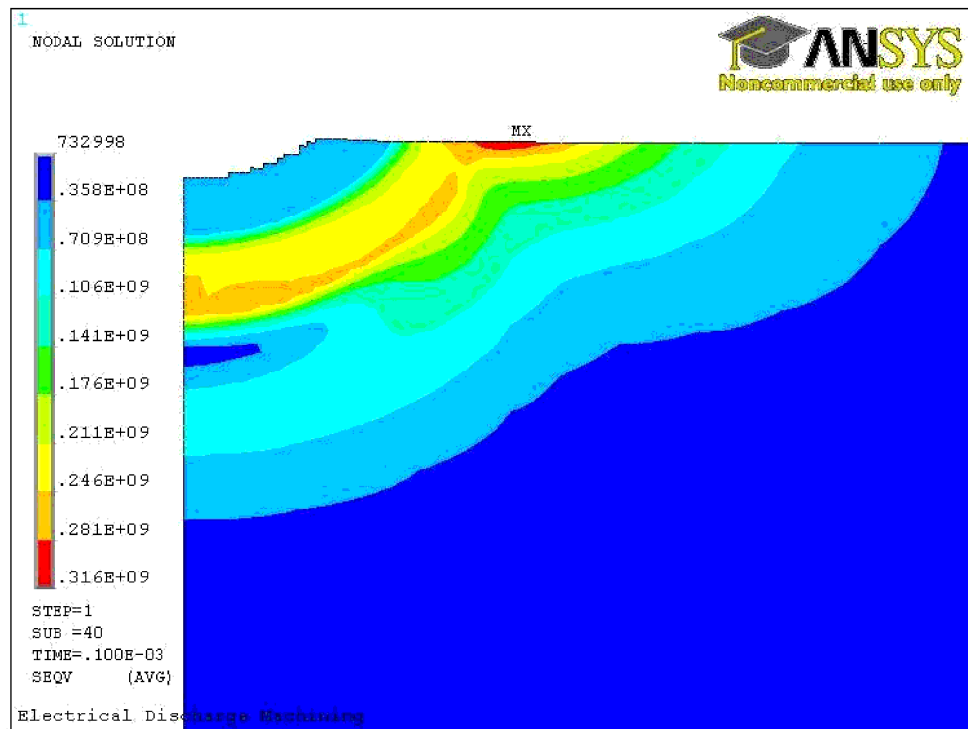


Fig. 4.27: Von Mises thermal stress at the end of pulse.

trend perhaps changed by the metallurgical alteration relating volumetric changes, as it is well known that the martensitic transformation from austenite with a concurrent increase in specific volume of about 3% [Mamalis et al. (1987)]

To understand the nature of residual stress entrapped in the workpiece after machining, the stresses developed at the end of cooling cycle are plotted. Fig. 4.28, Fig. 4.29 and Fig. 4.30 represents the radial, axial and shear components of the residual stress, respectively for  $I_p = 9A$  and  $T_{on} = 100 \mu s$ . It can be noted that the plots represented the state of the workpiece after crater formation, so the graphs profiles are initiated beyond the crater volume.

In Fig. 4.28, the residual stress in the radial direction are illustrated. The compressive stress induced, just beneath the crater, during pulse on time is converted to tensile stress at the end of cooling cycle. With the increasing distance from the crater, the stress decreases and changes to compressive in nature. The maximum radial tensile stress is observed just beneath the crater, attains a maximum value of 670 MPa. However, the minimum value attained is -215 MPa, and both the extreme values are observed along the line of symmetry. Axial and shear component of residual stresses are found to be comparatively small, although the stress patterns are found to be quite analogous to radial component. The maximum value of 236 MPa and 171 MPa, and minimum value of -122 MPa and -129 MPa are observed, for the axial and shear components of residual stress, respectively .

For clear visualisation of these stress variation at different section along the three paths are plotted (Fig. 4.22). Finite element analysis of EDM machining results of the radial, axial and shear components of residual stresses on these paths are depicted in Fig. 4.32, Fig. 4.33 and Fig. 4.34, respectively. It is clear from these figures that the radial component of residual stresses are dominant. As the surface path rotates towards the axis of symmetry, the axial component of residual stress gradually increases. The shear component increases to maximum along diagonal path and diminishes as it reaches the symmetry path. However, the radial component does not change much for these three paths.

The Von Mises residual stress distribution at the end of cooling cycle is illustrated in Fig.4.31, it can be seen that the stress increases from 1 MPa to 549 MPa, when

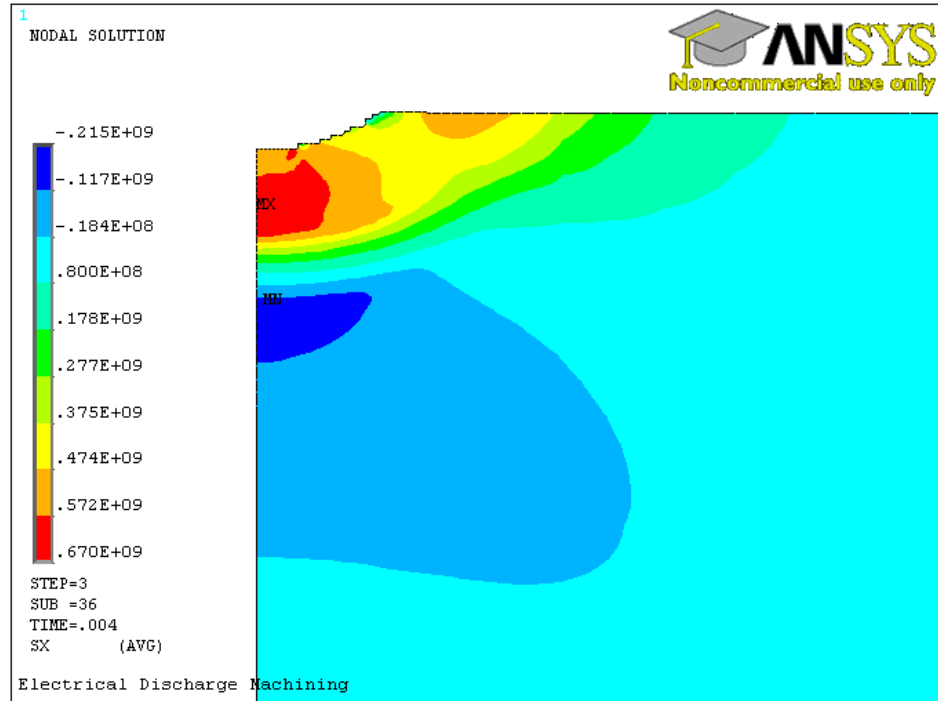


Fig. 4.28: Radial component of residual stress ( $\sigma_{rr}$ ) at the end of pulse period.

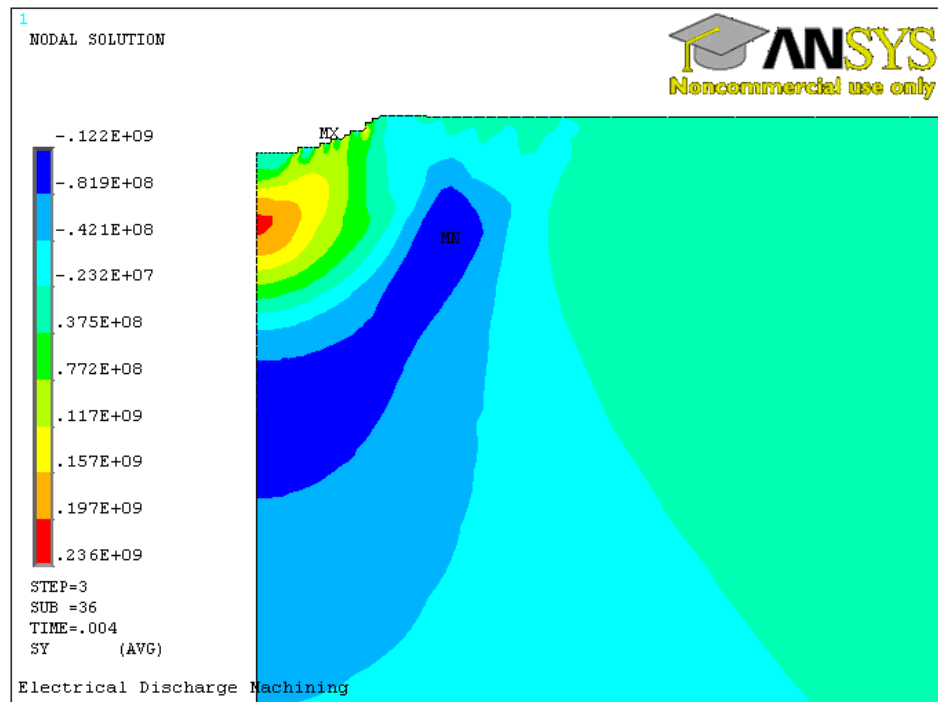


Fig. 4.29: Axial component of residual stress ( $\sigma_{zz}$ ) at the end of pulse period.

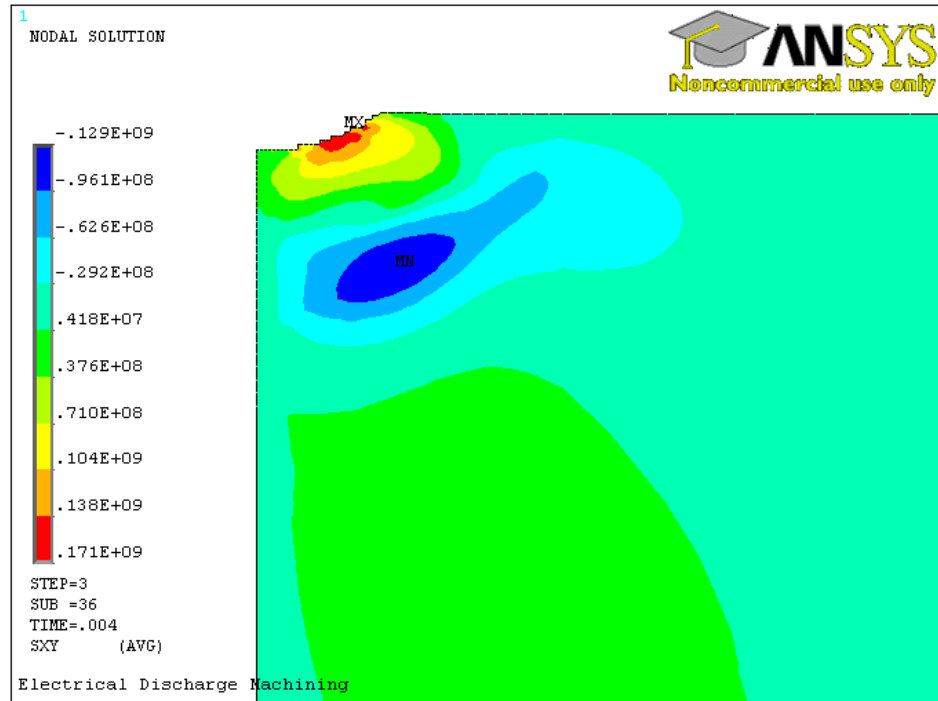


Fig. 4.30: Shear component of residual stress ( $\sigma_{rz}$ ) at the end of pulse period.

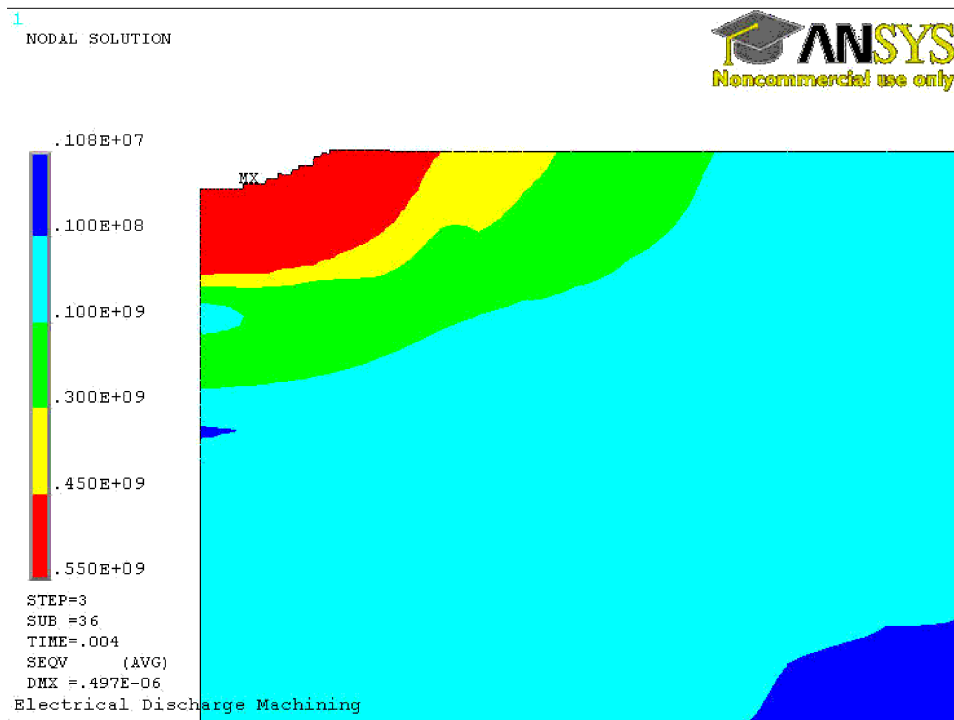


Fig. 4.31: Von Mises residual stress at the end of pulse period.



moved towards the crater. The iso stress lines are almost parallel and having the shape of the crater. At room temperature (300 K) the yield stress is 450 MPa, and hence the region at about  $42.2 \mu\text{m}$  depth yields, which is shown in Fig. 4.31 for  $I_p=9$  A and  $T_{on}=100 \mu\text{s}$ . These stresses are predominately tensile and on yielding sub surface cracks are developed. Similar, observations are made for various  $I_p/T_{on}$  parameter combinations 1/20, 1/100 and 9/20 and are found to be 11.5, 16.6, and  $23.06 \mu\text{m}$ , respectively.

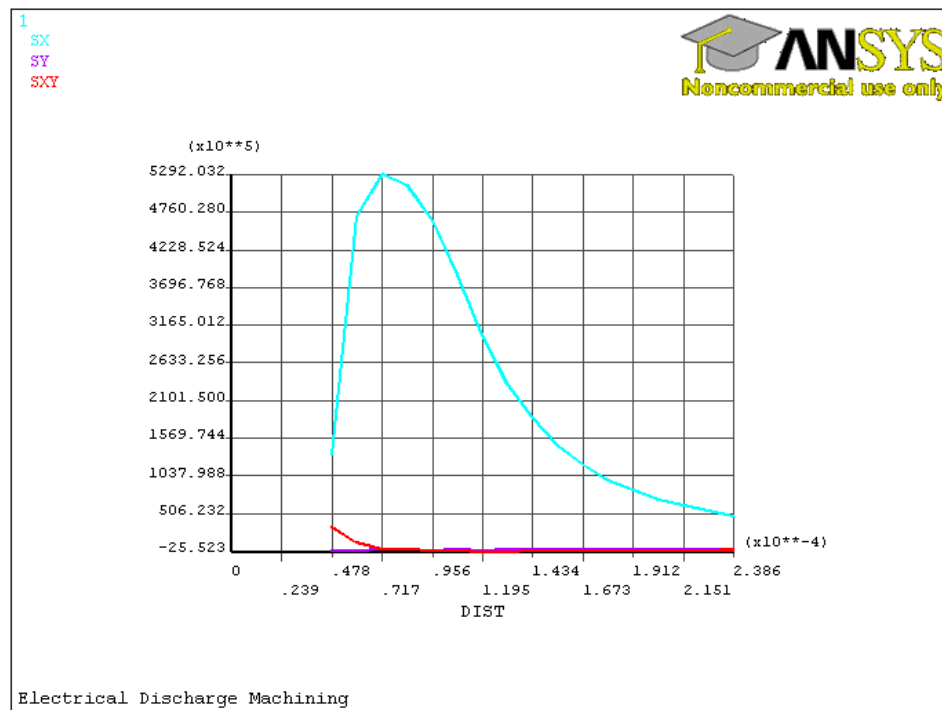


Fig. 4.32: Residual stresses on surface path.

#### 4.4.4 Effect of machining parameters on Temperature profile

The variation of temperature along the line of symmetry with respect to the depth of the workpiece has been presented before material ejection in this section for different pulse current and pulse duration. The peak temperature and its distribution depends upon the amount of spark energy supplied to workpiece and hence the pulse current and pulse duration has an significant impact on the temperature profile which are explained in the subsequent section.

Effect of current: The variation of temperature at the end of spark with depth of

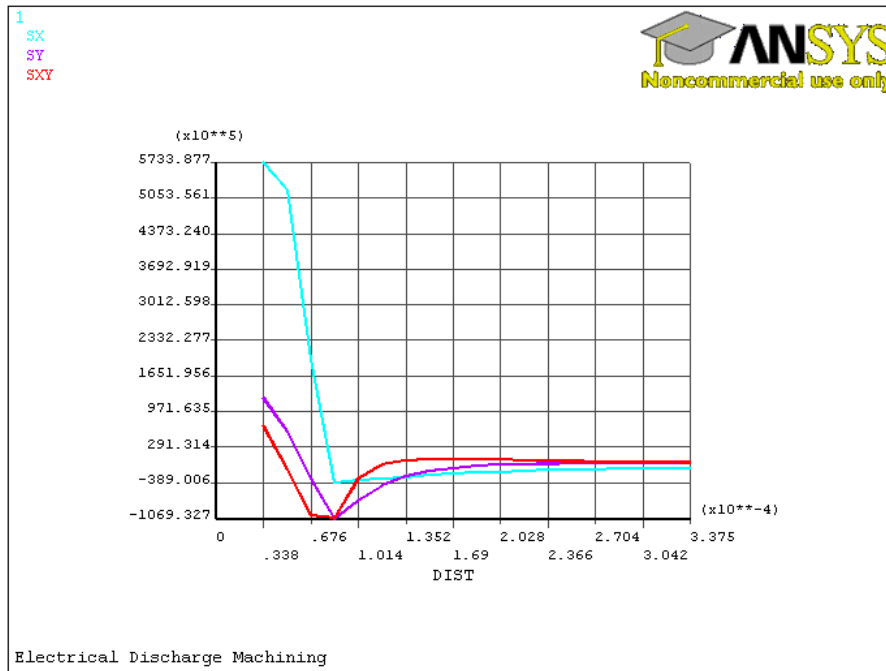


Fig. 4.33: Residual stresses on diagonal path.

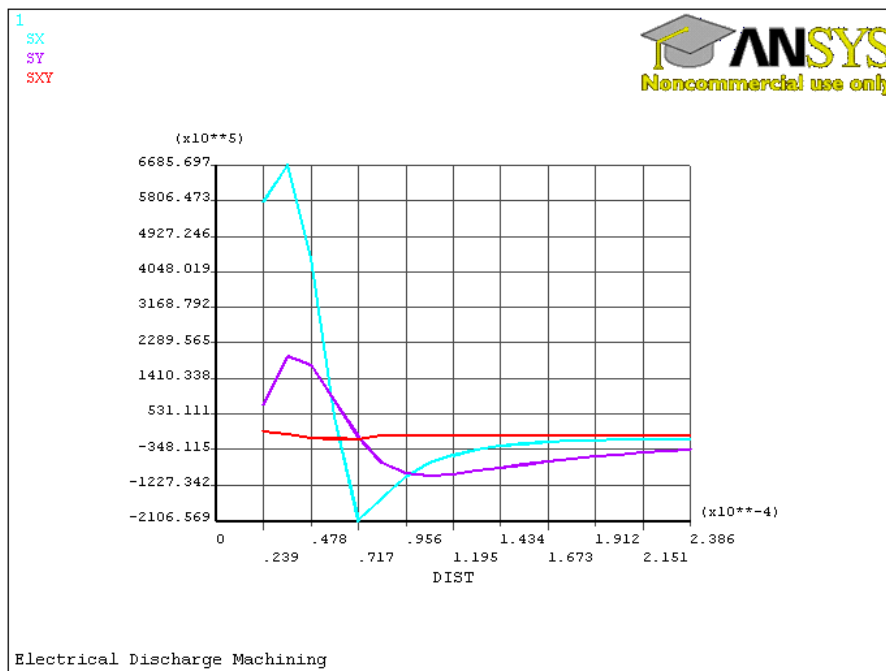


Fig. 4.34: Residual stresses on symmetry path.

the workpiece has been plotted for two different  $I_p$  and presented in Fig. 4.35. From these plots, it can be observed that with the increase in  $I_p$  the peak temperature goes on increasing. This is due to the fact that, with the increase in  $I_p$  the magnitude of the heat energy transferred to the workpiece increases. From the figure, it is observed that temperature shows inverse exponential relation with respect to the axial distance.

Effect of pulse duration: In Fig. 4.36, the effect of pulse duration is presented along the depth for  $I_p = 9A$  for  $T_{on} = 20 \mu s$  and  $100 \mu s$ . It could be noted that if  $T_{on}$  is higher, the spark radius  $R$  will also be larger and the heat will be distributed to a larger area, (as the plasma channel becomes wider with increase of  $T_{on}$ , the heat flux distribution becomes less steep), which may not produce the higher peak temperature, but will remove more material. In Fig. 4.36 presented, it can be clearly seen that the profile of  $T_{on} = 100 \mu s$ , though more heat is produced, but the peak temperature approaches 4000K. However, the profile of  $T_{on} = 20 \mu s$  with lower heat supplied to a radius of  $75 \mu m$  for a very short time, thus produces a peak temperature of slightly higher than 4000K. This may be attributed to, though less amount of heat is produced for  $T_{on} = 20 \mu s$ , it is concentrated to a smaller area that produces slightly higher peak temperature than that for larger  $T_{on}$ .

#### 4.4.5 Effect of machining parameters on thermal stress

It is believed that the Gaussian heat distribution is closest to the real life situation and FEM results show steep temperature gradient within the spark radius. These steep gradients are considered to be the main source of induced thermal stresses in the workpiece that are developed just after the material ejection.

Fig.4.37 corresponds to the nature of the thermal stress variation in radial direction along the centreline of workpiece. The machining conditions are stated in the plot. It can be noted that the thermal stresses obtained near the crater are compressive in nature for all cases with the maximum value -348 MPa for  $I_p = 1A$  and  $T_{on} = 20 \mu s$ . This stress gradually becomes tensile and then asymptotically become stress free with increasing depth. The trend of thermal stresses with other machining parameter setting are similar in nature and are tabulated in Table 4.6.

It can be clearly noticed that the profile is shifting outwards, i.e., depth where

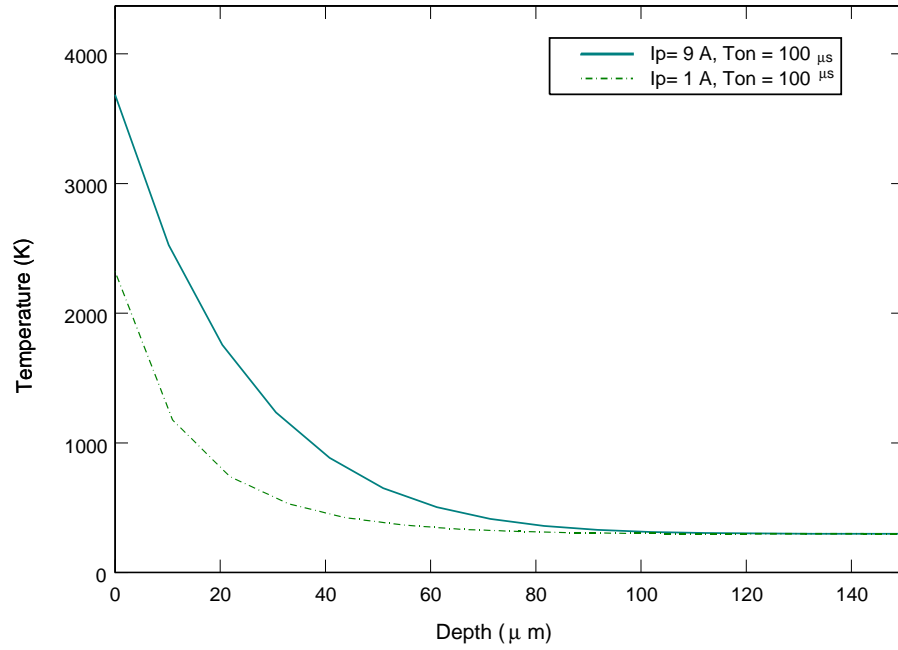


Fig. 4.35: The effect of  $I_p$  on the temperature variation with depth for  $T_{on}=100\mu\text{s}$

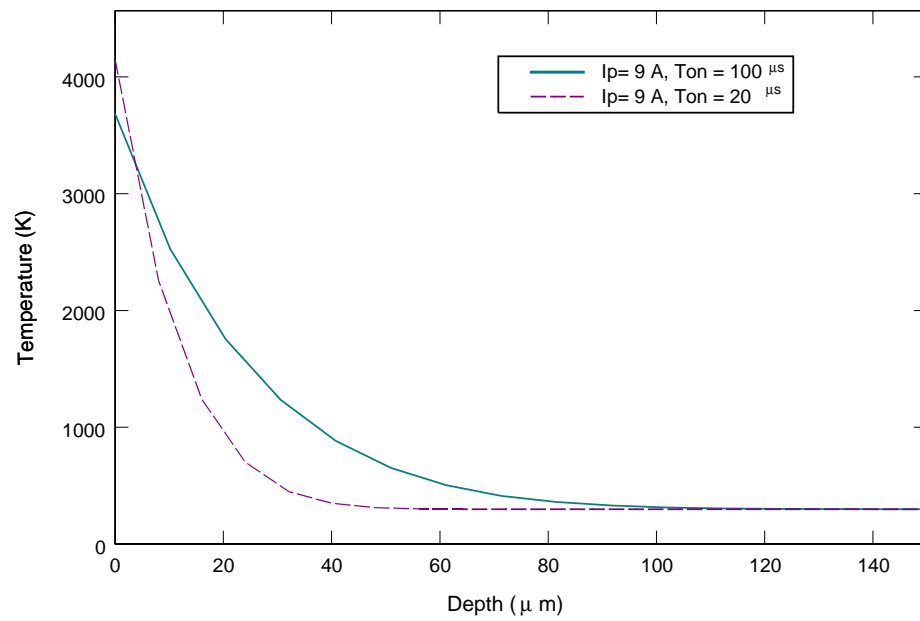


Fig. 4.36: The effect of  $T_{on}$  on the temperature distribution for  $I_p=9\text{A}$

the maximum compressive stress occur varies from 7.59  $\mu\text{m}$  to 16.05  $\mu\text{m}$  for 20  $\mu\text{s}$  and from 10.95  $\mu\text{m}$  to 40.78  $\mu\text{m}$  for 100  $\mu\text{s}$ . It can be inferred that as the spark energy increases with the increase in  $I_p$ , a higher temperature gradient is produced, so the heat flux can penetrate to more depth causing more HAZ. Similar trend is also observed for  $T_{on}$  (corresponding depth varies from 7.59  $\mu\text{m}$  to 10.95  $\mu\text{m}$  for 1 A and 16.04  $\mu\text{m}$  to 40.78  $\mu\text{m}$  for 9A) where with the increase of pulse on time, the stresses are induced deeper into the workpiece. Fig.4.38 represents the thermal stress directly following the heat flux in axial direction. Similar trend has been observed for the thermal stress distributions in radial direction. The maximum compressive stresses are located on the surface of the newly created crater and the magnitude is comparatively low. Also, with the increase in  $I_p$  from 1A to 9A the depth at which maximum thermal stress occurs increases from 30.33 to 48.11  $\mu\text{m}$  and 43.79 to 122.92  $\mu\text{m}$  for 20  $\mu\text{s}$  and 100  $\mu\text{s}$ , respectively. Similarly, with the increase of  $T_{on}$  from 20  $\mu\text{s}$  to 100  $\mu\text{s}$  the depth of maximum thermal stress increases from 30.33 to 43.79  $\mu\text{m}$  and 48.11 to 122.92  $\mu\text{m}$  for 1A and 9A, respectively, confirming the claim that with the increase in both  $I_p$  and  $T_{on}$ , the depth of maximum thermal stress increases. The shear stress  $\sigma_{rz}$  in the line of symmetry is found to be zero.

#### 4.4.6 Effect of machining parameters on residual stress

Investigating the plot in Fig. 4.39 minutely, it is found that radial components of the residual stresses in EDM are predominantly tensile in nature. The magnitude increases from the top surface to its maximum value which is approximately equal to 600 MPa. It is very interesting to observe that the magnitudes of the residual stress for all four cases are found to be almost equal. Thus, it can be concluded from this observation that the intensity of the peak stresses are found to be unaffected with respect to the magnitude of the spark energy produced. This peak intensity of the stress indicates the hot strength of the material machined. However, it is observed that as the spark energy increases, the depth at which the residual stress reaches its maximum, is found to be increase. Subsequently, the residual stress falls rapidly to fairly low value of compressive stress (Table 4.6).

Fig. 4.40 illustrates the residual stress in the axial direction. Around the crater,

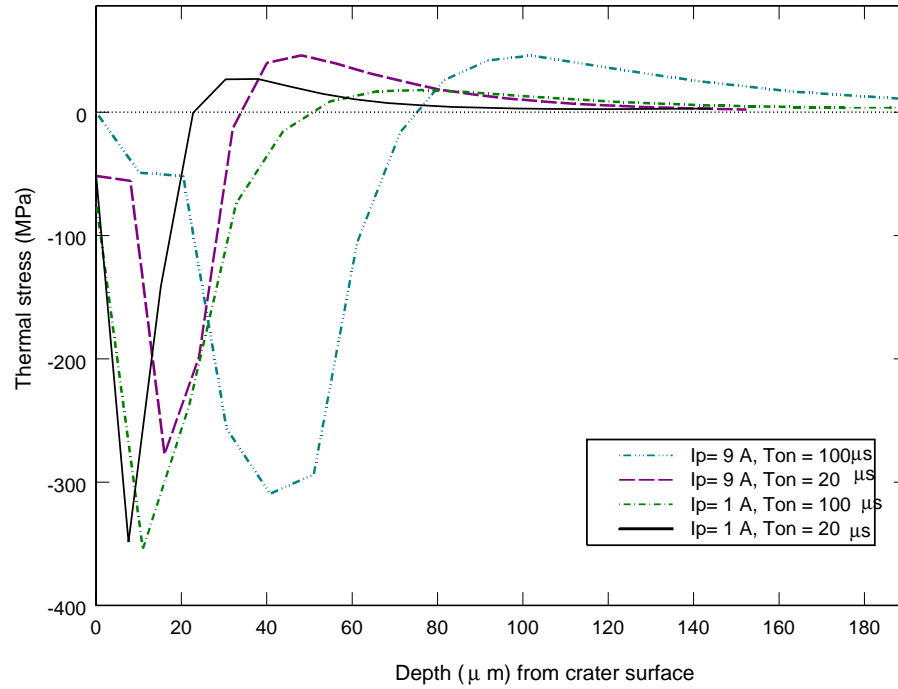


Fig. 4.37: Effect of  $I_p$  and  $T_{on}$  on thermal stress in radial direction along the centreline of workpiece.

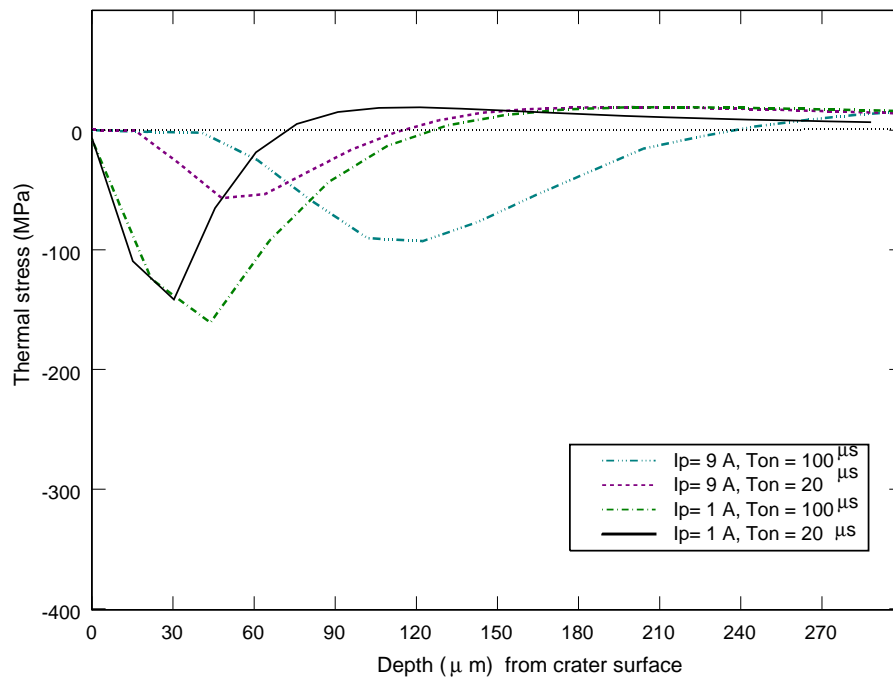


Fig. 4.38: Effect of  $I_p$  and  $T_{on}$  on thermal stress in axial direction along the centreline of workpiece.

tensile stresses are present, but they are not as large as those beneath the adjacent surface. These stresses reach a maximum value and then gradually decrease as the depth increases and become compressive in nature. On further increase of depth, these stresses asymptotically diminish to a zero value. Similar trend is obtained in Fig. 4.41 for shear stress. The magnitudes of shear residual stress are found to be in the range of approximately 10 MPa.

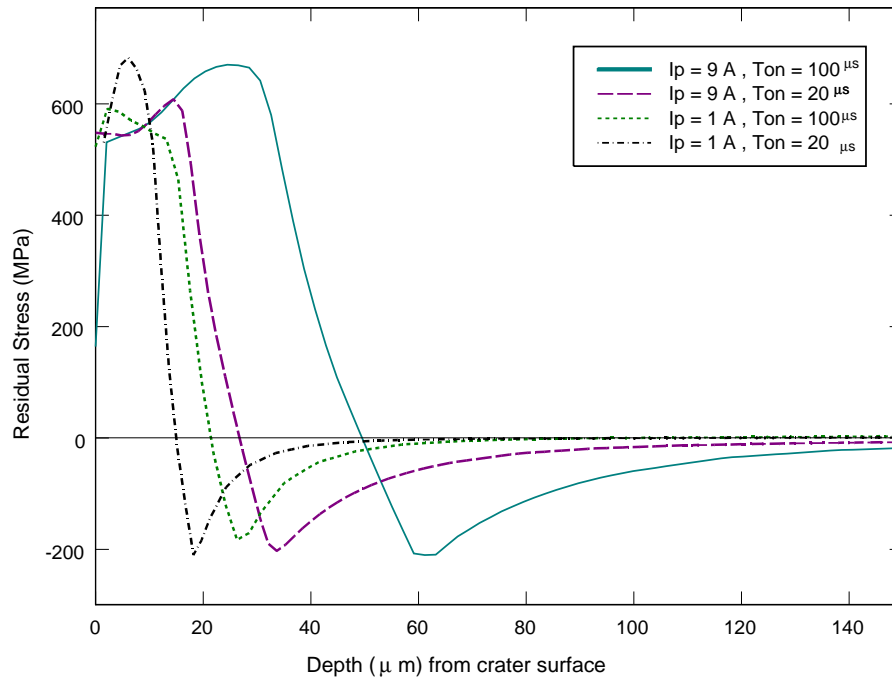


Fig. 4.39: FEA residual stress in radial direction ( $\sigma_{rr}$ ) along symmetric path

#### 4.4.7 Experimental Validation of residual stress

In Fig. 4.42, the graph shows the experimental results on residual stress ( $\sigma_\phi$  in Table 4.5) plotted along the depth of the workpiece. The 95% confidence interval is shown by the error bar on the experimental value. The effect of  $I_p$  and  $T_{on}$  are clearly indicated. The magnitude of peak of the residual stresses increases with increase both  $I_p$  and  $T_{on}$ . The experimental results show that there is a considerable rise in the residual stress as  $I_p$  or  $T_{on}$  increases resulting in a greater peak. With an increase of  $I_p$  from 1 A to 9 A at  $T_{on} = 100 \mu s$  the maximum residual stress increases from 588 MPa to 812 MPa, however, when  $T_{on}$  increases from 20 to 100

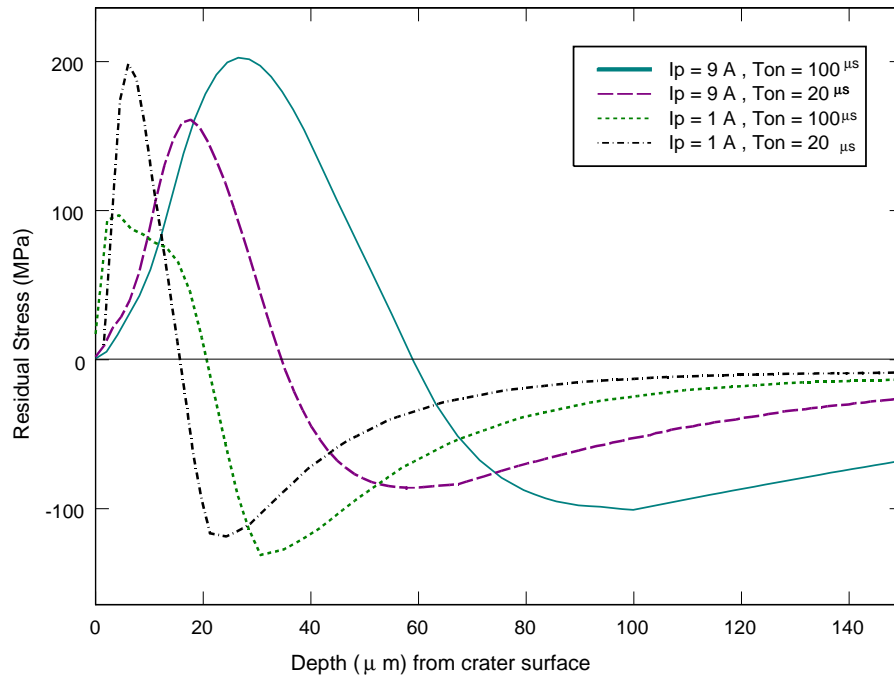


Fig. 4.40: FEA residual stress in axial direction ( $\sigma_{zz}$ ) along symmetric path.

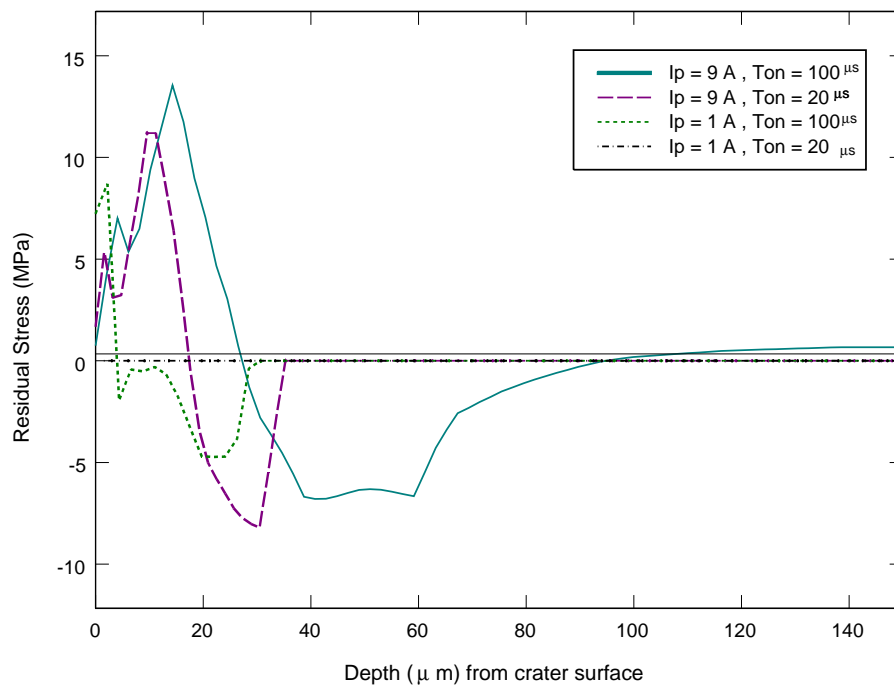


Fig. 4.41: FEA residual shear stress ( $\sigma_{rz}$ ) along symmetric path.



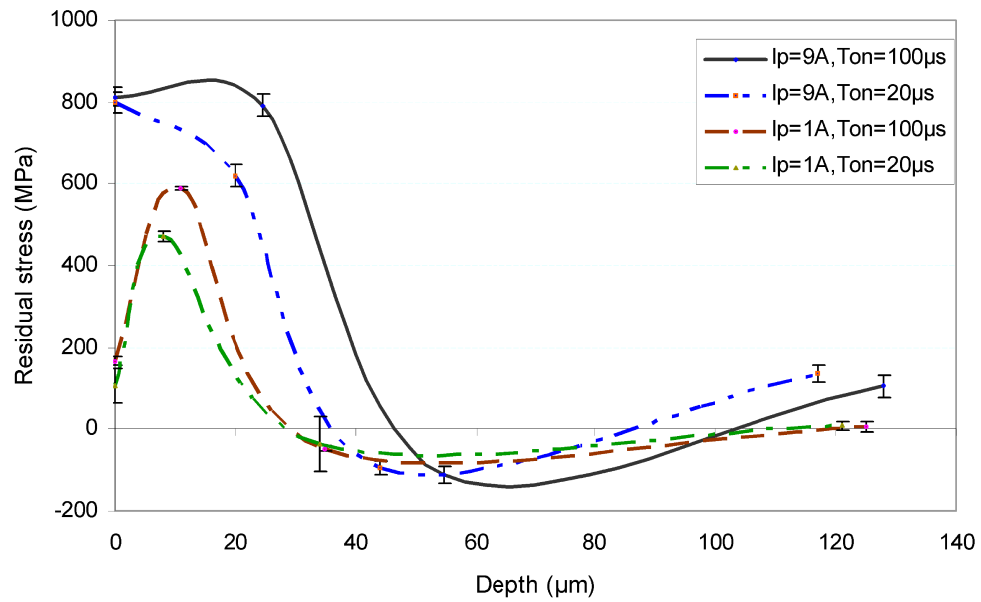


Fig. 4.42: Experimental residual stress in radial direction ( $\sigma_{rr}$ ) along symmetric path.

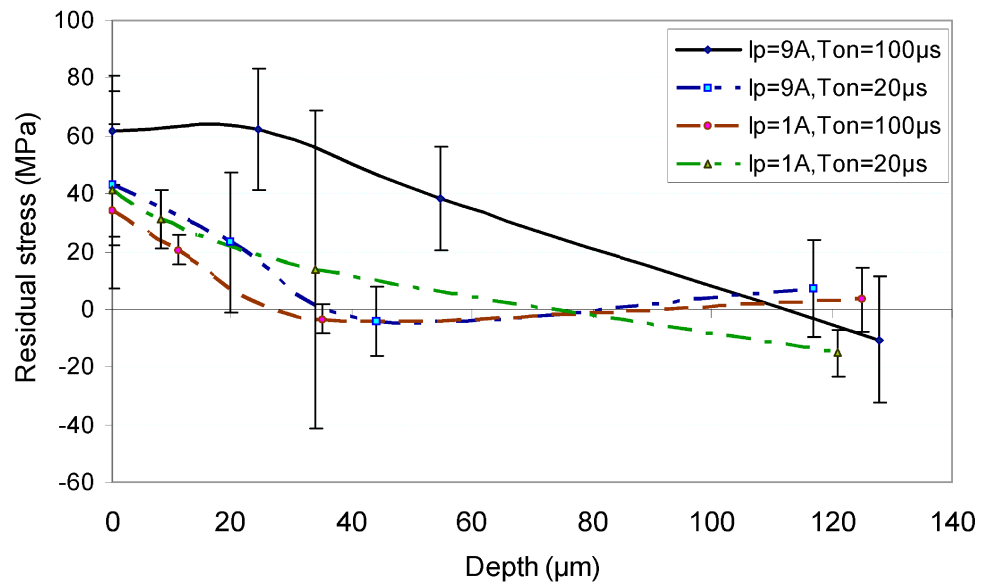


Fig. 4.43: Experimental residual shear stress ( $\sigma_{rz}$ ) along symmetric path.

at 1A it increases from 478 to 588 MPa and at 9 A it increases from 797.9 to 812 MPa (Table 4.5). Hence it can be seen that though residual stress increase by both of the factors but the effect of  $I_p$  is more prominent than  $Ton$ . The residual stresses entrapped on the surface are well agreeing with those results of Guu et al. (2003), however, for  $I_p=1$  A the values are slightly less while that of  $I_p=9$ A are higher. Consequently, the degree of the stimulated residual stress can be restricted efficiently by identifying a proper  $I_p$  and  $Ton$  value.

The experimental results show that the stress levels reaches its maximum values close to the surface, but diminish very rapidly in the sub-surface area, which is analogous with the FEM simulation results. Even though the magnitude of stresses do not match exactly with FEM results the nature of the stress variation along the depth is similar. This discrepancy is obvious because the simulation results are obtained for a single spark model, whereas, the experimental observations are for an EDMed surface which has been expose to multiple sparking. Once cracks occur, they reduce the stress level in the neighbourhood and work as stress relieving mechanism. Hence, the actual stress level of recast portion of the material differs from FEM analysis.

Fig 4.43 presents the residual shear stress ( $\sigma_{rz}$ ) along the symmetry path, obtained experimentally. It can be seen that these stresses are small when compared with the radial stresses component. The error in the estimation of these stresses are exceptionally large to make any inference on the impact of machining parameters.

Fig. 4.44 shows the graphical plot of the effects of the factors  $I_p$  and  $Ton$  on the peak residual stress measured experimentally and the depth where it occurs. As it can be noticeably distinguished in the graph that as  $I_p$  and  $Ton$  increase from the lower to higher level, there is a significant increase in peak tensile residual stress and the corresponding depth where it occurs.

## 4.5 Conclusion

In the present study, a two-dimensional axisymmetric model was developed to predict the EDM characteristics such as temperature, thermal and residual stresses. For the development of the model, AISI D2 steel was chosen and well-known finite element commercial software ANSYS 12.0 was used to simulate the effects of a single spark.

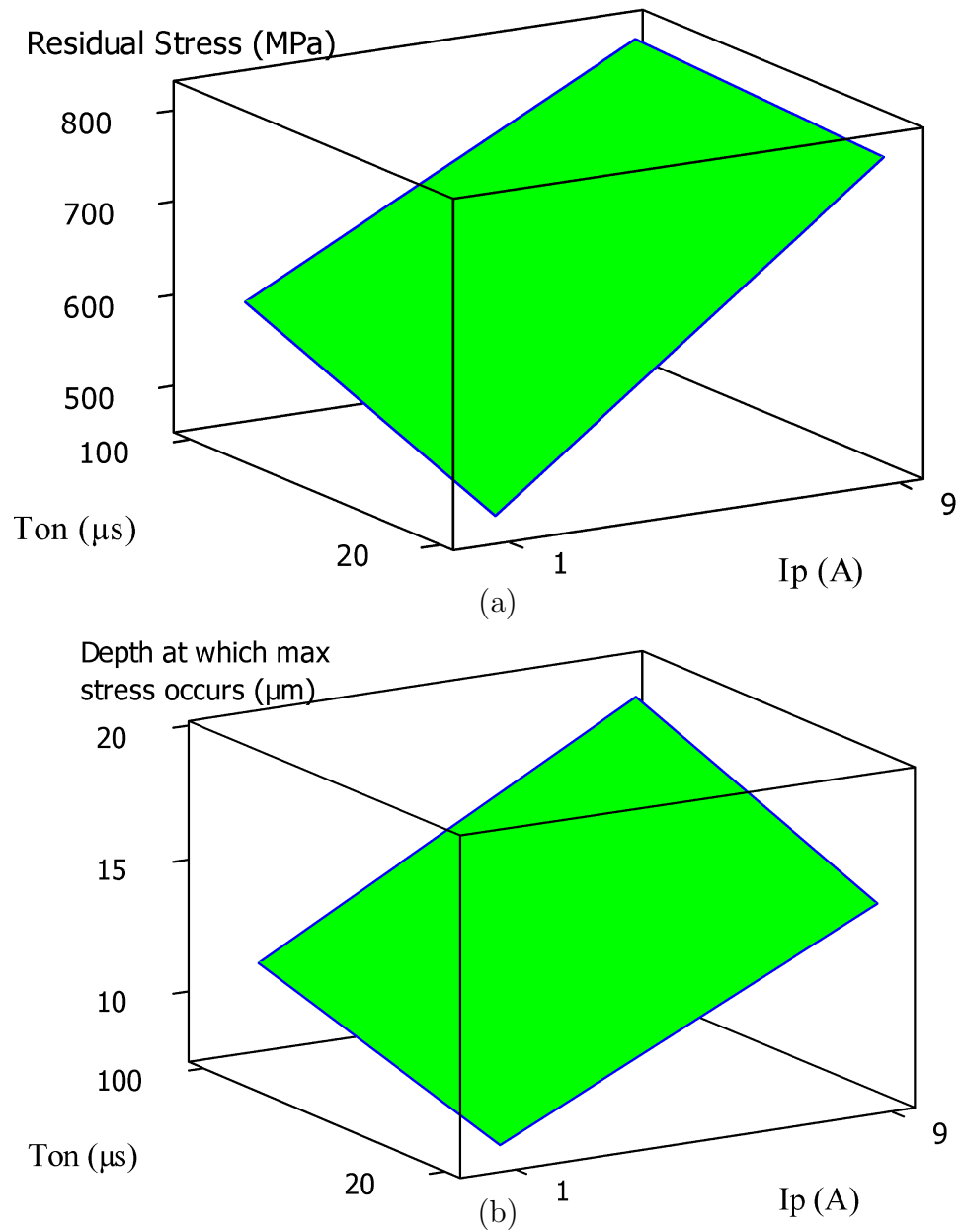


Fig. 4.44: Effect of  $I_p$  and  $T_{on}$  on (a) peak Tensile residual stress (b) Depth at which it occurs ( $\mu m$ ).

Table 4.6: Peak thermal and residual stress from FEM

Stresses	$I_p$ (A)	$T_{on}$ ( $\mu s$ )	Radial		Axial	
			depth( $\mu m$ )	Stress (MPa)	depth( $\mu m$ )	Stress(MPa)
Thermal	9	100	40.78	-309.34	122.32	-92.87
		20	16.04	-277.48	48.11	-56.91
	1	100	10.95	-354.52	43.79	-160.84
		20	7.59	-384.62	30.33	-141.62
Residual Tensile	9	100	24.47	670.17	26.5	202.63
		20	14.48	608.00	17.68	161.00
	1	100	2.19	590.71	4.38	96.90
		20	6.06	682.89	6.06	198.42
Residual Compressive	9	100	61.16	-210.30	99.09	-100.84
		20	33.68	-203.00	63.10	-86.00
	1	100	26.27	-183.13	30.65	-131.13
		20	18.20	-210.30	24.26	-118.66

The important features of the process such as temperature-dependent material properties, shape and size of heat source (Gaussian heat distribution), percentage fraction of heat contribution to the workpiece, pulse on/off time, material ejection fraction are taken into account in the development of the model. The temperature profiles and material transformations that occur in the workpiece material due to high temperature, deformations and transient operation are analysed. In this analysis it is assumed that 50% of the molten material is ejected from the material and rest is recast on the workpiece. There is a sharp temperature rise during the heating cycle and then it falls rapidly during quenching. It is observed that the compressive thermal stresses are developed beneath the crater and the tensile stresses occur away from the axis of symmetry. FEM results show that the peak temperature on the surface sharply increases with pulse current, whereas it is slightly more with lower pulse on time than that with higher pulse on time. The workpiece is severely affected by the thermal stresses to a larger depth with increasing pulse energy. The nature of residual stresses is predominantly tensile. It is very interesting to observe that the magnitudes of the radial component of the residual stresses acquired from FEM are dominant than other components for all the machining parameter combinations. The axial component of residual stress is minimum on the surface path and increases

---

as the path rotates towards the axis of symmetry. Von Mises residual stress show that the workpiece yields upto a depth of 11.5, 16.6, 23.06 and 42.2  $\mu\text{m}$  for 1/20, 1/100, 9/20 and 9/100 discharge current/ pulse on time parameter combinations, respectively. The experimental results shows that the stress levels reach its maximum values close to the surface, but diminish very rapidly to comparatively low values of compressive residual stresses in the sub-surface area. The trend of these stresses with depth has an excellent agreement with theoretical results. The magnitudes of the maximum tensile and compressive residual stresses are not effected by pulse energy, but the depth at which they occur, increases with the pulse energy. However, the shape of the graph of residual stress versus depth does not change with the machining parameters, in general.

# Chapter V

Soft computing models based  
prediction of MRR, TWR &  
Overcut

## 5. SOFT COMPUTING MODELS BASED PREDICTION OF MRR, TWR AND OVERCUT

### 5.1 *Introduction*

For last six decades, electrical discharge machining has been providing inimitable capabilities to machine “difficult to machine” materials with desire shape, size, and required dimensional accuracy. It has been successfully applied for machining in the advance industries like automotive, medical, aerospace, consumer electronics and optoelectronic industries development. In the past, there has been considerable improvement in EDM technology to enhance productivity, accuracy, and the versatility of the process. The major concern in the active research is to decide the optimal setting of the process parameters in such a way that material removal rate (MRR) and accuracy increases; and concurrently overcut (OC) or gap (G), tool wear and surface roughness should diminish.

A process can be understood better when a model reflects its behavior by its essential parameters. The factors that are important for the system are to be identified and different aspects of the process to be related while building the model. It is expensive, impractical or impossible to experiment directly with the process so a good model can be cost effective to predict the actual process very closely.

In this chapter, the focus is on the development of two neuro fuzzy models; Mamdani and Sugeno systems along with an ANN model for prediction of MRR, TWR and G in EDM process. There are a large number of factors to be considered for EDM process, so based on experience and literatures on EDM research and the working characteristics of the machine, the prime parameters chosen, in the present chapter, are discharge current, spark on-time, duty cycle (as given in Equation 1.1) and discharge voltage. The motivation, why these factors have been select is that these are often used among EDM researchers Dhar et al. (2007), Kung et al. (2009), Doniavi

et al. (2008) and Sohani et al. (2009) for the said responses and are found significantly influencing them. Extensive experiments were conducted by the author, and the proposed models used the experimental data on EDMed AISI D2 tool steel. The performances of the developed models are compared. Such a study would help in developing an appropriate model for simulation of the EDM process.

## 5.2 Description of the experiments

### 5.2.1 Equipment and workpiece material

A series of experiments were performed on a CNC electrical discharge die sinking machine using a cylindrical pure copper (99.9% Cu) as a tool electrode with a diameter of 30 mm and AISI D2 workpiece of diameter 100 mm and 10 mm thick (Fig. A.3). Commercial grade EDM oil was used as dielectric fluid, the power supply was linked with the tool electrode (tool: positive polarity, workpiece: negative polarity). A lateral flushing system was employed for effective flushing of machining debris from the working gap region with a pressure of  $0.4 \text{ kgf/cm}^2$ .

### 5.2.2 Experimental procedure

The workpiece was initially circular bar of diameter 100 mm and were cut into specimens of thickness 10 mm by a silicon carbide disc. The top and bottom faces of the workpiece were ground to make it flat and good quality surface finish prior to experimentation. The bottom of the cylindrical electrode was polished by a very fine grade emery sheet prior to every experimental run. Each treatment of the experiment was run for 15 minutes and the time was measured with a stopwatch of with an accuracy 0.1 s. The workpiece as well as the tool were detached from the machine, cleaned and dried up, to make it free from the dirt, debris and dielectric. They were weighed, before and after machining, on a precision electronics balance (Fig. A.5). The diameter of the cavity machined on workpiece was measured by a tool maker microscope (Fig. A.8) with an accuracy of  $1 \mu\text{m}$ .

### 5.2.3 Machining performance evaluations

- **Material Removal Rate**



MRR is calculated by using the volume loss from the workpiece divided by the time of machining. The calculated weight loss is converted to volumetric loss in  $mm^3/min$  as per Equation 5.1.

$$MRR = \frac{\Delta V_w}{t} = \frac{\Delta W_w}{\rho_w t} \quad (5.1)$$

where  $\Delta V_w$  is the volume loss from the workpiece,  $\Delta W_w$  is the weight loss from the workpiece,  $t$  is the duration of the machining process, and  $\rho_w = 7700 \text{ kg/m}^3$  the density of the workpiece.

- **Tool Wear Rate**

TWR is expressed as the volumetric loss of tool per unit time, expressed as

$$TWR = \frac{\Delta V_t}{t} = \frac{\Delta W_t}{\rho_t t} \quad (5.2)$$

where  $\Delta V_t$  is the volume loss from the electrode,  $\Delta W_t$  is the weight loss from the electrode,  $t$  is the duration of the machining process, and  $\rho_t = 8960 \text{ kg/m}^3$  the density of the electrode.

- **Radial Overcut or Gap (G)**

$G$  ( $\mu\text{m}$ ) is expressed as half the difference of diameter of the hole produced to the tool diameter, that is

$$G = \frac{(d_i - d_t)}{2} \quad (5.3)$$

where  $d_t$  is the diameter of the tool and  $d_i$  is the diameter of the impression or cavity produce by the tool on the workpiece.

### 5.2.4 Experimental design and parameter selection

Full factorial design is the usually adopted for designing an experiment in which all possible combinations of factors and their levels are considered. However, if the levels are different, a mixed level factorial designs are generally implemented. In this work, the process parameters,  $I_p$  and  $T_{on}$  are assigned with five levels, where as  $Tau$  and  $V$  are with three and two levels, respectively, yielding a total of 150 ( $= 5^2 \times 3^1 \times 2^1$ ) experiments (see Appendix B). The experimental condition are shown in Table 5.1. To eliminate the consequence of unaccounted factors on the responses the experiments were carried out in random order. The responses MRR, TWR and G has been observed for each experiments and the results obtained through a series of experiments for various sets of parametric combinations as planned have been exhibited in Table 5.2. The outcome of this factorial design facilitate to approximate all the main effects and their second order interactions in this research.

Table 5.1: Experimental conditions

Parameters	Units	Notations	Levels				
			1	2	3	4	5
Discharge Current	A	$I_p$	4	7	10	13	16
Pulse on Time	$\mu s$	$T_{on}$	100	200	300	400	500
Duty Cycle %	-	$Tau$	80	85	90		
Discharge Voltage	volt	$V$	40	60			
Dielectric used			Commercial grade EDM oil				
Dielectric flushing			Side flushing with pressure				
Work material			AISI D2 steel				
Electrode material			Electrolytic pure Copper				
Electrode polarity			Positive				
Work material polarity			Negative				

Table 5.2: Observations for MRR, TWR and G.

Run Order	$I_p$ A	$T_{on}$ $\mu s$	$Tau$ %	$V$ volt	MRR $\frac{mm^3}{min}$	TWR $\frac{mm^3}{min}$	G $\mu m$	Data Type*
1	10	400	85	40	25.545	0.030	0.210	Te
2	13	400	90	60	40.260	0.032	0.310	Te
3	16	400	85	60	40.494	-0.011	0.260	V
4	16	500	80	60	31.130	0.011	0.290	Tr
5	16	300	80	60	32.660	0.089	0.260	Te
6	13	200	80	60	27.234	0.301	0.210	Tr
7	7	100	80	40	14.500	0.190	0.100	Tr
8	10	400	90	40	29.065	0.011	0.220	Tr
9	4	100	90	60	6.870	0.089	0.005	Te
10	10	500	80	60	15.597	0.002	0.190	Te
11	16	200	90	60	48.290	0.491	0.280	Tr
12	4	100	90	40	8.221	0.045	0.010	Te
13	7	400	80	60	7.230	0.011	0.132	Te
14	16	200	80	40	39.560	0.636	0.270	Te
15	7	400	90	40	13.701	0.011	0.130	Tr
16	7	200	85	60	13.078	0.080	0.120	Tr
17	4	500	85	40	2.156	0.000	0.120	Te
18	10	100	85	40	28.080	0.569	0.150	Te
19	10	100	90	60	26.662	0.647	0.160	Tr
20	13	300	90	60	41.110	0.112	0.300	V
21	10	300	90	60	24.896	0.056	0.230	Tr
22	16	500	90	60	46.494	0.040	0.350	Te
23	13	100	85	40	40.920	0.982	0.190	Tr
24	10	200	80	40	22.520	0.190	0.180	Te

\*  $Tr$ =Training set,  $Te$ =Testing set,  $V$ =Validation set.

(continued on next page)

Table 5.2: Observation for MRR, TWR and G.(Contd.)

Run Order	$I_p$ A	$T_{on}$ $\mu s$	$Tau$ %	$V$ volt	MRR $\frac{mm^3}{min}$	TWR $\frac{mm^3}{min}$	G $\mu m$	Data Type*
25	4	100	80	60	5.532	0.100	0.038	Te
26	4	400	90	60	1.909	0.019	0.080	Te
27	10	400	80	40	20.961	0.040	0.212	Tr
28	13	200	90	40	49.052	0.424	0.240	Tr
29	4	300	80	60	3.320	0.022	0.080	Tr
30	10	400	80	60	16.429	0.016	0.180	Tr
31	10	500	80	40	19.039	0.012	0.220	Tr
32	7	500	85	40	8.430	-0.010	0.190	Te
33	13	500	80	60	26.558	0.009	0.236	V
34	16	300	80	40	38.540	0.212	0.280	Te
35	13	100	80	40	32.960	1.023	0.190	Tr
36	16	200	80	60	32.910	0.547	0.245	Tr
37	7	100	85	40	16.340	0.156	0.110	Tr
38	7	300	80	60	9.078	0.036	0.125	Tr
39	7	200	90	60	14.727	0.065	0.100	Tr
40	13	200	90	60	41.620	0.257	0.240	Te
41	16	500	85	40	49.403	-0.067	0.340	Te
42	13	500	85	60	31.974	-0.090	0.250	Te
43	4	500	80	60	1.700	0.000	0.100	Tr
44	10	300	80	40	21.970	0.060	0.190	Te
45	16	100	90	40	59.980	1.888	0.230	V
46	7	500	85	60	6.590	0.011	0.160	Te
47	10	100	80	60	19.360	0.424	0.150	Tr
48	7	200	80	40	13.571	0.077	0.140	Tr

\*  $Tr$ =Training set,  $Te$ =Testing set,  $V$ =Validation set.

(continued on next page)

Table 5.2: Observation for MRR, TWR and G.(Contd.)

Run Order	$I_p$ A	$T_{on}$ $\mu s$	$Tau$ %	$V$ volt	MRR $\frac{mm^3}{min}$	TWR $\frac{mm^3}{min}$	G $\mu m$	Data Type*
49	16	100	85	40	54.150	1.783	0.224	Tr
50	16	400	80	60	32.390	0.053	0.283	Tr
51	13	500	90	60	38.026	0.020	0.320	Te
52	13	100	90	40	49.270	1.038	0.200	Tr
53	13	200	80	40	32.790	0.310	0.220	Te
54	4	200	80	40	4.909	0.045	0.070	Te
55	13	300	85	60	34.660	0.055	0.210	V
56	16	200	90	40	59.790	0.563	0.260	Te
57	16	500	85	60	39.360	-0.112	0.297	Tr
58	7	400	85	40	11.351	0.010	0.160	V
59	13	400	85	40	39.688	0.011	0.250	Tr
60	10	300	80	60	17.960	0.052	0.170	Te
61	13	300	90	40	48.330	0.167	0.250	Te
62	10	400	85	60	20.364	0.022	0.198	Te
63	10	200	80	60	19.090	0.151	0.160	Tr
64	16	300	85	40	53.060	0.201	0.250	Tr
65	7	200	80	60	10.753	0.089	0.110	Te
66	7	500	80	60	5.930	0.001	0.150	Te
67	4	100	85	60	5.610	0.100	0.040	Tr
68	7	400	85	60	8.792	0.030	0.150	Tr
69	13	200	85	40	40.620	0.391	0.230	V
70	4	300	90	60	3.130	0.011	0.060	Tr
71	13	100	90	60	42.090	1.083	0.200	Te
72	10	500	85	60	17.500	-0.011	0.220	Tr

\*  $Tr$ =Training set,  $Te$ =Testing set,  $V$ =Validation set.

(continued on next page)

Table 5.2: Observation for MRR, TWR and G.(Contd.)

Run Order	$I_p$ A	$T_{on}$ $\mu s$	$Tau$ %	$V$ volt	MRR $\frac{mm^3}{min}$	TWR $\frac{mm^3}{min}$	G $\mu m$	Data Type*
73	16	100	80	60	33.560	1.584	0.220	V
74	4	400	85	60	1.990	0.011	0.110	Te
75	13	400	85	60	34.364	0.000	0.230	Te
76	13	500	90	40	43.039	0.000	0.270	Te
77	13	300	80	40	31.820	0.123	0.240	Te
78	4	400	80	60	2.380	0.009	0.091	Tr
79	16	500	90	40	56.570	0.063	0.310	Tr
80	7	100	90	60	16.286	0.313	0.050	Tr
81	4	100	85	40	8.240	0.078	0.065	Te
82	4	400	80	40	2.830	0.015	0.100	Te
83	13	500	85	40	38.065	-0.100	0.290	Tr
84	7	300	85	40	15.200	0.040	0.130	Te
85	7	500	90	60	7.000	0.011	0.150	Te
86	10	300	85	40	26.810	0.060	0.170	Te
87	16	100	85	60	41.580	1.507	0.219	Te
88	4	200	90	60	5.805	0.022	0.039	Tr
89	16	500	80	40	37.520	0.025	0.320	Tr
90	4	200	90	40	6.740	0.011	0.040	Te
91	4	200	85	40	7.930	0.011	0.090	Tr
92	10	200	85	60	22.740	0.190	0.150	Tr
93	13	200	85	60	35.230	0.301	0.198	Te
94	13	400	90	40	45.640	0.022	0.260	V
95	10	500	90	40	28.273	-0.019	0.240	Tr
96	16	100	90	60	48.540	1.696	0.220	Te

\*  $Tr$ =Training set,  $Te$ =Testing set,  $V$ =Validation set.

(continued on next page)

Table 5.2: Observation for MRR, TWR and G.(Contd.)

Run Order	$I_p$ A	$T_{on}$ $\mu s$	$Tau$ %	$V$ volt	MRR $\frac{mm^3}{min}$	TWR $\frac{mm^3}{min}$	G $\mu m$	Data Type*
97	4	300	85	60	4.230	0.022	0.090	Tr
98	4	500	90	60	1.455	0.000	0.086	Tr
99	7	300	85	60	12.310	0.060	0.130	Tr
100	16	300	90	40	59.120	0.252	0.269	Te
101	10	200	90	60	25.494	0.150	0.210	Tr
102	10	300	85	60	22.160	0.067	0.170	Tr
103	4	300	90	40	5.750	0.000	0.065	Tr
104	4	400	85	40	4.740	0.022	0.110	Tr
105	13	500	80	40	30.290	0.022	0.280	Tr
106	10	500	85	40	23.948	-0.056	0.240	Tr
107	16	200	85	40	53.930	0.714	0.274	Te
108	16	200	85	60	41.260	0.520	0.240	Tr
109	7	300	80	40	12.810	0.038	0.150	Tr
110	13	100	80	60	27.490	0.904	0.190	V
111	7	200	90	40	17.740	0.067	0.110	Te
112	10	200	85	40	27.780	0.268	0.189	Te
113	13	400	80	60	26.896	0.020	0.230	Tr
114	16	300	90	60	47.960	0.165	0.330	Tr
115	4	500	85	60	1.338	0.011	0.120	Tr
116	13	100	85	60	36.090	0.792	0.180	Tr
117	16	400	90	60	47.380	0.078	0.340	Tr
118	10	300	90	40	31.250	0.033	0.210	Te
119	13	400	80	40	30.831	0.063	0.270	Te
120	16	300	85	60	40.900	0.078	0.250	Tr

\*  $Tr$ =Training set,  $Te$ =Testing set,  $V$ =Validation set.

(continued on next page)

Table 5.2: Observation for MRR, TWR and G.(Contd.)

Run Order	$I_p$ A	$T_{on}$ $\mu s$	$Tau$ %	$V$ volt	MRR $\frac{mm^3}{min}$	TWR $\frac{mm^3}{min}$	G $\mu m$	Data Type*
121	7	300	90	40	15.860	0.023	0.120	V
122	7	300	90	60	12.750	0.030	0.120	Tr
123	4	500	90	40	2.013	0.000	0.100	Tr
124	10	100	90	40	33.780	0.547	0.160	Te
125	13	300	80	60	27.110	0.078	0.220	Te
126	7	500	90	40	10.140	-0.022	0.150	Te
127	10	200	90	40	33.052	0.145	0.200	Tr
128	7	100	80	60	11.990	0.190	0.088	Tr
129	10	400	90	60	22.250	0.022	0.240	Tr
130	10	100	80	40	23.480	0.625	0.160	Tr
131	7	400	80	40	11.030	0.018	0.170	Tr
132	16	400	80	40	38.377	0.089	0.300	V
133	4	500	80	40	2.117	0.006	0.110	Tr
134	16	100	80	40	39.810	1.800	0.230	Tr
135	4	300	80	40	3.532	0.022	0.090	Te
136	7	500	80	40	9.030	0.008	0.180	Te
137	7	100	90	40	19.010	0.257	0.060	Te
138	16	400	85	40	51.013	0.020	0.290	Tr
139	4	100	80	40	5.766	0.075	0.050	Tr
140	7	100	85	60	13.195	0.179	0.080	Te
141	7	400	90	60	9.780	0.022	0.140	Te
142	13	300	85	40	40.420	0.089	0.210	V
143	4	300	85	40	7.420	0.022	0.079	V
144	4	200	85	60	5.039	0.045	0.070	Tr

\*  $Tr$ =Training set,  $Te$ =Testing set,  $V$ =Validation set.

(continued on next page)



Table 5.2: Observation for MRR, TWR and G.(Contd.)

Run Order	$I_p$ A	$Ton$ $\mu s$	$Tau$ %	$V$ volt	MRR $\frac{mm^3}{min}$	TWR $\frac{mm^3}{min}$	G $\mu m$	Data Type*
145	4	200	80	60	4.597	0.067	0.056	Te
146	4	400	90	40	4.430	0.011	0.080	Tr
147	10	500	90	60	19.920	0.000	0.250	Tr
148	10	100	85	60	23.050	0.435	0.121	Te
149	16	400	90	40	57.680	0.089	0.280	Tr
150	7	200	85	40	16.169	0.070	0.142	V

Table 5.3 illustrates the ANOVA of MRR, TWR and G, the columns of the table describing the degrees of freedom (DF), the F-statistic, and its p-value. It can be noted that ANOVA is used for testing the null hypothesis ( $H_0$ ) of the experimental data with a confidence level of 95%. The p-value for the F statistic is expressing the probability of observing a value of F at least as large, if  $H_0$  is true then treatments has no effect. If p-value  $\geq 0.05$ , it is concluded that  $H_\alpha$  is true and the treatments have a statistically significant effect.  $I_p$ ,  $Ton$ ,  $Tau$  and  $V$  are significant for all the responses, where as some of the interactions exhibit significant impact. The  $R^2$  value indicates that the predictors explain 99.86%, 99.4% and 98.91% of the variance in MRR, TWR and G, respectively. The corresponding  $R_{adj}^2$  values are 99.78%, 99.08% and 98.31%, for MRR, TWR and G, respectively.  $R_{adj}^2$ , accounts for the number of predictors in the model. Both values indicate that the second order model fits the data well for all the responses.

The experimental investigation and analysis were carried out in different parametric combinations, for deriving an effective representation of the models, keeping in view of the present research objectives. It is very difficult to predict the output characteristics accurately by mathematical equation as EDM process is stochastic and random in nature. So the proposed algorithms, discussed in the next section, have been implemented here to model die-sinking EDM process. These techniques are especially worthwhile in processes where a dynamic non-linear relationship exists

Table 5.3: ANOVA for MRR,TWR and G

Source	DF	MRR			TWR			G		
		F	P	DoC	F	P	DoC	F	P	DoC
<i>Ip</i>	4	14755.92	0.000	87.61	781.42	0.000	19.38	1803.94	0.000	81.90
<i>Ton</i>	4	191.88	0.000	1.14	1857.15	0.000	46.05	268.13	0.000	12.17
<i>Tau</i>	2	1684.83	0.000	5.00	7.86	0.001	0.10	6.73	0.002	0.15
<i>V</i>	1	1634.56	0.000	2.43	22.14	0.000	0.14	23.17	0.000	0.26
<i>Ip* Ton</i>	16	5.84	0.000		331.54	0.000	32.88	0.69	0.793*	
<i>Ip* Tau</i>	8	223.85	0.000	2.66	2.82	0.007		27.76	0.000	2.52
<i>Ip* V</i>	4	123.1	0.000		12.34	0.000		1.82	0.131*	
<i>Ton* Tau</i>	8	4.55	0.000		5.55	0.000		6.23	0.000	
<i>Ton* V</i>	4	0.75	0.560*		4.20	0.004		3.69	0.008	
<i>Tau* V</i>	2	30.2	0.000		3.03	0.053*		42.39	0.000	
Error	96									
Total	149									
	S =	0.759310			0.0372374			0.0103811		
	$R^2$ =	99.86 %			99.40 %			98.91 %		
	$R^2_{Adj}$ =	99.78 %			99.08 %			98.31 %		
*Non-Significant at 95%										

and a complete understanding of the physical mechanisms is very difficult, as in the case of EDM process. One of the advantages of using these approaches is that a model can be constructed very easily based on the given inputs and outputs and can be trained to accurately predict process responses.

### 5.3 Proposed models

Artificial intelligence (AI) predictions have been getting interest to a large extent in order to solve problems that are scarcely solved by the use of conventional methods. They have been refers to have the ability to be trained like humans, by accumulating knowledge through recurring learning activities. For that reason the intention of this research is to propose multiple input single output models using the AI approaches to predict the responses such as MRR, TWR and G. A comparative analysis based on an ANN and two neuro-fuzzy techniques are presented and are explained as follows.

#### 5.3.1 Artificial neural network (ANN)

A feed-forward neural network with four input neurons, one hidden layer and one output neuron is used and the architecture of the model is depicted in Fig. 5.1. The activation function in the hidden layer is the hyperbolic tangent sigmoid transfer function, which standardizes or normalizes the data and hence the transformed data lie between -1 and 1. In the output layer, a the linear transfer function is used. The training algorithm selected is the Levenberg-Marquardt back-propagation because the algorithm yields fastest training (see D). Weights are randomly initialised, and the learning rate and momentum parameter were set at 0.05 and 1.05, respectively. The data set obtain from experiments are divide randomly in to three subsets namely; training, testing and validation sets, in 50%, 40% and 10% of the total data, respectively shown by the column 'Data Type' in Table 5.2. The training set is used to calculate the gradient and to form the weight factors and bias. The testing data is used to minimise the MSE while training and stop the training after appropriate epoch. The remaining 10% validation data set is used to calculate the prediction error to estimate the accuracy of the models on the unseen data set, which is elucidated in Section 5.4.2.

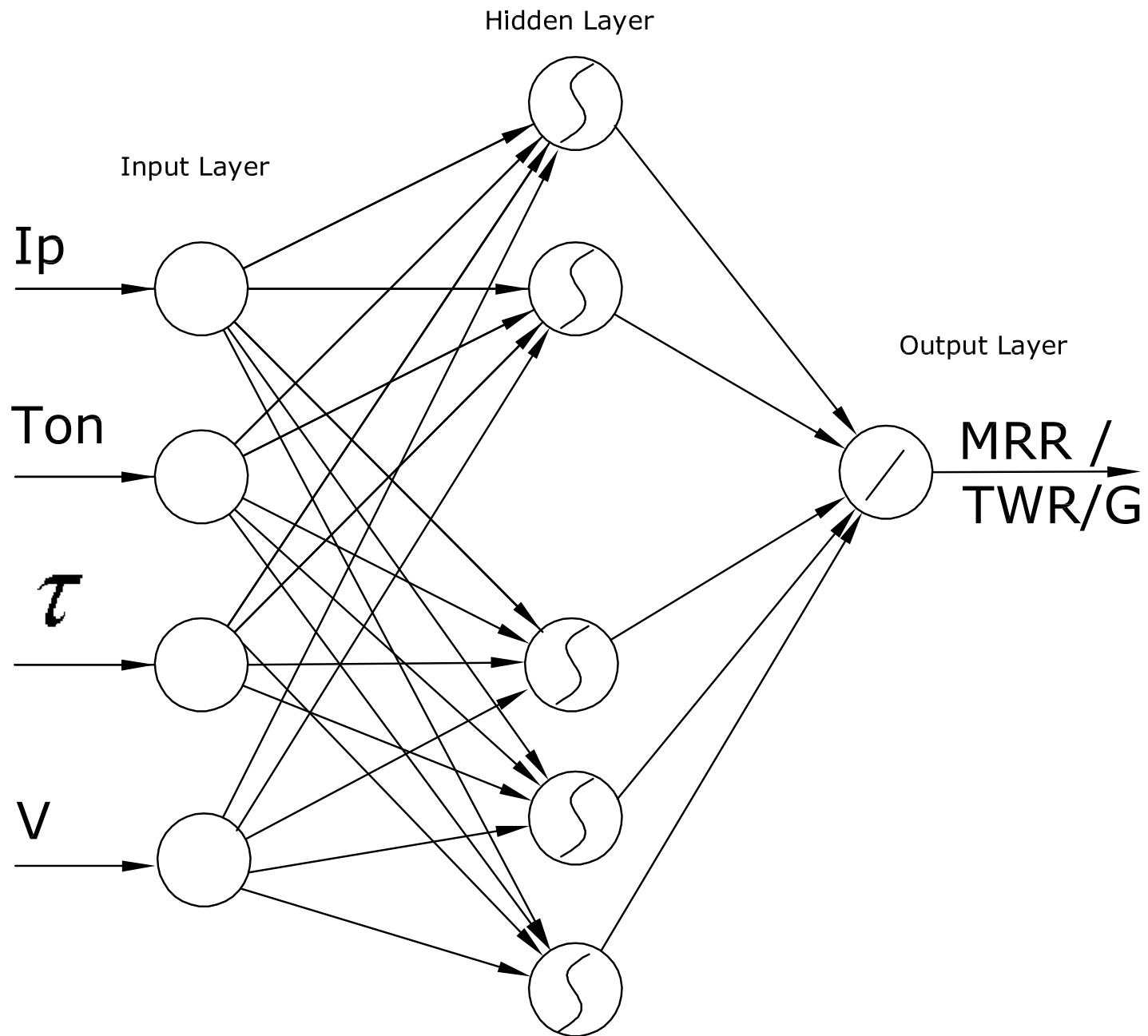


Fig. 5.1: Neural network architecture

An ANN has one input layer and one output layer with one or added hidden layers in between, whose computation nodes are respectively called hidden neurons or hidden units. The hidden neurons interfere between the external input and the network output, in some constructive mode. The numbers of hidden neurons are varied and the generalization performance is evaluated. The number of hidden neurons affects how well the network is able to separate the data. A large number of hidden neurons will make sure accurate learning, and the network is able to precisely predict the data it has been trained on, but its performance on new data, its capability to generalize, is compromised. With less hidden neurons, the network may not be able to learn the pattern of the data and the error may not be under an acceptable level. Thus, selection of the number of hidden neurons is a crucial decision. However, the numbers of hidden layer neurons are established using a simple trial-error method in all applications on the basis of least MSE in the testing data set. During the training, the MSE of the testing data is recorded after maximum epoch of 1000 and these are plotted against the number of nodes in the hidden layer for MRR, TWR and G in Fig. 5.2. The plot illustrates that there is an optimal number of nodes where the MSE, for each of these responses, exhibit a minimum value as explained by Tsai and Wang (2001c). The number of nodes in the hidden layer are found to be 110, 6 and 25 for MRR, TWR and G, respectively. Therefore, these ANN architectures are considered for modelling of the said responses and adequately trained. Now, the models are ready to predict the data for the validation data set and for the purpose of comparison.

### 5.3.2 Neuro-fuzzy (NF) models

Recently, researchers are working on hybrid models of ANN and fuzzy logic called neuro-fuzzy system or Fuzzy Inference System (FIS). The motivation for hybridization is the technique enhancement factor, multiplicity of application tasks and realizing multi functionality. The need for replacing these primary functions is to increase the execution speed and enhance reliability. A highly complex and ill-defined mathematical system can be modelled with a neuro-fuzzy system. It contains four major components: fuzzifier, inference engine, rule base, and defuzzifier. The system can extract knowledge in form of interpretable fuzzy linguistic rules. The system identifies

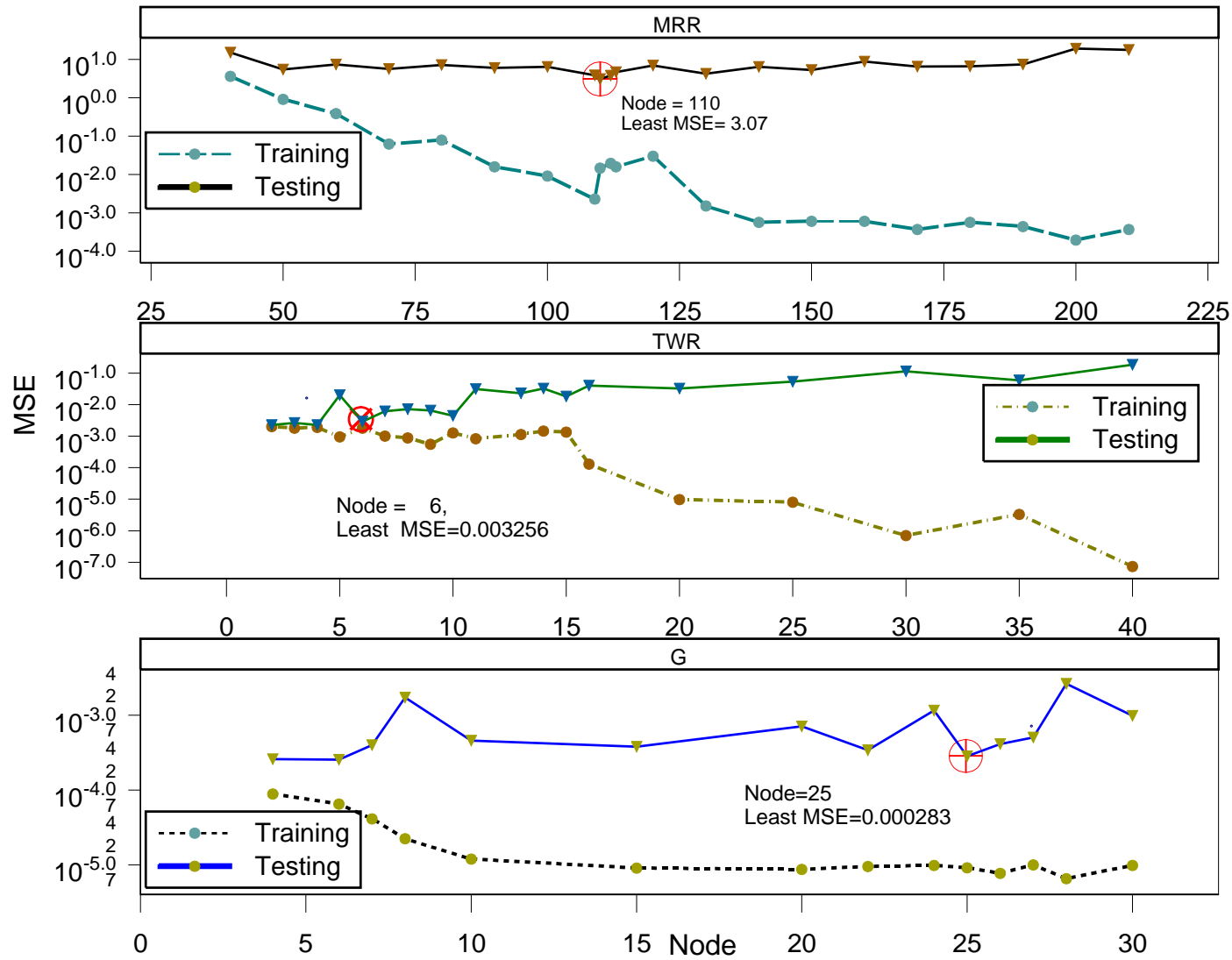


Fig. 5.2: Optimal number of neurons in the hidden layer in ANN model

the membership level of an input pattern to the different available membership classes and estimate the output associated with the physical phenomena. Depending on the types of inference operations upon "if-then rules", most fuzzy inference systems can be classified into two types; Mamdani system and Sugeno system.

#### *Mamdani system*

Mamdani system is the most commonly used and this work proposed a neuro-fuzzy inference system with four input variables and are responses such as MRR, TWR, and G. It is shown in Fig. 5.3, where layer 1 consists of fuzzification of input parameters. Each variable is fuzzified with Gaussian membership classes, since it is associated with product composition for ease in calculation, the same is used. The inference engine and rule base are depicted as layer 2. The rules are framed that can be expressed as: If x is A and y is B then output belongs to class C. Lastly, in the third layer, the inference mechanism weights each rule consequent values and a possible output is found using the centroid of area technique.

The same training, testing and validation sets are used as mentioned in Section 5.3.1. C++ codes were developed to simulate the model and extract the rule base from the training data. The input-output training data is clustered using the Mountain clustering technique Yager and Filev (1994) that yield 113, 112 and 118 rules to predict the responses MRR, TWR and G, respectively. The parameters used for clustering are stopping constant =0.0001, mountain building constant =1 and destruction constant of 4. The error signals between the inferred output value and the respective desired value are fine tuned by the Back-propagation technique Yager and Filev (1995). The gradient-descent method is applied to adjust each rule antecedents and consequent with a learning rate of 0.001 and a maximum epoch of 1000.

To find out the suitable architecture of the network for the above problem various architectures have been studied. Though, the choice for the number of membership classes for each of the variables can be numerous, an equal number of fuzzy classes are considered for all the variables. To establish the best number of such membership function, a simple trial-error method is used in all the applications on the basis of least MSE in the testing data set. MSE against the number of membership classes are

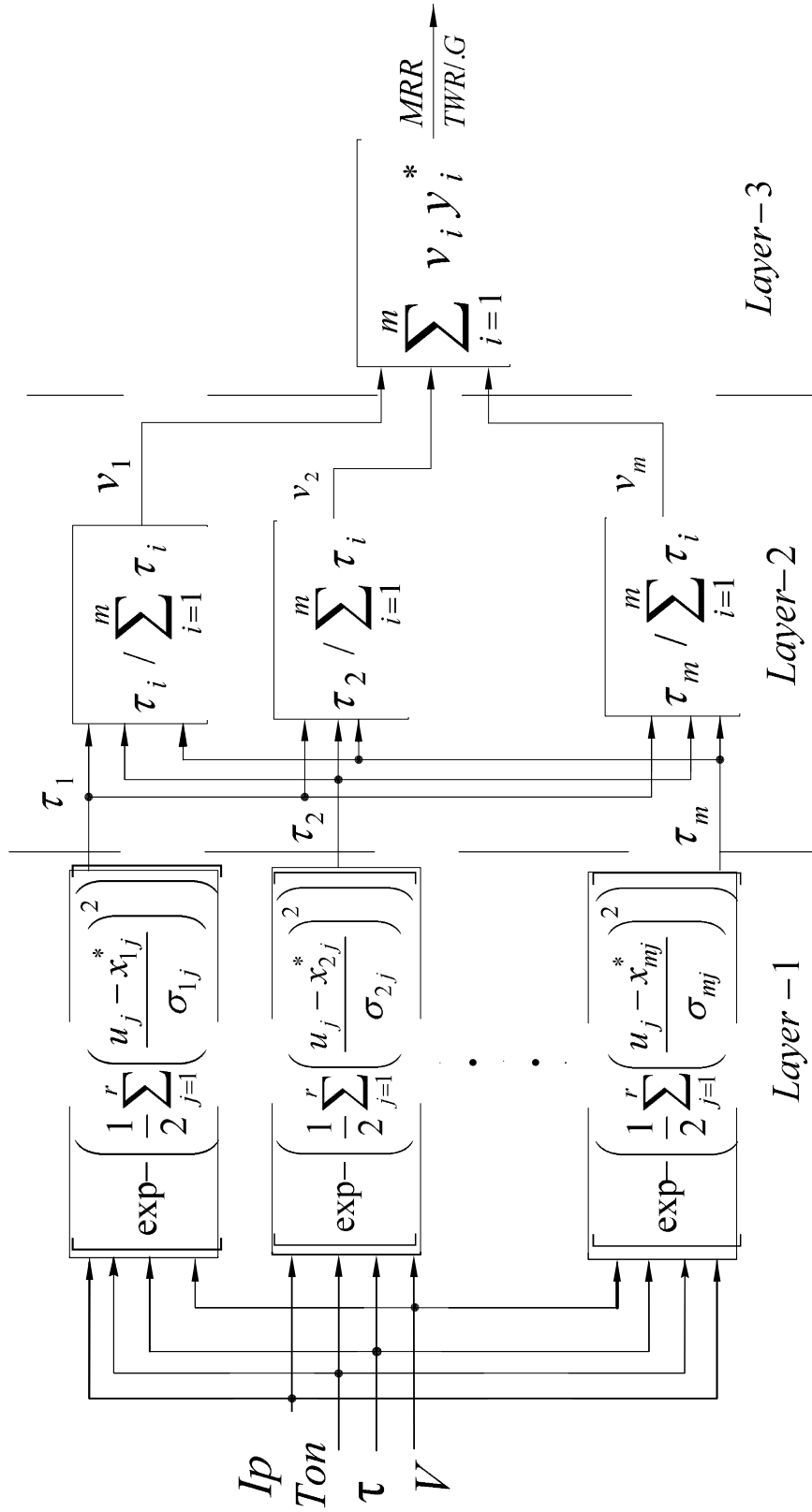


Fig. 5.3: Neuro fuzzy architecture



depicted in Fig. 5.4. It can be inferred from the plot that the number of membership classes are 3, 2 and 4 for MRR, TWR and G, respectively, which yields minimum MSE. These Mamdani architectures are considered for modelling of the said responses. It can be noted that the MSE's of the testing set are greater than that of the training set.

#### *Sugeno system*

Sugeno method follow the same input fuzzification and rule base formulation processes, but the output representation are signified in a different way. The main difference between Mamdani and Sugeno type fuzzy interface is the manner the crisp output is calculated from the fuzzy inputs. While Mamdani uses the technique of defuzzification of a fuzzy output, Sugeno method map the output to a linear equation of inputs or a constant, thus eliminating computationally expensive defuzzification process. The output can be calculated with a similar weighted average formula as the Mamdani approach (Centroid of area technique see Appendix E).

The modelling was carried out with the standard software [Matlab (2005)] with a hybrid optimisation method used in membership function parameter training, which is a combination of least-squares estimation with backpropagation technique. Since, the software was unable to converge with higher number of membership functions and resulted in large MSE, only two triangular membership functions are used to fuzzify the variables. These networks for various responses are trained as long as the MSE on testing data set is found to decrease, which resulted in 16 rules base for each of the networks.

#### *Learning behaviour*

The MSE for testing data set are calculated for each epoch and the learning continued until MSE is found to decrease. This inhibited the rule base to be over trained, otherwise it will increase the MSE in the training and validation data sets. While predicting MRR, the ANN model is the best in terms of accuracy with a MSE of 0.015, and the training took almost 662 epoch. The next accurate model is Sugeno type with MSE 17 times more than that of ANN model and followed by Mamdani

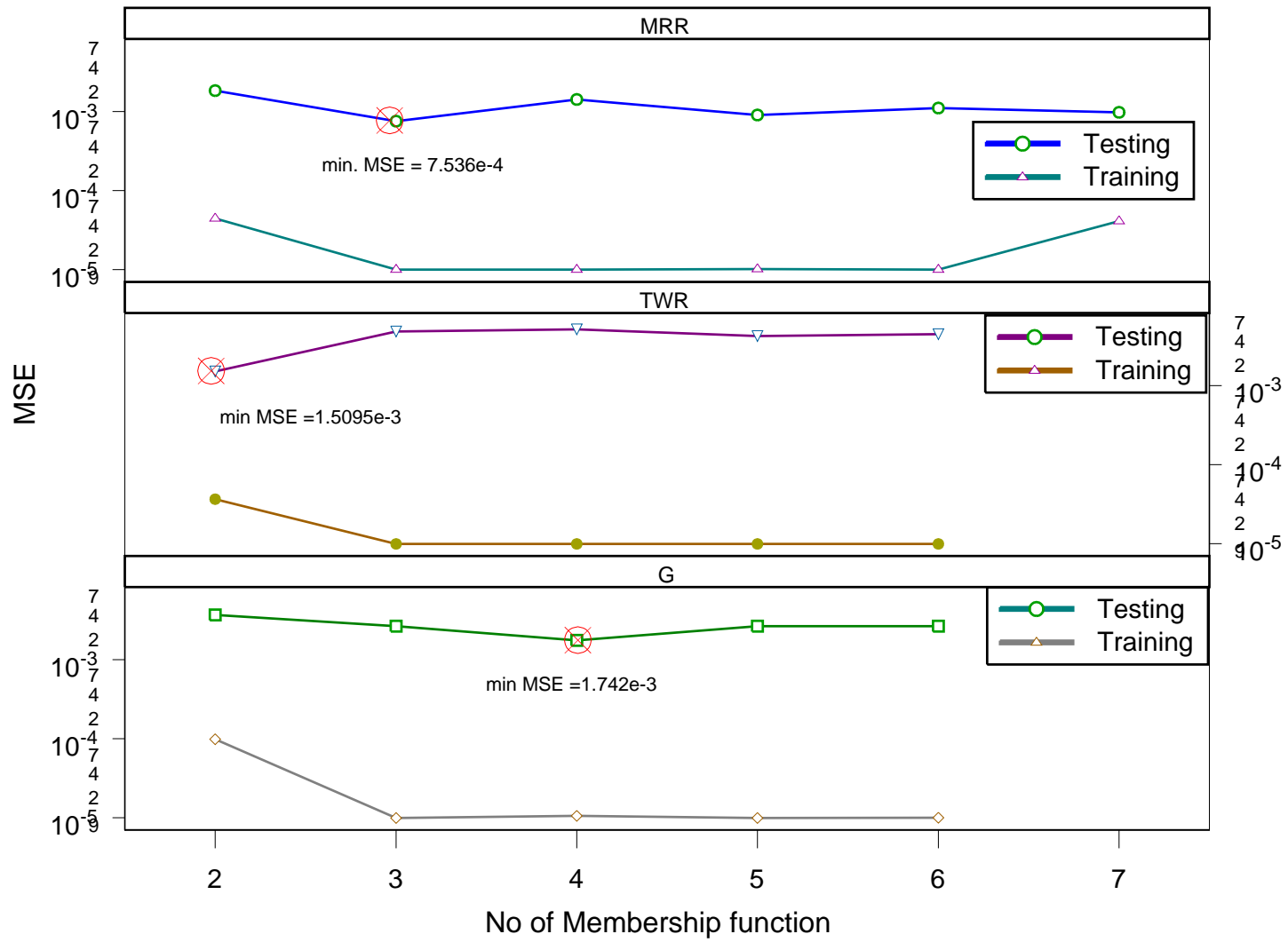


Fig. 5.4: Optimal number of membership functions in Mamdani model

model with the MSE of about 19 times more. When the models are evaluated in terms of speediness, Sugeno model is the best that converged with 6 epochs and then ANN and Mamdani model, which took almost 662 epochs and 925 epochs for training, respectively (Table 5.4).

Table 5.4: Learning behavior

Parameters	ANN		Sugeno		Mamdani	
	epoch	MSE	epoch	MSE	epoch	MSE
MRR	662	0.015	6	0.248	925	0.279
TWR	17	$197.0 \times 10^{-5}$	110	$12.0 \times 10^{-5}$	220	$4.80 \times 10^{-5}$
G	19	$9.16 \times 10^{-6}$	21	$20.8 \times 10^{-6}$	653	$4.16 \times 10^{-6}$

Nevertheless, in the case of TWR, when the models are compared in terms of accuracy the Mamdani model is found to be best with the smallest possible MSE of  $4.80 \times 10^{-5}$  and Sugeno and ANN models converged with MSE of 2.5 times and 41 times more than that of Mamdani model, respectively. Whereas, if the models are compared in terms of speed then the order is reversed. Finally, while predicting G, again Mamdani model predicts is superior in accuracy with MSE value of  $4.16 \times 10^{-6}$ , conversely ANN and Sugeno models predict with MSE 2.2 times and 5 times more, respectively. Nevertheless, when sequenced in terms of speed it is found that the order is ANN, Sugeno and Mamdani.

Therefore, it could be concluded from the study that Mamdani model is reasonably accurate in predicting the responses although it is comparatively slow in convergence. However, the MSE of the other two models are also comparable with this model and have good prediction capability.

#### 5.4 Result and Discussion

In this research, an ANN and two neuro-fuzzy models, Sugeno and Mamdani models, has been developed to predict MRR, TWR and G in EDM process. Four machining parameters namely pulse current, pulse duration, duty cycle and open circuit voltage are taken as input features. Full factorial design was used to conduct the experiments

for the said predictive models. The predicted dimensions from the three models are compared with the actual experimental data in terms of residuals and the average prediction error for all the responses.

#### 5.4.1 Analysis on responses

##### *Effect of machining parameters on MRR*

The main effect and the interaction effect of each factor can be graphically assessed by plotting the mean response versus factor levels. Fig. 5.5 shows that  $I_p$ ,  $Ton$ ,  $Tau$  and voltage have significant effects on MRR (see Table 5.3). In the table, the degree of contribution (DoC) of  $I_p$  is 87.61% and is the most significant factor among all the machining parameters. Furthermore,  $I_p$  is directly proportional to the MRR, i.e., by increasing  $I_p$  from 4 to 16 A, MRR increases significantly. This is expected because an increase in pulse current produces strong spark, which produces the higher temperature, causing more material to melt and erode from the workpiece. Besides, it is signify from this figure that the other factor does not influence much as compared with  $I_p$ . It is expected that when the  $Ton$  increases, the MRR usually increases up to a maximum value after which it starts to decrease. It is well known fact that the spark energy increases with the increase in  $Ton$ , and then it start to fall. The plot is probably beyond the peak, therefore, the MRR is decreasing with the increase of  $Ton$ . The plot for MRR with  $Ton$  for various  $I_p$  for  $Tau=85\%$  and  $V=40$  volt is shown in Fig. 5.6 that establishes similar conclusion shown by previous researchers Lee and Li (2001), Ghoreishi and Tabari (2007). In addition, for a larger  $Tau$ , the spark energy supply across the gap is for a greater duration comparatively than that of small  $Tau$ , and therefore there will be an increase in temperature and so will be MRR. Within the scope of this experiment,  $V$  is showing a downward trend, however, its influence on MRR is very less when compared with  $I_p$  (Table 5.3) and DoC is about 2.43%.

Fig. 5.7 portrays the interaction plot of MRR of EDM process, with each plot exhibit the interaction between two different machining parameters. An interaction between factors takes place when the variation in response from a level of a factor to another level varies from the change in response at the same two levels of a another factor, this implies that the effect of one factor is dependent upon another factor.

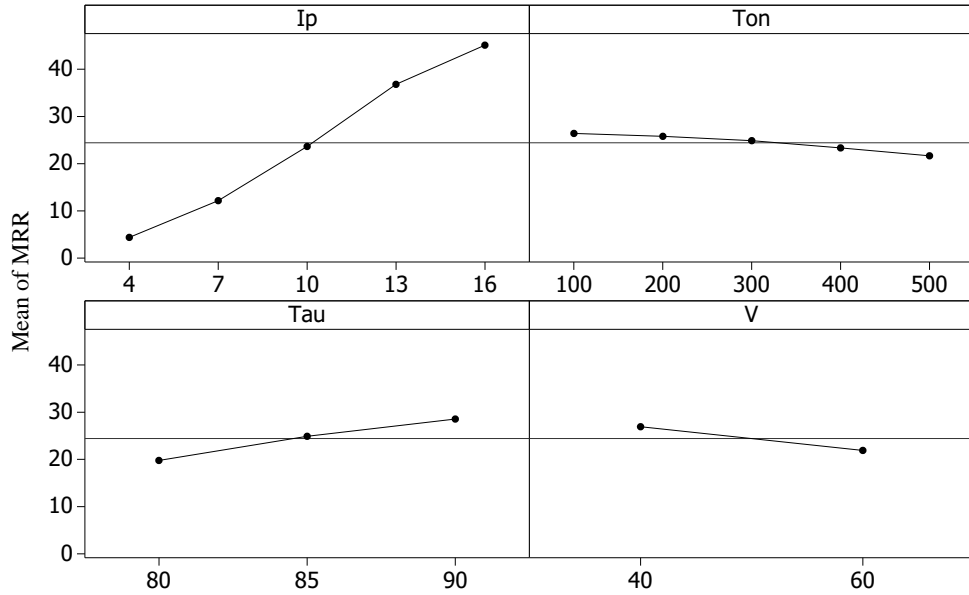


Fig. 5.5: Main effect plot of the factors on MRR

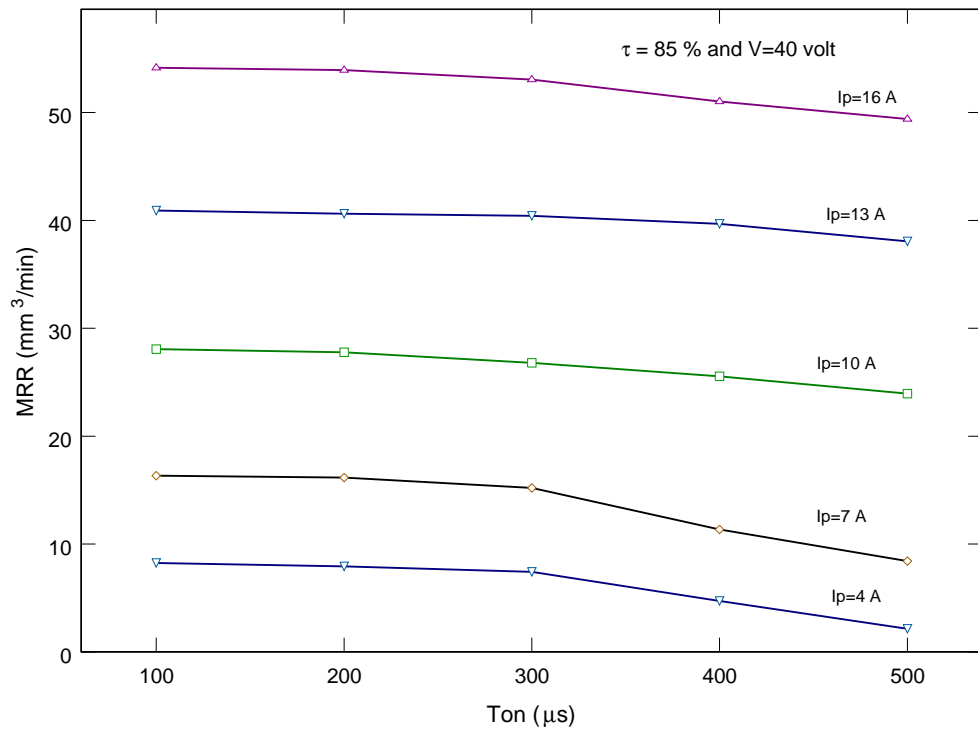


Fig. 5.6: Effect of pulse on-time ( $T_{on}$ ) on MRR

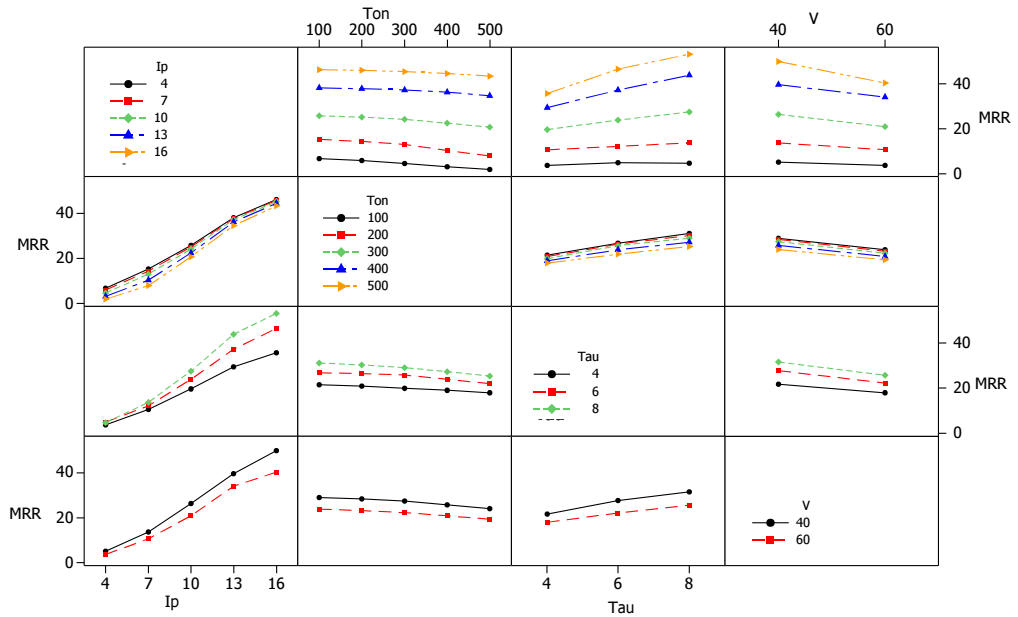


Fig. 5.7: Interaction effect plot of the factors on MRR

Assessment of the interaction plot reported in Fig. 5.7, shows that there exist some interaction among the parameters, except interaction between  $Ton$  and  $V$ , which is also confirmed by the ANOVA (Table 5.3). The most important interactions is  $Ip * Tau$  with DoC=2.66%. The DoC of the factors less than 1.00% are not presented.

Fig. 5.8 and Fig. 5.9 depict the scanning electron micrographs (SEM, Jeol, JSM-6480 LV, Japan) taken with the parametric combinations of 4 A/100 $\mu$ s/90%/40 V and 10A/100  $\mu$ s /90%/40V, respectively. From these figures it is observed that the size of the crater and the amount of molten material produced during the sparking is heavily dependent of the  $Ip$ . The main factor plot for MRR conforms, these observations based on SEM micro graphs.

*Effect of machining parameters on TWR*

The plot of main effects (Fig. 5.10) for TWR depicts that  $Ip$  and  $Ton$  have significant impact. TWR is increasing non-linearly with the current from 4 to 16 A. This is obvious, as the  $Ip$  increases the pulse energy increases and thus more heat energy is produced in the tool workpiece interface, leads to increase the melting and evaporation of the electrode. One can interpret that  $Ip$  has a significant direct impact on TWR. This figure shows that  $Ton$  is reciprocally proportional to TWR. The decrease of TWR is more rapid (0.4633  $mm^3/min$ ) when  $Ton$  increases from 100  $\mu$ s to 200  $\mu$ s

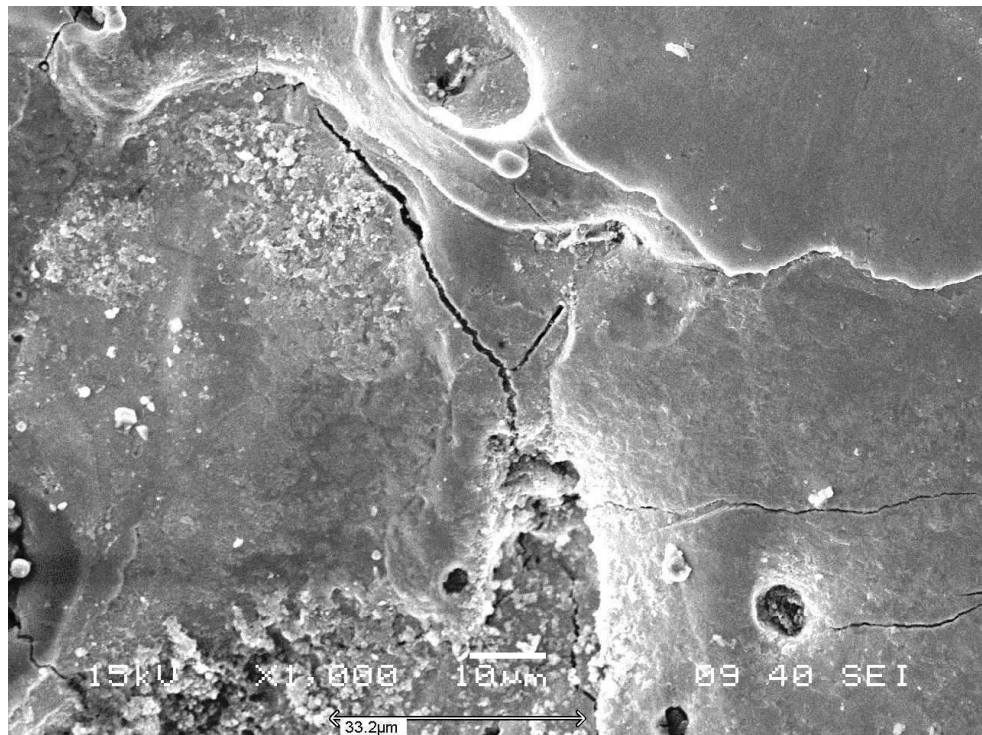


Fig. 5.8: SEM Micrograph at 4A/100µs/90%/40 V

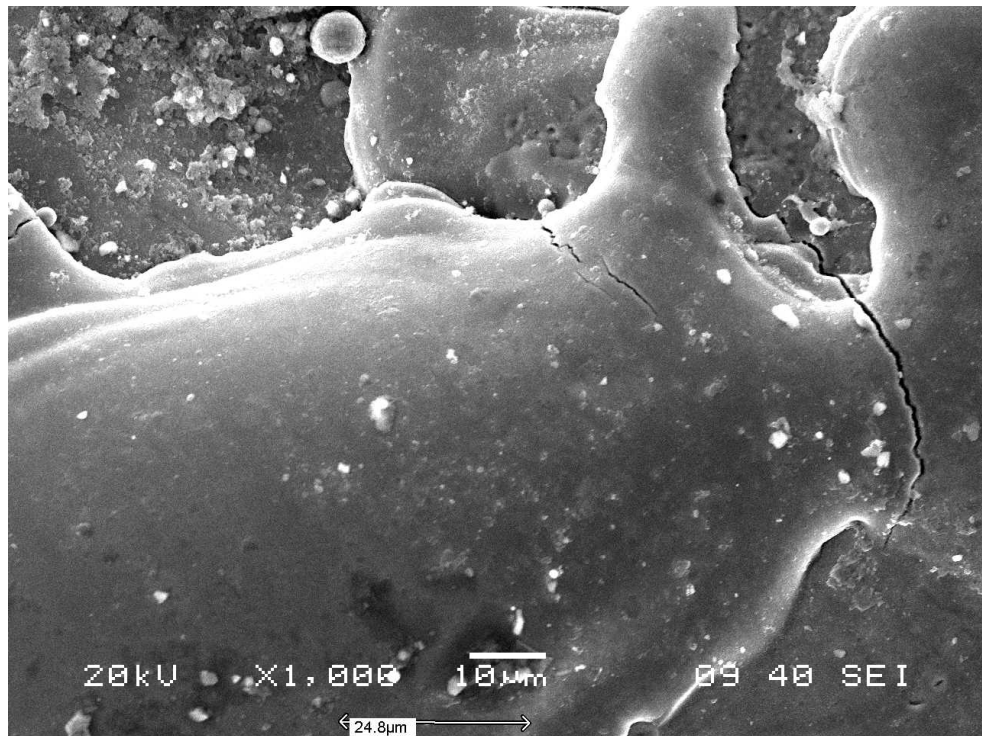


Fig. 5.9: SEM Micrograph at 10A/100µs/90%/40 V

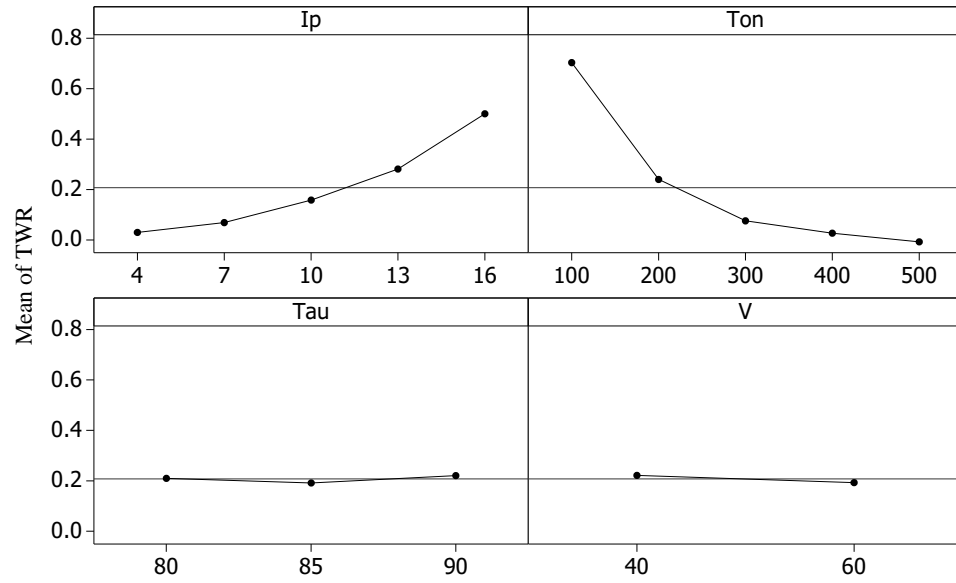


Fig. 5.10: Main effect plot of the factors on TWR

as compared to  $0.018699 \text{ mm}^3/\text{min}$  when  $Ton$  increases from 400 to 500  $\mu\text{s}$ . This is probably, when the  $Ton$  is high, the spark energy is also high at the tool workpiece interface, and due to this the plasma channel expands. This leads to results in growth of heat source radius at the surface of the tool, consequently reduces the electrode wear. As pure copper is reasonably more conductive than that of AISI D2 steel, therefore the release of heat is quick at the time of machining, the longer time for heat transfer from the molten crater to the body of tool, which results in a lesser amount of material removal from the crater, this in turn declines TWR at higher  $Ton$  [Dhar et al. (2007), Sohani et al. (2009)].

Fig. 5.10 suggests that  $Tau$  and voltage has a subtle effect on TWR. It is obvious from this figure that by changing  $Tau$  from 80% to 90% and voltage from 40 to 60 during this process, TWR fluctuates very less as compared to  $Ip$  and  $Ton$  and hence the effect of  $Tau$  and voltage on electrode wear is almost negligible [Dhar et al. (2007)]. Consequently, it could be noted that the effect of  $Tau$  and  $V$  is very less as compared to  $Ip$  and  $Ton$ , which can also be conformed from the ANOVA (Table 5.3). Interaction plot for TWR in Fig. 5.11 demonstrates interactions among experimental factors. However, a certain interaction can be observed between the factors except between  $Tau$  and  $V$ . The most influencing interactions is  $Ip^*Ton$ . The factors  $Ton$ ,  $Ip^*Ton$  and  $Ip$  has DoC of 46.05%, 32.88% and 19.38%, respectively, and are contributing almost 98.31% of the variation of the response.



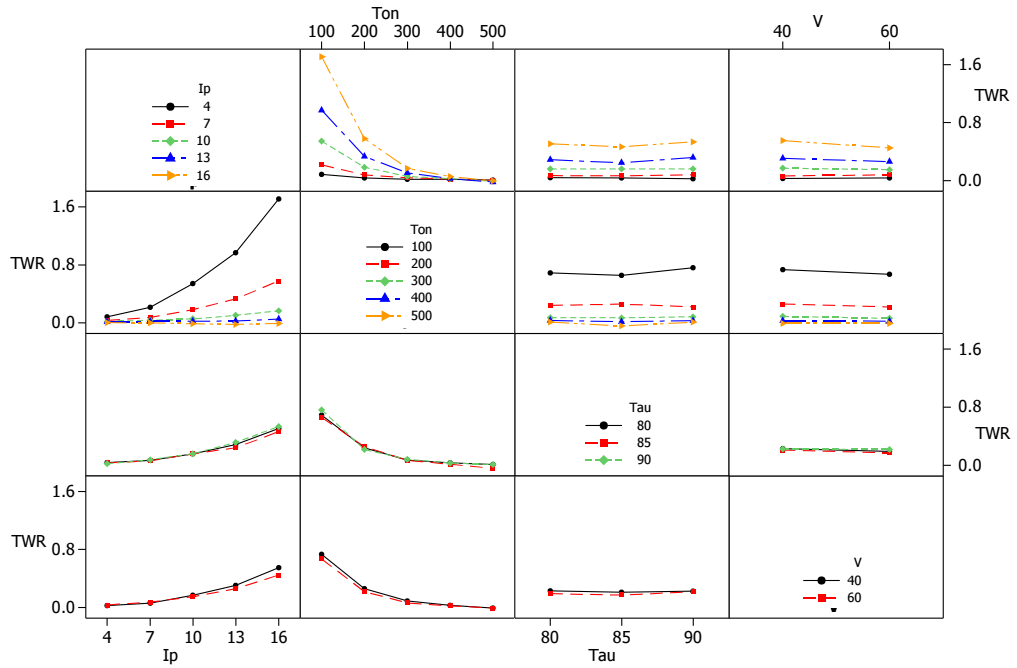


Fig. 5.11: Interaction effect plot of the factors on TWR

Effect of machining parameters on G

Overcut G is the deviation between the dimension of the electrode and the size of the cavity, it is inherent to the EDM process which is unavoidable though adequate compensation are provided at the tool design. To achieve the accuracy, minimisation of G is essential. Therefore factors affecting G is essential to recognize. Fig. 5.12 and Fig. 5.13 represents the plot of main effects and interaction effect for G, respectively. It is observed that the  $I_p$  and  $Ton$  are significant factors varying linearly with the response. Overcut increases with the pulse energy [Jeswani (1981)], and as  $I_p$  and  $Ton$  increases the pulse energy increases, which is responsible for production of spark at the tool workpiece interface. However, the impact of  $I_p$  is more compared to  $Ton$  as DoC's are 81.9% and 12.17%, respectively. The other two factors  $Tau$  and voltage has very little effect on G as compared to  $I_p$ . Although, they are significant and with the increase of  $Tau$  from 80% to 90%, the value of G increases. In addition, G is inversely proportional to  $V$ . The influence of  $Tau$  and  $V$  can be noted from ANOVA Table 5.3 and Fig. 5.10.

The interaction plots are presented in Fig. 5.13 portrays the interactions among all the parameters are significant, except at two subplot, i.e., the interaction of  $I_p * Ton$ , and  $I_p * V$ . These results are in good concurrence with the values of contribution

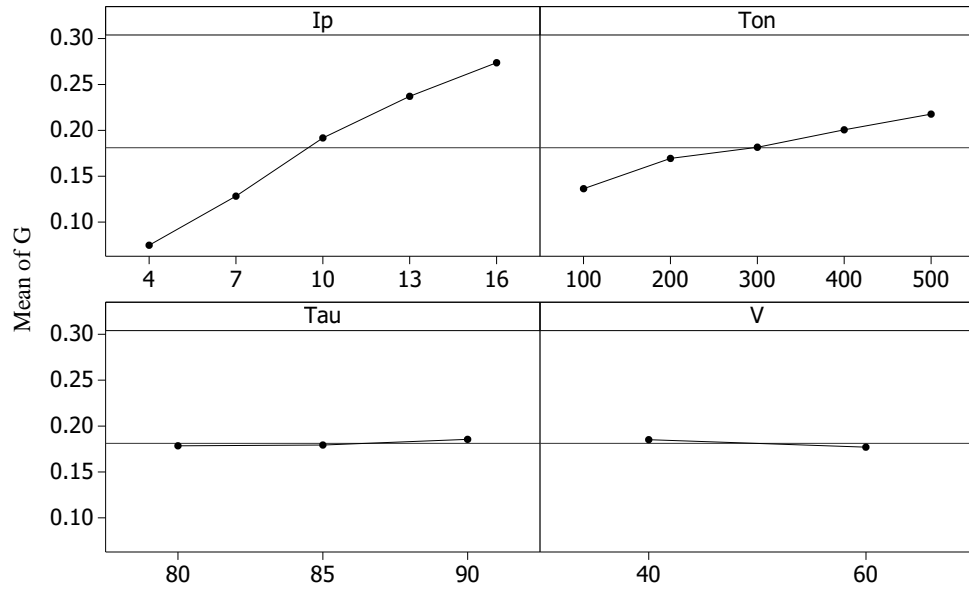


Fig. 5.12: Main effect plot of the factors on G

percentages summarised in ANOVA Table 5.3. The interaction  $Ip^*Tau$  has maximum DoC of 2.52%.

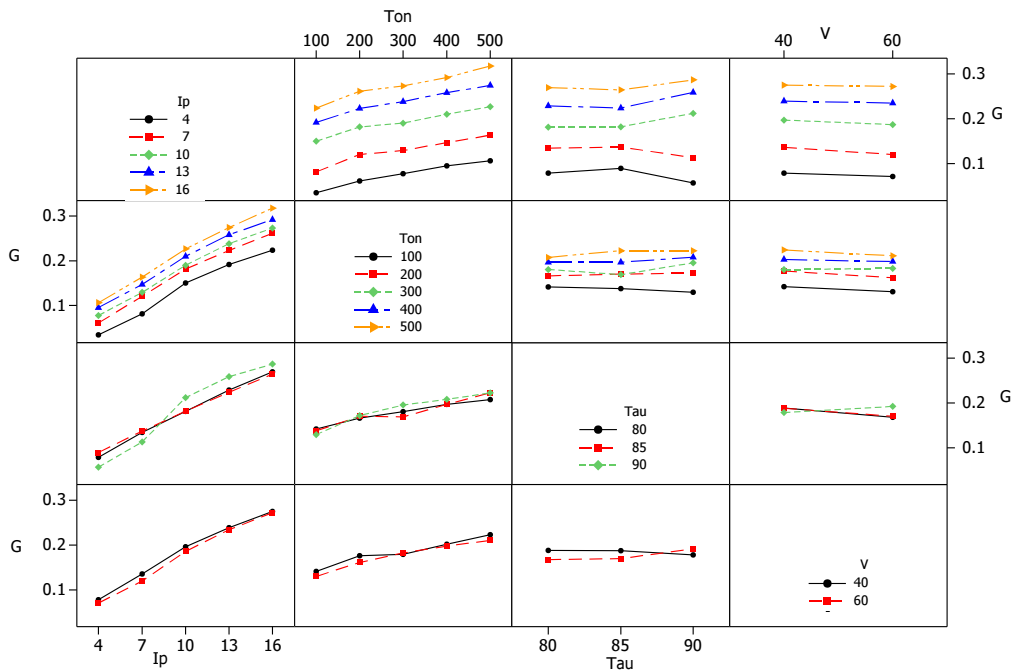


Fig. 5.13: Interaction effect plot of the factors on G

### 5.4.2 Model validation

The generalization capability of any model can be well judged only with completely unused dataset. Hence, it is decided to test all the models using totally unseen data,

not previously used for training as well as testing purpose. If these developed models succeed the validation process, it connotes that the model can be useful not only to the parameter range of experimental conditions used in model building, but also to the range of experimental conditions used in the model validation.

Fig. 5.14 demonstrates that the residuals obtained from the difference between the experimental and the predicted values of MRR for ANN, Sugeno system and Mamdani system model of the validation set. The residuals range from -4.69 to 5.808 for ANN, -6.71 to 5.5 for the Sugeno system model and -2.25 to 3.21 for the Mamdani system model, which shows that Mamdani model is much more accurate in prediction of MRR than other two models. Fig. 5.15 reveals the residuals value of the TWR for ANN, Sugeno and Mamdani systems of the validation set. The residuals of TWR of ANN, Sugeno's system and Mamdani system model range from -0.0295 to 0.0701, -0.1282 to 0.432 and -0.024 to 0.7  $mm^3/min$ , respectively. However, as depicted in Fig. 5.15, the ANN model approximates better than the other two in predicting TWR. The difference of the predicted and measured overcut 'G' is depicted in Fig. 5.16 which is evident that the Mamdani system model approximates the overcut better than the other two models. The residuals range from -0.0245 to 0.0233, -0.0432 to 0.0201 and -0.023 to 0.0152 mm for ANN, Sugeno and Mamdani models, respectively.

To illustrate the highest accuracy of the predictive model, the parity graphs are plotted between predicted values of MRR versus experimental values in Fig. 5.17 for the proposed models. The represented data refer to all training, testing and validation data sets. These plots also present straight lines to make them easier to interpret. It may be seen that there is an excellent fit between the predicted values and the experimental data without any bias. All three models could predict the MRR very accurately and except for one or two outliers in the Sugeno model, almost all the values are very close to the line. It could be noted that closer the value to the line, more is the accuracy. Conclusively, it can be said that the ANN and Mamdani model are comparatively more accurate than the Sugeno system in predicting MRR. The coefficient of determination ( $R^2$ ) of Sugeno system, ANN and Mamdani models are 99.05%, 99.36% and 99.6%, respectively, showing the accuracy of the prediction and conforms to the effectiveness of the models in predicting MRR. Therefore, the models

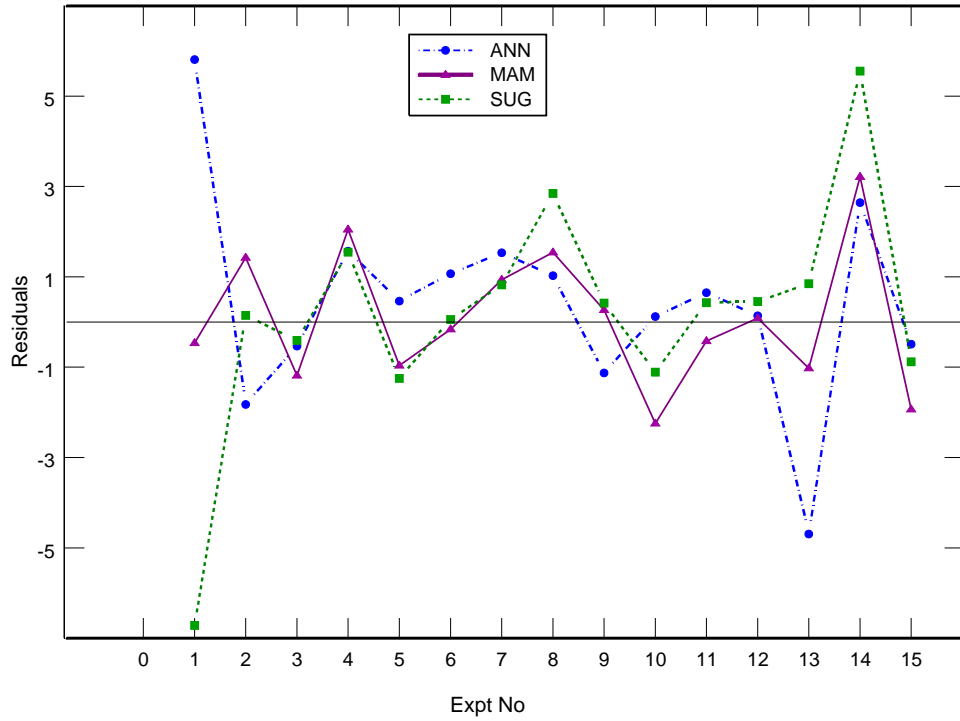


Fig. 5.14: Residuals of the validation data on MRR for the models.

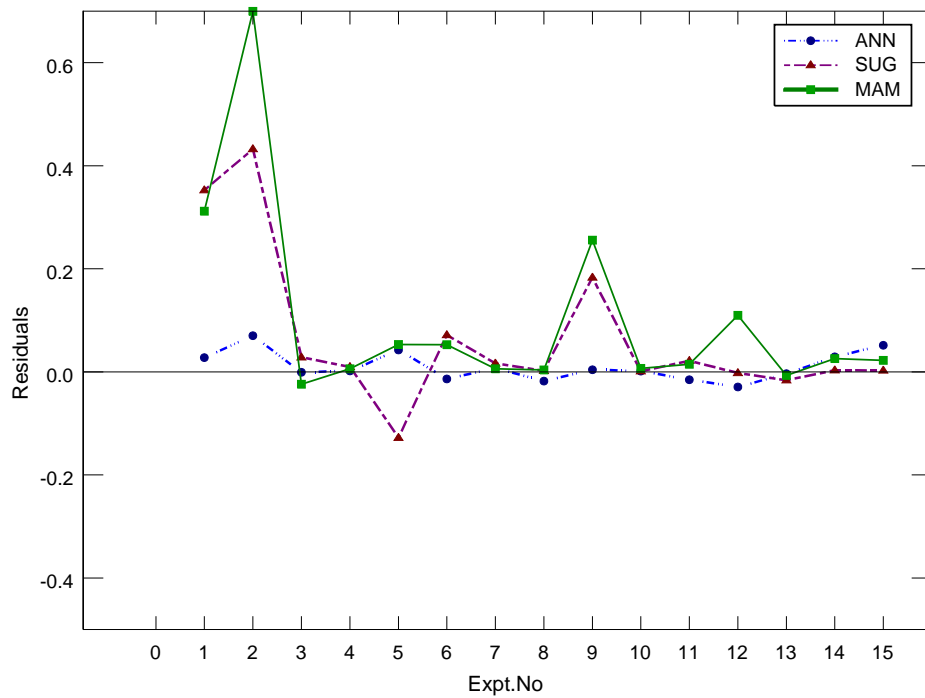


Fig. 5.15: Residuals of the validation data on TWR for the models.

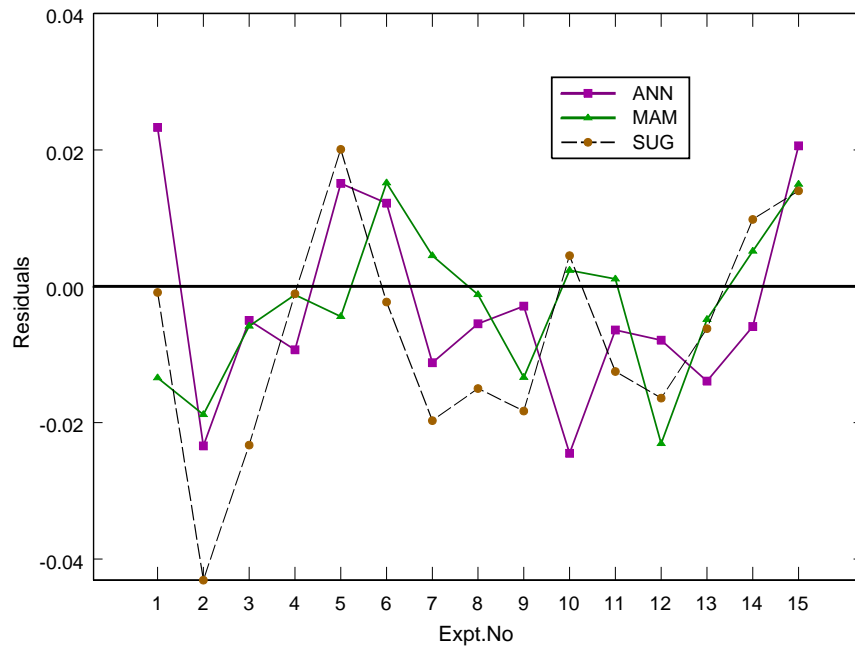


Fig. 5.16: Residuals of the validation data on G for the models.

can be sequenced as Mamdani, ANN and Sugeno models, in terms of accuracy in predicting MRR.

Similar, the parity plots for showing accuracy of the model in predicting TWR also illustrated in Fig. 5.18, it may be seen that there is an excellent fit between the predicted and the experimental data without any bias. Almost all the values are very close to the line, consequently the ANN model is more accurate in predicting TWR as compare to other two neuro-fuzzy models with co-efficient of determination ( $R^2$ ) 98.6%. However, few outliers exists in neuro-fuzzy models. Eventually, the Sugeno system is comparatively more accurate than Mamdani system model in predicting TWR, with co-efficient of determination ( $R^2$ ) 94.43% and 92.12%, respectively. Hence the model can be sequenced as ANN, Sugeno and Mamdani models, in terms of accuracy in predicting TWR.

Fig. 5.19 render the corresponding plot for the prediction of G in which it is clear that the ANN model is more accurate than the Mamdani and Sugeno models. The coefficients of determination ( $R^2$ ) for ANN, Mamdani and Sugeno systems are 97.8%, 97.45% and 96.86%, respectively, conforms the model sequence for the prediction of overcut.

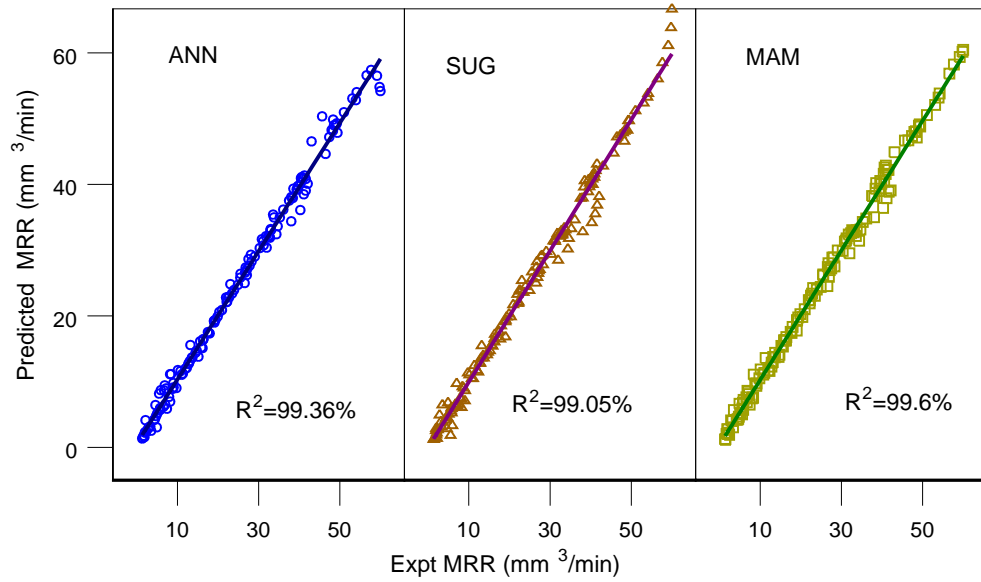


Fig. 5.17: Comparison of model predictions with experimental MRR

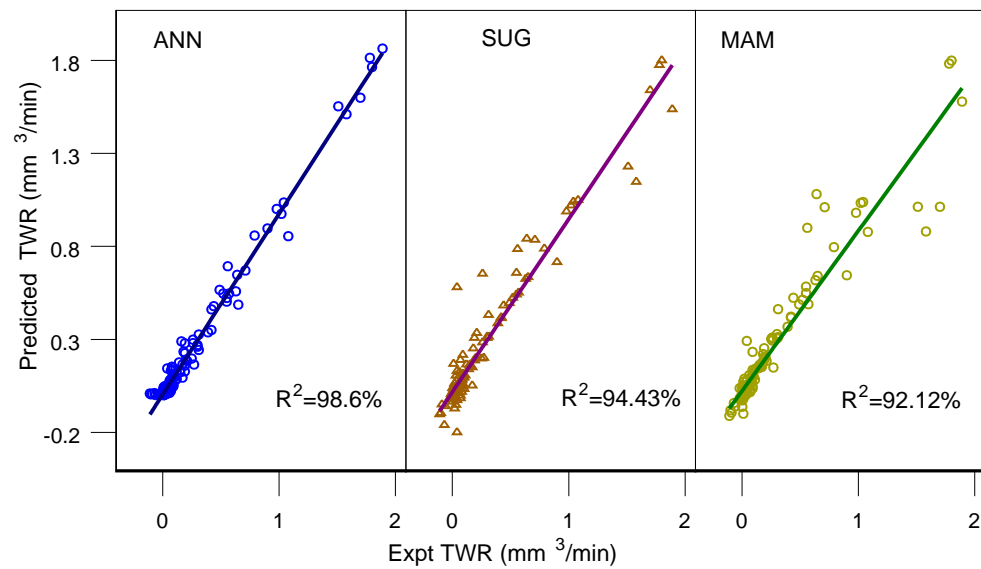


Fig. 5.18: Comparison of model predictions with experimental TWR

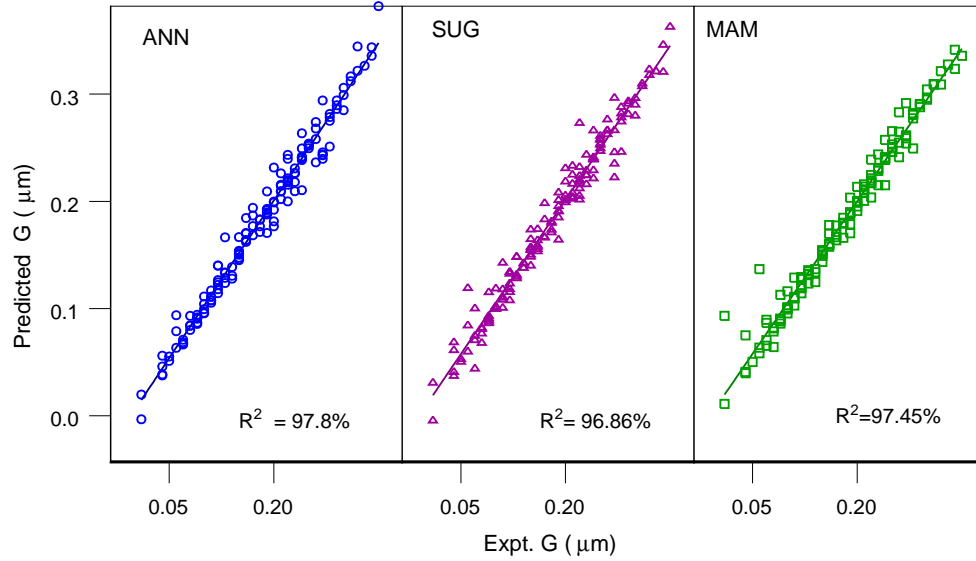


Fig. 5.19: Comparison of model predictions with experimental G

#### Prediction error

Prediction error is a powerful tool that assesses the performance of a proposed model, in which the prediction model is validated with a new set of data that was not earlier used to develop or test the model. Prediction error has been defined as follows

$$\text{Prediction error \%} = \frac{|\text{Expt. Value} - \text{Pred. Value}|}{\text{Expt. Value}} \times 100 \quad (5.4)$$

where Expt. Value = experimental value and Pred. Value = predicted value by the model.

A comparison of predicted and experimental values are listed in Table 5.5, Table 5.6 and Table 5.7 for MRR, TWR and G, respectively. To estimate the precision of the prediction model, percentage prediction error and average percentage error were used. The average prediction error is calculated by averaging the prediction error of responses. The experimental values were evaluated with the predicted values from the developed models and it was found that the average absolute prediction errors of MRR model are ranging from 5.42%, 4.94% and 4.98% for ANN, Sugeno system and Mamdani system, respectively. The average absolute prediction errors of TWR model are ranging from 15.21 %, 14.25% and 16.22 % for ANN, Sugeno system and Mamdani system, respectively. The percentage error seems to be more because the values of TWR are very small and sometimes even negative. The prediction errors of

overcut are however 6.51%, 7.19% and 4.29% for ANN, Sugeno system and Mamdani system, respectively. Consequently, the prediction accuracy of the model emerges agreeable.

## 5.5 Conclusion

This research demonstrated a comparative analysis of the modelling approaches by an artificial neural network and two neuro-fuzzy systems (Sugeno and Mamdani type) for the prediction of MRR, TWR and overcut of AISI D2 tool steel using EDM. A mixed-level full factorial design of experiments was employed to generate the input-output database necessary for the development of the models. The ANN and the neuro-fuzzy models are developed using these experimental data and the performance of the models are compared based on prediction accuracy.

- The analysis of variance reveals that the discharge current is the most dominant factor, followed by  $Ton$ ,  $Tau$  and  $V$ , for the responses MRR and G. Whereas, the same for TWR is  $Ton$ ,  $Ip$ ,  $V$  and  $Tau$ . The responses MRR, TWR and G are directly proportional to the discharge current in the EDM process.
- The performance of ANN, Sugeno and Mamdani system models for predicting MRR, TWR and G are found to be comparable in terms of the prediction accuracy and speed. However, the Mamdani model is converging with a lower MSE than the Sugeno system, and the ANN network is in general converging much faster than the other two.
- The average prediction errors in MRR are below 6% and below 7.2% for overcut prediction for all the proposed models. Eventually, the average prediction errors for TWR of all the models are comparatively high and are in the range of 14-16%.
- Satisfactory agreement between the experimental and proposed model results were obtained from using this type of network. Hence, it can be said that ANN, Sugeno system, Mamdani system model can be used successfully model EDM



process, resulting in reliable predictions, and providing a possible way to avoid time and money-consuming experiments.

Table 5.5: Testing the capability of all the models for prediction of MRR

Run Order	Experimental Parameters				Expt value	Model Prediction			Prediction Error		
	$I_p$	$Ton$	$Tau$	$V$		ANN	SUG	MAM	ANN	SUG	MAM
3	16	400	85	60	40.490	40.352	40.035	40.406	0.34	1.12	0.21
20	13	300	90	60	41.110	38.468	35.554	37.893	6.43	13.51	7.82
33	13	500	80	60	26.560	24.991	25.014	24.513	5.91	5.82	7.71
45	16	100	90	40	59.980	54.172	66.699	60.444	9.68	11.20	0.77
55	13	300	85	60	34.660	33.636	31.815	33.120	2.96	8.21	4.44
58	7	400	85	40	11.350	11.228	12.459	13.598	1.07	9.77	19.80
69	13	200	85	40	40.620	41.111	41.500	42.555	1.21	2.17	4.76
73	16	100	80	60	33.560	35.388	33.413	32.133	5.45	0.44	4.25
94	13	400	90	40	45.640	50.333	44.793	46.665	10.28	1.86	2.25
110	13	100	80	60	27.490	28.618	27.070	27.224	4.10	1.53	0.97
121	7	300	90	40	15.860	15.213	15.432	16.281	4.08	2.70	2.65
132	16	400	80	40	38.380	37.919	39.630	39.342	1.20	3.26	2.51
142	13	300	85	40	40.420	40.954	40.830	41.605	1.32	1.01	2.93
143	4	300	85	40	7.420	5.885	6.596	6.487	20.69	11.10	12.57
150	7	200	85	40	16.170	15.101	16.116	16.330	6.61	0.34	0.99
Average prediction error(%)									5.42	4.94	4.98

Table 5.6: Testing the capability of all the models for prediction of TWR

Run Order	Experimental Parameters				Expt value	Model Prediction			Prediction Error		
	$I_p$	$T_{on}$	$Tau$	$V$		ANN	SUG	MAM	ANN	SUG	MAM
3	16	400	85	60	-0.120	-0.090	-0.096	-0.100	25.00	20.00	16.67
20	13	300	90	60	0.110	0.081	0.107	0.080	26.36	2.73	23.49
33	13	500	80	60	0.010	0.008	0.013	0.010	19.00	25.00	18.50
45	16	100	90	40	1.890	1.863	1.537	1.580	1.46	18.66	16.50
55	13	300	85	60	0.060	0.078	0.058	0.060	30.17	3.17	6.27
58	7	400	85	40	0.010	0.009	0.009	0.010	13.00	12.00	21.50
69	13	200	85	40	0.390	0.338	0.387	0.370	13.26	0.69	5.70
73	16	100	80	60	1.580	1.510	1.148	0.980	4.44	27.36	37.96
94	13	400	90	40	0.020	0.024	0.023	0.020	18.00	13.20	13.51
110	13	100	80	60	0.900	0.896	0.717	0.760	0.43	20.34	15.06
121	7	300	90	40	0.023	0.025	0.019	0.020	8.70	16.96	4.35
132	16	400	80	40	0.090	0.078	0.072	0.070	13.78	19.80	18.14
142	13	300	85	40	0.090	0.091	0.086	0.110	1.11	4.23	26.80
143	4	300	85	40	0.020	0.013	0.024	0.020	34.00	19.50	7.01
150	7	200	85	40	0.070	0.084	0.081	0.060	19.43	16.14	11.82
Average prediction error(%)									15.21	14.25	16.22

Table 5.7: Testing the capability of all the models for prediction of G

Run Order	Experimental Parameters				Expt value	Model Prediction			Prediction Error		
	$I_p$	$T_{on}$	$Tau$	$V$		ANN	SUG	MAM	ANN	SUG	MAM
3	16	400	85	60	0.260	0.268	0.276	0.283	3.04	6.31	8.87
20	13	300	90	60	0.300	0.306	0.290	0.295	1.97	3.27	1.72
33	13	500	80	60	0.240	0.249	0.241	0.241	3.88	0.46	0.51
45	16	100	90	40	0.200	0.177	0.231	0.213	11.65	15.45	6.70
55	13	300	85	60	0.210	0.216	0.225	0.211	2.62	7.14	0.58
58	7	400	85	40	0.160	0.185	0.156	0.158	15.31	2.81	1.48
69	13	200	85	40	0.230	0.209	0.216	0.215	8.96	6.09	6.51
73	16	100	80	60	0.220	0.243	0.273	0.239	10.64	24.14	8.56
94	13	400	90	40	0.260	0.274	0.266	0.265	5.35	2.38	1.87
110	13	100	80	60	0.190	0.193	0.208	0.203	1.53	9.63	7.03
121	7	300	90	40	0.120	0.126	0.133	0.119	5.33	10.42	0.91
132	16	400	80	40	0.300	0.285	0.280	0.304	5.03	6.70	1.48
142	13	300	85	40	0.210	0.215	0.233	0.216	2.38	11.10	2.77
143	4	300	85	40	0.100	0.111	0.100	0.095	11.20	0.30	4.50
150	7	200	85	40	0.140	0.128	0.142	0.125	8.71	1.64	10.84
Average prediction error(%)									6.51	7.19	4.29

# Chapter VI

## Conclusion

## 6. CONCLUSION

In this research, the surface integrity, productivity and accuracy of AISI D2 tool steel components using copper electrode have been investigated for EDM process. The experiments were conducted under various parameter settings of Discharge Current ( $I_p$ ), Pulse On-Time ( $T_{on}$ ), Duty Factor ( $Tau$ ) and Discharge Voltage ( $V$ ). RSM modelling was performed for WLT, SCD and Surface roughness. ANSYS software was used for FEM modelling of residual stress on EDMed surface and sub-surfaces. Finally, the soft computing techniques were employed for modelling of MRR, TWR and Radial overcut. These responses were validated experimentally.

### *RSM modelling for WLT and SCD*

1. It is found that  $I_p$  is the most dominating parameter followed by  $T_{on}$  for WLT and SCD. WLT is directly proportional to  $I_p$ ,  $T_{on}$  and  $Tau$ . But, SCD is inversely proportional to  $I_p$  and  $T_{on}$  and varies directly with  $V$ .
2. The average SCD is inversely proportional to the average pulse power and its value decreases from  $0.0547 \mu/mm^2$  to  $0.0146 \mu/mm^2$ , when power level change from 36w to 486 w. However, the WLT increases monotonically with power from  $17.25 \mu$  to  $35.72 \mu$  for the same change in power level.
3. The prime aim should be to select factors such that formation of the white layer is minimum, though it tends to increase the SCD, but as the cracks are limited to the white layers only, which is generally removed by polishing.
4. The optimal parameter settings for WLT were found to be  $I_p=1$  A,  $T_{on}=50 \mu s$ ,  $Tau=80$  % and  $V=40$  volt, within the parameter range of this study. According to the confirmatory test results, the RSM model could predict WLT with an

---

average prediction error of 5.76%. The prediction error for the proposed RSM model for SCD was found to be 5.79 % for the same parameter setting.

### *RSM modelling for SR*

5.  $I_p$  is the most dominating parameter influencing the SR.  $T_{on}$  and  $T_{au}$  are other two parameters that significantly influence the SR.
6. The results reveal that, within the parameter range of this study,  $I_p$ ,  $T_{on}$  and  $T_{au}$  should be at their low levels ( $I_p=1A$ ,  $T_{on}= 50 \mu s$  and  $T_{au} 80\%$ ) for better surface finish.
7. The size of the crater increases with an increase in  $I_p$  and  $T_{on}$ , since these factors are responsible for producing stronger spark energy,so bigger crater and rough surface are produced.

### *FEM modelling for RS*

8. It is observed that the compressive thermal stresses are developed beneath the crater and the tensile stresses are occur away from the axis of symmetry.
9. FEM results show the peak temperature on the crater surface sharply increases with  $I_p$  and slightly decreases with  $T_{on}$ . The peak temperature of 3800 K was attained on the crater surface with  $I_p= 9A$ , whereas the same for  $I_p= 1A$ , it is 2300 K.
10. The workpiece is severely affected by the thermal stresses to a larger depth with increasing pulse energy. The nature of residual stresses is predominantly tensile.
11. FEM results show that the magnitudes of the radial component of the residual stress on the surface are predominant than the other components for all the machining parameter combinations. The maximum value of this stress is 529.2 MPa for  $I_p= 9 A$  and  $T_{on} = 100 \mu s$ , which occurs at a distance of  $71.7 \mu$ . The axial component of residual stress is minimum on the surface and increases as the path rotating towards the symmetry path.

12. The experimental results indicate that the radial component of residual stress reaches its maximum value close to the surface, but diminishes very rapidly to comparatively low value of compressive residual stress in the sub-surface area. The trend of this stress with depth has an excellent agreement with FEM results.
13. FEM result shows that radial components of the residual stress, predominantly tensile in nature. The magnitude increases from the top surface to its maximum value of approximately 600 MPa for all combinations of machining parameter setting. But, the depth at which this stress occurs, increases with the pulse energy. However, the shape of the graph of residual stress versus depth does not change with the machining parameters, in general.

#### *Soft computing modelling for MRR, TWR and G*

14. The analysis of variance reveals that the  $I_p$  is the most dominant factor, followed by  $Ton$ ,  $Tau$  and  $V$ , for the responses MRR and G. Whereas, the same for TWR is  $Ton$ ,  $I_p$ ,  $V$  and  $Tau$ .
15. The performance of ANN, Sugeno and Mamdani system models for predicting MRR, TWR and G are found to be comparable in terms of the prediction accuracy. The average absolute prediction errors of MRR model are ranging from 5.42%, 4.94% and 4.98% for ANN, Sugeno system and Mamdani system, respectively.
16. For TWR model average absolute prediction errors are ranging from 15.21 %, 14.25% and 16.22 % for ANN, Sugeno system and Mamdani system, respectively.
17. The average absolute prediction errors of overcut are 6.51%, 7.19% and 4.29% for ANN, Sugeno system and Mamdani system, respectively.
18. However, the Mamdani model is converging with a lower MSE than the Sugeno system and the ANN network is in general converging much faster than the



other two.

This research study portrays the surface integrity phenomena, productivity and accuracy with statistical, finite element modelling and soft computing modelling in EDMed surfaces in detail. These findings will be ready to lend a hand to the EDM researchers and manufacturing engineers in selecting the appropriate parametric combinations for EDMing AISI D2 tool steel. It is expected these models and experimental data in this work to become a powerful tool and data in the hands of EDM researchers to not only extend the understanding of the process but also for better process and product design.

### *6.1 Major Contribution*

1. The performance of ANN, Sugeno and Mamdani system models for predicting MRR, TWR and G are found to be comparable in terms of the prediction accuracy and speed.
2. The trend of the radial component of the residual stress with depth obtained from XRD results and FEM predictions have an excellent agreement.
3. FEM results show that the workpiece yields upto depth of 11.5, 16.6, 23.06 and 42.2  $\mu\text{m}$  for 1/20, 1/100, 9/20 and 9/100 discharge current/ pulse on time parameter combinations, respectively.

## 6.2 Recommendations for Future Research

Analysis of the results acquired from the current work advocates quite a few possible extensions to the research. A few of them are listed

1. Very little work has been reported yet to explore the effect of non-electrical parameters like workpiece rotation and electrode rotation.
2. Apart from the existing modelling in FEM of single discharge, there are ample scope for modelling for the multi-spark modelling and process simulation.
3. Soft computing modelling of other hybridization technique and optimization of these are still not employed extensively, hence, in future it will be an emerging area.
4. The multi objective optimisation of all these responses can be performed.
5. Soft computing model can be attempted for WLT, SCD and SR.
6. The experiments can be performed using with different dielectrics like deionised water and other environment friendly dielectric fluid.

## APPENDIX

## A. EQUIPMENTS USED

### *Machine and Equipment*

This machine was used to machine on the AISI D2 tool steel for conducting the Experiments



Fig. A.1: Die Sink EDM, Brand : Electronica Elektra Plus; Model : PS 50ZNC

Table A.1: Technical Specifications of electro discharge machine

Machine Tool	PS50 ZNC
Work tank internal dimensions (W x D x H)	800 x500 x 350 mm
Work table dimensions	550 x 350 mm
Transverse(X,Y,Z)	300, 200, 250 mm
Maximum job weight	300 kg
Maximum electrode weight	100 kg
Maximum job height above the table	250 mm
Feed motor / servo system for Z axis	DC Servo
Position measuring system (X, Y, Z)	Incremental linear scale
Dielectric system	Integral with the machine tool
Dielectric capacity	400 Litres
Filter element	10 $\mu$ paper cartridge 2 nos.
Pulse Generator	S 50 ZNC
Pulse generator type	MOSFET
Current range, Ip	0-50 A
Pulse on time range Ton	0.5-4000 $\mu$ s
Duty factor range, Tau	50-93%
open circuit voltage, V	40-60 v
Power supply	3 phase, AC 415 V*, 50 Hz
Connected load	6KVA includes PF unit

*Workpiece Material and Electrode Material*



Fig. A.2: Copper Electrode and AISI D2 workpiece for MRR, TWR and OC

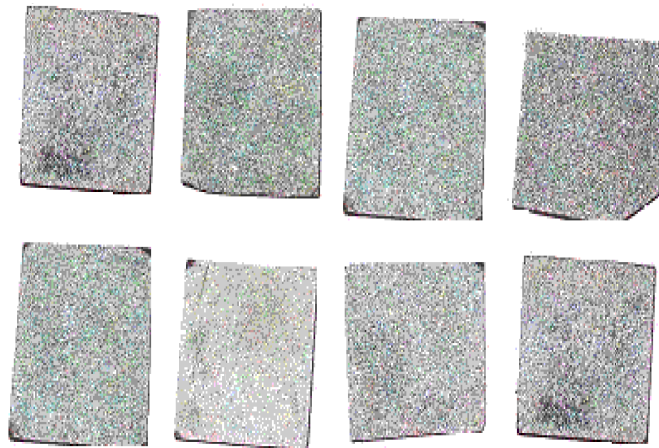


Fig. A.3: AISI D2 workpiece for WLT, SCD, SR and RS

Table A.2: Chemical composition of AISI D2 (wt %)

Cr	Mo	V	C	Mn	Si	Ni	Fe
12	0.80	0.10	1.52	0.30	0.3	0.3	Balance

Table A.3: Thermal properties of workpiece material (Kansal et al., 2007)

Temperature (K)	Thermal conductivity (W/m°C)	Coefficient of thermal expansion (/°C)	Specific heat (J/kg/K)
298	29.0	$5.71 \times 10^{-6}$	412.21
673	29.5	$6.90 \times 10^{-6}$	418.36
1100	30.7	$10.20 \times 10^{-6}$	421.83
1990	32.3	$12.00 \times 10^{-6}$	431.00

Table A.4: Temperature dependent modulus of elasticity, Poisson's ratio and density of Tool steel (Bhadeshia, 2002)

Temperature (K)	$E$ (GPa)	$\nu$	Density ( $kg/m^3$ )
300	210	0.28	7700
600	193	0.3	
900	165	0.31	
1200	120	0.33	

Table A.5: Temperature dependent yield stress of steel (Barsoum, 2008; Jonsson et al., 1985)

Temperature (K)	Yield stress (MPa)	Tangent modulus (GPa)
300	450	0.99526
600	230	14.77512
900	140	9.42857
1200	30	0.49793

Tangent modulus is defined as the slope of a stress-strain curve at a specified point on that curve;

*Induction furnace*

The workpieces are heat treated in this furnace to remove the residual stress.



*Fig. A.4: Induction furnace*  
Brand : BYSAKH and Co. Calcutta, INDIA  
Model : OKAY Electric Muff Furnace



### *Weighing machine*

Precision balance was used to measure the weigh of the workpiece and tool.



*Fig. A.5: Electronic Balance*  
Brand:SHINKO DENSHI Co. LTD, JAPAN, Model: DJ 300S  
Capacity: 300 gram  
Accuracy: 0.001 gram

### *Surface Roughness Analyser*

Surface roughness of the EDMed component was measured using this machine.



*Fig. A.6: Talysurf Surface Roughness Analyser*  
Brand : Taylor Hobson, Model : Surtronic 3<sup>+</sup>

*Grinder and polisher*

This polisher and grinder was used to remove the layers while measuring the residual stress. Polished consecutively on silicone carbide paper with grit sizes 120, 220, 320, 400, and 800. Polishing process was done by using Mecaprex polishing cloth. Finally, the specimen was polished with diamond paste of  $1\ \mu\text{m}$ . The surface was subsequently electro polished with a slurry of Trinity diamond compound and HIFIN Fluid-“OS” Type.



Fig. A.7: Electro Polishing

*Tool maker microscope*

This machine was used to measure the radial overcut which was occurs during EDM



Fig. A.8: Tool maker microscope  
Make : Carl Zeiss, Germany  
Accuracy : 0.001 mm

*Scanning electron microscopy (SEM)*

This equipment was used to analyse and measure the thickness of white layer, surface crack analysis and qualitative analysis of the surface.



*Fig. A.9:* Scanning electron microscopy  
Brand:Jeol, Japan  
Model:Jeol JSM-6480LV,

*X-Ray Diffraction*



*Fig. A.10:* Panalytical MRD System for Bulk Texture and Residual Stress Measurement

Brand : Philips X'Pert MRD horizontal goniometer

Model :PW3050/65 HR

Courtesy: National Facility of Texture & OIM  
Department of Metallurgical Engg and Materials Science,  
Indian Institute of Technology - Bombay, Mumbai, India

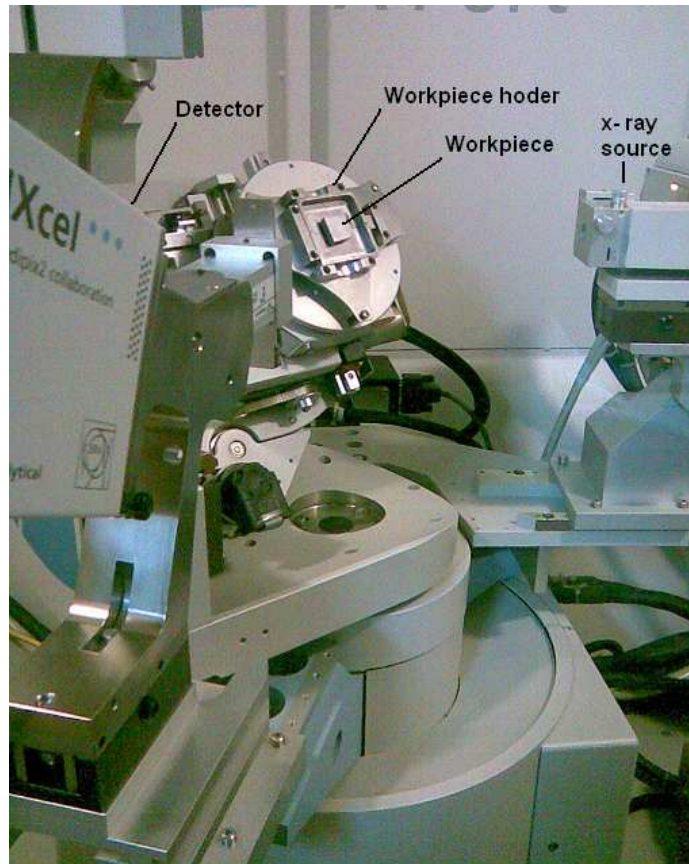


Fig. A.11: X-ray texture and/or residual stress measurements  
Courtesy: National Facility of Texture & OIM  
Department of Metallurgical Engg and Materials Science,  
Indian Institute of Technology - Bombay, Mumbai, India

## B. DESIGN OF EXPERIMENTS

With the advance of modern technology, the products and processes are becoming extremely complicated. In engineering and scientific decision-making, experiments are an essential part and quite often they have to deal with such processes where no scientific theory or principles are available. In such circumstances, to develop new products and processes, Design of Experiments (DOE) techniques become extremely essential to explain the statistical significance of an effect that a particular factor exerts on the dependent quality parameter of interest in a cost-effective and confident manner. Since the expense of experimentation is climbing quickly, it is becoming difficult for the analyst, who is already constrained by resources and time, to investigate the various factors that are affecting these complex processes by trial and error methods. Thus, the analyst will be interested for a technique which will identify “vital few” factors in the most efficient manner then directs the process to its best setting to meet the growing demand for enhanced quality and better productivity. However, in case of industrial goal, it is usually to extract the maximum amount of unbiased information about the factors which are affecting a production process from as few observations as possible. It has been used around since the 1920's and has been used fruitfully in industry since the 1950's.

DOE is a tool to develop an experimentation strategy. It is extensively used in the improvement of manufacturing processes to maximize yield and reduce variability. To achieve these objectives, properly designed experiments are much more efficient than that of one-factor-at-a-time experiments, which involve changing a single factor at a time to study the effect of the factor on the response. When the effect that a factor has on the response is changed due to the presence of one or more other factors, that relationship is called an ‘interaction’. Sometimes the interaction effects are more significant than the individual factor effect. This is because the application



environment of the response comprises the presence of many of the factors together instead of isolated occurrences of single factors at different times.

Some of the most popular experimental strategies are Factorial design, Taguchi's design, and RSM. 'Factorial' or 'Classical DOE' was the first technique used with DOE, which allows to distinguish which factors are most significant and helps in identifying important interactions among the factors. It doesn't predict the best factor levels to meet the goals. The main aim of Taguchi's design is to find a 'robust' answer that is insensitive to factor variations and noise. RSM consists of an experimental strategy for exploring the settings of input variables and to develop a quadratic model suitably approximating relationship between the response and the input parameters. Subsequently, optimizing the levels or values of the input variables that produce desirable response value. this method is described in details in the next section.

### *Response surface methodology*

RSM is a specific DOE for developing, improving, and optimizing products and processes. It is a combination of statistical and optimization methods that can be used to model and optimize designs. It has many applications in design, analysis and enhancement of products and processes. As a collection of statistical and mathematical methods, using these one can essentially predict the best combination of factors to meet the goals.

Since, the relation is either too complex or unknown, therefore an empirical approach is essential. Frequently, for a system with non-linear behaviour, a second-order model is suitable in a comparatively small region of the variable space. The method of least squares estimation is used to estimate the coefficients in the polynomials (Montgomery, 2003).

### *Procedure of RSM*

RSM is sequential in nature and at the outset, screening experiments are conducted to reduce the list of contestant variables to a comparatively few. The techniques for the analysis of the second-order model are presented by Myers and Montgomery (1995). The steps shown below are typical of a response surface experiment. Depending on



the experiment, one may carry out some of the steps in a different order, perform a given step more than once, or eliminate a step.

- Choose the response for an experimental investigation. Determine what the influencing factors are, that is, what the process conditions are those influence the values of the response variable.
- Create the response surface experiment design according to a central composite design.
- Set the factor levels and replicate the design.
- Randomize the design to change the order of the runs.
- Perform the experiment and collect the response data.
- Analyze the response surface design to fit a model to the experimental data.
- Optimize the response to obtain a numerical and graphical analysis.

#### *Formulas used*

A second-order model is given as below:

$$y = \beta_0 + \sum_{i=1}^m \beta_i x_i + \sum_{i=1}^m \beta_{ii} x_i^2 + \sum_{i,j=1, i \neq j}^m \beta_{ij} x_i x_j + e \quad (\text{B.1})$$

Where  $y$  = response,  $x_i$  =  $m$  independent variables

$\beta_i$ ,  $\beta_{ii}$  = unknown coefficients are the estimates of the population regression coefficients and  $e$  = random error term.

In Equation B.1, let the square terms of the variables  $x_{ii}^2 = x_j$  for  $(i = 1, 2, \dots, m)$  and  $j = m + 1, m + 2, \dots, 2m$ . Similarly, let the interaction terms  $x_{ij}^2 = x_j$  for  $(i = 1, 2, \dots, m)$  and  $j = 2m + 1, 2m + 2, \dots, 2m + 1 + \frac{k(k+1)}{2}$ .

Equation B.1 can be written as a multiple linear regression model as follows:

$$y = \sum_{i=0}^p \beta_i x_i + e \quad (\text{B.2})$$

where  $p = 2m + 1 + \frac{m(m+1)}{2}$ . In matrix notation, the above equation (Equation B.2) can be represented as:

$$\mathbf{Y} = \mathbf{X}\mathbf{b} + \mathbf{e} \quad (\text{B.3})$$

where  $\mathbf{Y}$  = an  $(n \times 1)$  vector of the observations, where  $n$ =number of observations ( $n > p$ ),

$\mathbf{X}$  = a design matrix  $(n \times p)$  in canonical form of the variables,

$\mathbf{b}$  = an  $(p \times 1)$  vector of the regression coefficients, and

$\mathbf{e}$  = an  $(n \times 1)$  vector of random errors.

**Design matrix  $\mathbf{X}$ :** The design matrix has  $n$  rows and several blocks of columns, corresponding to the terms in the model.

**Coefficients,  $\beta_i$ :** Coefficients are the estimates of the population regression coefficients,  $b_i$ . In matrix terms, the vector of coefficients  $\mathbf{b}$  is calculated by the formula:

$$\mathbf{b} = (\mathbf{X}'\mathbf{X})^{-1}(\mathbf{X}'\mathbf{Y}).$$

The  $\mathbf{b}$ ,  $\mathbf{Y}$ ,  $\mathbf{e}$  and  $\mathbf{X}$  vectors or matrix for response WLT from Table 2.2 are as shown below.

$$\mathbf{b} = \left[ b_0 \quad b_1 \quad b_2 \quad b_3 \quad b_4 \quad b_5 \quad b_6 \quad b_7 \quad b_8 \quad b_9 \quad b_{10} \quad b_{11} \quad b_{12} \quad b_{13} \quad b_{14} \right]'$$

$$\mathbf{Y} = \begin{bmatrix} 39.21 \\ 31.23 \\ 25.68 \\ 16.81 \\ 26.00 \\ 37.02 \\ 19.43 \\ 25.51 \\ 9.43 \\ 19.50 \\ 32.85 \\ 31.59 \\ 18.89 \\ 23.18 \\ 46.60 \\ 31.59 \\ 25.64 \\ 17.18 \\ 27.65 \\ 6.19 \\ 30.07 \\ 21.04 \\ 29.60 \\ 40.59 \\ 27.30 \\ 32.87 \\ 22.87 \\ 31.66 \\ 27.49 \\ 25.74 \end{bmatrix} \quad \mathbf{e} = \begin{bmatrix} e_0 \\ e_1 \\ e_2 \\ e_3 \\ e_4 \\ e_5 \\ e_6 \\ e_7 \\ e_8 \\ e_9 \\ e_{10} \\ e_{11} \\ e_{12} \\ e_{13} \\ e_{14} \\ e_{15} \\ e_{16} \\ e_{17} \\ e_{18} \\ e_{19} \\ e_{20} \\ e_{21} \\ e_{22} \\ e_{23} \\ e_{24} \\ e_{25} \\ e_{26} \\ e_{27} \\ e_{28} \\ e_{29} \end{bmatrix}$$



**Fitted values or predicted values,  $\hat{y}$ :** The fitted values are point estimates of the mean response for the given values of the predictors.

**Residuals,  $e_i$ :** Residuals are the difference between the observed values and predicted or fitted values. For the  $i^{th}$  observation it is expressed as:

$$e_i = (y_i - \hat{y}_i)$$

**Standardized or studentized residuals,  $z_i$ :** The residual  $e_i$  scaled by its standard deviation. The observations having more than  $\pm 2$  standardized residual are identified as outliers with 95% confidence. The formula is:

$$z_i = \frac{e_i}{\text{sqrt}[MSE(1 - h_i)]}$$

where MSE = mean square error and  $h_i$  = leverage. The denominator is an estimator of the standard deviation of  $e_i$ .

**Standard error of fitted value (SE fit):** The estimated standard deviation of the fitted value at a given predictor point  $\mathbf{X}'_0 = [\mathbf{1}, \mathbf{x}_{1,0}, \dots, \mathbf{x}_{m,0}]$  is given formula as

$$\sqrt{(s^2[\mathbf{X}'_0(\mathbf{X}'\mathbf{X})^{-1}\mathbf{X}_0])}$$

where  $s^2$  = MS Error.

**Confidence interval:** The range in which the estimated mean response for a given set of predictor values is expected to fall. The interval is defined by lower and upper limits, which is calculated from the confidence level and the standard error of the fits. The formula is:

$$\hat{y}_0 \pm t(1 - \alpha/2; n - p) * s(\hat{y}_0)$$

where  $\alpha$  = chosen risk value, n = number of observations, p = number of predictors, and

$$s(\hat{y}_0) = \sqrt{[s^2(\mathbf{X}'_0(\mathbf{X}'\mathbf{X})^{-1}\mathbf{X}_0)]}$$

where  $s^2$  = mean square error.

**Leverages:** This statistic indicate whether an observation has unusual predictor values compared to the rest of the data. An observation with large leverage value will exert significant influence on the fitted value as well as on the regression model.

The leverage of the  $i^{\text{th}}$  observation,  $h_i$  is the  $i^{\text{th}}$  diagonal element of the hat matrix  $\mathbf{H}$ , which is a  $(n \times n)$  projection matrix specified as:

$$\mathbf{H} = \mathbf{X}(\mathbf{X}'\mathbf{X})^{-1}\mathbf{X}'$$

Its value falls between 0 and 1 and the observations with considerable large leverage should be examined.

### Central composite design

The Central Composite Design (CCD) is a design extensively used for approximating second order response surfaces. It is possibly the most widely accepted set of second order designs. It was presented initially by Box and Wilson (1951), the CCD has been popular among the researchers. There are  $2^m$  numbers of cube points, axial points and centre points (at least 3-5 points). If the design is blocked the center points are divided equally among the blocks. A face centered design  $\alpha = 1$  is chosen so that the axial points lie on the face of the cube as shown in Fig. B.1 for two variables. The two important properties of CCD are orthogonality and rotatability. An orthogonal block design allows for model terms and block effects to be estimated independently and minimize the variation in the regression coefficients. A rotatable design provides the desirable property of constant prediction variance at all points that are equidistant from the design center, thus improving the quality of the prediction.

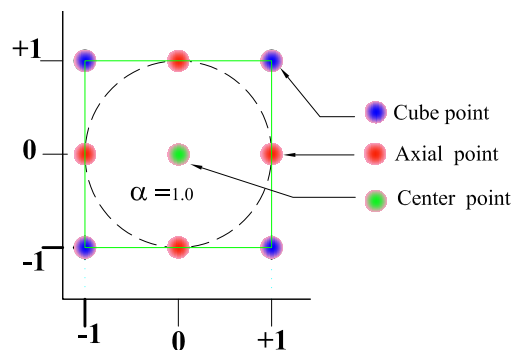


Fig. B.1: Two-Variable Face Centered CCD

## Analysis of Variance (ANOVA)

Experimental factors will influence the response and so will be due to unknown causes or measurement errors in experiments, there exists some variability. Every experimental data set is most likely to shown certain variability, but wheather such change is due to inputs factors or dur to random factors is to be answered by ANOVA. The method tries to carry out the following.

- Decomposes the deviation of the experimental data in relation to possible sources; the source may be from the main effect, from the interaction, or may be from experimental error.
- Measures the magnitude of variation due to all sources.
- Recognize the main and interactions effects which have significant effects on variation of data.

### Sum of Squares (SS)

The distance between any point in a set of data and the mean of the data is the deviation. Sum of Squares is the sum of all such squared deviations.  $SS_{Total}$  is the total variation in the data.  $SS_{Regression}$  is the portion of the variation explained by the model, while  $SS_{Error}$  is the portion not explained by the model and is attributed to error. The calculations are:

$$SS_{Total} = \sum_i^n \sum_j^r (y_{ij} - \bar{y}_{..})^2 \quad (B.4)$$

$$SS_{Error} = \sum_i^n \sum_j^r (y_{ij} - \hat{y}_i)^2 \quad (B.5)$$

$$SS_{Regression} = SS_{Total} - SS_{Error} \quad (B.6)$$

where  $y_{ij} = i^{th}$  observed response of  $j^{th}$  replicate,  $\hat{y}_i = i^{th}$  fitted response, and  $\bar{y}_{..} =$  mean of all  $(n \times r)$  obeservations.

The sum of squares for r set of replicates are calculated and added together to create the pure error sum of squares ( $SS_{PE}$ ). Sum of square error  $SS_{Error}$  is the sum of pure error sum of squares  $SS_{PE}$  and sum of squares lack of fit  $SS_{LOF}$ .

$$SS_{PE} = \sum_i^n [\sum_j^r (y_{ij} - \bar{y}_{i.})^2] \quad (\text{B.7})$$

$$SS_{LOF} = SS_E - SS_{PE} \quad (\text{B.8})$$

where  $\bar{y}_{i.}$  = mean of r replicates of  $i^{th}$  observed response.

### Degree of Freedom

It depicts the number of independent variables needed to calculate the sum of squares the response data. The degrees of freedom for each component of the model are:

$$\begin{aligned} DF_{Regression} &= t - 1 \\ DF_{Error} &= n - t \\ DF_{Total} &= n - 1 \\ DF_A &= a - 1 \\ DF_B &= b - 1 \\ DF_{AB} &= (a - 1)(b - 1) \\ DF_{PE} &= n - m \end{aligned} \quad (\text{B.9})$$

where n = number of observations, t = number of terms in the model, a, b = number of levels of factors A and B, respectively. DOF of pure error  $DF_{PE}$  is n - m, where n = number of observations and m = the number of distinct x-values.

### Mean Square

In an ANOVA, the term Mean Square refers to an estimate of the population variance based on the variability among a given set of measures. The calculation for the mean square for the model terms is:

$$MS_{Term} = \frac{AdjSS_{Term}}{DF_{Term}} \quad (\text{B.10})$$

**F-value:** F-value is the measurement of distance between individual distributions. More the F-value, less is the P-value. F is a test to determine whether the interaction



and main effects are significant. The formula for the model terms is:

$$F = \frac{MS_{Term}}{MS_{Error}} \quad (\text{B.11})$$

Larger values of F support rejecting the null hypothesis that there is not a significant effect

**P-value:** P-value is used in hypothesis tests helps to decide whether to reject or fail to reject a null hypothesis. The p-value is the probability of obtaining a test statistic that is at least as extreme as the actual calculated value, if the null hypothesis is true. A commonly used cut-off value for the p-value is 0.10.

#### Model Adequacy Check

The adequacy of the underlying model can be checked from ANOVA as follows: It is always necessary to examine the fitted model to ensure that it provides an adequate approximation to the true system.

$R^2$  (R-sq): Coefficient of determination; indicates how much variation in the response is explained by the model. The higher the  $R^2$ , the better the model fits your data. The formula is:

$$R^2 = 1 - \frac{SS_{Error}}{SS_{Total}} \quad (\text{B.12})$$

Another presentation of the formula is:

$$R^2 = \frac{SS_{Regression}}{SS_{total}} \quad (\text{B.13})$$

**Adjusted  $R^2$**  (R-sq adj): Adjusted  $R^2$  accounts for the number of factors in your model. The formula is:

$$R^2 = 1 - \frac{MS_{(Error)}}{SS_{Total}/DF_{Total}} \quad (\text{B.14})$$

**Lack-of-fit test:** This test checks the straight line fit of the model. To calculate the pure error lack-of-fit test:

1. Calculate the pure error mean square:

$$MS_{PE} = \frac{SS_{PE}}{DF_{PE}}$$

2. Calculate the lack-of-fit mean square:

$$MS_{LOF} = \frac{SS_{LOF}}{DF_{SSE} - DF_{PE}}$$

3. Calculate the F-statistic =  $MS_{LOF}/MS_{PE}$  and corresponding p-value.

Large F-values and small p-values suggest that the model is inadequate.

### C. X-RAY DIFFRACTION TECHNIQUE

Residual stresses in a workpiece are a function of its material processing and machining history. The influence of which can be found by considering the material behaviour under real loading conditions. The main result of residual stresses on a mechanical component is the deformation due to the new state of equilibrium. There are several techniques using which residual stress can be measured. Hole drilling method, curvature method, Cutting method, X-Ray Diffraction (XRD), Neutron diffraction, electron diffraction method Electrical Resistance Method, are some of the examples. Among these, X-Ray Diffraction technique is most widely used Non Destructive technique for residual stress measurement. When a metal is under stress (residual), the elastic strains developed can alter spacing of the atomic planes in the metallic crystal structure. XRD technique makes use of the fact and can measure these inter atomic spacing, which is indicative of the elastic strain in the specimen and hence, to the stress.

XRD technique uses scanning of a selected peak with the specimen orientated at an increasing angle to the incident beam. The x-ray beam is directed onto the sample surface at the required location. The diffracted beam is detected by a position-sensitive proportional counter. The angular position ( $2\theta$ ) of the diffracted beam is used to determine the distance (d-spacing) between parallel planes of atoms using Bragg's law.

Diffraction occurs at an angle  $2\theta$ , defined by Bragg's Law:

$$n\lambda = 2d\sin\theta \tag{C.1}$$

where  $n$  is an integer value,  $\lambda$  is the wavelength of the X-ray beam (typically of the range 0.7 to 2  $\text{\AA}$ ) and  $\theta$  is the angle between the atomic planes and the incident (and diffracted) X-ray beam.

A change in the plane spacing ( $d$ ), causes a shift in the diffraction angle ( $2\theta$ ). In the figure a specimen is shown and surface set at two angles to the impinging X-ray,  $\psi = 0$  and  $\psi = \psi$  respectively. At  $\psi = 0$ , tensile stresses which may be present, result in a Poisson's ratio contraction and therefore a reduction the lattice spacing and slight increase in diffraction angle  $2\theta$  (Zwilsky, 1990). If the sample is then tilted through some known angle  $\psi$  (Fig. C.1 (b)), the tensile stress present in the surface increases the lattice spacing ( $d_\psi$ ) over the stress free state, and decreases  $2\theta$ . By measuring the alteration in an angular position of the diffraction peak for at least two orientations (such as  $\psi = 0$  and  $\psi = \psi$ ) of the sample, facilitates the measurement of the residual stress present in the surface lying in the plane of diffraction.

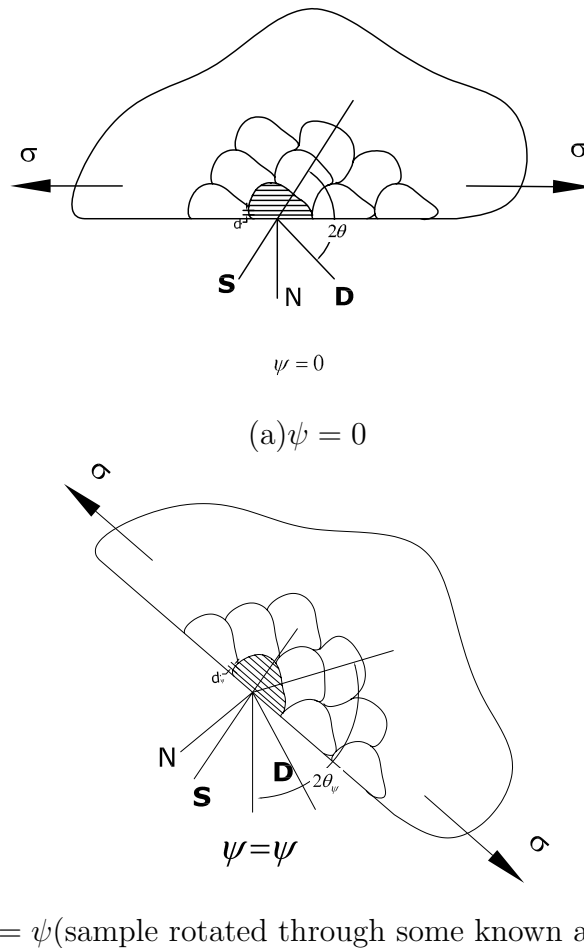


Fig. C.1: Schematic diagram of x-ray diffraction stress measurement of the orientation of the measured lattice planes related specimen structure. D:x-ray detector; S: X-ray source; N: normal to the surface.

In the surface a plane stress condition is assumed, i.e., a stress distribution de-

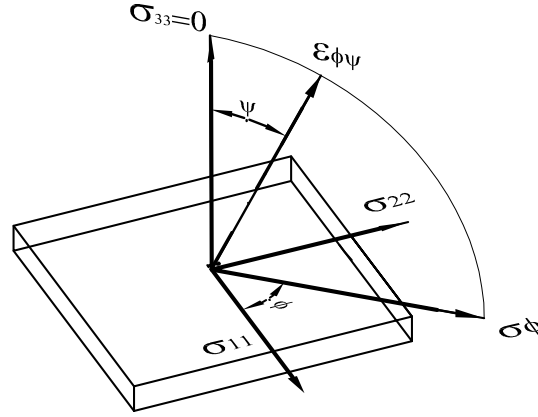


Fig. C.2: Plane stress elastic model of a flat specimen

scribed by principal stresses  $\sigma_{11}$  and  $\sigma_{22}$  exist in the plane of the surface with no stress in the perpendicular of the surface ( $\sigma_{33} = 0$ ) (Fig. C.2). The surface stress component,  $\sigma_{\phi}$  is

$$\sigma_{\phi} = \sigma_{11}\cos^2\phi + \sigma_{22}\sin^2\phi \quad (\text{C.2})$$

The strain component ( $\sigma_3$ ) perpendicular to the surface exists as a result of Poissons ratio contraction, caused by the two principal stresses. In general the strain is given as :

$$\epsilon_{33} = \frac{\sigma_3}{E} - \frac{\nu}{E}(\sigma_{11} + \sigma_{22}) \quad (\text{C.3})$$

In the situation described by Fig. C.1(b), the strain is as follows:

$$\epsilon_{\phi\psi} = \frac{1 + \nu}{E}(\sigma_{11}\cos^2\phi + \sigma_{22}\sin^2\phi)\sin^2\psi - \frac{\nu}{E}(\sigma_{11} + \sigma_{22}) \quad (\text{C.4})$$

Substituting Equation C.3 into Equation C.5, yields the strain ( $\epsilon_{\phi\psi}$ ) in the sample surface at an angle  $\phi$  from the principal stress  $\sigma_{11}$ :

$$\epsilon_{\phi\psi} = \frac{d_{\psi} - d_0}{d_0} = \left[ \frac{1 + \nu}{E}\sigma_{\phi}\sin^2\psi \right] - \left[ \left( \frac{\nu}{E} \right) (\sigma_{11} + \sigma_{22}) \right] \quad (\text{C.5})$$

where  $\sigma_{\phi}$  is the stress component along the  $\phi$  direction. When the  $\psi$  angle is set to 90 degrees, then the strain vector lies in the plane of the surface. Generally the XRD machine is set up according to the parameters detailed with the equipment and

initially a broad scan is carried out to find a chosen peak with the highest intensity. The specimen is then tilted at many  $\psi$  angles to obtain the data and a straight line is fitted by least square regression and plotted as a line graph (as shown in Fig. 4.11). The slope of the line which best fits the measured points is calculated as shown in Fig. 4.11. Equation C.5 shows that the slope of this graph is given as:

$$\text{Slope of Graph} = \frac{1 + \nu}{E} \sigma_{\phi} \quad (\text{C.6})$$

Stress is measured from the slop of the fitted line

$$\sigma_{\phi} = \frac{E}{1 + \nu} (\text{Slope of Graph}) \quad (\text{C.7})$$

## D. ARTIFICIAL NEURAL NETWORK

A neural network is designed from the inspiration of human brains to perform a particular task of interest; the network is usually implemented using electronic components or simulated in software on a digital computer. To achieve good performance, neural networks employ a massive interconnection of simple computing cells referred to as “neurons” or “processing units”.

Aleksander and Morton (1990) defined ANN as “A neural network is a massively parallel distributed processor that has a natural propensity for storing experimental knowledge and making it available for use”. It resembles the brain in two respects:

1. Knowledge is acquired by the network through a learning process.
2. Interneuron connection strengths known as synaptic weights are used to store the knowledge.

### *Model of a neuron*

How the brain trains itself to process information is not understood completely yet, so theories are abound. In the human brain, a typical neuron gather signals from others through a host of fine structures called dendrites. The neuron sends out spikes of electrical activity through axon that is generally a long and thin stand. Generally the axon is splits into thousands of branches. Towards the end of every branch, a synapse exists which exchange the activity from the axon into electrical effects that excite activity from the axon into electrical effects, which inhibit or excite activity in the associated neurons. A neuron collects excitatory input that is adequately big as compared to the inhibitory input and it sends a spike of electrical activity down its axon. Learning of the network takes place by altering the effectiveness of the synapses so that the influence of one neuron on another alters.

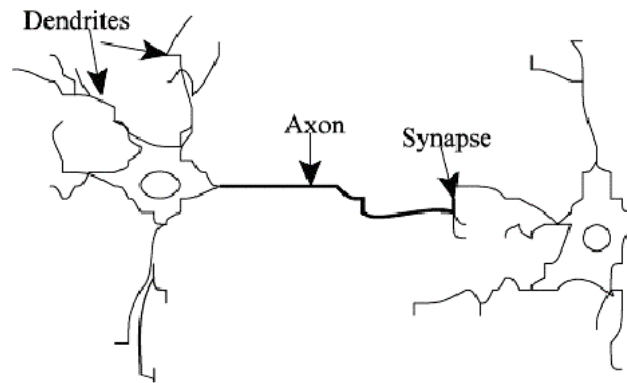


Fig. D.1: A Biological Neuron

In simulating biological neurons, first the essential features of neurons and their interconnections are deduced. To simulate these features a computer program is usually used. Nevertheless, since the knowledge of neurons is deficient and computing power is limited, the models are essentially gross idealizations of real networks of neurons. A neuron is an information-processing unit that is essential to the operation of a neural network. Fig. D.2 shows the model for a neuron having three basic elements of the neuron as:

1. A set of synapses or connecting links, each of which is characterized by a weight or strengths of its own.
2. An adder for summing the input signals, weighted by the respective synapses of the neuron; the operation described here a linear combiner.
3. An activation function for limiting the amplitude of the output of a neuron. the activation function is also referred to in the literature as a squashing function in that it squashes (limits) the permissible amplitude range of the output signal to some finite value.

A detailed mathematical model of a neuron is shown in Fig. D.2. Models may include an externally applied threshold that has the effect of lowering the net input of the activation function. On the other hand, the net input of the activation function may be increased by employing a bias term rather than a threshold. In mathematical terms, it can be described as a neuron  $m$  by writing the following pair of equations:



$$r_m = \sum_{n=1}^N w_{1mn}x_n + b_{1m} \quad (\text{D.1})$$

$$y_m = f(r_m) \quad (\text{D.2})$$

Where  $x_1, x_2, \dots, x_N$  are the inputs;  $w_{m1}, w_{m2}, \dots, w_{mN}$  are the synaptic weights of neuron  $m$ ;  $r_m$  is the linear combiner output;  $b_m$  is the bias term;  $f$  is the activation function; and  $y_m$  is the output signal of the neuron.

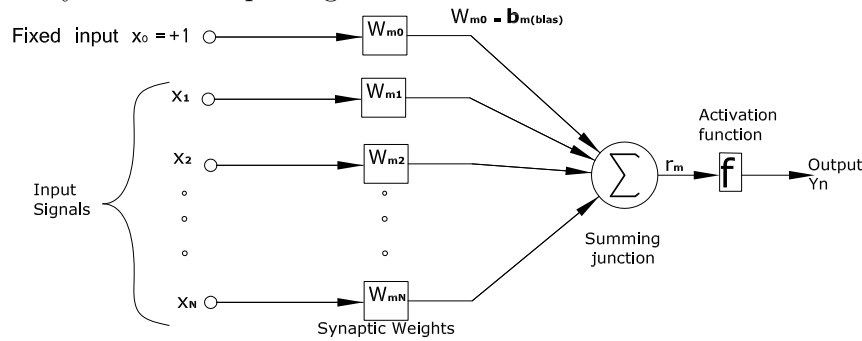


Fig. D.2: Mathematical model of a neuron

The scalar input  $x$  is transmitted through a connection that multiplies its strength by the scalar weight  $w$ , to form the product  $wx$ , again a scalar. The neuron shown in Fig. D.2 has a bias  $b_m$  but bias term may not be used depending on the situation. You may view the bias as simply being added to the product  $wx$  as shown by the summing junction or as shifting the function  $f$  to the left by an amount  $b_m$ . The bias is much like a weight, except that it has a constant input of 1. The transfer function net input  $r_m$ , again a scalar, is the sum of the weighted input  $wx$  and the bias  $b_m$ . This sum is the argument of the transfer function  $f$  which takes the argument  $r_m$  and produces the output  $y_m$ . Note that  $w$  and  $b$  are both adjustable scalar parameters of the neuron.

### Network topologies

The topology of a network is defined by the number of layers, the number of units per layer, and the interconnection patterns between layers. They are divided based on the pattern of connections: Feed-forward networks : In this network the data flow from input units to output units is strictly feed-forward. Processing of the data can

extend to several layers of units, but there is no feedback connections i.e., network connections extending from outputs of units to inputs in the same layer or preceding layers are not allowed. A feed-forward network is used in this thesis.

### *Feed-forward networks of layered neurons*

The manner in which the neurons of a neural network are structured is intimately linked with the learning algorithm (rule) used to train the network. supervised learning algorithms is used in this modelling.

The power of single neuron can be greatly amplified by using multiple neurons in a network of layered connectionist architecture. Neurons layered in such a way that it is also called feed-forward artificial neural network and abbreviated to FANN.

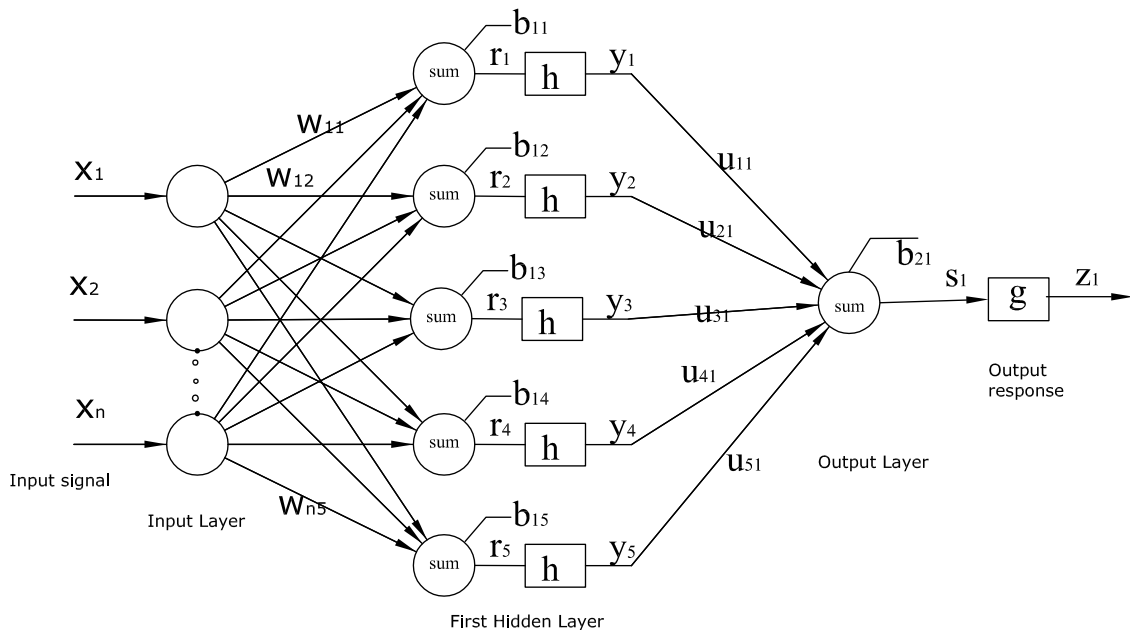


Fig. D.3: A representation of a simple 3-layer feed-forward ANN

The network shown in Fig. D.3 is the most popular network architecture in use for many problems. The network has a simple interpretation as a form of input-output model, with the weights and thresholds (biases) the free parameters of the model. Such networks can model functions of almost arbitrary complexity, with the number of layers, and the number of units in each layer, determining the function complexity. Important issues in MLP design include specification of the number of hidden layers

and the number of units in these layers.

On the left is the layer of inputs, or branching, nodes, which are not artificial neurons. A feature vector  $\mathbf{x} = (x_1, \dots, x_N)$  that represents a pattern enter the input layer on the left with each component  $x_n$  entering one and one input node. From each  $n^{\text{th}}$  input (branching) node, the  $n$ th component  $x_n$  fans out to each of the  $M$  neurons in the middle layer. Thus each  $m$ th hidden (middle) neurons has a fan-in of all  $N$  input components. As each  $x_n$  enters the  $m^{\text{th}}$  neuron of the hidden layer, it is modified via multiplication by the synaptic weight  $w_{nm}$  for that connection line. All resulting products  $w_{nm}x_n$  at the  $m^{\text{th}}$  hidden neuron are summed over  $n$  to yield

$$r_m = \sum_n w_{nm}x_n \quad (\text{D.3})$$

$$y_m = h(r_m) \quad (\text{D.4})$$

is the activation output. Doing the same for the output layer it is obtained

$$r_m = \sum_m u_{mj}y_m \quad (\text{D.5})$$

and

$$z_j = g(S_j) \quad (\text{D.6})$$

### *Activation functions*

Activation functions for the hidden units are needed to introduce non-linearity into the network that makes multilayer networks powerful. Without non-linearity, hidden units would not make nets more powerful than just plain perceptrons (which do not have any hidden units, just input and output units). Almost any non-linear function does the job, except for polynomials. For back propagation learning, the activation function must be differentiable, and it helps if the function is bounded; the sigmoidal functions such as logistic and tanh and the Gaussian function are the most common choices.

The threshold transfer function gives a perceptron the ability to classify input vectors by dividing the input space into two regions. Specifically, outputs will be 0 if

the net input  $n$  is less than 0, or 1 if the net input  $n$  is 0 or greater.

A sigmoidal activation function is used in this study shown in Fig. D.4.

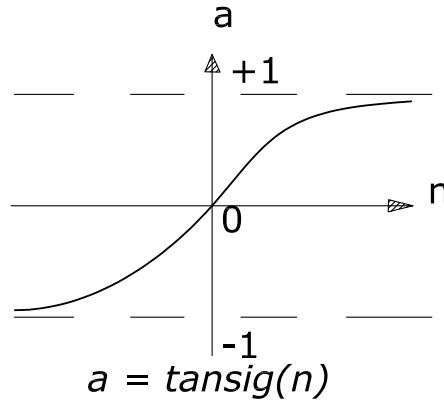


Fig. D.4: Hyperbolic tangent sigmoid transfer function

A sigmoid function:  $y = \frac{1}{[1+\exp(-net)]}$ , where  $\exp(x)$  means  $e^x$ .

### *Network Learning*

The functionality of a neural network is determined by the combination of the topology (number of layers, number of units per layer, and the interconnection pattern between the layers) and the weights of the connections within the network. The topology is usually held fixed, and the weights are determined by a certain training algorithm. The process of adjusting the weights to make the network learn the relationship between the inputs and targets is called learning, or training. Many learning algorithms have been invented to help find an optimum set of weights that results in the solution of the problems. They can roughly be divided into two main groups:

#### *Supervised Learning*

The network is trained by providing it with inputs and desired outputs (target values). These input-output pairs are provided by an external teacher, or by the system containing the network. The difference between the real outputs and the desired outputs is used by the algorithm to adapt the weights in the network (Fig. D.5). It is often thought as a function approximation problem which for a given training data consisting of pairs of input patterns  $x$ , and corresponding target  $t$ , the goal is to find a function  $f(x)$  that closely matches the desired output for each training input.

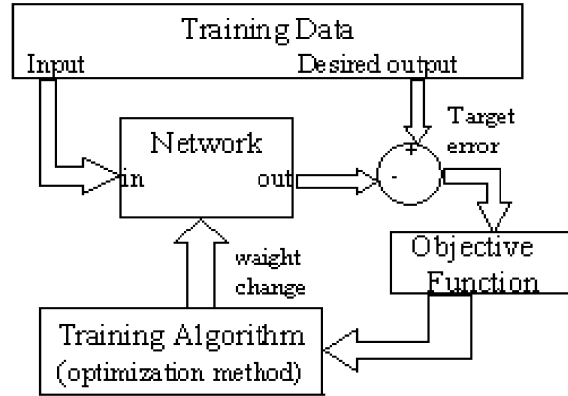


Fig. D.5: Supervised learning model

An objective function (or cost function) has to be defined for training a network and to provide an unambiguous numerical rating of system performance. Selection of an objective function is very important because the function represents the objective and decides what will be the training algorithm. One of the most commonly used objective function is the sum of squares error function,

$$E = \frac{1}{NP} \sum_{p=1}^p \sum_{i=1}^N (t_{pi} - y_{pi})^2 \quad (\text{D.7})$$

where  $p$  indexes the patterns in the training set,  $i$  indexes the output nodes, and  $t_{pi}$  and  $y_{pi}$  are, respectively, the target and actual network output for the  $i$ th output unit on the  $p$ th pattern. In real world applications, it may be necessary to complicate the function with additional terms to control the complexity of the model.

### Learning Algorithm

The Levenberg-Marquardt (LM) algorithm is used in this study due to its capability to converge in less number of iterations and also it is not been affected by overlearning. It is an iterative procedure, which establishes the least number of a function and it is expressed as the sum of squares of nonlinear functions. This algorithm was designed to approach second-order training speed without computing the Hessian matrix. Just similar to training feedforward networks, the performance function has the structure of a sum of squares and thus the Hessian matrix can be estimated as

$$\mathbf{H} = \mathbf{J}'\mathbf{J} \quad (\text{D.8})$$

and the gradient can be computed as

$$\mathbf{g} = \mathbf{J}' \mathbf{e} \quad (\text{D.9})$$

where,  $\mathbf{J}$  is the Jacobian matrix, which is the first derivatives of the network errors relating to the weights and biases, and  $\mathbf{e}$  is a vector of network errors. The Jacobian matrix can be calculated through a standard backpropagation technique that is much less complex than computing the Hessian matrix (Matlab, 2005). The LM algorithm uses this approximation to the Hessian matrix in the subsequent Newton-like update:

$$\mathbf{X}_{\mathbf{k}+1} = \mathbf{X}_{\mathbf{k}} - [\mathbf{J}'\mathbf{J} + \mu\mathbf{I}]^{-1}\mathbf{J}'\mathbf{e} \quad (\text{D.10})$$

When the scalar  $\mu$  is zero, this is just Newton's method, using the approximate Hessian matrix. When  $\mu$  is large, this becomes gradient descent with a small step size. Newton's method is faster and more accurate near an error minimum, so the aim is to shift toward Newton's method as quickly as possible. Thus,  $\mu$  is decreased after each successful step (reduction in performance function) and is increased only when a tentative step would increase the performance function. In this way, the performance function is always reduced at each iteration of the algorithm.

## E. NEURO-FUZZY

### *Introduction*

System modelling: is the process of constructing a model to predict the behaviour of a target system. Conventional modelling techniques are mostly based on linear models with fast computation and rigorous mathematical support. System modelling based on conventional mathematical tools (e.g., differential equations) is not well suited for dealing with ill-defined and uncertain systems. On the other hand, neuro-fuzzy modelling represents non-linear identification techniques that require massive computation but without mathematical proofs of convergence to global minima or the like. By contrast, a fuzzy inference system employing fuzzy if then rules can model the qualitative aspects of human knowledge and reasoning processes without employing precise quantitative analyses.

In this perspective, an Adaptive-Network-based Fuzzy Inference System (ANFIS), which can serve as a basis for constructing a set of fuzzy if-then rules with appropriate membership functions to generate the stipulated input-output pairs is discussed. The next section introduces the basics of fuzzy if-then rules and fuzzy inference systems.

### *Fuzzy set*

Fuzzy systems offers a mathematic calculus to translate the subjective human knowledge of the real processes. A fuzzy set is a generalization of an ordinary set by allowing a degree (or grade) of membership for each element. Fuzzy Logic (FL) is a superset of conventional (Boolean) logic that has been extended to handle the concept of partial truth - truth values between “completely true” and “completely false”. This is a way to manipulate practical knowledge with some level of uncertainty. Fuzzy systems are suitable for uncertain or approximate reasoning, especially for the system whose mathematical model is hard to derive. The fuzzy sets theory was initiated by Zadeh

(1965). It is based on FL reasoning which employs linguistic rules in the form of if-then statements.

Fig. E.1 shows the traditional crisp and fuzzy version of the sets “Short” and “Tall”. The variable “HEIGHT” in this system can be divided into a range of “states”, such as: ‘SHORT’, “MEDIUM” and “TALL”. Defining the bounds of these states is a bit tricky. Is a man 5’10” is MEDIUM or TALL ? It’s ambiguous. The fuzzy set will allow partial membership to deal with ambiguity by classifying the man as particularly SHORT, MEDIUM OR TALL at the same time.

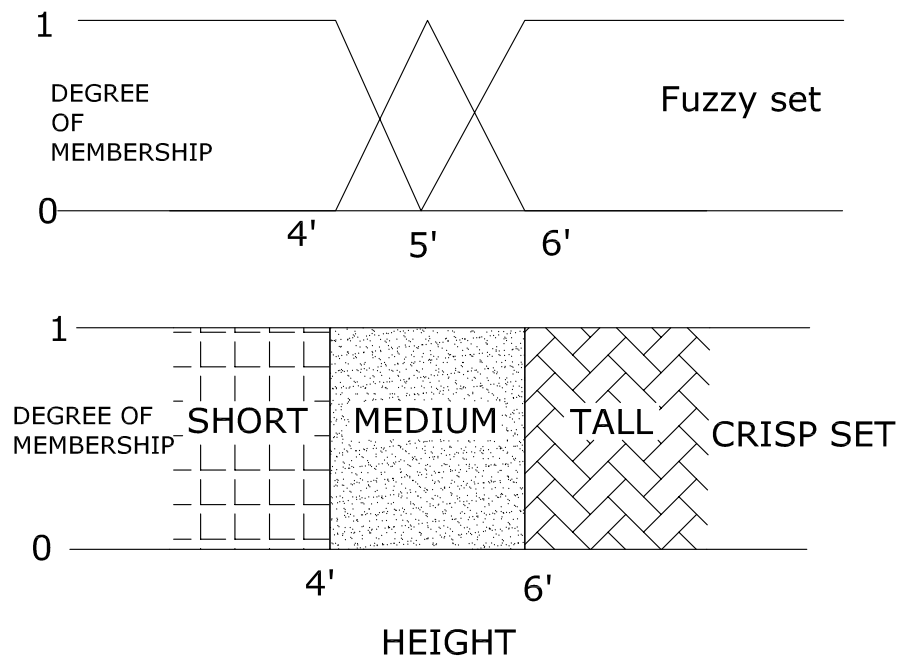


Fig. E.1: Crisp and Fuzzy sets for SHORT, MEDIUM and TALL

### *Fuzzy Inference Systems*

Fuzzy inference systems are also known as fuzzy-rule-based systems, fuzzy models, fuzzy associative memories (FAM), or fuzzy controllers when used as controllers. Basically a fuzzy inference system is composed of five functional blocks

- A rule base containing a number of fuzzy if-then rules;
- A database which defines the membership functions of the fuzzy sets used in the fuzzy rules;



- A decision-making unit which performs the inference operations on the rules;
- A fuzzification interface which transforms the crisp inputs into degrees of match with linguistic values;
- A defuzzification interface which transform the fuzzy results of the inference into a crisp output.

Usually, the rule base and the database are jointly referred to as the knowledge base.

The steps of fuzzy reasoning (inference operations upon fuzzy if-then rules) performed by fuzzy inference systems are:

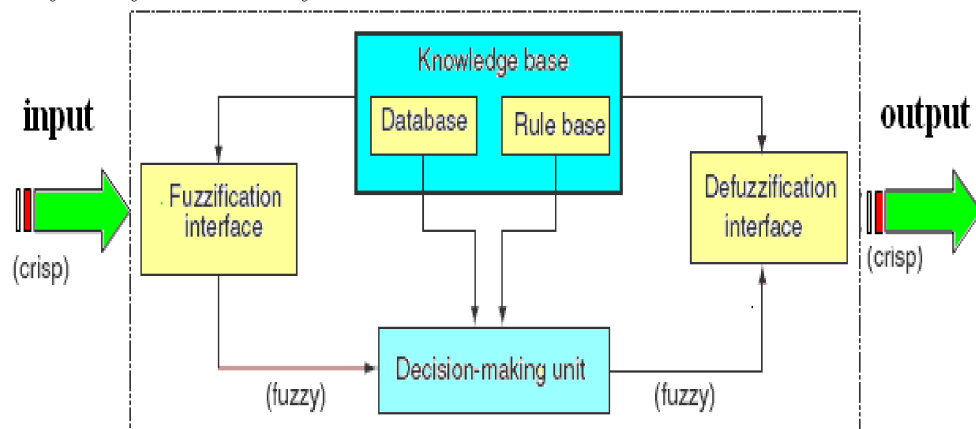


Fig. E.2: Fuzzy inference system

Several types of fuzzy reasoning have been proposed in the literature by Sivaraman et al. (2007). Depending on the types of fuzzy reasoning and fuzzy if-then rules employed, most fuzzy inference systems can be classified into three types (Fig. E.3):

Type 1: The output membership function has to be monotonically non-decreasing. Then, the overall output is the weighted average of each rules crisp output induced by the rule strength and output membership functions.

Type 2: Mamdani type: The operation applied to the qualified fuzzy outputs is max, and the crisp value of output is, most usually, the center of gravity of resulting fuzzy set. There are, also, the other methods to find the crisp output like: bisector of area, maximum criterion, mean of maxima, etc

Type 3: Sugeno's type: Each rules output is a linear combination of input variables. The crisp output is the weighted average of each rules output

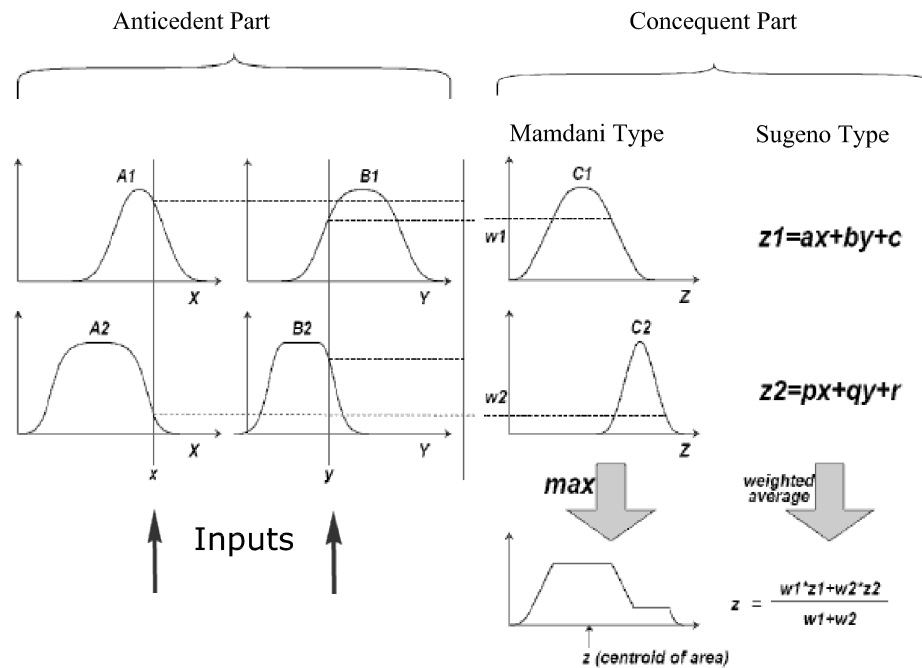


Fig. E.3: Commonly used fuzzy if-then rules and fuzzy reasoning mechanisms

Fig. E.3 utilizes a two-rule two-input fuzzy inference system to show different types of fuzzy rules and fuzzy reasoning mentioned above. Be aware that most of the differences lie in the specification of the consequent part (monotonically non-decreasing or bell-shaped membership functions, or crisp function) and thus the defuzzification schemes (weighted average, centroid of area, etc) are also different.

### Mamdani's Fuzzy Inference Method

Mamdani and Assilian (1975) fuzzy inference method is the most commonly seen fuzzy methodology. Mamdani's effort was based on Zadeh (1973) paper on fuzzy algorithms for complex systems and decision processes. Mamdani type inference, as defined it for the Fuzzy Logic Toolbox, expects the output membership functions to be fuzzy sets. After the aggregation process, there is a fuzzy set for each output variable that needs defuzzification. It is possible, and in many cases much more efficient, to use a single spike as the output membership functions rather than a distributed fuzzy set. This is sometimes known as a singleton output membership function, and it can be thought of as a pre-defuzzified fuzzy set. It enhances the efficiency of the defuzzification process because it greatly simplifies the computation required by the more general Mamdani method, which finds the centroid of a two-

dimensional function. Rather than integrating across the two-dimensional function to find the centroid, the weighted average of a few data points.

An example of a Mamdani inference system is shown in Fig. E.3. To compute the output of this FIS given the inputs, six steps has to be followed:

1. Determining a set of fuzzy rules
2. Fuzzifying the inputs using the input membership functions
3. Combining the fuzzified inputs according to the fuzzy rules to establish a rule strength
4. Finding the consequence of the rule by combining the rule strength and the output membership function
5. Combining the consequences to get an output distribution
6. Defuzzifying the output distribution (this step is only if a crisp output (class) is needed).

The following is a more detailed description of this process

#### *Creating Fuzzy Rules*

Fuzzy rules are a collection of linguistic statements that describe how the FIS should make a decision regarding classifying an input or controlling an output. Suppose that the fuzzy inference system has two inputs and one output. If two rules are combined then:

R1: If x is A1 and y is B1 then z is C1

R2: If x is A2 and y is B2 then z is C2

#### *Fuzzification*

The purpose of fuzzification is to map the inputs from a set of sensors (or features of those sensors such as amplitude or spectrum) to values from 0 to 1 using a set of input membership functions. In the example shown in Fig.E.3, there are two

inputs,  $x$  and  $y$  shown at the lower left corner. These inputs are mapped into fuzzy numbers by drawing a line up from the inputs to the input membership functions above and marking the intersection point. These input membership functions, as discussed previously, can represent fuzzy concepts such as “large” or “small,” “old” or “young,” “hot” or “cold,” etc.

### *Consequence*

The consequence of a fuzzy rule is computed by the rule strength by combining the fuzzified inputs using the fuzzy “AND” process as shown in Fig.E.3. In this example, the fuzzy “min” is used to combine the membership functions to compute the rule strength.

### *Combining Outputs into an Output Distribution*

The outputs of all of the fuzzy rules must now be combined to obtain one fuzzy output distribution. This is usually, but not always, done by using the fuzzy “OR”. The output membership functions on the right-hand side of the figure are combined using the fuzzy OR to obtain the output distribution shown on the lower right corner of Fig. E.3.

### *Defuzzification of Output Distribution*

In many occasion, it is desired to come up with a single crisp output from an FIS. This crisp number is obtained in a process known as defuzzification. There are two common techniques for defuzzifying:

- Center of mass. This technique takes the output distribution and finds its center of mass to come up with one crisp number. This is computed as follows:

$$z = \frac{\sum_{j=1}^q z_j u_c(Z_j)}{\sum_{j=1}^q u_c(Z_j)}, \quad (\text{E.1})$$

where  $z$  is the center of mass and  $u_c$  is the membership in class  $c$  at value  $z_j$ . An example outcome of this computation is shown in Fig. E.4(a).

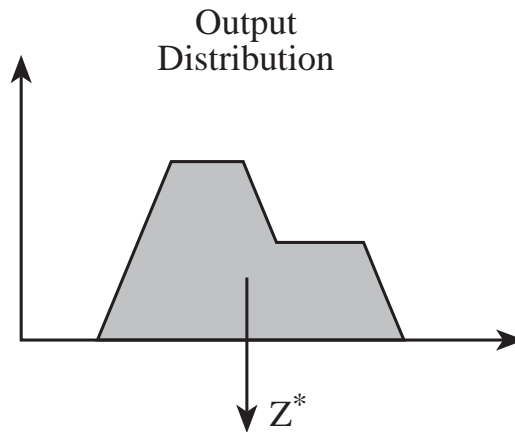


Fig. E.4: Defuzzification using the centre of mass

where  $z$  is the mean of maximum,  $z_j$  is the point at which the membership function is maximum, and  $l$  is the number of times the output distribution reaches the maximum level. An example outcome of this computation is shown in Fig. E.4(b).

#### *Learning fuzzy model parameters via Back-propagation*

The final estimates of the parameters of the fuzzy model are obtained by tuning the crude (approximate) values obtained from the Mountain-clustering method, see Section E. The successful coupling of fuzzy logic with neural networks has supplied a new and powerful tool for parameter identification of fuzzy models with the use of the back-propagation method. This algorithm works on a gradient descent method. For each training pattern presented to the input layer of the network, error at the nodes in the output layer of the network is calculated. The propagation of error of the nodes from the output layer to the nodes in the hidden layers takes place. These errors are used to update the weights of the network. The amount of weights to be added or subtracted to the previous weight is governed by the delta rule. By tuning the initial model parameters via back-propagation learning algorithm the final model parameters are obtained (Fig. E.5). This learning algorithm minimizes the instantaneous errors; it is a local minimizer. In some special cases it can be trapped at a local minimum. The problem of initial parameter estimates is of crucial importance in this method of learning.

Another important issue is the correct determination of the number of rules, that is the problem of structure identification, which can be solved by mountain-clustering

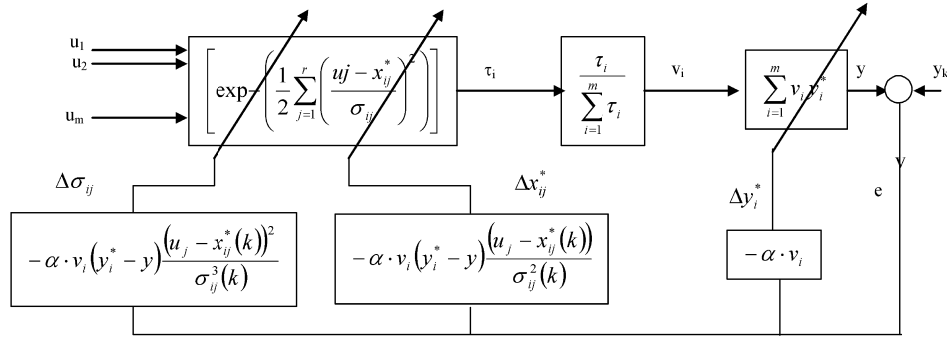


Fig. E.5: Block-diagram of the back-propagation learning algorithm

method by generating the cluster centers. These cluster centers can act as nuclei (or) focal points for rules in the initial rule base. Therefore, an initial structure of the model is obtained.

### Sugeno Fuzzy Method

In this section, the basics of Sugeno fuzzy model, which is implemented into the neural-fuzzy system is explained. The Sugeno fuzzy model was proposed by Takagi and Sugeno (1985) in an effort to formalize a system approach to generating fuzzy rules from an input-output data set. It is also known as Sugeno-Takagi model. A typical fuzzy rule in this model has the format

- R 1: IF x is A1 and y is B1 THEN z1 = ax+by+c
- R 2: IF x is A2 and y is B2 THEN z2 = px+qy+r

where A1, B1, A2 and B2 are fuzzy sets in the antecedent; z's = f(x, y) are crisp functions in the consequent. Usually f(x, y) is a polynomial in the input variables x and y, but it can be any other functions that can appropriately describe the output of the output of the system within the fuzzy region specified by the antecedent of the rule. When f(x, y) is a first-order polynomial, then it is called the first-order Sugeno fuzzy model.

The first two parts of the fuzzy inference process, fuzzifying the inputs and applying the fuzzy operator, are exactly the same. The main difference between Mamdani

and Sugeno is that the Sugeno output membership functions are either linear or constant. The output level  $z_i$ 's of each rule is weighted by the firing strength  $w_i$  of the rule. For example, for an AND rule with  $X = x$  and  $Y = y$ , the firing strength is

$$w_1 = \mu A1(x) \times \mu B1(y) w_2 = \mu A2(x) \times \mu B2(y) \quad (\text{E.2})$$

where  $\mu A1(x)$  and  $\mu B1(y)$  are the membership functions for  $X$  and  $Y$  for rule 1. The final output of the system is the weighted average of all rule outputs, computed as

$$z = \frac{w_1 \times z_1 + w_2 \times z_2}{w_1 + w_2} \quad (\text{E.3})$$

### *Comparison Between Sugeno and Mamdani Method*

The major difference of Mamdani and Sugeno is that the Sugeno output membership functions are either linear or constant. As the difference lies in the consequents of their fuzzy rules, thus their aggregation and defuzzification procedures differ suitably. The number of the input fuzzy sets and fuzzy rules needed by the Sugeno fuzzy systems depend on the number and locations of the extrema of the function to be approximated. In Sugeno method a large number of fuzzy rules must be employed to approximate periodic or highly oscillatory functions. The minimal configuration of the Sugeno fuzzy systems can be reduced and becomes smaller than that of the Mamdani fuzzy systems if non-trapezoidal or non-triangular input fuzzy sets are used. Sugeno controllers usually have far more adjustable parameters in the rule consequent and the number of the parameters grows exponentially with the increase of the number of input variables. Less mathematical results exist for Sugeno fuzzy controllers than do for Mamdani fuzzy controllers, particularly those on Sugeno fuzzy control system stability. Mamdani is easy to form compared to Sugeno method.

Because of the linear dependence of each rule on the input variables of a system, the Sugeno method is ideal for acting as an interpolating supervisor of multiple linear controllers that are to be applied, respectively, to different operating conditions of a dynamic non-linear system. A Sugeno FIS is extremely well suited to the task of smoothly interpolating the linear gains that would be applied across the input

---

space; it is a natural and efficient gain scheduler. Similarly, a Sugeno system is suited for modelling non-linear systems by interpolating between multiple linear models. Because it is a more compact and computationally efficient representation than a Mamdani system, the Sugeno system lends itself to the use of adaptive techniques for constructing fuzzy models. These adaptive techniques can be used to customize the membership functions so that the fuzzy system best models the data.

### *Advantages of Sugeno and Mamdani Method*

#### Advantages of the Sugeno Method

- It is computationally efficient.
- It works well with linear techniques (e.g., PID control).
- It works well with optimization and adaptive techniques.
- It has guaranteed continuity of the output surface.
- It is well suited to mathematical analysis.

#### Advantages of the Mamdani Method

- It is intuitive.
- It has widespread acceptance.
- It is well suited to human input.

Fuzzy inference system is the most important modelling tool based on fuzzy set theory. The FISs are built by domain experts and are used in automatic control, decision analysis, and various other expert systems.

### *Mountain-Clustering Method*

The mountain clustering method is a grid-based three-step process for identifying the approximate locations of cluster centers in data sets with clustering tendencies (Yager and Filev, 1994). Assume the data consists of a set of  $k$  points  $(x_k, y_k)$  in the input-output space (or) object space (or) X Y space containing the data points.



The first step in the mountain method is to generate the potential cluster centres. For this discretize the object space by gridding  $x$  and  $y$  with equidistant lines. The intersection of these grid lines, called nodes form a set of potential cluster centres, which are represented by  $N$ . An element of each potential cluster centre,  $N$  can be represented as  $N_{ij}(x_i, y_j)$ .

The second step is the construction of mountain function,  $M$ , which is defined on the set of potential cluster centres. Mathematically for each point  $N_{ij}(x_i, y_j)$  in  $N$  is as shown below:

$$M(N_{ij}) = \sum_{k=1}^m e^{-\alpha d(N_{ij}, O_k)} \quad (\text{E.4})$$

Where  $O_k$  is the  $k^{\text{th}}$  data point  $(x_k, y_k)$ ,  
 $\alpha$  is mountain building parameter, a positive constant, and  
 $d(N_{ij}, O_k)$  is a measure of distance between  $N_{ij}$  and  $O_k$  given by

$$d(N_{ij}, O_k) = \sqrt{(X_i - x_k)^2 + (Y_j - y_k)^2} \quad (\text{E.5})$$

The third step is to use the mountain function to generate the cluster centers. The node with the highest value of mountain function is selected as a cluster center. In order to get the next cluster center; the effect of the cluster centre just identified is removed by a destruction of the mountain function given by

$$\hat{M}_{k+1}(N_{ij}) = \hat{M}_k(N_{ij}) - M_k^* e^{-\beta d(N_{ij}^*, N_{ij})} \quad (\text{E.6})$$

Where  $M_k$  is the original mountain function,  $\beta$  is mountain revising constant (a positive constant)  $N_k^*$  and  $M_k^*$  are the location of and score at the just identified cluster center, and  $d(N_k^*, N_{ij})$  is a distance measure. This process is repeated until all nodes are exhausted or the mountain function reaches a limiting value.

Starting with the observed data pairs  $(x_k, y_k)$ , the mountain clustering method provides a collection of cluster centers  $(x_i^*, y_i^*)$ . The estimates of the parameters of the antecedent and consequent fuzzy sets are obtained from the data. Therefore, using this method an initial estimation of the antecedent and consequent fuzzy sets of the rules of the linguistic model can be obtained.

## REFERENCES

- Abu Zeid, O. (1996). The role of voltage pulse off-time in the electrodischarge machined AISI T1 high-speed steel. *Journal of Materials Processing Technology*, 61(3):287–291.
- Aleksander, I. and Morton, H. (1990). *An Introduction to Neural Computing*. International Thomson Computer Press.
- Allen, P. and Chen, X. (2007). Process simulation of micro electro-discharge machining on molybdenum. *Journal of Materials Processing Technology*, 186:346–355.
- Ansys-12.0 (2010). *ANSYS Advanced analysis procedure manual*. ANSYS Inc., Canonsburg, Pennsylvania c SAS IP, Inc.
- Barsoum, Z. (2008). *Residual Stress Analysis and Fatigue Assessment of Welded Steel Structures*. PhD thesis, School of Engineering Sciences, KTH, Stockholm,.
- Bhadeshia, H. K. D. H. (2002). *Handbook of Residual Stress and Deformation of Steel*. ASM International,, Materials Park, Ohio, USA.
- Bhattacharya, R., Jain, V. K., and Ghoshdastidar, P. S. (1996). Numerical simulation of thermal erosion in EDM process. *Journal of the Institution of Engineers (India), Part PR: Production Engineering Division*, 77(1):13–19.
- Bhattacharyya, B., Gangopadhyay, S., and Sarkar, B. R. (2007). Modelling and analysis of EDMed job surface integrity. *Journal of Materials Processing Technology*, 189:169–177.
- Bleys, P., Kruth, J., Lauwers, B., Zryd, A., Delpretti, R., and Tricarico, C. (2002). Real-time tool wear compensation in milling EDM. *CIRP Annals - Manufacturing Technology*, 51(1):157–160.

- Boothroyd, G. and Winston, A. K. (1989). *Non-Conventional Machining Processes. Fundamentals of Machining and Machine Tools*. Marcel Dekker, New York, p 491.
- Caydas, U. and Hascalik, A. (2007). Modeling and analysis of electrode wear and white layer thickness in die-sinking EDM process through response surface methodology. *International Journal of Advanced Manufacturing Technology*, 38(11-12):1148–1156.
- Chiang, K. (2008). Modeling and analysis of the effects of machining parameters on the performance characteristics in the EDM process of Al<sub>2</sub>O<sub>3</sub>+TiC mixed ceramic. *International Journal of Advanced Manufacturing Technology*, 37(5-6):523–533.
- Cogun, C. and Savsar, M. (1990). Statistical modelling of properties of discharge pulses in electric discharge machining. *International Journal of Machine Tools and Manufacture*, 30:467–474.
- Das, S., Klotz, M., and Klocke, F. (2003). EDM simulation: Finite element-based calculation of deformation, microstructure and residual stresses. *Journal of Materials Processing Technology*, 142:434–451.
- Dauw, D. (1988). Geometrical simulation of the EDM die-sinking process. *Ann. CIRP*, 37 (1 ):191–196.
- Dauw, D. and Snoeys, R. (1986). On the derivation and application of a real-time tool wear sensor in EDM. *CIRP Annals - Manufacturing Technology*, 35(1):111–116.
- Dhar, S., Purohit, R., Saini, N., Sharma, A., and Kumar, G. H. (2007). Mathematical modeling of electric - discharge machining of cast Al-4Cu-6Si alloy-10 wt.% SiCP composites. *Journal of Materials Processing Technology*, 194:24–29.
- Dibitono, D. D., Eubank, P. T., Patel, M. R., and Barrufet, M. A. (1989.). Theoretical model of the electrical discharge machinings process I: A simple cathode erosion model. *Journal of Applied Physics*,, 66:4095–4103.
- Dieter, G. E. (1997). ASM handbook material selection and design. *ASM International Handbook Committee*, 20.

- Doniavi, A., Eskandarzade, M., Abdi, A., and Totonchi, A. (2008). Empirical modeling of EDM parameters using grey relational analysis. *Asian journal of Scientific Research*, 1(5):502–509.
- Dvivedi, A., Kumar, P., and Singh, I. (2008). Experimental investigation and optimisation in EDM of al 6063 SiCp metal matrix composite. *International Journal of Machining and Machinability of Materials*, 3(3-4):293 – 308.
- Ekmekci, B. (2007). Residual stresses and white layer in electric - discharge machining (EDM). *Applied Surface Science*, 253:9234–9240.
- Ekmekci, B. (2009). White layer composition, heat treatment, and crack formation in electric - discharge machining process. *Metallurgical and Materials Transactions B: Process Metallurgy and Materials Processing Science*, 40(1):70–81.
- Ekmekci, B., Elkoca, O., Tekkaya, A. E., and Erden, A. (2005). Residual stress state and hardness depth in electric discharge machining: De-ionized water as dielectric liquid. *Machining Science and Technology*, 9(1):39–61.
- Ekmekci, B., Tekkaya, A. E., and Erden, A. (2006). A semi-empirical approach for residual stresses in electric discharge machining (EDM). *International Journal of Machine Tools and Manufacture*, 46:858–868.
- El-Taweel, T. (2008). Multi-response optimization of EDM with Al-Cu-Si-TiC P/M composite electrode. *International Journal of Advanced Manufacturing Technology*, pages 1–14.
- Erden, A. (1983). Effect of materials on the mechanism of electric discharge machining. *Trans. ASME J. Eng. Mater. Technology*, 108:247–251.
- Erden, A., Arinc, F., and Kogmen, M. (1995). Comparison of mathematical models for electric - discharge machining. *Journal of Material Processing and Manufacturing Science*, 4:163–176.
- Eubank, P. T., Patel, M. R., Barrufet, M. A., and Bozkurt, B. (1989.). Theoretical

- model of the electrical discharge machinings process I. a simple cathode erosion model,. *Journal of Applied Physics*, Vol. 66:4095–4103.
- Gadalla, A. and Tsai, W. (1989). Machining of WC-Co composites. *Materials and Manufacturing Processes*, 4(3):411–423.
- Gangadhar, A., Shunmugam, M., and Philip, P. K. (1992). Pulse train studies in EDM with controlled pulse relaxation,. *Int. J. Mach. Tools Manuf.*, 32 (5):651–657.
- Gao, Q., Zhang, Q., Su, S., Zhang, J., and Ge, R. (2008). Prediction models and generalization performance study in electrical discharge machinings. *Applied Mechanics and Materials*, 10-12:677–681.
- Garcia Navas, V., Ferreres, I., Maranon, J. A., Garcia-Rosales, C., and Gil Sevillano, J. (2008). Electro-discharge machining (EDM) versus hard turning and grinding-comparison of residual stresses and surface integrity generated in AISI O1 tool steel. *Journal of Materials Processing Technology*, 195:186–194.
- Ghanem, F., Braham, C., and Sidhom, H. (2003). Influence of steel type on electrical discharge machined surface integrity. *Journal of Materials Processing Technology*, 142:163–173.
- Ghoreishi, M. and Tabari, C. (2007). Investigation into the effect of voltage excitation of pre-ignition spark pulse on the electro-discharge machining (EDM) process. *Materials and Manufacturing Processes*, 22(7):833–841.
- Guu, Y. and Hocheng, H. (2001a). High cycle fatigue of electrical-discharge machined AISI D2 tool steel. *International Journal of Materials and Product Technology*, 16(6-7):642–657.
- Guu, Y. H. (2005). Afm surface imaging of AISI D2 tool steel machined by the EDM process. *Applied Surface Science*, 242:245–250.
- Guu, Y. H. and Hocheng, H. (2001b). Improvement of fatigue life of electrical discharge machined AISI D2 tool steel by TiN coating. *Materials Science and Engineering A*, 318:155–162.

- Guu, Y. H., Hocheng, H., Chou, C. Y., and Deng, C. S. (2003). Effect of electrical discharge machinings on surface characteristics and machining damage of AISI D2 tool steel. *Materials Science and Engineering A*, 358:37–43.
- Hardbound, D. O., editor (1992). *ASM Handbook*, volume 18 of *Friction, Lubrication, and Wear Technology*. ASM Publication.
- Hascalyk, A. and Caydas, U. (2004). Experimental study of wire electrical discharge machinings of AISI D5 tool steel. *Journal of Materials Processing Technology*, 148:362–367.
- Ho, K. H. and Newman, S. T. (2003). State of the art electrical discharge machinings (EDM). *International Journal of Machine Tools and Manufacture*, 43:1287–1300.
- Jaharah, A. G., C.G.Liang, Wahid, S. Z., Rahman, M. N. A., and Hassan, C. H. C. (2008). Performance of copper electrode in electrical discharge machinings (EDM) of AISI H13 harden steel. *International Journal of Mechanical and Materials Engineering*, 3(1):25–29.
- Jeswani, M. (1981). Electrical discharge machinings in distilled water. *Wear*, 72(1):81–88.
- Jilani, S. T. and Pandey, P. (1982). Analysis and modelling of EDM parameters. *Precision Engineering*, 4:215–221.
- Jonsson, M., Karlsson, L., and Lindgren, L.-E. (1985). Deformations and stresses in butt-welding of large plates with special reference to the mechanical material properties. *J. Eng. Mater. Technol.*, 107:265–271.
- Jyh-Shing and Jang, R. (1993). ANFIS : Adaptive-network-based fuzzy inference system. *IEEE Transactions on systems, man, and cybernetics*, 23:665–685.
- Kanagarajan, D., Karthikeyan, R., Palanikumar, K., and Sivaraj, P. (2008). Influence of process parameters on electric - discharge machining of WC/30%Co composites. *Proceedings of the Institution of Mechanical Engineers, Part B: Journal of Engineering Manufacture*, 222(7):807–815.

- Kansal, H. K., Singh, S., and Kumar, P. (2007). Technology and research developments in powder mixed electric discharge machining (PMEDM). *Journal of Materials Processing Technology*, 184:32–41.
- Karthikeyan, R., Lakshmi Narayanan, P. R., and Naagarazan, R. S. (1999). Mathematical modelling for electric - discharge machining of aluminium-silicon carbide particulate composites. *Journal of Materials Processing Technology*, 87:59–63.
- Keskin, Y., Halkaci, H., and Kizil, M. (2006). An experimental study for determination of the effects of machining parameters on surface roughness in electrical discharge machinings (EDM). *International Journal of Advanced Manufacturing Technology*, 28(11-12):1118–1121.
- Khan, A. (2008). Electrode wear and material removal rate during EDM of aluminum and mild steel using copper and brass electrodes. *International Journal of Advanced Manufacturing Technology*, 39(5-6):482–487.
- Khan, A., Ali, M., and Haque, M. (2009). A study of electrode shape configuration on the performance of die sinking EDM. *International Journal of Mechanical and Materials Engineering*, 4(1):19–23.
- Kiyak, M. and Cakir, O. (2007). Examination of machining parameters on surface roughness in EDM of tool steel. *Journal of Materials Processing Technology*, 191:141–144.
- Kohnke, P. (2004). ANSYS, theory reference, SAS IP,.
- Kruth, J., Stevens, L., Froyen, L., and Lauwers, B. (1995). Study of the white layer of a surface machined by die-sinking electro-discharge machining. *CIRP Annals - Manufacturing Technology*, 44(1):169 – 172.
- Kung, K. Y., Horng, J. T., and Chiang, K. T. (2009). Material removal rate and electrode wear ratio study on the powder mixed electrical discharge machinings of cobalt-bonded tungsten carbide. *International Journal of Advanced Manufacturing Technology*, 40(1-2):95–104.

- Kunieda, M. and Kobayashi, T. (2004). Clarifying mechanism of determining tool electrode wear ratio in EDM using spectroscopic measurement of vapor density. *Journal of Materials Processing Technology*, 149(1-3):284–288.
- Kunieda, M., Kowaguchi, W., and Takita, T. (1999). Reverse simulation of die-sinking EDM. *CIRP Annals - Manufacturing Technology*, 48(1):115–118.
- Kunieda, M. and Masuzawa, T. (1988). A fundamental study on a horizontal EDM. *CIRP Annals - Manufacturing Technology*, 37(1):187–190.
- Kunieda, M. and Yoshida, M. (1997). Electrical discharge machinings in gas. *CIRP Annals - Manufacturing Technology*, 46(1):143–X31.
- Kuppan, P., Rajadurai, A., and Narayanan, S. (2007). Influence of EDM process parameters in deep hole drilling of inconel 718. *International Journal of Advance Manufacturing Technology*, 38:74–84.
- Lee, H. T., Hsu, F. C., and Tai, T.-Y. (2004). Study of surface integrity using the small area EDM process with a copper-tungsten electrode. *Materials Science and Engineering A*, 364:346–356.
- Lee, H. T. and Tai, T. Y. (2003). Relationship between EDM parameters and surface crack formation. *Journal of Materials Processing Technology*, 142:676–683.
- Lee, L., Lim, L., and Wong, Y. (1990.). Towards a better understanding of the surface features of electro-discharge machined tool steels. *J. Mater. Process. Technol.*, 24:513–523.
- Lee, L., Lim, L., and Wong, Y. (1992). Towards crack minimisation of EDMed surfaces. *Journal of Materials Processing Tech.*, 32(1-2):45–54.
- Lee, L. C., Lim, L. C., Narayanan, V., and Venkatesh, V. C. (1988). Quantification of surface damage of tool steels after EDM. *International Journal of Machine Tools and Manufacture*, 28(44):359–372.



- 
- Lee, S. H. and Li, X. P. (2001). Study of the effect of machining parameters on the machining characteristics in electrical discharge machinings of tungsten carbide. *Journal of Materials Processing Technology*, 115:344–358.
- Lee, T. C. and Lau, W. S. (1991). Some characteristics of electrical discharge machinings of conductive ceramics,. *Mater. Manuf. Processes*, 6 (4):635–648.
- Lim, L., Lee, L., Wong, Y., and Lu, H. (1991). Solidification microstructure of electrodischarge machined surfaces of tool steels. *Materials Science and Technology*, 7(3):239–248.
- Madhu, P., Jain, V., Sundararajan, T., and Rajurkar, K. (1991). Finite element analysis of EDM process. *Processing of Advanced Materials*, 1:161–173.
- Mamalis, A., Vosniakos, G., Vacevanidis, N., and Junzhe, X. (1988). Residual stress distribution and structural phenomena of high-strength steel surfaces due to EDM and ball-drop forming. *CIRP Annals - Manufacturing Technology*, 37(1):531–535.
- Mamalis, A. G., Vosniakos, G. C., Vaxevanidis, N. M., and Prohaszka, J. (1987). Macroscopic and microscopic phenomena of electro-discharge machined steel surfaces: An experimental investigation. *Journal of Mechanical Working Technology*, 15:335–356.
- Mamdani, E. H. and Assilian, S. (1975). An experiment in linguistic synthesis with a fuzzy logic controller,”. *International Journal of Man-Machine Studies*,, 7(1):1–13,.
- Mandal, D., Pal, S. K., and Saha, P. (2007). Modeling of electrical discharge machining process using back propagation neural network and multi-objective optimization using non-dominating sorting genetic algorithm-II. *Journal of Materials Processing Technology*, 186:154–162.
- Marafona, J. and Chousal, J. A. G. (2006). A finite element model of EDM based on the Joule effect. *International Journal of Machine Tools and Manuf.*, 46:595–602.
- Marafona, J. and Wykes, C. (2000). A new method of optimising material removal

- rate using EDM with copper tungsten electrodes. *International Journal of Machine Tools & Manufacture*, 40:153–164.
- Marafona, J. D. and Araujo, A. (2009). Influence of workpiece hardness on EDM performance. *International Journal of Machine Tools and Manuf.*, 49(9):744–748.
- Masuzawa, T., Fujino, M., Kobayashi, K., Suzuki, T., and Kinoshita, N. (1985). Wire electro-discharge grinding for micro-machining. *CIRP Annals - Manufacturing Technology*, 34(1):431–434.
- Matlab (2005). *Matlab User Manual, Version 7.1*. The MathWorks, Inc, 24 Prime Park Way Natick, MA 01760-1500.
- Minitab14 (2003). *Minitab User Manual Release 14*. State College, PA, USA,.
- Mohd Abbas, N., Solomon, D. G., and Fuad Bahari, M. (2007). A review on current research trends in electrical discharge machining (EDM). *International Journal of Machine Tools and Manufacture*, 47:1214–1228.
- Mohri, N., Suzuki, M., Furuya, M., Saito, N., and Kobayashi, A. (1995). Electrode wear process in electrical discharge machinings. *CIRP Annals - Manufacturing Technology*, 44(1):165–168.
- Mohri, N., Takezawa, H., Furutani, K. and Ito, Y., and Sata, T. (2000). New process of additive and removal machining by EDM with a thin electrode. *CIRP Annals - Manufacturing Technology*, 49(1):123–126.
- Montgomery, D. C. (2001). *Design and Analysis of Experiments*. Wiley, New York.
- Montgomery, D. C. (2003). *Applied Statistics and Probability for Engineers*. John Wiley & Sons, Inc., third edition edition.
- Myers, R. and Montgomery, D. (1995). *Response Surface Methodology, Process and Product Optimization Using Designed Experiments*. Wiley, New York.
- Panda, D. K. and Bhoi, R. K. (2005). Artificial neural network prediction of material removal rate in electro - discharge machining. *Materials and Manufacturing Processes*, 20:645–672.

- 
- Pandey, P. C. and Jilani, S. T. (1986). Plasma channel growth and the resolidified layer in EDM. *Precision Engineering*, 8:104–110.
- Pandey, P. C. and Shan, H. S. (1980). *Modern Machining Processes*. Tata McGraw-Hill, New Delhi.
- Patel, M. R., Maria, B. A., Eubank, P. T., and D.DiBitonto (1989.). Theoretical models of the electrical discharge machinings process II - the anode erosion model. *Journal of Applied Physics*, 66/9:4104,.
- Pradhan, B.B.and Bhattacharyya, B. (2009). Modelling of micro-electrodischarge machining during machining of titanium alloy Ti-6Al-4V using response surface methodology and artificial neural network algorithm. *Proceedings of the Institution of Mechanical Engineers, Part B: Journal of Engineering Manuf.*, 223(6):683–693.
- Pradhan, M. K. and Biswas, C. K. (2009). Neuro-fuzzy model and regression model a comparison study of MRR in electrical discharge machining of D2 tool steel. *International Journal of Engineering and Applied Sciences*, 5:328–333.
- Pradhan, M. K., Das, R., and Biswas, C. K. (2009a). Comparisons of neural network models on surface roughness in electrical discharge machining. *Proceedings of the Institution of Mechanical Engineers, Part B: Journal of Engineering Manufacture*, 223(7):801–808.
- Pradhan, M. K., Das, R., and Biswas, C. K. (2009b). Prediction of surface roughness in electrical discharge machining of D2 steel using regression and artificial neural networks modeling. *Journal of Machining and Forming Technologies*, 2(1-2):25–46.
- Prevéy, P. S. (1993). X-ray diffraction residual stress techniques. *ASM Handbook*.
- Puertas, I., Luis, C. J., and Alvarez, L. (2004). Analysis of the influence of EDM parameters on surface quality, MRR and ew of WC-Co. *Journal of Materials Processing Technology*, 153-154(1-3):1026–1032.
- Rajurkar, K. and Pandit, S. (1988). Recent progress in electrical discharge machine

- technology and research. *Proceedings of Manufacturing International 88, Atlanta, GA.*, pages 219–226.
- Rajurkar, K. and Yu, Z. (2000). 3D micro-EDM using CAD/CAM. *CIRP Annals - Manufacturing Technology*, 49(1):127–130.
- Ramasawmy, H., Blunt, L., and Rajurkar, K. (2005). Investigation of the relationship between the white layer thickness and 3d surface texture parameters in the die sinking EDM process. *Precision Engineering*, 29(4):479–490.
- Rebello, J. C., Morao Dias, A., Kremer, D., and Lebrun, J. L. (1998). Influence of EDM pulse energy on the surface integrity of martensitic steels. *Journal of Materials Processing Technology*, 84:90–96.
- Roethel, F., Garbajs, V., and Kosec, L. (1976). Contribution to the micro-analysis of the spark eroded surfaces. *Ann CIRP*, 25(1):135–140.
- Salah, N. and Ghanem, F. and Atig, K. (2006). Numerical study of thermal aspects of electric - discharge machining process. *International Journal of Machine Tools and Manufacture*, 46(7-8):908–911.
- Salah, N. B., Ghanem, F., and Atig, K. B. (2008). Thermal and mechanical numerical modelling of electric discharge machining process. *Communications in Numerical Methods in Engineering*, 24(12):2021–2034.
- Salonitis, K., Stournaras, A., Stavropoulos, and P., Chryssolouris, G. (2009). Thermal modeling of the material removal rate and surface roughness for die-sinking EDM. *International Journal of Advanced Manufacturing Technology*, 40(3-4):316–323.
- Schumacher, B. (2004). After 60 years of EDM the discharge process remains still disputed. *Journal of Materials Processing Technology*, 149(1-3):376–381.
- Shankar, P., Jain, V. K., and Sundararajan, T. (1997). Analysis of spark profiles during EDM process. *Machining science and technology*, 1:195–217.

- 
- Singh, A. and Ghosh, A. (1999). A thermo-electric model of material removal during electric discharge machining. *International Journal of Machine Tools and Manufacture*, 39:669–682.
- Singh, S., Maheshwari, S., and Pandey, P. (2004). Some investigations into the electric - discharge machining of hardened tool steel using different electrode materials. *Journal of Materials Processing Technology*, 149(1-3):272–277.
- Sivanandam, S., Sumathi, S., and Deepa, S. (2007). *Introduction to Fuzzy Logic Using MATLAB*. Springer.
- Snoeys, R., Staelens, F., and Dekeyser, W. (1986). Current trends in nonconventional material removal processes. *Ann. CIRP*, 35(2):467–480.
- Sohani, M., Gaitonde, V., Siddeswarappa, B., and Deshpande, A. (2009). Investigations into the effect of tool shapes with size factor consideration in sink electrical discharge machinings (EDM) process. *International Journal of Advanced Manufacturing Technology*, pages 1–15.
- Soni, J. S. and Chakraverti, G. (1996). Experimental investigation on migration of material during EDM of die steel (T215 Cr12). *Journal of Materials Processing Technology*, 56(1-4):439–451.
- Staelens, F. and Kruth, J. (1989). A computer integrated machining strategy for planetary EDM. *CIRP Annals - Manufacturing Technology*, 38(1):187–190.
- Tai, T. and Lu, S. (2009). Improving the fatigue life of electro-discharge-machined SDK11 tool steel via the suppression of surface cracks. *International Journal of Fatigue*, 31(3):433–438.
- Takagi, T. and Sugeno, M. (1985). Fuzzy identification of systems and its applications to modeling and control. *IEEE Transactions on Systems, Man and Cybernetics*, 15(1):116–132. cited By (since 1996) 4817.
- Thomson, P. (1989). Surface damage in electrodischarge machining. *Materials Science and Technology*, 5(11):1153–1157.

- Tsai, K.-M. and Wang, P.-J. (2001a). Comparisons of neural network models on material removal rate in electrical discharge machinings. *Journal of Materials Processing Technology*, 117:111–124.
- Tsai, K.-M. and Wang, P.-J. (2001b). Predictions on surface finish in electrical discharge machinings based upon neural network models. *International Journal of Machine Tools and Manufacture*, 41:1385–1403.
- Tsai, K.-M. and Wang, P.-J. (2001c). Semi-empirical model of surface finish on electrical discharge machining. *International Journal of Machine Tools & Manufacture*, 41:1455–1477.
- Valentincic, J. and Junkar, M. (2004). A model for detection of the eroding surface based on discharge parameters. *International Journal of Machine Tools and Manufacture*, 44:175–181.
- Wang, C. C. and Chow, H., Yang, L. D., and Lu, C. (2009). Recast layer removal after electrical discharge machinings via taguchi analysis: A feasibility study. *Journal of Materials Processing Technology*, 209(8):4134–4140.
- Wang, K., Gelgele, H. L., Wang, Y., Yuan, Q., and Fang, M. (2003). A hybrid intelligent method for modelling the EDM process. *International Journal of Machine Tools and Manufacture*, 43:995–999.
- Wang, P.-J. and Tsai, K.-M. (2001). Semi-empirical model on work removal and tool wear in electrical discharge machining. *Journal of Materials Processing Technology*, 114(1):1–17.
- Wang, C. C. and Lin, Y. (2009). Feasibility study of electrical discharge machinings for W/Cu composite. *International Journal of Refractory Metals and Hard Materials*, 27(5):872–882.
- Wong, Y. and Noble, C. (1986). Electrical discharge machinings with transverse tool movement. In *Proceedings of the 26th International Machine Tools Design and Research Conference*, pages 399–413, Manchester, UK.

- Yadav, V., Jain, V. K., and Dixit, P. M. (2002). Thermal stresses due to electrical discharge machinings. *International Journal of Machine Tools and Manufacture*, 42:877–888.
- Yadava, V., Jain, V. K., and Dixit, P. M. (2002). Temperature distribution during electro-discharge abrasive grinding. *Machining Science and Technology*, 6(1):97–127.
- Yager, R. and Filev, D. (1994). Approximate clustering by the mountain clustering,. *IEEE Transactions on Systems Man and Cybernetics*,, 24,:338–358.
- Yager, R. and Filev, D. (1995). *Essentials of Fuzzy Modeling and Control*. New York: John Wiley & Sons, Inc. John Wiley & Sons, Inc.
- Yeo, S., Kurnia, W., and Tan, P. (2008). Critical assessment and numerical comparison of electro-thermal models in EDM. *Journal of Materials Processing Technology*, 203(1-3):241–251.
- Youshen, Y. and Yoshitsugu, M. (1992.). Finite element analysis of residual stress in electrical discharge machining,. *Chiba, Japan*.
- Yu, Z., Masuzawa, T., and Fujino, M. (1998). Micro-EDM for three-dimensional cavities - development of uniform wear method. *CIRP Annals - Manufacturing Technology*, 47(1):169–x34.
- Zadeh, L. (1965). Fuzzy sets. *Information and Control*, 8(3):338–353.
- Zadeh, L. A. (1973). Outline of a new approach to the analysis of complex systems and decision processes. *IEEE Transactions on Systems, Man and Cybernetics*, SMC-3(1):28–44. cited By (since 1996) 1886.
- Zeid, O. (1997). On the effect of electrodischarge machining parameters on the fatigue life of AISI D6 tool steel. *Journal of Materials Processing Technology*, 68(1):27–32.
- Zwilsky, K. M. (1990). ASM international handbook properties and selection: Irons, steels, and high-performance alloys. 1.

## BIODATA

**MOHAN KUMAR PRADHAN**  
**mohanrkl@gmail.com, mohankpradhan@manit.ac.in**  
**Mob: - + 91 94371-88111, 8889152316**  
**S/O- Sri Prafulla Chandra Pradhan**  
**At- Kadokora, P.O- Jayant garh.**  
**Dist- West singhbhum,**  
**Jharkhand State, PIN-833214**

### *EDUCATION*

2010 Ph. D. Dissertation Submitted

1999 M.Tech, N.I.T. Rourkela.

### *Personal Information:*

Date of Birth: 15-03-1973

Nationality Indian

### *WORK EXPERIENCE*

**Sr. Lecturer**, Dept. of Mech. Engg., SIET, Dhenkanal, Odissa, India, 2003-2006.

**Lecturer**, Dept. of Mech. Engg., PIET, Rourkela, Odissa, India, 2000-2002.

### *PROFESSIONAL AFFILIATIONS*

Associate member of Institution of Engineers (India) A/517324/9

Life Member of Indian Society of Technical Education LM-44193

Member of the IACSIT 53122865k

International Association of Engineers (IAENG) 105531

---



---

### Published papers in referred journals

---

1. M. K. Pradhan and C. K. Biswas, "Neuro-fuzzy and Neural network based prediction of various responses in Electrical discharge machining of AISI D2 Steel," *International Journal of Advance Manuf. Tech. Springer*, Vol. 50, pp-591-610/2010.
2. M. K. Pradhan and C. K. Biswas, "Investigation in to the effect off process parameters on Surface roughness in EDM of AISI D2 Steel by Response Surface Methodology', *International Journal of Precision Technology*, Inderscience, Vol. 2, No.1, pp-64-80, 2011.

---

### Published papers in journals (Outside the scope of present work)

---

1. M. K. Pradhan and C. K. Biswas, "Comparisons of neural network models on surface roughness in Electrical Discharge Machining", *Proc. IMechE Vol. 223 Part B: Journal of Engineering Manuf.*, Vol. 223, Number 7, pp- 801-808/ 2009.
2. M. K. Pradhan, R. Das, and C. K. Biswas, "Prediction of Surface Roughness in Electrical Discharge Machining of D2 steel Using Regression and Artificial Neural Networks Modelling," *Journal of Machining and Forming Technologies*, vol. 2 No- 1-2, pp-25-46, 2009.
3. M. K. Pradhan and C. K. Biswas, "Investigations into the effect of process parameters on MRR in EDM of AISI D2 steel by response surface methodology," *Journal of Mechatronics and Intelligent Manufacturing (JoMIM)*, Vol. 1, issue no.3-4, 2010.
4. M. K. Pradhan and C. K. Biswas, "Multi-response optimisation of EDM AISI D2 tool steel using response surface methodology," *International Journal of Machining and Machinability of Materials (IJMMM)*, Vol .9, pp- 66-85, 2011.

5. M. K. Pradhan and C. K. Biswas, "Predictive modelling and analysis of surface roughness in electro-discharge machining of D2 tool steel using regression and neural networks approach", *International Journal of Design and Manufacturing Technologies*, vol.-3, No-2, 2009.
6. M. K. Pradhan, R. Das and C. K. Biswas, "Prediction of material removal rate using Recurrent Elman Networks in Electrical Discharge Machining of AISI D2 tool steel", *International Journal of Manufacturing Technology And Industrial Engineering. (IJMTIE)*1(1) June 2010, pp. 29-37.
7. R. Das, and M. K. Pradhan "Prediction of surface roughness in Electrical Discharge Machining of SKD 11 steel using Recurrent Elman Networks", *Jordan Journal of Mechanical and Industrial Engineering (JJMIE)*(In Press).
8. M. K. Pradhan and R. Das, "Recurrent neural Networks in estimation of MRR in EDM of AISI D2 tool steel", *Proc. IMechE Part B: Journal of Engineering Manuf.* (In Press).
9. M. K. Pradhan and C. K. Biswas, "Neuro-fuzzy model and regression model a comparison study of MRR in electrical discharge machining of D2 tool steel," *International Journal of Engineering and Applied Sciences*, vol. 5, pp. 328-333, 2009.
10. M. K. Pradhan and C. K. Biswas, "Modelling and analysis of process parameters on surface roughness in EDM of AISI D2 tool steel by RSM approach," *International Journal of Engineering and Applied Sciences*, vol. 5, pp. 346-351, 2009.
11. M. K. Pradhan and C. K. Biswas, "Investigating the effect of machining parameters on EDMed components A RSM approach", *International Journal of Mechanical Engineering*, 7,No-1 pp. 47-64, 2010.

---

### Articles presented in International/National Conferences

---

1. M. K. Pradhan and C. K. Biswas, "Neuro-fuzzy model on material removal rate in electrical discharge machining in AISI D2 steel," in *Proceedings of the 2nd International & 23rd All India Manufacturing Technology, Design and Research Conference (AIMTDR) Conference*, vol. 1, (IIT Madras, Chennai, India), pp. 469–474, Dec 2008.
2. M. K. Pradhan and C. K. Biswas, "Influence of process parameters on surface roughness in EDM of AISI D2 steel: A RSM approach," in *International Conference on Emerging Research and Advances in Mechanical Engineering ERA*, vol. 1, (Velammal Engg. College, Chennai, India.), pp. 709–714, March 2009.

---

### Articles presented in International/National Conferences (Outside the scope of present work)

---

1. M. K. Pradhan and C. K. Biswas, "Modelling of residual stresses of EDMed AISI 4140 steel," in *Proceedings of the International Conference on Recent Advances in Materials, Processing and Characterization (RAM)*, vol. 1, (V.R.S. Engineering College, Vijayawada, India.), pp. 49–55, July, 2008.
2. M. K. Pradhan and C. K. Biswas, "Modelling of machining parameters for MRR in EDM using response surface methodology," in *Proceedings of the National Conference on Mechanism Science and Technology: From Theory to Application*, vol. 1, (NIT, Hamirpur, India.), pp. 535–542, Nov 2008.
3. M. K. Pradhan, R. Das, and C. K. Biswas, "Predictive modelling of surface roughness in electrical discharge machining using neural networks: Comparison study," in *Proceedings of the International Conference on Fascinating Advancement in Mechanical Engineering*, vol. 1, pp. 7–13, December 2008.
4. M. K. Pradhan and C. K. Biswas, "Influence of process parameters on MRR in EDM of AISI D2 steel: A RSM approach," in *Proceedings of the Interna-*

- 
- tional Conference on Advances in Mechanical Engineering(ICAME-08)*, vol. 1, (S.V.N.I.T, Surat, India), pp. 872–877, Dec 2008.
5. R. Das and M. K. Pradhan, “Comparison of regression and feed forward network models for surface roughness prediction with EDMed surface,” in *International Conference on Emerging & Futuristic System and Technology, (ICE-FST’09)*, vol. 1, (Laxmi Devi Inst. of Engg. & Tech., Chikaani, Rajasthan, India), 2009.
  6. M. K. Pradhan, R. Das and C. K. Biswas, “Prediction of material removal rate using recurrent Elman networks in electrical discharge machining of D2 steel,” in *Proceedings of the International Conference on Advances in Mechanical Engineering(ICAME-09)*, , vol. 1, (S.V.N.I.T, Surat, India.), August 2009.